Hybrid convolution quadrature methods for modelling time-dependent waves with broadband frequency content

Jacob Rowbottom

Supervisors: Dr. David Chappell and Dr. Jonathan Crofts

A thesis submitted in partial fulfilment of the requirements of Nottingham Trent University for the degree of Doctor of Philosophy

September 2021

Abstract

This work proposes two new hybrid convolution quadrature based discretisations of the wave equation for interior domains with broadband Neumann boundary data or source terms. The convolution quadrature method transforms the time-domain wave problem into a series of Helmholtz problems with complex-valued wavenumbers, in which the boundary data and solutions are connected to those of the original problem through the Z-transform. The hybrid method terminology refers specifically to the use of different approximations of these Helmholtz problems, depending on the frequency. For lower frequencies we employ the boundary element method, while for more oscillatory problems we develop two alternative high frequency approximations based on plane wave decompositions of the acoustic field on the boundary. In the first approach we apply dynamical energy analysis to numerically approximate the plane wave amplitudes. The phases will then be reconstructed using a novel approach based on matching the boundary element solution to the plane wave ansatz in the frequency region where we switch between the low and high frequency methods. The second high frequency method is based on applying the Neumann-to Dirichlet map for plane waves to the given boundary data.

Acknowledgements

I would like to thank the following people, without whom I would not have been able to complete this research.

I would like to thank my supervisor, Dr. David Chappell, for his invaluable advice, continuous support, and patience during my PhD study. His immense knowledge and experience has encouraged me through my academic research. I would also like to thank my co-supervisor Dr. Jonathan Crofts for his feedback and support during my studies. I would like to thank all my colleagues and friends from the New Hall Block room 247, with a special thanks to Dr. Martin Richter for proof reading my thesis.

Finally, I would like to express my biggest gratitude to my partner, Nat Isherwood, my parents, Dave and Mel Rowbottom, and my brother, Josh Rowbottom. Without their tremendous understanding, inspiration and encouragement over the past few years, it would have been impossible for me to have completed my research.

Declaration

I declare that the research contained in this thesis, unless otherwise formally indicated within the text, is the original work of the author. The thesis has not been previously submitted to this or any other university for a degree, and does not incorporate any material already submitted for a degree.

Signed: J Rowbottom

Dated: 26/04/2022

Publications resulting from this research

1. J. Rowbottom, D.J. Chappell, Towards a hybrid Convolution Quadrature method for the wave equation, *Proceedings of Conference UKBIM12*, (2019), pp. 9–14, .

2. J. Rowbottom, D.J. Chappell, On the development of a hybrid model based on the Convolution Quadrature Boundary Element Method, *Proceedings of Conference WAVES 19*, (2019), pp. 176–177.

3. J. Rowbottom, D.J. Chappell, A hybrid BEM/DEA convolution quadrature method for modelling time-dependent acoustic wave problems with broadband frequency content, *Proceedings of Conference e-Forum Acusticum 2020*, (2020).

4. J. Rowbottom, D.J. Chappell, On hybrid convolution quadrature approaches for modelling time-domain wave problems with broadband frequency content, submitted to *Int. J. Numer. Methods. Eng.*, **122** (4) (2021), pp.7581–7806.

Contents

List of symbols and operators

Ω	Domain of the body
Γ	Boundary of the domain
Φ	Solution to the wave equation
$\boldsymbol{x}$	Position variable in Cartesian coordinates
t	Time variable
P	Point source excitation term
c	Wave speed
ω	Angular frequency
u	Solution to the Helmholtz equation
k	Wavenumber
$\boldsymbol{x}_0$	Source point position in Cartesian coordinates
$\hat{\mathbf{n}}$	Unit normal vector pointing outwards of the domain
G_k	Free-space Green's function for the Helmholtz equation
σ	Density function for the Indirect BEM
L_k	A boundary integral operator
M_k	A boundary integral operator
S_k	Single-layer potential

D_k	Double-layer potential
b_m	Basis functions
ϕ_j	Unknown basis coefficients
r_m	Residual term
$\boldsymbol{x}_i$	Collocation point in Cartesian coordinates
E_m	An element on a divided boundary
s	Arclength
s_i	Collocation point parameterised by arclength
h	Boundary element length
L	Boundary length
γ_ϵ	Euler - Mascheroni constant
G_0	Free-space Green's function for the Laplace equation
T	Final time
F	Neumann boundary condition
U	Incident solution of the wave equation
V	Reverberant solution of the wave equation
P_0	Temporal source profile
ζ	Laplace transform parameter
G	Free-space Green's function for the wave equation
H	Heaviside step - function
$\mathcal{S}$	Time-domain single-layer potential
$\mathcal{D}$	Time-domain double-layer potential
$\mathcal{V}$	A time-domain boundary integral operator
$\mathcal{K}$	A time-domain boundary integral operator
Δt	Time-step
N	Number of time-steps
$\gamma(z)$	Quotient of the generating polynomials of a multistep method

λ	Radius of circular contour
$\widetilde{N}$	Number of frequencies
$\widetilde{F}$	Transformed Neumann boundary condition in the frequency domain
M	Number of boundary elements
α	Bandwidth of the Gaussian pulse wave
t_0	Position of the peak of the Gaussian pulse wave
S	Phase
A_κ	Amplitude
$\widetilde{A}$	Time - dependant amplitude
$\widetilde{S}$	Time - dependant phase
$\boldsymbol{p}$	Momentum coordinate
$\mathcal{H}$	Hamiltonian
$\boldsymbol{X}$	Phase - space coordinate
$\mathcal{E}$	Energy
$\mathcal{L}^\tau$	Frobenius - Perron Operator
ρ	Stationary density
w	Dissipative factor
θ	Local angle formed between an outgoing ray trajectory and a unit normal vector pointing inwards from the boundary
ϕ^τ	Continuous boundary flow map
$\phi_{i,j}$	Discrete boundary flow map
$\mathcal{B}_j$	A boundary integral operator
D	Euclidean distance
μ	Damping coefficient
ρ_0	Initial density
ρ_Ω	Interior density
Θ	Ray trajectories parametrised by polar angle

χ	Test functions
Ψ	Global direction set
Λ	Number of ray directions in the global ray set
φ	Local ray directions
I_κ	Sub divisions of local direction range
ξ	Angle between interior normal vector and the ray leaving the boundary
$N_{\boldsymbol{x}}$	Number of interior points
γ_κ	Unknown gamma coefficients
Θ_0	Angle the Gaussian pulse from the Neumann boundary condition enters the domain
W	Normal derivative of the Neumann boundary condition

List of abbreviations

BDF2	Second order Backwards Difference Formula
BE	Backward Euler
BEM	Boundary Element Method
BIE	Boundary Integral Equation
BVP	Boundary Value Problem
CQ	Convolution Quadrature
CQBEM	Convolution Quadrature Boundary Element Method
DEA	Dynamical Energy Analysis
EOC	Estimated Order of Convergence
FEM	Finite Element Method
FFT	Fast Fourier Transform
FP	Frobenius-Perron
GPU	Graphics Processing Unit
HFA	High Frequency Approximation
ODE	Ordinary Differential Equation
PDE	Partial Differential Equation
SHFA	Simple High Frequency Approximation

Chapter 1

Introduction

The understanding and prediction of wave behaviour is important for a wide range of applications in acoustics, elasticity, electromagnetics and quantum mechanics. Although waves are inherently time-dependent in nature, simplified single frequency models are often employed since they reduce the dimensionality by assuming time-harmonic oscillations. However, fully time-dependent models are essential when the wave sources themselves undergo fundamental changes during the time period being considered [139]. Examples include linear vibrations induced by a structural shock, acoustic emissions in the presence of structural fatigue and electromagnetic compatibility problems in malfunctioning devices. As well as requiring full time-domain simulations, these wave problems also often include high frequency content; this is clearly the case when modelling sharp impulses such as shocks, but is also true of acoustic emissions from large built-up structures [3, 175]. The importance of high-frequencies for electromagnetic wave applications is also increasing due to the demand for ever faster mobile communication networks using wave further up the electromagnetic spectrum.

Significant progress has recently been made in time-dependent wave simulation methods; notable are the new-found tractability of finite-difference methods due to the emergence of graphics processing unit (GPU) processing [32, 134], the relatively recent development of full space-time adaptive grid discretisations [73, 142], and the continued rise of the Convolution Quadrature (CQ) method including (implicit) high-order Runge-Kutta implementations for a variety of wave equations [15, 20]. Despite these recent advances, all numerical wave equation solvers share the limitation that high frequency content in the time-domain

signal requires a discretised model containing many degrees of freedom. The computational cost will scale with at least the square of the upper frequency band limit, and often worse depending on the choice of method and the number of spatial dimensions to be modelled.

The remainder of this chapter consists of a detailed literature review on numerical methods for the wave equation, the Convolution Quadrature Boundary Element Method (CQBEM) and high frequency methods. In Chapter 2, we solve the Helmholtz equation via both the direct and the indirect Boundary Element Method (BEM) for a variety of boundary conditions. We numerically solve the resulting Boundary Integral Equations (BIEs) using either the collocation method or the Galerkin method, with both constant and linear basis functions and make comparisons between the results. In Chapter 3, we will apply a direct convolution quadrature boundary element method to numerically solve an initial boundary value problem for the wave equation with Neumann boundary conditions. Numerical results are presented for different domains. In Chapter 4, we approximate the solution of the two-dimensional Helmholtz equation at high frequencies via Dynamical Energy Analysis (DEA), which uses a boundary integral operator based model for transporting densities along ray trajectories in phase-space, between intersections with the boundary of a domain or subdomain. We perform numerical experiments for a number of domains when considering either a source point excitation or a constant line source expressed as a Dirichlet boundary condition. In Chapter 5, we propose the development of a new hybrid method in which the low frequency content will be modelled via a convolution quadrature boundary element method and the high frequency content will instead be approximated by either DEA or via an incident illumination approximation where only the direct contribution of the source term on the boundary is considered and reflected contributions are assumed to play an insignificant role. Finally in Chapter 6, we conclude our research from this work and outline areas for future study.

1.1 Numerical methods for the wave equation

Numerical methods are used to find approximations of solutions to differential equations and are typically used to solve problems in real world applications that are of complex nature. It might take a long time to compute a result to sufficient accuracy and some methods might never provide a high enough

accuracy. Since the birth of the modern computer in the second half of the 20th century, the rapid growth in computational power and resources has fuelled the development of many numerical methods, such as the finite difference, finite element and boundary element methods [4].

1.1.1 Finite difference method

The finite difference method involves constructing a mesh or grid, by discretising the independent variables typically at equally spaced nodes where we approximate the dependent variable. We then replace the derivatives in the differential equation with finite difference formulae that are derived using Taylor's theorem. The result is then a system of algebraic equations that are solved to find an approximate solution. The method was first developed by Euler in 1768 in one dimension [61], but was then further developed by Runge in 1908 [162]. Twenty years later Courant, Friedrichs and Lewy applied the finite difference method to find an approximate solution to the Dirichlet problem for Laplace's equation [190]. This was also one of the earliest numerical methods to be applied the wave equation. The derivatives are approximated by difference formulae as discussed in Mitchell and Griffiths [137] for up to two spatial dimensions. However, the method is limited by the great amount of computation and memory required, particularly in three dimensions. Fine discretisations in space and time are usually required to meet the constraints of accuracy, stability and minimum grid dispersion. Villarreal and Scales [195] overcame these limitations by using the domain decomposition method to split the domain into a number of sub-domains and then applied parallel processing techniques to solve for each sub-domain concurrently.

Finite difference methods have been used to solve three-dimensional time-domain electromagnetic problems such as the one considered in [177]. In [177] the electromagnetic problem is solved via a tetrahedral mesh based method known as Unstructured Transmission Line Modeling (UTLM). The UTLM combines the use of a tetrahedral mesh to discretise in space and a time domain electromagnetic solver that is unconditionally stable. High level of parallelisation makes the method able to consider solving broadband large-scale simulations in an accurate and stable manner [135, 178, 179]. We remark that not all finite difference methods use equally spaced nodes or meshes such as the method discussed in [66] which adopts an unstructured mesh finite difference time-domain (FDTD) method for solving electromagnetic problems. The method considers

using an unstructured co-volume staggered mesh and a generalisation of the Yee FDTD method [204]. The use of staggered meshes results in an explicit algorithm that is second order accurate in both space and time. The method is also advantageous due to its of low computational cost and the scheme preserves the energy and amplitude of waves, is free of divergence and can be parallelised. Earlier work in electromagnetic using the FDTM can be found in [29, 68, 126]. In general the finite difference method is easy to implement for simple problems and geometries. However the method becomes more difficult to implement if the geometry becomes too complex or irregular, particularly for implementing boundary conditions, and may require a large number of mesh points to discretise the full domain to sufficient accuracy.

1.1.2 Finite element method

The finite element method (FEM) was originally proposed in 1943 by Courant [49], but was then later popularized in the 1960s by Argyris and Clough through their computational work [21]. The method involves discretising the domain into elements, which contain nodes that represent an unknown value in a system of equations. Therefore each element has an associated set of equations. Combining all elements together leads to the construction of a system of equations, which may be solved to find an approximate solution. The first application of FEM in acoustic problems was discussed by Gladwell in 1965 [72]. In the 1970s, further research was completed in acoustics using FEM by Craggs, Milner and Bernhard, who applied the method to analyse frequency responses and model acoustics in rooms, cavities and irregular enclosures [50, 51, 52, 136].

The advantage of the finite element method over the finite difference method is that it can be easily applied to irregular domains and for all types of boundary conditions. However, the FEM is not efficient at approximating spatial variables for higher frequencies due to the interpolation and dispersion errors. The dispersion errors arise from the difference between the numerical wavenumbers and the physical wavenumbers, such that they become the dominant error term at high frequencies [193]. In addition, at higher frequencies the FEM requires a larger number of elements and computational expense in order to achieve errors within an appropriate tolerance. More recent research has been conducted for FEM in room acoustics by Okuzuno [143], in which he compared an explicit time-domain FEM with an iterative model, and discovered that the FEM model was better for modelling higher acoustic impedances. The FEM has been found

to not always be effective when solving wave propagation problems using piecewise polynomial approximation techniques [75, 89, 115] due to the accuracy of the numerical solution decreasing as the wavenumber increases.

For solving transient wave problems via the FEM, the numerical wave propagation velocity may become significantly different to the physical velocity due large period elongations and amplitude decay [24, 46]. Therefore when high frequency content is present, we find significant errors in the numerical solution unless the mesh is fine enough to model the rapidly varying waves [81]. For the case of time harmonic wave problems, the partition of unity FEM was proposed by Kacimi to calculate the solution at high frequencies [95]. For this approach the wave solutions are incorporated into the spatial approximation, which is difficult when solving practical wave problems as we do not usually know which waves need to be calculated [81]. Many smoothed FEM based approaches have also been shown to reduce numerical dispersion errors at low to mid frequencies in interior problems [85]. The FEM has proven to be effective in the low frequency range for structural vibration and acoustic problems, however for high frequencies the wavelength becomes very small and therefore a large number of elements are required for the adequate resolution of the wave behaviour.

1.1.3 Boundary element method

Boundary element methods (BEMs) were pioneered by Rizzo [155] and Jawson [92] in the 1960s with their work on integral equations for boundary value problems (BVPs), and since the late eighties BEMs are becoming more popular for applications in physics and engineering [97, 203]. The BEM involves reformulating a partial differential equation (PDE) in terms of an integral equation and applying boundary conditions, so that the integral equation is defined on the boundary of the domain. The resulting equations are known as boundary integral equations (BIEs). The BEM requires us to discretise along the boundary only, whereas with the finite element method and finite difference method, we discretise over the whole domain. This reduces the complexity of calculation as the dimension of the problem is reduced and results in a more computationally efficient model to solve. For these reasons, we shall use the boundary integral method to solve the interior acoustic problem. Since the introduction of BEM, a number of different approaches have been developed for its application to the wave equation, which we discuss below - see also Costabel [48].

Time stepping

Time stepping methods reduce the hyperbolic problem of the wave equation to an elliptic problem by using a time discretisation of the initial boundary value problem. The difficulty is that when solving the problem at each time step we require a new non-zero initial condition, that is given by the problem from the previous time step. This means that a particular solution of the stationary problem must be included in the solution at each time step. Methods have been derived to overcome this issue, such as Newton potentials which require the whole domain to be discretised. This defeats the purpose of using the boundary element method to some extent, as one of its main advantages is that it only discretises over the boundary rather than the whole domain. Some alternative methods are discussed by Costabel [48], such as fast solution methods using radial basis functions (dual reciprocity method) and higher fundamental solutions [140, 146].

Another idea is to consider all the time steps together as a discrete convolution equation. The discrete convolution operator, which has (time-dependent) coefficients that are elliptic partial differential operators, has a fundamental solution that can be used to construct a boundary integral method. This fundamental solution can be given explicitly for simple time discretisation schemes, such as the backward Euler method [25], or more generally can be constructed from Laplace transforms using the operational quadrature method of Lubich [121]. However, it is known that the application of a time-domain BEM may lead to instabilities in the time-stepping methods [33]. This disadvantage causes issues for solving engineering problems using a time-domain BEM [82, 130]. These issues may be overcome by a careful choice of A-stable time stepping method in the operational quadrature method, as discussed in further Section 1.2.

Space-time integral equations

Space-time integral equations have been applied to wave propagation problems since the 1960s. This method uses the fundamental solution of the initial value problem. The boundary integral equations are either constructed directly via Green's second identity or indirectly using single and double layer potentials [127, 187]. The integral equations obtained are of convolution type in time. Numerical methods constructed from space-time integral equations are global in time, meaning they compute the solution in one step for the entire time

interval [48].

Friedman and Shaw [64] and Mitzner [138] were the first to apply the collocation boundary element method to the hard surface scattering problem in the 1960s. However, since then the increase of available computational power has made longer run times feasible revealing that there are problematic instabilities in the time marching solutions [28, 163]. A number of methods have been suggested to resolve this. One approach, developed by Rynne [164], filtered out the instabilities by introducing space and time averaging. A review of the various schemes proposed is given by Davies and Duncan [53]. Birgisson et al. [28] applied a modified time stepping method to improve the stability of their schemes. One scheme involved halving alternate time steps, which did improve stability but instabilities could still develop at later times. Another scheme involved increasing the current time step by a small increment and was found to eliminate any evidence of instability for a sufficiently large value. Yu et al. [206] applied a similar technique to a two-dimensional acoustic problem and showed that the stability of the results was greatly improved by increasing the current time step. However, this method introduces amplitude decay, meaning that high frequency responses are damped out of the solution [36].

In 1983, Mansur developed a direct BEM formulation in the time-domain for the scalar wave equation and for elastodynamics problems with zero initial conditions [127]. This is of interest to engineers due to the variables representing physical quantities. Antes then presented this formulation for elastodynamics with non-zero initial conditions in [6].

Ding et al. [54] numerically solved the space-time integral equations by applying the Galerkin method for the problem of hard surface scattering in the time-domain. In this case the boundary integral equations are written in a variational formulation and the discrete scheme is written in a matrix operator form, which preserves the time convolution character of the boundary integral equations. An explicit time-marching scheme is formed when a Courant-Friedrichs-Lewy condition is applied to the time-step. Ha-Duong [79] later extended this study to the case of an absorbing obstacle. Ha-Duong et al. [80] also derived an integral equation that combines the time and normal derivatives of the classical integral equations for the surface solution and proved the stability of the approach. However, variational Galerkin methods can be difficult to implement due to evaluating high dimensional integrals and dense matrices, which makes it difficult to model large scale problems effectively [38]. Yu et al. [207] compared the Galerkin and collocation methods for the two-dimensional acoustic radiation

problem. The results showed that for this problem the Galerkin method gave stable results in cases that the collocation method was unstable. The linear system that arises from a classical Galerkin discretisation of the retarded potential boundary integral equations [14] leads to a Toeplitz system matrix, where the matrix blocks are sparse. However, the numerical quadrature for computing the coefficients of the system matrix has to be computed over intersections of the boundary element and the region over which the wave has travelled. Computing integrals over these intersections is difficult to implement in general and we therefore seek alternative approaches.

Recently, adaptive space-time mesh refinements have been applied to the time-domain BEM formulation of the wave equation. These adaptive methods have been explored by Gläefke [73] for two-dimensional problems, for which he does not separate the time-domain from the spatial domain, but instead refines the mesh of a space-time cylinder. The adaptive mesh refinement allows flexibility as we can have a more refined grid at a specific area of our mesh that needs greater precision. However, this flexibility comes at a cost as for each time-step one has to solve a full space-time system [208]. Gimperlein et al. [69, 70, 71] have further investigated adaptive space-time mesh refinement for modelling sound emission from tyres.

Fourier and Laplace transforms

These methods involve solving frequency domain Helmholtz problems for a range of (possibly complex) frequencies and then transforming them to the time-domain using a numerical method for the inversion of the Fourier or Laplace transform. Laplace and Fourier transforms can be used to transform from the time -domain to the frequency domain to solve problems for many frequencies. The advantage of the using these methods is that instead of solving a problem in space and time, such as for the space-time integral equations, we instead solve a system of Helmholtz boundary integral equations in space only, at these fixed frequencies. Early examples of work using these transforms includes Dubner and Abat [55] and Durbin [56]. As well as these works, an example of solving transient problems with non-homogeneous initial conditions using a discrete Fourier transform can be found in [128]. Here the inverse transformation is performed using an approximation based on linear multi-step methods for ordinary differential equations, which was first introduced as the operational quadrature method by Lubich [119], and will be discussed further in the next section.

1.2 Convolution quadrature BEM

We now take a more in-depth look at boundary element methods via Fourier and Laplace transforms and in particular the convolution quadrature boundary element method (CQBEM). We note that convolution quadrature (CQ) is an alternative name for Lubich's operational quadrature that is more commonly used in the context of numerically solving the wave equation. The CQBEM employs a convolution quadrature approach for the time discretisation and a boundary element method for the space discretisation. The CQ approach was developed by Lubich in the late eighties [119, 120, 121] and Lubich and Schneider [122]. The method provides a simple way to obtain a stable time stepping scheme using the Laplace transform of the kernel function, due to an implicit regularization in time [153]. For the discretisation of boundary integral equations, its main advantage is that it avoids having to evaluate the convolution kernel in the time-domain and one instead solves a simplified system of frequency domain boundary integral equations in the spatial region [153]. In this section we discuss the literature surrounding different projection methods that can be applied for the space discretisation. Projection methods approximate the solutions of boundary integral equations by projecting them onto finite dimensional sub-spaces, meaning that the approximate solution can be expressed as a linear combination of a finite set of basis functions [4, 7, 102].

1.2.1 Galerkin method

The Galerkin method generates an approximate solution by assuming it can be expressed in the form of a linear combination of basis functions and imposing a weak form of the original integral equation. This involves multiplying the integral equation by each of the basis functions in turn and integrating over the boundary. Imposing that the weak form is solved exactly for each basis function generates a set of equations that can be solved to give an approximate solution. This involves computing an additional boundary integral, resulting in a more complicated implementation and greater computational costs than most alternative methods [4]. However, the Galerkin method has a well-studied and reasonably widely applicable stability and convergence theory [13, 191], and can be applied to problems with singular integrals [194].

Since Lubich first developed the convolution quadrature method in the eighties, additional refinements have been proposed to reduce the computational

complexity of the method. Hackbusch et al. [77] combined Fast Fourier Transform (FFT) techniques with a data sparse approximation so that the matrix blocks are approximated by data sparse representations based on a simple cut off strategy. This reduces the storage cost without changing the computational complexity of the method and was extended by Kress and Sauter [103] to reduce the storage further. More research on this approach was completed by Banjai and Sauter [15], who developed a variant of the panel clustering method [77] to further reduce the storage and computational costs. The mathematical analysis within this research provided asymptotic estimates with significantly improved storage and computational costs compared to the previously proposed approaches for the solution of the wave equation using the convolution quadrature method.

More recently, Banjai and co-authors [16, 17, 18] have made significant progress in developing CQ methods for time-dependent wave simulations, including high-order Runge-Kutta implementations for a variety of wave equations. Betcke et al. [26] considered a convolution quadrature formulation for the parallel space-time evaluation of the wave equation. In particular, they decouple the number of frequency domain solutions from the number of time steps. This allows one to overresolve in the frequency domain by computing more frequency solutions than there are time steps. This is important if the overall error is dominated by the convolution quadrature approximation and provides exponentially fast convergence as the number of frequencies is increased.

1.2.2 Collocation method

The collocation method involves approximating the solution to an integral equation by assuming that the solution can be expressed as a linear combination of basis functions and then imposing that the integral equation must be solved exactly at a finite number of points, known as collocation points. The collocation method is relatively easy to implement, including for the singular integrals typically encountered in boundary element methods.

The first direct collocation CQBEM approach was proposed by Schanz and Antes [167], who showed that a critical time step size exists such that for any value below this critical time step, the method becomes unstable. This critical value depends on the underlying multistep method. The CQ method is particularly useful for solving visco-elasticity and poroelasticity problems, where the fundamental solutions are only available in closed form in the frequency

domain [168, 170]. The direct collocation CQBEM was then extended to other applications such as 3D viscoelastic and 3D elastodynamic problems by Gaul and Schanz [67], as well as in poroelastic applications by Schanz [169, 170].

The first direct collocation formulation of the CQBEM for the 2D scalar wave propagation problems was employed by Abreu, Carrer and Mansur [1], in which the authors used piecewise linear basis functions. The results were reliable and depended on the choice of time step for the stability of the results. In 2006, Abreu, Carrer and Mansur [2] developed CQBEM collocation schemes with pseudo-force initial conditions. This method consists of replacing the initial conditions by pseudo-forces, as previously CQ formulations were only applied to problems with homogeneous initial conditions. In 2010, Schanz applied Banjai's CQBEM [15] formulation to elastodynamics with a collocation based implementation [171]. The results showed that the method reduces the storage requirement to the size of one complex valued system matrix and shows the same sensitivity to the time step size as the older formulation presented by Schanz [170]. However, the limitation of this reduction is that a system of equations has to be solved for each time-step.

In 2015 Schanz, Ye and Xiao [172] compared the convolution quadrature method with a discrete Fourier transform approach, both with the collocation boundary element method in space. Both methods have the same inverse transformation, however, the CQ approach uses complex frequencies and as a result the methods determine different numerical solutions. The numerical experiments show that the discrete Fourier transform needs fewer frequencies to be calculated and is consequently faster. However, the CQ method leads to lower error levels for a fixed mesh size. For this formulation, the CQ method is therefore more efficient than the discrete Fourier transform and fewer iterations are needed in the iterative linear system solver. This is due to the imaginary part of the complex frequencies in the CQ method improving the condition number of the resulting system matrix. The discrete Fourier transform would not be a suitable approach for the undamped acoustic wave equation problem we are considering, since the real frequencies can potentially coincide with cavity resonances leading to serious issues for the numerical solution scheme. Recently, a generalised CQ formulation with Runge-Kutta methods was applied to solve acoustic wave problems by Schanz [173]. The method allows for a variable adaptive time-step size and the results showed that the convergence order is preserved, even for non-smooth solutions. However, the order of convergence is limited by the spatial discretisation.

As discussed in [131, 132] and then summarised in [23] it is known that BIEs lead to less pollution effect (dispersion) than FEMs, a further advantage of implementing a BEM based method as opposed to the FEM or FDMs. Evidence of the pollution effect in FEMs and FDMs can be found in [8, 9, 90, 200]. The effect of numerical damping in the BEM for the solving the Helmholtz equation has been studied in [62], but the pollution effect for BEM is not primarily caused by a phase error but instead by numerical damping and it shows that the effect of numerical damping increases as the frequency values increase [132]. Therefore, we expect no pollution effect for the CQBEM scheme, but we do expect to see numerical damping. In a recent paper by Galkowski and Spence [65], it has been rigorously shown that the BEM for the Helmholtz scattering problem does not suffer from the pollution effect if hk is sufficiently small and the obstacle is non-trapping.

More recently, Mavaleix-Marchessoux et al. [133] numerically solved three-dimensional transient acoustic problems for large scale domains using a collocation based CQBEM. The high frequency content was approximated by an infinite plate model, which can be calculated simply. The high frequency approximation was found to be effective for dealing with high frequency boundary data approximating an underwater explosion and for large complex geometries.

1.3 High-frequency methods

For modelling high frequencies, the CQBEM will require a large number of boundary elements to model the more rapidly oscillating waves. When numerically solving the wave equation, the accuracy of the solution is determined by the number of elements or grid points. Therefore, when we consider large frequencies this approach is no longer feasible due to a large computational cost to retain appropriate accuracy. We seek a method for numerically solving the wave equation, where the boundary condition includes broadband frequency content. In this section we initially focus on methods for effectively treating high frequency waves.

1.3.1 Time-domain

Here we consider numerical methods for simulating waves at high frequencies using variants of geometrical optics [161], which are asymptotic approximations obtained when the frequency tends to infinity. Instead of oscillating wave

fields, which are modelled by standard wave equations, the unknowns are the phase and amplitude, which vary more slowly and hence are easier to calculate numerically. There are a number of different mathematical models that can be formulated for geometrical optics. One example is the kinetic formulation, which is based on the assumption that rays are trajectories of particles following Hamiltonian dynamics in which we want to determine a phase-space density function that satisfies the Liouville equation [58, 59]. Another formulation is to express the phase and amplitude as solutions of partial differential equations, where the phase function satisfies the eikonal equation and the amplitude satisfies a transport equation. Geometrical optics can also be formulated in terms of the ray equations, which are a system of ODEs obtained by applying the method of characteristics to the eikonal equation [57]. However, a drawback of geometrical optics is that the diffraction effects at boundaries are lost and the approximation breaks down at caustics. These issues can be addressed by more detailed models such as the geometrical theory of diffraction [99], which explicitly takes information from the domain and boundary condition to then add a term that includes diffraction.

There are a number of numerical methods to solve these high frequency wave models. Solutions of the ray equations can be approximated directly by solving the ODEs with numerical methods, giving a solution in terms of the phase and amplitude along a ray. Interpolation must be applied to obtain the quantities everywhere in the domain. This is the basis of ray tracing [34, 93, 107, 192] and is classically used to determine the travel time of a wave from one source point to all points in a domain, together with the corresponding amplitude at those points. One can obtain solutions at specific points via ray shooting [117], which shoots rays from the point source in different directions. The result at the receiver is interpolated from the solutions along rays. Alternatively, one can obtain a solution at a particular point via ray bending. In this method the ODEs are considered as a non-linear elliptic boundary value problem and can be solved using variants of Newton's method. The calculations can be performed simply for piecewise homogeneous domains, since the solutions of the ray equations are given at the boundaries and on the interfaces between media such that the rays are straight lines satisfying the reflection law and Snell's law at interfaces.

Ray tracing has many applications, including seismology [35], electromagnetics [117], and room acoustics. The first attempt to model room acoustics was in 1968 by Krokstad et al. [105], who utilised ray tracing for computing time-energy responses. Schroeder [174] proposed a similar idea but was limited to

two-dimensional spaces. Stephensen [185] showed that it was computationally advantageous to have multiple simultaneous receivers in one simulation to model concert halls. He also showed that more accurate results can be achieved by taking into account the distance of a ray path inside a receiver, which enabled the use of any shaped receiver [186]. The growth of available computational power allowed for further possibilities for the prediction of the acoustical behaviour in rooms. The rendering equation, which has been applied to computational graphics since the 1980s [98], has also been applied to room acoustics and led to a method known as acoustic radiance transfer [180]. However, its general application to complex domains requires simplifying assumptions to obtain an appropriate numerical solution with reasonable computational requirements. The stability of ray tracing solutions increases as the number of rays increased, but it is hard to know how many must be used to obtain reliable results. Vorländer has studied the relation between the number of rays and the obtained accuracy, and showed that the required number of rays is proportional to the volume of space [198]. Two reviews of geometrical optics in room acoustics can be found in [166, 199]. Recently, ray-based methods have been further developed for heterogeneous problems including ray approximations of the heterogeneous Green's function for medical applications [159].

Wave front methods are related to ray tracing, but instead of individual rays, the location of many rays emitted from one source is computed at fixed time points. Those points form a wave-front and its behaviour is tracked in phase-space, which is beneficial for problems including caustics. This method was first introduced by Vinje et al. [161, 196]. The level-set method was later introduced by Osher and Sethian [144], as a method for tracking interfaces and shapes by realising them as the zero-level set of higher-dimensional smooth surfaces. This technique has been applied to problems in multiphase flow, image processing and visualisation, see [145, 176] for example. Moment-based methods instead track the time dynamics of beams or interfaces in phase space [205]. Brenier and Corrias [31] originally proposed this method for finding multivalued solutions to geometrical optics problems in the one-dimensional homogeneous case. It was then developed further to two-dimensional problems by Engquist and Runborg [59, 160].

Transient statistical energy analysis (TSEA) is a variation of statistical energy analysis (SEA) which has been adapted to approximate shock-response problems. Statistical Energy Analysis is a method in which a system is divided up into subsystems whereby the energy density in each subsystem is assumed

to be approximately constant and the solution is assumed to be independent of the ray or wave direction [124], see the next section for more details on SEA. A number of authors have previously investigated the TSEA model, although often the energy variable is treated as the energy in a frequency band rather than a function of both time and frequency and mostly problems with only two subsystems are investigated. A disadvantage of TSEA is that due to its diffusive nature, it cannot predict localisation effects where, even at large times, energy remains localised in a subsystem [111]. Some contributions from authors who have achieved good accuracy using the TSEA method can be found in [106, 148, 157]. Whereas some work which demonstrates its limitations can be found in [87, 156, 188]. However, the poor results in some of the latter references may be due to the system or frequency range selected and because only a single realisation rather than ensemble of systems was investigated.

1.3.2 Frequency domain

Ray and front tracking methods, such as the ones discussed in Section 1.3.1, often become inefficient when considering frequency domain wave problems in bounded domains, such as to determine the wave field in a finite cavity driven by a continuous excitation. Multiple reflections of rays can lead to an exponential increase in the number of ray paths that need to be considered resulting in long and complicated computations. Frequency domain approaches have been developed to combat these issues, such as SEA [63, 124] and Dynamical Energy Analysis (DEA) [42, 189].

In SEA, a structure is split into subsystems and ergodicity of the underlying ray dynamics as well as quasi-equilibrium conditions in each subsystem are assumed [63]. That is, the energy density in each subsystem is assumed to be approximately constant and the solution is assumed to be independent of the ray or wave direction. These assumptions result in a simplified model of SEA equations based only on flow rates between subsystems [202]. SEA is a popular method for solving vibro-acoustic problems in the mid to high frequency range and was initially proposed by Lyon and Smith in 1962 [124]. The original formulation of SEA was based on the energy flow between pairs of coupled oscillators and is known as the modal approach to SEA. However, due to the implicit assumptions within the method Lyon developed, it does not provide a practical tool for calculating parameters used in an SEA model. Suitable methods for estimating these parameters were the subject of debate within the mechanical

engineering community [63], leading to a number of methods to obtain estimates of SEA parameters [125]. One method includes a representation of the SEA equations based on wave approaches, in which a complex subsystem is represented as a collection of propagating wavetypes. The energy storage capacity of a given subsystem is related to the expected velocity and dimension of the subsystem. This wave approach was analysed by Langley to model elastic wave transmission through plate/beam junctions [108]. The disadvantage of SEA is that the underlying assumptions are often hard to verify a-priori, or are only justified when an additional averaging over equivalent subsystems is considered, such as structures originating from the same production line that are identical up to manufacturing tolerances. These limitations have been discussed by Langley [109, 110] and more recently by Le Bot [112, 113, 114]. Improvements to SEA were made using random matrix theory by Reynders et al. in 2014 [154]. The method employs a nonparametric model of uncertainties in geometry, material properties and boundary conditions. The response of a nonparametric random subsystem is then defined by its full displacement as opposed to its total energy. The result is an efficient method that can be applied to a wider range of problems than SEA, with no additional assumptions.

Another approach is the energy finite element method developed by Nefske and Sung [141]. This approach is based on the heat conduction equation in steady state and leads to a continuous analysis of structures opposed to SEA's discrete analysis. This approach is well studied for the one-dimensional systems such as rods or beams [30, 201], but its wider applicability is unclear.

DEA is based on a linear operator approach for propagating ray densities and was first introduced in [189]. The solution in a subsystem is typically represented by a basis expansion, in contrast to SEA where the solution in each subsystem is typically represented by a single value, the mean ray density. One main advantage of DEA is that the choice of subsystem splitting is no longer important since some of the SEA assumptions are removed. The elements of a mesh can even be used as substructures where energy can flow freely between neighbouring mesh cells, providing flexibility for many potential applications. A number of approaches have been developed to obtain efficient discretisations of the DEA boundary operator. In [41, 42] a BEM for the stationary Liouville equation was proposed, which extended DEA to larger structures and three-dimensional applications. However, the high dimensionality and quadrature routines near singularities meant that the simulations required long computations. The Discrete Flow Mapping (DFM) [10, 11, 43, 44] approach was proposed

to improve the efficiency of these high-dimensional problems. DFM provides an efficient numerical implementation of DEA on meshes and facilitates the computation of phase-space densities on complex two-dimensional shell structures by making use of the geometric simplicity of typical mesh elements. Further extensions of DFM have been considered in [10] to model wave energy densities in three dimensions, in which the densities are transported along ray trajectories through tetrahedral mesh elements. Numerical results have demonstrated the convergence and efficiency of DFM for a full-scale vehicle cavity mesh [10].

1.3.3 Hybrid methods

Shorter and Langley developed a hybrid method [183] whereby a system can be split into "deterministic" components with only a few distinct natural frequencies modelled via the FEM and "statistical" components with high modal overlap, which are modelled with SEA. The modal overlap is the number of modes of a system that are excited at a given frequency. The FEM and SEA models are coupled together via a diffuse reciprocity relationship [182], which relates the two sets of variables obtained from these methods. Hawes et al. [84] extended Shorter and Langley's method [183] to predict the structural response under an impulsive and time-varying excitation by deriving a transient hybrid FE-SEA method. In this approach, a power balance equation that determines the power in each SEA subsystem was derived. This equation can be time-integrated, which leads to a time -domain version of the subsystem energies and deterministic response. Simulation results were provided for a system of two plates coupled by a beam. The results for the deterministic system exhibited oscillatory behaviour after an impulse, which was not predicted by the hybrid method.

Anderson et al. [5] recently developed a frequency/time hybrid integral equation for the time dependent wave equation in two and three dimensions. The method relies on a combination of a finite difference formula for the time discretisation and a Fourier transform to reduce the time-domain wave equation to a set of Helmholtz equations for a range of frequencies. A Nyström method is then applied to numerically solve the integral equations at all frequencies. A difficulty that arises when solving the Fourier integrand is the increase in oscillation as time increases, which requires finer discretisations resulting in larger numbers of frequency-domain models to solve. To address this issue, the hybrid method employs a smoothly time-windowed Fourier transformation

technique, which re-centers the solution in time and thus effectively handles the fast oscillations that occur in the solution as a function of the Fourier-transform variable. A new quadrature method is used to evaluate the windowed Fourier transform integral, which requires computation of certain discrete scaled convolutions that are evaluated by an FFT based algorithm. The results of this method show a fast convergence in both space and time. It can produce arbitrarily large time evaluation of scattered fields at $\mathcal{O}(1)$ cost, as well as being suitably parallelizable in time and space.

1.4 Summary and outlook

To begin, we investigated which numerical method would be the most suitable to approximate solutions to the wave equation. We considered the FDM, the FEM and the BEM, and it was determined that the BEM would be the most appropriate option. The BEM reformulates a PDE in terms of a BIE, which is simpler for implementing boundary conditions in comparison to the other numerical methods. The FDM and the FEM require a large number of mesh points in order to discretise a full domain to sufficient accuracy. The advantage of the BEM is that it is only necessary to discretise over the boundary, therefore reducing the dimensionality of the problem. We then discussed further the application of the BEM to the wave equation.

We decided that using Fourier and Laplace transforms would be a promising approach since it transforms time-domain wave problems to the frequency domain. The advantage of this is that we are now only required to solve a system of Helmholtz BIEs (in space), at fixed frequencies, as opposed to solving a problem in space-time. Therefore the problem has been simplified further. Alternative approaches, such as time-stepping methods, can lead to instabilities in the time-domain BEM.

We then took a more in-depth look at the BEM for the wave equation via Fourier and Laplace transforms, considering the CQBEM. The CQBEM employs a convolution quadrature method for the time-discretisation and a BEM for the space discretisation. We then looked further into the different projection methods that can be applied for the space discretisation, including the collocation method and the Galerkin method. We will investigate this further in Section 2.7 when we compare the two projection methods for discretising the BIE that arise when applying the BEM to the Helmholtz equation.

We discussed that the CQBEM would not be efficient for broadband boundary data since the system of integral equations would require a large number of time-steps and boundary elements to model the highly oscillatory wave components. We therefore considered other options to model the high frequency content. We decided that geometrical optics methods, such as ray tracing methods, were not a viable option since they become inefficient when considering reverberant wave problems in bounded domains. Multiple reflections can lead to an exponential increase in the number of ray paths to consider resulting in long computations. We then considered frequency domain approaches such as SEA and DEA. We found that a DEA approach would be more advantageous because it is more widely applicable than SEA with fewer limiting assumptions.

A new hybrid method will therefore be proposed for solving the wave equation subject to broadband frequency content whereby the lower frequency content will be modelled via the CQBEM and the higher frequency content will be modelled in terms of a plane-wave expansion. We will investigate how DEA can be used to determine the plane wave amplitudes and develop a novel method for recovering the phases. We will also propose a simple high-frequency approximation, based on the assumption that reflected wave contributions are very small compared to those related to the prescribed boundary data. This work has also been subject of a recent journal paper [158].

Chapter 2

Boundary element method for the Helmholtz equation

In this chapter we consider solving the two-dimensional Helmholtz equation via both the direct and the indirect BEM with a variety of boundary conditions. We numerically solve the resulting BIEs using either the collocation method or the Galerkin method, with both piecewise constant and piecewise linear basis functions. Numerical experiments are conducted to investigate the behaviour of the solution for a variety of different domains. A comparison is made in terms of both the accuracy and efficiency of the methods considered.

2.1 The Helmholtz equation

Let $\Omega \subset \mathbb{R}^2$ be a domain with boundary $\Gamma = \partial\Omega$. The inhomogeneous two-dimensional wave equation is defined as

$$\Delta\Phi - \frac{1}{c^2}\frac{\partial^2\Phi}{\partial t^2} = P(\boldsymbol{x}, t), \tag{2.1}$$

where Φ is the solution in two-dimensional space $\boldsymbol{x} = (x_1, x_2) \in \Omega$ and time $t > 0$. Here P defines a source term within Ω and $c > 0$ is the wave speed. The operator $\Delta = \frac{\partial^2}{\partial x^2} + \frac{\partial^2}{\partial y^2}$ denotes the Laplacian in $\mathbb{R}^2$. We assume that $\Phi(\boldsymbol{x}, t)$ has harmonic time dependence with frequency f, such that we can write the solution $\Phi(\boldsymbol{x}, t) = u(\boldsymbol{x})e^{i\omega t}$ and $P(\boldsymbol{x}, t) = g(\boldsymbol{x})e^{i\omega t}$, where $\omega = 2\pi f$ is the

angular frequency. Substituting this into (2.1) leads to

$$\Delta u e^{i\omega t} + \frac{\omega^2}{c^2} u e^{i\omega t} = g e^{i\omega t}.$$

By dividing through by $e^{i\omega t}$, we obtain the inhomogeneous Helmholtz equation

$$\Delta u + k^2 u = g, \tag{2.2}$$

where $k = \omega/c$ is the wavenumber [36]. In the following we will first consider the case when $g = 0$, corresponding to the homogeneous Helmholtz equation, together with one of the following boundary conditions:
Dirichlet condition (or pressure condition):

$$u(\boldsymbol{x}) = f(\boldsymbol{x}), \quad \boldsymbol{x} \in \Gamma, \tag{2.3a}$$

Neumann condition (or velocity condition):

$$\frac{\partial u(\boldsymbol{x})}{\partial \hat{\mathbf{n}}} = f(\boldsymbol{x}), \quad \boldsymbol{x} \in \Gamma, \tag{2.3b}$$

Robin condition (or impedance condition):

$$\frac{\partial u(\boldsymbol{x})}{\partial \hat{\mathbf{n}}} + h(\boldsymbol{x}) u(\boldsymbol{x}) = f(\boldsymbol{x}), \quad \boldsymbol{x} \in \Gamma, \tag{2.3c}$$

where the functions f, h are known and $\hat{\mathbf{n}}$ is the outward unit normal to Γ.

We will also consider the case when $f = 0$ in the above boundary conditions and $g(\boldsymbol{x}) = \delta(\boldsymbol{x} - \boldsymbol{x}_0)$ corresponding to a point source at $\boldsymbol{x}_0 \in \Omega$. The Dirac δ models an impulse or density of an idealised point mass as a function equal to zero everywhere except at zero - see Appendix A. In our numerical experiments later in Section 2.8.2, we consider this case together with the Neumann boundary condition (2.3b). We rewrite the solution to the Boundary Value Problem (BVP) (2.2), (2.3b), as $u(\boldsymbol{x}) = v(\boldsymbol{x}) + w(\boldsymbol{x})$ and substitute this into the Helmholtz equation, which leads to

$$\Delta(v(\boldsymbol{x}) + w(\boldsymbol{x})) + k^2(v(\boldsymbol{x}) + w(\boldsymbol{x})) = \delta(\boldsymbol{x} - \boldsymbol{x}_0),$$

and splitting up the left hand side we obtain

$$(\Delta v(\boldsymbol{x}) + k^2 v(\boldsymbol{x})) + (\Delta w(\boldsymbol{x}) + k^2 w(\boldsymbol{x})) = \delta(\boldsymbol{x} - \boldsymbol{x}_0).$$

The boundary condition may be written as

$$\frac{\partial u(\boldsymbol{x})}{\partial \hat{\mathbf{n}}} = \frac{\partial}{\partial \hat{\mathbf{n}}}(v(\boldsymbol{x}) + w(\boldsymbol{x})) = 0,$$

leading to

$$\frac{\partial v(\boldsymbol{x})}{\partial \hat{\mathbf{n}}} = -\frac{\partial w(\boldsymbol{x})}{\partial \hat{\mathbf{n}}}. \tag{2.4}$$

Let us now assume that v satisfies the homogeneous Helmholtz equation with boundary condition (2.4). This means that w satisfies $\Delta w(\boldsymbol{x}) + k^2 w(\boldsymbol{x}) = \delta(\boldsymbol{x} - \boldsymbol{x}_0)$ and hence extending to the whole of $\mathbb{R}^2$ we have that $w = G_k$, where G_k is the free-space Green's function for the Helmholtz equation - see Appendix A. Explicitly, we find

$$G_k(\boldsymbol{x}, \boldsymbol{x}_0) = -\frac{i}{4} H_0^{(1)}\left(k \left\|\boldsymbol{x} - \boldsymbol{x}_0\right\|\right) \tag{2.5}$$

where $H_0^{(1)}$ is the zeroth order Hankel function of the first kind and $\|\cdot\|$ is the Euclidean norm.

The boundary condition (2.4) to the homogeneous Helmholtz problem for v can therefore be rewritten as

$$\frac{\partial v(\boldsymbol{x})}{\partial \hat{\mathbf{n}}} = -\frac{\partial G_k(\boldsymbol{x}, \boldsymbol{x}_0)}{\partial \hat{\mathbf{n}}}. \tag{2.6}$$

We can express the right hand side of (2.6) as

$$\frac{\partial G_k}{\partial \hat{\mathbf{n}}} = \frac{\partial G_k}{\partial r} \cdot \frac{\partial r}{\partial \hat{\mathbf{n}}},$$

where $r = \|\boldsymbol{r}\|$ and $\boldsymbol{r} = \boldsymbol{x} - \boldsymbol{x}_0$. Here $\frac{\partial G_k}{\partial r}$ and $\frac{\partial r}{\partial \hat{\mathbf{n}}}$ are given by

$$\frac{\partial G_k}{\partial r} = -\frac{i}{4} k H_1^{(1)}(kr),$$
$$\frac{\partial r}{\partial \hat{\mathbf{n}}} = \frac{\boldsymbol{r} \cdot \hat{\mathbf{n}}}{r}.$$

Therefore we can write $\frac{\partial G_k}{\partial \hat{\mathbf{n}}}$ as

$$\frac{\partial G_k}{\partial \hat{\mathbf{n}}} = -\frac{ik(\boldsymbol{r} \cdot \hat{\mathbf{n}}) H_1^{(1)}(kr)}{4r}. \tag{2.7}$$

We can then numerically solve the homogeneous Helmholtz equation $\Delta v(\boldsymbol{x}) + k^2 v(\boldsymbol{x}) = 0$ with the boundary condition (2.6) using either the indirect or direct

BEM as described in Sections 2.2 and 2.3. The final solution to the original inhomogeneous BVP is then calculated for $\boldsymbol{x} \in \Omega$ via $u(\boldsymbol{x}) = v(\boldsymbol{x}) + G_k(\boldsymbol{x}, \boldsymbol{x}_0)$.

For the case when $k = 0$ in the homogeneous Helmholtz equation, we then have instead the Laplace equation, which physically represents that there is a potential and no wave propagation. Resonant solutions are non-trivial solutions of the Helmholtz equation for the case when $f = g = 0$, and only exist for particular values of k called resonant wavenumbers. The solution at these resonant wavenumbers is non-unique, since $u = 0$ is also a solution.

We now consider two methods to reformulate the Helmholtz equation as an integral equation, the indirect and the direct method. The indirect formulations assume that the solution to the PDE may be represented using formulae known as the single and double layer potentials, in which we solve for a non physical quantity known as a layer density [100]. The direct method involves applying a set of integral relations known as Green's identities to derive a boundary integral representation of a given PDE; this method is often applied in engineering problems as we solve in terms of physical quantities [36]. In the next section we consider the indirect method and then in Section 2.3 we describe the direct BEM.

2.2 Boundary integral formulation via the indirect method

Let u be the solution to the Helmholtz equation in (2.2), which satisfies one of the boundary conditions (2.3a)-(2.3c) on Γ. Then for $\boldsymbol{y} \in \mathbb{R}^2$, the indirect single-layer potential formulation assumes that the solution can be expressed in terms of a source density function σ defined on the boundary Γ as follows

$$u(\boldsymbol{x}) = \int_\Gamma G_k(\boldsymbol{x}, \boldsymbol{y})\sigma(\boldsymbol{y}) d\Gamma_{\boldsymbol{y}}, \quad \boldsymbol{x} \in \Omega \cup \Gamma. \tag{2.8}$$

Equation (2.8) can be used to solve the Dirichlet BVP by applying the boundary condition (2.3a) to (2.8) and calculating the density function σ. This leads to the following BIE:

$$f(\boldsymbol{x}) = \int_\Gamma G_k(\boldsymbol{x}, \boldsymbol{y})\sigma(\boldsymbol{y}) d\Gamma_{\boldsymbol{y}}, \quad \boldsymbol{x} \in \Gamma, \tag{2.9}$$

where we have made use of the continuity of G_k across Γ - see Appendix A. Once σ has been calculated, we substitute the density function σ back into (2.8) to determine the solution u of the Dirichlet BVP.

For the Neumann BVP we differentiate (2.8) with respect to the external unit normal $\hat{\mathbf{n}}_{\boldsymbol{x}}$ at a point $\boldsymbol{x}$ on the boundary, which yields the BIE

$$\frac{\partial u}{\partial \hat{\mathbf{n}}_{\boldsymbol{x}}}(\boldsymbol{x}) = \int_\Gamma \frac{\partial G_k}{\partial \hat{\mathbf{n}}_{\boldsymbol{x}}}(\boldsymbol{x},\boldsymbol{y})\sigma(\boldsymbol{y})d\Gamma_{\boldsymbol{y}} + \frac{1}{2}\sigma(\boldsymbol{x}), \quad \boldsymbol{x} \in \Gamma, \tag{2.10}$$

for points $\boldsymbol{x}$ on a smooth part of Γ. The jump discontinuity of the double-layer potential (integral in (2.10)) has been applied to give the additional term on the right hand side [4, 102]. Now, by applying the Neumann boundary condition (2.3b) to equation (2.10), the density function σ can be calculated and the solution to the Neumann BVP can be approximated by substituting σ into (2.8) as before.

For simplicity in future sections, we introduce the following boundary integral operators

$$(L_k\sigma)(\boldsymbol{x}) := \int_\Gamma G_k(\boldsymbol{x},\boldsymbol{y})\sigma(\boldsymbol{y})d\Gamma_{\boldsymbol{y}}, \quad \boldsymbol{x} \in \Gamma, \tag{2.11}$$

$$(M_k\sigma)(\boldsymbol{x}) := \int_\Gamma \frac{\partial G_k}{\partial \hat{\mathbf{n}}_{\boldsymbol{y}}}(\boldsymbol{x},\boldsymbol{y})\sigma(\boldsymbol{y})d\Gamma_{\boldsymbol{y}}, \quad \boldsymbol{x} \in \Gamma. \tag{2.12}$$

Here $\hat{\mathbf{n}}_{\boldsymbol{y}}$ is the external unit normal to Γ at the point $\boldsymbol{y}$. We also define the single-layer and double-layer potentials, S_k and D_k respectively, as follows

$$(S_k\sigma)(\boldsymbol{x}) := \int_\Gamma G_k(\boldsymbol{x},\boldsymbol{y})\sigma(\boldsymbol{y})d\Gamma_{\boldsymbol{y}}, \quad \boldsymbol{x} \in \Omega, \tag{2.13}$$

$$(D_k\sigma)(\boldsymbol{x}) := \int_\Gamma \frac{\partial G_k}{\partial \hat{\mathbf{n}}_{\boldsymbol{y}}}(\boldsymbol{x},\boldsymbol{y})\sigma(\boldsymbol{y})d\Gamma_{\boldsymbol{y}}, \quad \boldsymbol{x} \in \Omega, \tag{2.14}$$

to distinguish between the boundary and domain operators. Finally in this section, we note that there are a number of alternative ways to obtain an indirect boundary integral formulation for the Helmholtz equation, such as the double layer potential formulation which is based on the ansatz $u = D_k\sigma$, in place of (2.8). However, in this work we consider only the simplest single-layer formulation as a test case for the various discretisation methods described later in sections 2.4 and 2.5.

2.3 Boundary integral formulation via the direct method

We now discuss the direct method which is based on Green's identities. We first state the Gauss' divergence theorem, which will be used in the derivation of Green's first identity.

Theorem 2.1 (Divergence Theorem) *If $\boldsymbol{F}$ is a vector field in a domain $\Omega \subset \mathbb{R}^2$ with boundary Γ, then*

$$\iint_{\Omega} (\nabla \cdot \boldsymbol{F})\, d\Omega = \int_{\Gamma} (\boldsymbol{F} \cdot \hat{\boldsymbol{n}})\, d\Gamma. \tag{2.15}$$

Proof. See Spiegel [184].

Setting $F = \phi\nabla\psi$ in Theorem 2.1 leads to Green's first identity as follows:

Theorem 2.2 (Green's first identity) *Let $\Omega \in \mathbb{R}^2$ be a domain with a closed boundary Γ and let ϕ and ψ be functions defined on Ω with continuous second derivatives, then*

$$\iint_{\Omega} (\phi\Delta\psi + \nabla\phi \cdot \nabla\psi)\, d\Omega = \int_{\Gamma} \phi \frac{\partial\psi}{\partial\hat{\boldsymbol{n}}} d\Gamma. \tag{2.16}$$

Proof. From [184] we consider the identity,

$$(\phi\Delta\psi + \nabla\phi \cdot \nabla\psi) = \nabla \cdot (\phi\nabla\psi).$$

We integrate the above identity over Ω resulting in

$$\int_{\Omega} (\phi\Delta\psi + (\nabla\phi) \cdot (\nabla\psi)) d\Omega = \int_{\Omega} \nabla \cdot (\phi\nabla\psi) d\Omega.$$

We then apply Theorem 2.1, to the right hand side, which gives

$$\int_{\Gamma} (\phi\nabla\psi) \cdot \hat{\mathbf{n}}\, d\Gamma = \int_{\Gamma} \phi(\nabla\psi \cdot \hat{\mathbf{n}}) d\Gamma = \int_{\Gamma} \phi \frac{\partial\psi}{\partial\hat{\mathbf{n}}} d\Gamma. \quad \square$$

Corollary 2.2.1 (Green's second identity) *Let $\Omega \in \mathbb{R}^2$ be a domain with a closed boundary Γ and let ϕ and ψ be functions defined on Ω with continuous second derivatives, then*

$$\iint_{\Omega} (\phi\Delta\psi - \psi\Delta\phi) d\Omega = \int_{\Gamma} \left(\phi \frac{\partial\psi}{\partial\hat{\mathbf{n}}} - \psi \frac{\partial\phi}{\partial\hat{\mathbf{n}}} \right) d\Gamma. \tag{2.17}$$

Proof.
Follows by exchanging ψ and ϕ in equation (2.16) and then subtracting the result from (2.16). □

A direct BIE formulation results from Green's second identity by letting $\phi = u$ and $\psi = G_k$. Here, u is the solution to the homogeneous Helmholtz BVP (2.2) with $g = 0$, together with one of the boundary conditions (2.3a)-(2.3c) and G_k is given by (2.5) and satisfies (see Appendix A)

$$\Delta G_k(\boldsymbol{x}, \boldsymbol{y}) + k^2 G_k(\boldsymbol{x}, \boldsymbol{y}) = \delta(\boldsymbol{x} - \boldsymbol{y}), \tag{2.18}$$

where δ denotes the Dirac delta distribution as before. Substituting u and G_k into (2.17) gives

$$\begin{aligned} &\int_\Gamma \left(u(\boldsymbol{y}) \frac{\partial G_k}{\partial \hat{\mathbf{n}}_{\boldsymbol{y}}}(\boldsymbol{x}, \boldsymbol{y}) - G_k(\boldsymbol{x}, \boldsymbol{y}) \frac{\partial u}{\partial \hat{\mathbf{n}}_{\boldsymbol{y}}}(\boldsymbol{y}) \right) d\Gamma_{\boldsymbol{y}} \\ &= \int_\Omega \left(G_k(\boldsymbol{x}, \boldsymbol{y}) \Delta u(\boldsymbol{y}) - u(\boldsymbol{y}) \Delta G_k(\boldsymbol{x}, \boldsymbol{y}) \right) d\Omega_{\boldsymbol{y}}. \end{aligned} \tag{2.19}$$

Rearranging both the homogeneous Helmholtz equation and (2.18) yields $\Delta u = -k^2 u$ and

$$\Delta G_k(\boldsymbol{x}, \boldsymbol{y}) = \delta(\boldsymbol{x} - \boldsymbol{y}) - k^2 G_k(\boldsymbol{x}, \boldsymbol{y}),$$

respectively. Then substituting these relations into the integrand on the right hand side of equation (2.19) leads to

$$\int_\Omega \left(G_k(\boldsymbol{x}, \boldsymbol{y}) \Delta u(\boldsymbol{y}) - u(\boldsymbol{y}) \Delta G_k(\boldsymbol{x}, \boldsymbol{y}) \right) d\Omega_{\boldsymbol{y}} = -\int_\Omega u(\boldsymbol{y}) \delta(\boldsymbol{x} - \boldsymbol{y}) d\Omega_{\boldsymbol{y}}. \tag{2.20}$$

The position of the point $\boldsymbol{x}$ then determines the value of the right hand side of equation (2.19). If $\boldsymbol{x} \in \Omega$, we can then use the sifting property of the delta distribution (see Appendix A) to evaluate the right hand side of (2.20) as follows

$$-\int_\Omega u(\boldsymbol{y}) \delta(\boldsymbol{x} - \boldsymbol{y}) d\Omega_{\boldsymbol{y}} = -u(\boldsymbol{x}). \tag{2.21}$$

If $\boldsymbol{x} \notin (\Omega \cup \Gamma)$, that is outside our domain and away from the boundary, then since $\boldsymbol{x} \neq \boldsymbol{y}$, the right hand side of (2.19) is equal to zero by (2.20).

Finally, we consider the case when $\boldsymbol{x} \in \Gamma$. Let $\boldsymbol{x}$ be located on a smooth part of Γ and consider a small circle with radius ϵ centered at $\boldsymbol{x}$, then taking $\epsilon \to 0$ the point $\boldsymbol{x}$ is surrounded by a semicircle in Ω and (2.21) instead evaluates to

$-\frac{1}{2}u(\boldsymbol{x})$ [100]. Hence for $\boldsymbol{x} \in \Gamma$ we obtain

$$\int_{\Gamma} \left(u(\boldsymbol{y}) \frac{\partial G_k(\boldsymbol{x}, \boldsymbol{y})}{\partial \hat{\mathbf{n}}_{\boldsymbol{y}}} - G_k(\boldsymbol{x}, \boldsymbol{y}) \frac{\partial u(\boldsymbol{y})}{\partial \hat{\mathbf{n}}_{\boldsymbol{y}}} \right) d\Gamma_{\boldsymbol{y}} = -\frac{1}{2} u(\boldsymbol{x}). \tag{2.22}$$

We note that the above is arranged form of (2.10). Taking all of the above into account we can write

$$\int_{\Gamma} \left(G_k(\boldsymbol{x}, \boldsymbol{y}) \frac{\partial u(\boldsymbol{x})}{\partial \hat{\mathbf{n}}_{\boldsymbol{y}}} - u(\boldsymbol{x}) \frac{\partial G_k(\boldsymbol{x}, \boldsymbol{y})}{\partial \hat{\mathbf{n}}_{\boldsymbol{y}}} \right) d\Gamma_{\boldsymbol{y}} = \begin{cases} 0, & \boldsymbol{x} \notin (\Omega \cup \Gamma), \\ \frac{1}{2} u(\boldsymbol{x}), & \boldsymbol{x} \in \Gamma, \\ u(\boldsymbol{x}), & \boldsymbol{x} \in \Omega. \end{cases} \tag{2.23}$$

In our numerical examples, later in Section 2.8, we are interested in applying the Neumann boundary condition (2.3b). For convenience we rewrite the solution at the boundary position $\boldsymbol{x} \in \Gamma$ in boundary integral operator notation as

$$\left(\frac{1}{2} I + M_k \right) u(\boldsymbol{x}) = \left(L_k f \right)(\boldsymbol{x}), \tag{2.24}$$

where f is the Neumann boundary data in (2.3b) and I represents the identity operator, $Iu = u$. Furthermore, the interior solution when $\boldsymbol{x} \in \Omega$ may be expressed as

$$u(\boldsymbol{x}) = \left(S_k f \right)(\boldsymbol{x}) - \left(D_k u \right)(\boldsymbol{x}). \tag{2.25}$$

2.4 Discretisation via the collocation method

We first consider solving a BIE of the form $Av = B$ for the case of Dirichlet boundary conditions (2.3a) using the collocation method. In Section 2.5, we will discuss discretising the BIE via the Galerkin method. Here A, v and B are combinations of linear operators and functions depending on whether the indirect or the direct method is used, as detailed in Table 2.1.

The collocation method and the Galerkin method are two of the most common methods for numerically solving BIEs of this form, and are examples of projection methods as we explain below [7]. Let X be a normed linear space and X_m be a subspace of X that is spanned by the basis functions $b_1, ..., b_m$. We seek an approximate solution for v by a function $v_m \in X_m$ in the form of a

	Indirect	Direct
A	L_k	$\frac{1}{2}I + M_k$
v	σ	u
B	f	$L_k f$

Table 2.1: Function and operator assignments in the BIE $Av = B$ for the indirect and direct methods.

linear combination of basis functions, b_j, as follows

$$v_m(\boldsymbol{x}) = \sum_{j=1}^{m} \phi_j b_j(\boldsymbol{x}), \tag{2.26}$$

where $\phi_1, ..., \phi_m$ are unknown constants that need to be determined. Note that v_m will not solve the boundary integral equation $Av = B$ exactly, but does solve the equation

$$Av_m = B + r_m, \tag{2.27}$$

where r_m is the residual. For a good approximation we require r_m to be very small. In the collocation method we pick m distinct points called collocation points, $\boldsymbol{x}_1, \boldsymbol{x}_2, ..., \boldsymbol{x}_m$ such that the residual is zero at those m points i.e. $r_m(\boldsymbol{x}_i) = 0$ for all $i = 1, 2, ..., m$. We also divide the boundary Γ into m elements $E_1, E_2, ..., E_m$.

From this point on, we consider applying the collocation method only to the BIE (2.9) derived from the indirect method to demonstrate in further detail the application of the collocation method to a BIE. A similar process can also be followed for the direct case instead. Substituting (2.26) into the integral equation (2.9) at the collocation points, one obtains the following boundary integral equations

$$\sum_{j=1}^{m} \phi_j \left(\int_{\Gamma} G_k(\boldsymbol{x}_i, \boldsymbol{y}) b_j(\boldsymbol{y}) d\Gamma_{\boldsymbol{y}} \right) = f(\boldsymbol{x}_i), \quad i = 1, 2, ..., m, \tag{2.28}$$

in which we need to determine the unknown coefficients ϕ_j for $j = 1, 2, ..., m$. In our numerical examples discussed later in Section 2.7.1, we consider two choices of basis functions, piecewise constant and piecewise linear. The simplest collocation method is based on piecewise constant basis functions, which are

defined as

$$b_j(\boldsymbol{y}) = \begin{cases} 1 & \text{if } \boldsymbol{y} \in E_j, \\ 0 & \text{otherwise,} \end{cases} \tag{2.29}$$

for $j = 1, 2, ..., m$ and the collocation point $\boldsymbol{x}_i$ is chosen to be at the centre of the element E_i as highlighted by the yellow circles in Figure 2.1. Since $b_j(\boldsymbol{y}) = 1$ only if $\boldsymbol{y} \in E_j$, then (2.28) simplifies to

$$\sum_{j=1}^{m} \phi_j \int_{E_j} G_k(\boldsymbol{x}_i, \boldsymbol{y}) d\Gamma_{\boldsymbol{y}} = f(\boldsymbol{x}_i), \quad i = 1, 2, ..., m. \tag{2.30}$$

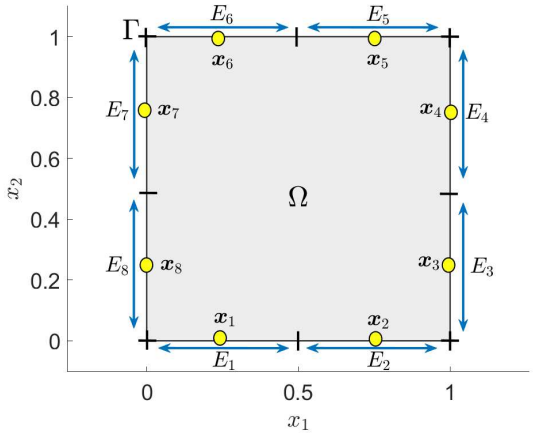

Figure 2.1: Example of the unit square domain discretised via the collocation based BEM with piecewise constant basis functions for $m = 8$. The collocation points $\boldsymbol{x}_i$ are highlighted by the yellow circles chosen to be at the centre of each element E_i for $i = 1, 2, ..., 8$.

For piecewise linear basis functions we let h denote the arclength of element E_j and $\boldsymbol{y}_j$ denote the Cartesian coordinates of the boundary node connecting E_j and E_{j+1}, see Figure 2.2. Note that $E_{m+1} \equiv E_1$. Unlike in the piecewise constant case, the piecewise linear basis functions extend over two neighbouring elements and the collocation points $\boldsymbol{x}_i$ are chosen to be the element end points, as highlighted by the red circles in Figure 2.2. For simplicity, we parameterise $\boldsymbol{x}_i$ and the integration point $\boldsymbol{y}$ by an arclength parameter. For the collocation point, we denote $s_i \in [0, L)$ for $i = 1, 2, ..., m$ and for the integration point we denote $t(\boldsymbol{y}) \in [0, L)$, where L is the boundary length. Finally, we denote

$t_j = t(\boldsymbol{y}_j)$ for $j = 1, 2, ..., m$. The piecewise linear basis functions are then defined as follows

$$b_j(\boldsymbol{y}) = \begin{cases} \dfrac{t(\boldsymbol{y}) - t_{j-1}}{h} & \text{if } t_{j-1} \leq t(\boldsymbol{y}) \leq t_j, \\ \dfrac{t_{j+1} - t(\boldsymbol{y})}{h} & \text{if } t_j \leq t(\boldsymbol{y}) \leq t_{j+1}, \\ 0 & \text{otherwise.} \end{cases} \tag{2.31}$$

The BIEs (2.28) with piecewise linear basis functions for $i = 1, 2, ..., m$, may then be written as

$$\begin{aligned} f(\boldsymbol{x}_i) = \sum_{j=1}^{m} \phi_j \Big(& \int_{E_j} G_k(\boldsymbol{x}_i, \boldsymbol{y}) \frac{(t(\boldsymbol{y}) - t_{j-1})}{h} d\Gamma_{\boldsymbol{y}} \\ & + \int_{E_{j+1}} G_k(\boldsymbol{x}_i, \boldsymbol{y}) \frac{(t_{j+1} - t(\boldsymbol{y}))}{h} d\Gamma_{\boldsymbol{y}} \Big). \end{aligned} \tag{2.32}$$

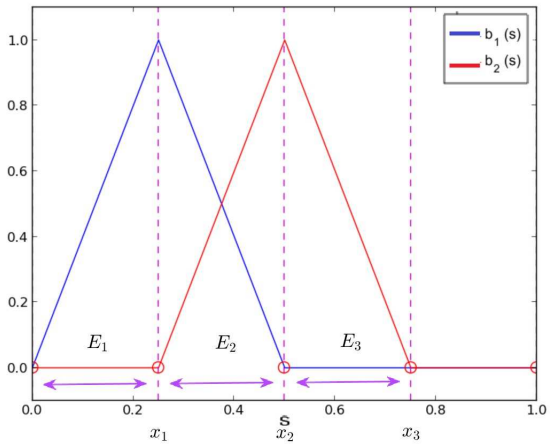

Figure 2.2: Illustration of the piecewise linear basis functions with their corresponding nodes highlighted by red circles, in an element with length $h = 0.25$. Element boundaries are indicated by dotted vertical lines.

2.5 Discretisation via the Galerkin method

We now consider solving BIEs of the form $Av = B$ for the case of Dirichlet boundary conditions (2.3a) by applying a Galerkin method. Like the collocation method, the Galerkin method approximates v as a linear combination of basis functions, b_j, for $j = 1, 2, ..., m$, as defined in equation (2.26) where $\phi_1, ..., \phi_m$ are unknown constants that need to be determined. As before, v_m does not solve the integral equation exactly, but does solve equation (2.27). For a good approximation we again require r_m to be very small.

In the Galerkin method, an approximate solution is obtained by enforcing

$$\langle r_m, b_i \rangle = \int_\Gamma r_m(\boldsymbol{x}) b_i(\boldsymbol{x}) d\Gamma_{\boldsymbol{x}} = 0, \quad \text{for} \quad i = 1, 2, ..., m. \tag{2.33}$$

That is, the inner product of r_m and b_i is set to be zero [7]. Again, we only demonstrate thoroughly the application of the Galerkin method for the indirect boundary integral equation (2.9), but a similar procedure can be followed for the direct method. We begin by substituting our approximation for v (2.26), into the BIE (2.9). We then impose (2.33) by multiplication with a test function $b_i(\boldsymbol{x})$ and then integrate with respect to $\boldsymbol{x}$ over Γ. This yields the following boundary integral equations

$$\sum_{j=1}^{m} \phi_j \left(\int_\Gamma \int_\Gamma G_k(\boldsymbol{x}, \boldsymbol{y}) b_i(\boldsymbol{x}) b_j(\boldsymbol{y}) d\Gamma_{\boldsymbol{x}} d\Gamma_{\boldsymbol{y}} \right) = \int_\Gamma f(\boldsymbol{x}) b_i(\boldsymbol{x}) d\Gamma_{\boldsymbol{x}}, \tag{2.34}$$

for $i = 1, 2, ..., m$, where we need to determine the unknown coefficients $\phi_1, ..., \phi_m$ [4].

We first write the BIEs (2.34) with piecewise constant basis functions by dividing the boundary Γ into m elements $E_1, E_2, ..., E_m$ and employing the basis functions given by (2.29). Since $b_j(\boldsymbol{y}) = 1$ only if $\boldsymbol{y} \in E_j$ and $b_i(\boldsymbol{x}) = 1$ only if $\boldsymbol{x} \in E_i$, then (2.34) simplifies to the following system of BIEs

$$\sum_{j=1}^{m} \phi_j \left(\int_{E_i} \int_{E_j} G_k(\boldsymbol{x}, \boldsymbol{y}) d\Gamma_{\boldsymbol{x}} d\Gamma_{\boldsymbol{y}} \right) = \int_{E_i} f(\boldsymbol{x}) d\Gamma_{\boldsymbol{x}}, \tag{2.35}$$

for $i = 1, 2, ..., m$.

For piecewise linear basis functions (2.31) we also divide Γ into m elements as before. The resulting system of BIEs is more complex and may be written

as follows

$$\begin{aligned}\sum_{j=1}^{m}\phi_j\Bigg(&\int_{E_i}\int_{E_j} G_k(\boldsymbol{x},\boldsymbol{y})\left(\frac{s(\boldsymbol{x})-s_{i-1}}{h}\right)\left(\frac{t(\boldsymbol{y})-t_{j-1}}{h}\right)d\Gamma_{\boldsymbol{x}}d\Gamma_{\boldsymbol{y}}\\ &+\int_{E_i}\int_{E_{j+1}} G_k(\boldsymbol{x},\boldsymbol{y})\left(\frac{s(\boldsymbol{x})-s_{i-1}}{h}\right)\left(\frac{t_{j+1}-t(\boldsymbol{y})}{h}\right)d\Gamma_{\boldsymbol{x}}d\Gamma_{\boldsymbol{y}}\\ &+\int_{E_{i+1}}\int_{E_j} G_k(\boldsymbol{x},\boldsymbol{y})\left(\frac{s_{i+1}-s(\boldsymbol{x})}{h}\right)\left(\frac{t(\boldsymbol{y})-t_{j-1}}{h}\right)d\Gamma_{\boldsymbol{x}}d\Gamma_{\boldsymbol{y}}\\ &+\int_{E_{i+1}}\int_{E_{j+1}} G_k(\boldsymbol{x},\boldsymbol{y})\left(\frac{s_{i+1}-s(\boldsymbol{x})}{h}\right)\left(\frac{t_{j+1}-t(\boldsymbol{y})}{h}\right)d\Gamma_{\boldsymbol{x}}d\Gamma_{\boldsymbol{y}}\Bigg)\\ &=\int_{E_i} f(\boldsymbol{x})\left(\frac{s(\boldsymbol{x})-s_{i-1}}{h}\right)d\Gamma_{\boldsymbol{x}}+\int_{E_{i+1}} f(\boldsymbol{x})\left(\frac{s_{i+1}-s(\boldsymbol{x})}{h}\right)d\Gamma_{\boldsymbol{x}},\end{aligned}\tag{2.36}$$

for $i = 1, 2, ..., m$. Here $s(\boldsymbol{x}) \in [0, L)$ is the arclength parameter for the point $\boldsymbol{x} \in \Gamma$ and $s_i = s(\boldsymbol{x}_i)$.

2.6 Singularity subtraction

The boundary integral operator L_k (2.11), which is used in the BIEs formulated from both the direct and indirect methods, has a singularity when $\boldsymbol{x} = \boldsymbol{y}$. In the collocation method, the BIEs (2.28) may therefore contain a weak singularity when $\boldsymbol{x}_i = \boldsymbol{y}$, and then the integrand diverges. This is also the case for the Galerkin method when $\boldsymbol{x} = \boldsymbol{y}$ for the BIEs (2.34), since direct numerical integration of G_k leads to problems with this singularity. We therefore implement a singularity subtraction procedure to overcome these issues and calculate the finite valued integral.

To begin, we let $r = \|\boldsymbol{r}\|$ and $\boldsymbol{r} = \boldsymbol{x} - \boldsymbol{y}$, and then note that the Hankel function $H_0^{(1)}(kr)$ appearing in G_k can be expressed as $H_0^{(1)}(kr) = J_0(kr) + iY_0(kr)$, where J_0 and Y_0 are zeroth order Bessel functions of the first and second kind, respectively. We find the Puiseux series expansion of $H_0^1(kr)$ about $r = 0$ by using the Puiseux series expansions for $J_0(kz)$ and $Y_0(kz)$ about $z = 0$, which can be found in Section 8.4 of [74]. The series expansion of the Hankel function is then given by

$$H_0^{(1)}(kr) = 1+\frac{2i}{\pi}\left(\ln\left(\frac{kr}{2}\right)+\gamma_\epsilon\right)+r^2\left(-\frac{1}{4}-\frac{i}{2\pi}\left(\ln\left(\frac{kr}{2}\right)+\gamma_\epsilon-1\right)\right)+\mathcal{O}(r^4),$$

where γ_ϵ is the Euler - Mascheroni constant [74]. This expansion tells us that

as $r \to 0$, then omitting $\mathcal{O}(r^2)$ we have

$$H_0^{(1)}(kr) - \frac{2i}{\pi} \ln\left(\frac{kr}{2}\right) = 1 + \frac{2i\gamma_\epsilon}{\pi},$$

and thus using the laws of logarithms,

$$H_0^{(1)}(kr) - \frac{2i}{\pi} \ln(r) = 1 + \frac{2i}{\pi}\left(\gamma_\epsilon + \ln\left(\frac{k}{2}\right)\right). \tag{2.37}$$

Hence for $k \neq 0$, the left hand side of (2.37) is finite and non-singular in the limit $r \to 0$. Multiplying (2.37) by $-i/4$ we obtain

$$G_k(\boldsymbol{x}, \boldsymbol{y}) - \frac{1}{2\pi} \ln(r) = -\frac{i}{4} + \frac{1}{2\pi}\left(\gamma_\epsilon + \ln\left(\frac{k}{2}\right)\right).$$

Therefore, we replace G_k in (2.11) with $(G_k(\boldsymbol{x}, \boldsymbol{y}) - G_0(\boldsymbol{x}, \boldsymbol{y})) + G_0(\boldsymbol{x}, \boldsymbol{y})$, where G_0 is the free space Green's function for the two-dimensional Laplace equation given by

$$G_0(\boldsymbol{x}, \boldsymbol{y}) = \frac{1}{2\pi} \ln(\|\boldsymbol{x} - \boldsymbol{y}\|), \tag{2.38}$$

see Appendix A. In the boundary integral operator L_k (2.11) when $\boldsymbol{x}$ and $\boldsymbol{y}$ are in the same boundary element, we instead calculate

$$\begin{aligned}(L_k\sigma)(\boldsymbol{x}) = &\left(\int_\Gamma \left(G_k\left(\boldsymbol{x}, \boldsymbol{y}\right) - G_0(\boldsymbol{x}, \boldsymbol{y})\right) \sigma(\boldsymbol{y}) d\Gamma_{\boldsymbol{y}} \right. \\ &\left. + \int_\Gamma G_0(\boldsymbol{x}, \boldsymbol{y}) \sigma(\boldsymbol{y}) d\Gamma_{\boldsymbol{y}} \right).\end{aligned} \tag{2.39}$$

The first integral in (2.39) has a non-singular kernel and can be evaluated using standard quadrature rules. In our numerical examples, the integrals are calculated via the `integral` command in MATLAB which uses a vectorised adaptive quadrature method. For more details on the `integral` command in MATLAB we refer the reader to [181]. For the case when $\boldsymbol{x}$ and $\boldsymbol{y}$ belong to the same boundary element, the final integral in (2.39) has an exact representation when either piecewise constant or piecewise linear basis functions are employed. We first substitute the approximation for σ given by (2.26) into the integral resulting in

$$\sum_{j=1}^{m} \phi_j \int_{E_j} G_0(\boldsymbol{x}, \boldsymbol{y}) b_j(\boldsymbol{y}) d\Gamma_{\boldsymbol{y}}, \tag{2.40}$$

where ϕ_j, $j = 1, 2, ..., m$, are unknown constants to be determined and b_j are either piecewise constant basis functions defined by (2.29) or piecewise linear basis functions defined by (2.31). The exact calculation of the integral (2.40) for both cases of basis functions can be found in Appendix B.

This procedure is only used to evaluate the single-layer boundary integral operator (2.11) and is not required for the double-layer boundary integral operator M_k (2.12), as in our numerical examples for the direct BEM we only consider polygonal domains. Therefore, the boundary is made up of straight line edges such that the unit normal vector is perpendicular to the boundary and thus $\boldsymbol{r} \cdot \hat{\mathbf{n}} = 0$ in equation (2.7). Therefore $\partial G_k / \partial \hat{\mathbf{n}} = 0$ whenever $\boldsymbol{x}$ and $\boldsymbol{y}$ belong to the same edge, including the case when $\boldsymbol{x} = \boldsymbol{y}$.

2.7 Numerical examples for the indirect BEM

In this section we aim to determine which spatial discretisation method and basis functions to implement in our future development of methods for the time-domain. We therefore consider solving the indirect BIE (2.9) with Dirichlet boundary conditions, as it is the simplest to implement and compare the discretisation methods against one another. We present the results for solving the Helmholtz Dirichlet BVP (2.2)-(2.3a) via the indirect BEM discretising first with the collocation method and then with the Galerkin method. For both methods we consider the cases when Ω is a unit circle, a unit square and an L shaped domain for both piecewise constant and piecewise linear basis functions. Figure 2.3 displays a flowchart that details the equation that is required to determine the unknown density coefficients ϕ_j depending on which discretisation method and piecewise basis functions are being implemented to (2.9). Once the density function σ from (2.26) has been calculated the interior solution is found via (2.8). In the numerical examples considered we examine the errors and estimated order of convergence (EOC) at different values of the wavenumber k. We compare results firstly between the different basis functions for each discretisation method, and then we compare both discretisation methods against each other. The MATLAB code for these examples are available from the following URL: https://github.com/JacobRowbottom/BEM/tree/main/Indirect .

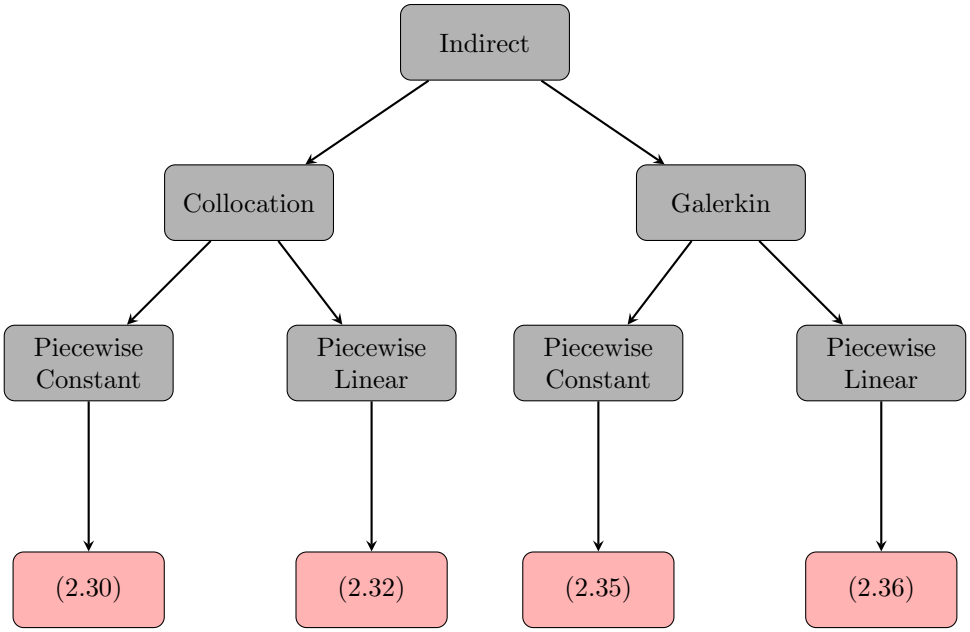

Figure 2.3: Flow chart displaying the corresponding BIE required for each discretisation method and piecewise basis function combination.

2.7.1 Collocation method

We implement the indirect BEM for the BVP defined by (2.2)-(2.3a) discretising with the collocation method and consider both piecewise constant and piecewise linear basis functions for a variety of domains.

Circle domain

We first consider the homogeneous Helmholtz equation (2.2) with $g = 0$ and a Dirichlet boundary condition (2.3a) for the case when Ω is a unit circle centered at the origin. For simplicity, we also parameterise $\boldsymbol{x}_i$ and the point $\boldsymbol{y}$ by an arclength parameter, which we denote as $s_i \in [0, L)$ and $t \in [0, L)$ respectively, where $L = 2\pi$ is the perimeter of the circle. We consider a BVP with exact solution

$$u(r, \theta) = \frac{J_1(kr)\sin(\theta)}{J_1(k)},$$

where $r \in [0, 1]$ is the radial coordinate in Ω and $\theta \in [0, 2\pi)$ is the angular coordinate - see Appendix C.1 for details. The boundary condition for this

problem is therefore $u(1,\theta) = \sin(\theta)$. The distance between the two points s_i and t is the length of a chord $2\sin\left(\frac{s_i - t}{2}\right)$. Therefore the free space Green's function can be written as

$$G_k(\boldsymbol{x}_i, \boldsymbol{y}) = -\frac{i}{4} H_0^{(1)} \left(2k \sin \left(\frac{s(\boldsymbol{x}_i) - t(\boldsymbol{y})}{2} \right) \right).$$

Figure 2.4 shows the numerical and analytical solutions for the Helmholtz equation in a unit circle for different values of k. From the figure we can see how the solution inside the circle varies due to the increase of the wavenumber k. Physically this represents an increase in the oscillation of the wave within the domain.

	Results at $k = 1$		Results at $k = 10$		Results at $k = 25$	
m	Error	EOC	Error	EOC	Error	EOC
16	7.3514e-04	-	0.0531	-	0.1739	-
32	8.0972e-05	3.65	0.0036	3.88	0.0056	4.96
64	1.1107e-05	3.00	4.0965e-04	3.14	2.6283e-04	4.41
128	1.3875e-06	3.00	5.0148e-05	3.03	2.8537e-05	3.20
256	1.7341e-07	2.95	6.2366e-06	3.00	3.4551e-06	3.05

Table 2.2: Relative errors and estimated orders of convergence for the collocation method based indirect BEM with constant basis functions in a circle domain at the point (0.5, 0.5) for different k values.

	Results at $k = 1$		Results at $k = 10$		Results at $k = 25$	
m	Error	EOC	Error	EOC	Error	EOC
16	4.8145e-04	-	0.0219	-	0.0089	-
32	5.9507e-05	3.02	0.0022	3.32	0.0018	2.31
64	7.4087e-06	3.01	2.6891e-04	3.03	1.5697e-04	5.83
128	9.2514e-07	3.00	3.3305e-05	3.01	1.8552e-05	3.08
256	1.1561e-07	3.00	4.1538e-06	3.00	2.2892e-06	3.01

Table 2.3: Relative errors and estimated orders of convergence for the collocation method based indirect BEM with piecewise linear basis functions in an unit circle domain at the point (0.5, 0.5) for different k values.

We first apply piecewise constant basis functions to numerically solve the BIEs for this example. Table 2.2 shows the relative errors and the convergence rates, which are estimated by $\log_2(\text{Error}(m/2)/\text{Error}(m))$ as we double the num-

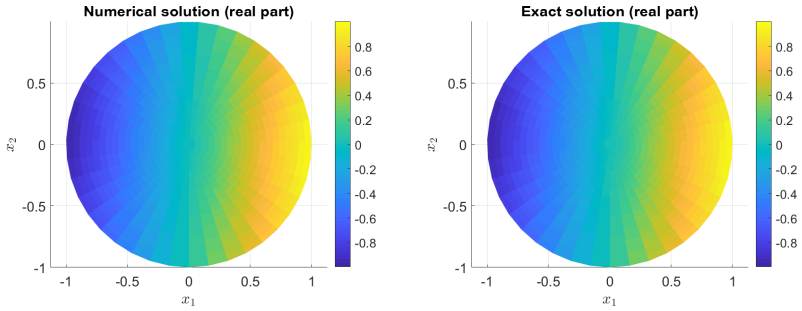

(a) $k = 1$ (b) $k = 1$

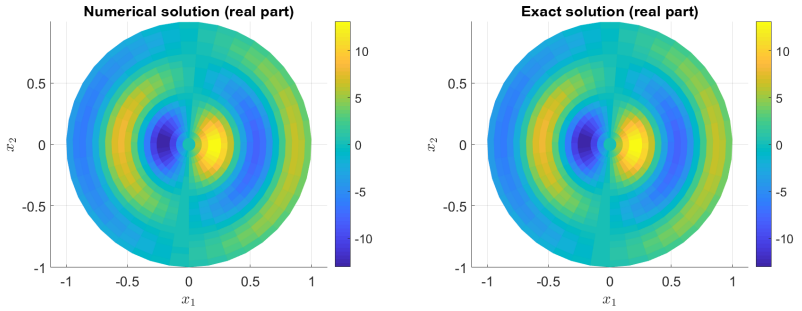

(c) $k = 10$ (d) $k = 10$

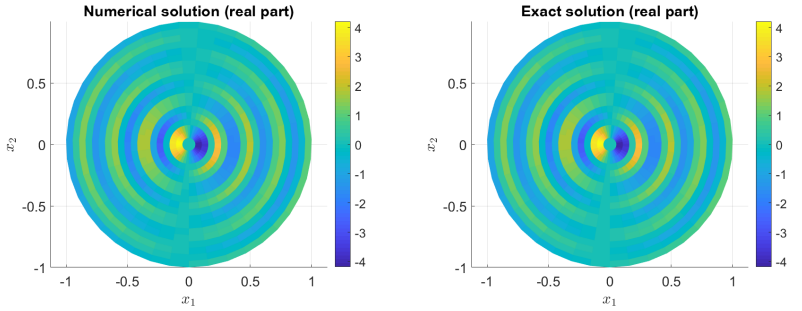

(e) $k = 25$ (f) $k = 25$

Figure 2.4: Comparison between the exact and numerical solutions of the Dirichlet BVP for the Helmholtz equation in a unit circle domain. The numerical solution was calculated using the collocation method based indirect BEM with piecewise constant basis functions and $m = 256$ boundary elements.

ber of boundary elements, where $\text{Error}(m)$ is the relative error for the numerical solution with m boundary elements. From this table we see that the errors are very small for a relatively small number of boundary elements. The convergence

rate is also much faster than expected for piecewise constant interpolation since from Taylor series based arguments for piecewise polynomial interpolation we would only expect first order convergence. This could be due to using an exact representation of the smooth boundary Γ, instead of straight line segments.

Table 2.3 presents the relative errors and the EOC for different values of the wavenumber, when $k = 1$, $k = 10$, and $k = 25$ calculated using piecewise linear basis functions. By examining this table we can see that errors are very small and are converging consistently at a cubic rate. If we compare this to the errors and EOC for constant basis functions from Table 2.2, we identify that as the wavenumber increases, the errors and convergence rate are very similar, and the errors for the piecewise linear basis functions are slightly smaller compared to the errors for the constant basis functions.

Square domain

We now consider solving the homogeneous Helmholtz equation (2.2) with $g = 0$ and Dirichlet boundary conditions (2.3a) for a unit square domain $\Omega = \{(x_1, x_2) \in \mathbb{R}^2 : 0 \leq x_1 \leq 1, 0 \leq x_2 \leq 1\}$. The boundary conditions are defined as

$$u(x_1, 0) = \cos(kx_1), \qquad \text{for} \quad 0 \leq x_1 \leq 1, \tag{2.41a}$$

$$u(0, x_2) = 1, \qquad \text{for} \quad 0 \leq x_2 \leq 1, \tag{2.41b}$$

$$u(x_1, 1) = \cos(kx_1), \qquad \text{for} \quad 0 \leq x_1 \leq 1, \tag{2.41c}$$

$$u(1, x_2) = \cos(k), \qquad \text{for} \quad 0 \leq x_2 \leq 1. \tag{2.41d}$$

The exact solution to the above BVP is $u(\boldsymbol{x}) = \cos(kx_1)$ and is independent of x_2 - see Appendix C.2.

Figure 2.5 shows the numerical and analytical interior solutions of the Dirichlet BVP for the Helmholtz equation with $k = 1$, $k = 10$ and $k = 25$. As we can see from the figure, as k increases, the rate of oscillation of the wave increases through the domain. We observe that the numerical and analytical solutions appear to be identical. This observation is further supported from the error and convergence results from Table 2.4 and Table 2.5, which indicate that the errors are small and that the numerical results converge quickly. When comparing between piecewise constant and piecewise linear basis functions we can determine that there is no significant difference in errors or convergence rates, and the errors for the piecewise constant case are typically lower. Comparing

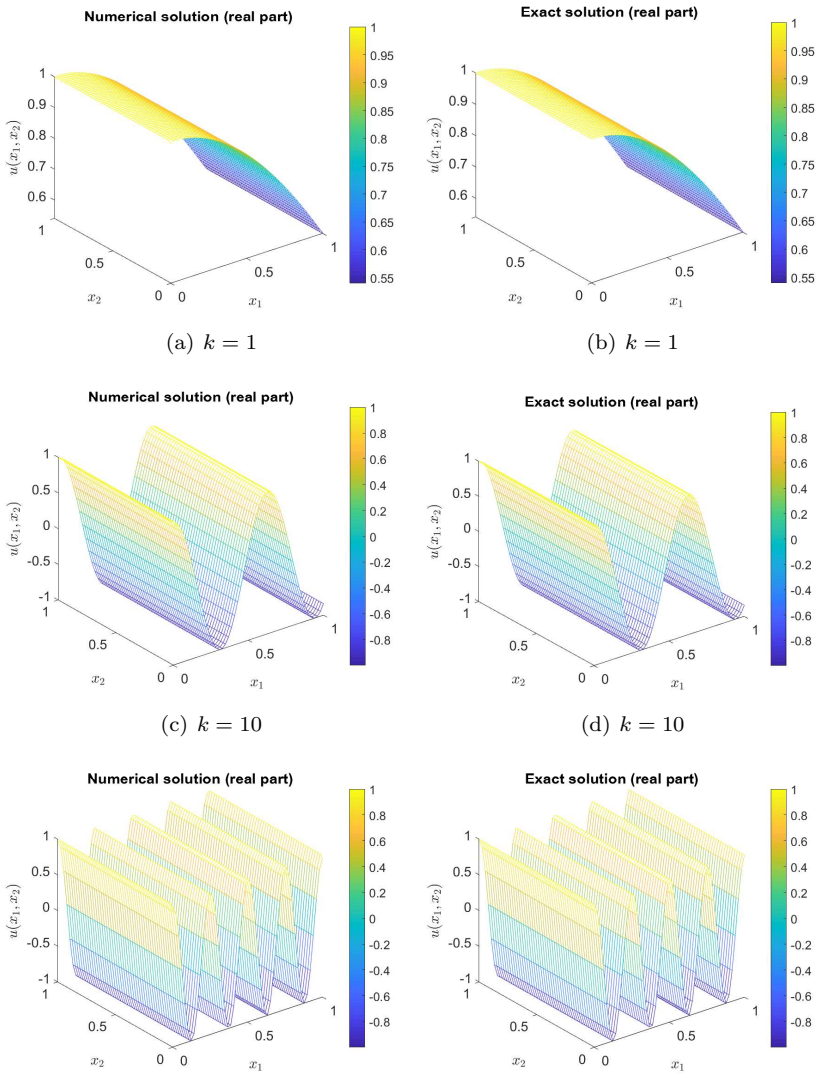

(a) $k = 1$ (b) $k = 1$

(c) $k = 10$ (d) $k = 10$

(e) $k = 25$ (f) $k = 25$

Figure 2.5: Comparison between the exact and numerical solutions of the Dirichlet BVP for the Helmholtz equation in a unit square domain. The numerical solution was calculated using the collocation method based indirect BEM with piecewise constant basis functions and $m = 256$ boundary elements.

the convergence and error results with the results obtained from the unit circle example, we find that in general the EOCs for the circle case are higher. This

	Results at $k = 1$		Results at $k = 10$		Results at $k = 25$	
m	Error	EOC	Error	EOC	Error	EOC
16	0.0010	-	0.6869	-	1.0024	-
32	1.8753e-04	2.41	0.1622	2.08	0.4546	1.14
64	3.3180e-05	2.50	0.0275	2.56	0.0210	4.44
128	5.6822e-06	2.55	0.0045	2.61	0.0028	2.86
256	9.5180e-07	2.58	7.4676e-04	2.59	4.5502e-04	2.67

Table 2.4: Relative errors and estimated orders of convergence for the collocation method based indirect BEM with constant basis functions in a unit square domain at the point (0.5, 0.5) for different k values.

	Results at $k = 1$		Results at $k = 10$		Results at $k = 25$	
m	Error	EOC	Error	EOC	Error	EOC
16	0.0025	-	1.8031	-	0.9601	-
32	4.1083e-04	2.61	0.3240	2.48	0.3422	1.49
64	6.6934e-05	2.68	0.0521	2.64	0.0345	3.31
128	1.0804e-05	2.63	0.0083	2.65	0.0050	2.79
256	1.7006e-06	2.67	0.0013	2.67	7.7812e-04	2.68

Table 2.5: Relative errors and estimated orders of convergence for the collocation method based indirect BEM with piecewise linear basis functions in an unit square domain at the point (0.5, 0.5) for different k values.

is because the solution along the boundary Γ for the square domain example is not smooth at the corners, unlike the circle domain example which has a smooth boundary solution.

L-shaped domain

We define a BVP for the homogeneous Helmholtz equation (2.2) with $g = 0$ and Dirichlet boundary conditions (2.3a) on an L-shaped domain, as shown in Figure 2.6. The boundary conditions are defined as follows

$$u(0, x_2) = \cos(kx_2), \qquad \text{for} \quad 0 \leq x_2 \leq 0.5, \tag{2.42a}$$

$$u = 0, \qquad \text{otherwise.} \tag{2.42b}$$

This represents a wave along the left edge of the domain, with zero everywhere else, as shown in Figure 2.6, where $f(\boldsymbol{x}) = \cos(kx_2)$. Figure 2.7 shows the

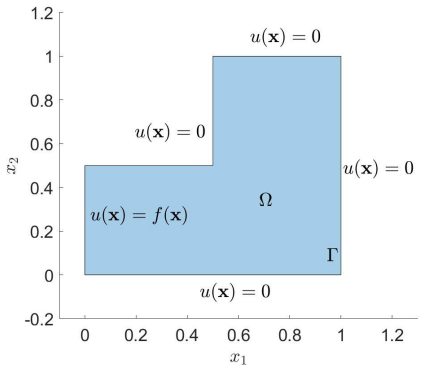

Figure 2.6: L-shaped domain and boundary conditions.

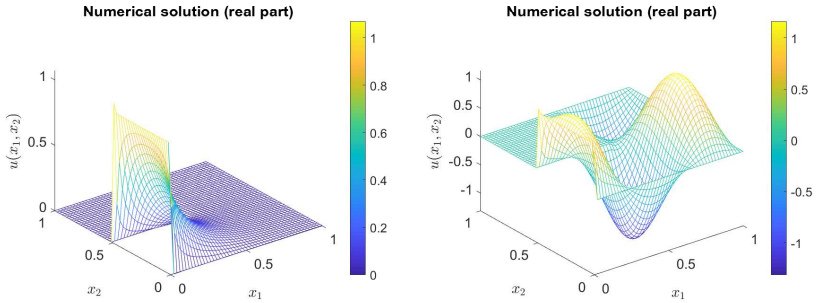

(a) $k = 1$

(b) $k = 10$

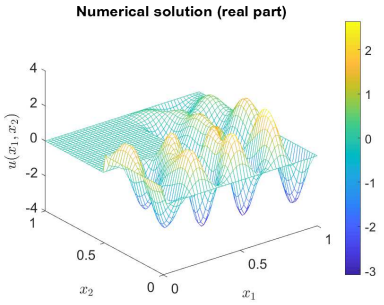

(c) $k = 25$

Figure 2.7: Numerical solutions of the Dirichlet BVP for the Helmholtz equation in an L-shaped domain. The numerical solution was calculated using the collocation method based indirect BEM with piecewise constant basis functions and $m = 256$ boundary elements.

numerical interior solutions of the Helmholtz equation in an L-shaped domain for $k = 1$, 10 and 25. In these figures we have set the upper left quadrant of the plot to be zero to highlight the shape of the reverse L. However when $k = 1$ this is difficult to see due to the slow oscillation but as we increase k, we observe a more oscillatory interior solution as before.

	Results at $k = 1$		Results at $k = 10$		Results at $k = 25$	
m	Error	EOC	Error	EOC	Error	EOC
16	0.0011	-	0.0467	-	0.7972	-
32	9.1508e-05	3.59	0.0086	2.44	0.4749	0.75
64	2.0944e-05	2.13	0.0033	1.38	0.0579	3.04
128	1.5418e-05	0.44	0.0013	1.34	0.0119	2.28
256	7.1546e-06	1.11	4.9735e-04	1.38	0.0033	1.85

Table 2.6: Relative errors and estimated orders of convergence for the collocation method based indirect BEM with piecewise constant basis functions in an L-shaped domain at the point (0.75,0.25) for different k values.

	Results at $k = 1$		Results at $k = 10$		Results at $k = 25$	
m	Error	EOC	Error	EOC	Error	EOC
16	0.0018	-	0.0953	-	3.5782	-
32	1.8382e-04	3.29	0.0067	3.83	1.6832	1.09
64	5.9063e-05	1.64	0.0029	1.21	0.1702	3.31
128	2.2842e-05	1.37	0.0014	1.05	0.0339	2.32
256	9.0978e-06	1.28	5.7747e-04	1.38	0.0092	1.88

Table 2.7: Relative errors and estimated orders of convergence for the collocation method based indirect BEM with piecewise linear basis functions in an L-shaped domain at the point (0.75,0.25) for different k values.

Since there is not an exact solution to this problem, we calculate an approximate error by calculating the relative error, Error(m), between two approximate solutions as we double the number of boundary elements

$$\text{Error}(m) = \frac{|u_m - u_{2m}|}{|u_{2m}|}. \tag{2.43}$$

Table 2.6 shows the approximate errors and the EOC for the Helmholtz problem in an L-shaped domain for different values of k calculated using piecewise constant basis functions. From the table we find that the errors for $k = 10$

and $k = 25$, and in particular for $k = 25$ when m is small, are quite large but they do eventually become smaller for larger values of m. We also see from the table that the EOC has not converged, yet but the estimated convergence rate is mostly above first order. Table 2.7 shows the corresponding results for piecewise linear basis functions. Comparing the piecewise linear basis functions with the piecewise constant basis functions, we notice that the error and convergence rates are similar. Both sets of results show an increase in error as we increase k, as well as an inconsistent convergence rate. As for the unit square domain, the errors are slightly smaller for piecewise constant basis functions and we note that the solution for the example here is discontinuous at the corners of the left edge. It is therefore not surprising that the errors are lower when using a discontinuous set of basis functions (piecewise constant) compared to a continuous one (piecewise linear).

2.7.2 Galerkin method

We look to numerically evaluate the Galerkin discretised BIEs (2.34) for a unit circle, a unit square and an L-shaped domain. We again consider both piecewise constant and piecewise linear basis functions. We examine the errors and EOC at different values of k.

Unit circle domain

As before, we consider the homogeneous Helmholtz equation (2.2) with $g = 0$ and Dirichlet boundary condition $u(r, \theta) = \sin(\theta)$ on a circle domain, which results in an exact solution given by $u(r, \theta) = \frac{J_1(kr)\sin(\theta)}{J_1(k)}$ - see Appendix C.1.

	Results at $k = 1$		Results at $k = 10$		Results at $k = 25$	
m	Error	EOC	Error	EOC	Error	EOC
16	5.0005e-04	-	0.0264	-	0.1532	-
32	5.9528e-05	3.07	0.0022	3.59	0.0018	6.40
64	7.4102e-06	3.00	2.6897e-04	3.03	1.5697e-04	3.52
128	9.2589e-07	3.00	3.3332e-05	3.01	1.8567e-05	3.08
256	1.1599e-07	3.00	4.1672e-06	3.00	2.2966e-06	3.02

Table 2.8: Relative errors and estimated orders of convergence for the Galerkin method based indirect BEM with piecewise constant basis functions in a unit circle at the point (0.5, 0.5) for different k values.

	Results at $k = 1$		Results at $k = 10$		Results at $k = 25$	
m	Error	EOC	Error	EOC	Error	EOC
16	6.2237e-07	-	4.2174e-04	-	0.0078	-
32	5.9556e-08	3.39	2.4060e-06	7.45	1.5861e-06	12.26
64	3.9467e-09	3.92	6.9107e-07	1.80	2.5048e-07	2.66
128	9.0815e-10	2.12	4.2340e-07	0.71	2.6458e-07	-0.08
256	3.8972e-10	1.22	6.2844e-08	2.75	1.7680e-07	0.58

Table 2.9: Relative errors and estimated orders of convergence for the Galerkin based indirect BEM with piecewise linear basis functions in a unit circle at the point (0.5, 0.5) for different k values.

Tables 2.8 and 2.9 show the relative error and EOC between the numerical and analytic solutions for $k = 1$, $k = 10$ and $k = 25$, for both piecewise constant and piecewise linear basis functions. Comparing the results for piecewise constant basis functions with the results from using the collocation method, we find that the errors and EOC are very similar for all values of k and that the errors increase as k gets larger, as expected. Both tables 2.2 and 2.8 show that for $k = 1$, $k = 10$ and $k = 25$, the solution converges at cubic rate, which as we have already discussed, is faster than expected. However, the errors are slightly smaller when using the Galerkin method. In Table 2.9 we observe that the errors for all values of k are small, even for a small number of boundary elements. We find that the Galerkin method is more accurate with piecewise linear basis functions than piecewise constant basis functions, as would usually be expected [4]. But unlike the convergence rates for the piecewise constant basis functions in Table 2.8, we observe that the convergence rates for piecewise linear basis functions are more inconsistent. In this case the errors are significantly smaller than those given by the collocation method in Table 2.3.

Square domain

We consider the homogeneous Helmholtz equation (2.2) with $g = 0$ and the boundary conditions (2.41a) - (2.41c), which gives an exact solution of $u(\boldsymbol{x}) = \cos(kx_1)$ - see Appendix C.2.

Tables 2.10 and 2.11 show the relative error and EOC between the numerical and analytic solutions for $k = 1$, $k = 10$ and $k = 25$, for both piecewise constant and piecewise linear basis functions. From these tables we determine that as k increases so does the error, which is expected. Comparing the results of the

	Results at $k = 1$		Results at $k = 10$		Results at $k = 25$	
m	Error	EOC	Error	EOC	Error	EOC
16	0.0020	-	1.0745	-	0.5479	-
32	3.3018e-04	2.60	0.2748	1.97	0.4500	0.28
64	5.4463e-05	2.60	0.0438	2.65	0.0310	3.86
128	8.8885e-06	2.62	0.0069	2.67	0.0042	2.88
256	1.4384e-06	2.62	0.0011	2.65	6.5151e-04	2.69

Table 2.10: Relative errors and estimated orders of convergence for the Galerkin method based indirect BEM with piecewise constant basis functions in a unit square at the point (0.5, 0.5) for different k values.

	Results at $k = 1$		Results at $k = 10$		Results at $k = 25$	
m	Error	EOC	Error	EOC	Error	EOC
16	3.0011e-05	-	0.2076	-	0.5870	-
32	9.0044e-09	11.70	0.0034	5.93	0.0476	3.62
64	7.3582e-09	0.29	9.1827e-05	6.17	6.5978e-04	6.17
128	3.5512e-09	1.05	5.5918e-06	4.03	1.7274e-05	5.26
256	1.1165e-09	1.67	2.8979e-07	4.27	1.0704e-06	4.01

Table 2.11: Relative errors and estimated orders of convergence for the Galerkin method based indirect BEM with piecewise linear basis functions in a unit square at the point (0.5, 0.5) for different k values.

errors and EOC for piecewise constant basis functions from Table 2.10 with those for the collocation method in Table 2.4, we notice the error results for all values of k are again converging at a consistent rate of approximately 2.6. We also notice that the errors are smaller for the collocation method. From Table 2.11 we observe that the errors are smaller for piecewise linear basis functions, in particular when $k = 1$, but do increase as k increases. The convergence rates for piecewise linear basis functions are again inconsistent as with the circle results in Table 2.9. In contrast with the piecewise constant basis function results, for piecewise linear basis functions the Galerkin method gives the smaller error values.

L-shaped domain

We consider the BVP for the homogeneous Helmholtz equation (2.2) with $g = 0$

on an L-shaped domain with boundary conditions (2.42a) - (2.42b), which has no exact solution. We therefore calculate the relative error between two consecutive solutions as we double the number of elements via (2.43).

	Results at $k = 1$		Results at $k = 10$		Results at $k = 25$	
m	Error	EOC	Error	EOC	Error	EOC
16	0.0240	-	1.3799	-	2.4839	-
32	0.0205	0.26	0.9846	0.49	1.6000	0.63
64	0.0023	3.16	0.0582	4.08	1.0062	0.67
128	2.7651e-04	3.06	0.0128	2.18	0.4124	1.29
256	3.1711e-05	3.12	0.0042	1.61	0.0335	3.62

Table 2.12: Relative errors and estimated orders of convergence for the Galerkin method based indirect BEM with piecewise constant basis functions in an L-shaped domain at the point (0.75, 0.25) for different k values.

	Results at $k = 1$		Results at $k = 10$		Results at $k = 25$	
m	Error	EOC	Error	EOC	Error	EOC
16	2.3156	-	0.1117	-	1.1647	-
32	0.0658	5.14	0.0146	2.94	1.7418	-0.58
64	0.0059	3.48	0.0013	3.49	0.3196	2.45
128	5.1637e-04	3.51	5.8522e-04	1.15	0.0092	5.12
256	2.1010e-04	1.30	2.2806e-04	1.35	0.0028	1.72

Table 2.13: Relative errors and estimated orders of convergence for the Galerkin method based indirect BEM with piecewise linear basis functions in an L-shaped domain at the point (0.75, 0.25) for different k values.

Table 2.12 shows the relative errors and the EOC for the Galerkin based indirect BEM with piecewise constant basis functions on an L-shaped domain for different values of k. From the table we find that the errors for $k = 10$ and $k = 25$ are quite large but they do decrease as we increase m. We also see that the EOC is inconsistent for $k = 10$ and $k = 25$, which would require more tests at larger values of m to check if they do eventually stabilise. Comparing the results from Table 2.12 with those for the piecewise constant collocation method in Table 2.6, we see that for all k values the errors in Table 2.6 are smaller. However, the solutions appear to converge at a faster rate in Table 2.12 and so the Galerkin method may eventually become more accurate than the collocation method for large m. Table 2.13 then shows the relative errors

and convergence rates for piecewise linear basis functions. From this table we find the errors are larger in comparison to the unit circle and square cases but we still observe small errors for large m and all values of k. In comparison to the error results for the piecewise linear collocation method in Table 2.7, we again observe smaller error results from using the collocation method when $k = 1$, but the Galerkin method gives smaller errors for $k = 10$ and $k = 25$.

2.7.3 Comparison of discretisation methods

For the collocation method results in Section 2.7.1, comparing the results between piecewise constant and piecewise linear basis functions we observed that all tables showed reasonably small errors, in particular for all examples when $k = 1$ and also for all values of k in circle example, as the numerical solution matched the exact solution well. The results of Section 2.7.1 show that if the solution is smooth, then piecewise linear basis functions result in smaller errors. However, if the solution is not differentiable (or less regular), which is the case for the unit square and L-shape examples, then piecewise constant basis functions perform better. Comparing the different basis function results for the Galerkin method in Section 2.7.2, we arrive at a similar conclusion that both choices of basis function give results with small errors. The main advantage of using the continuous piecewise linear basis functions appears to be for domains with smooth boundaries and smooth solutions, but we will not be limiting our study to these smooth cases. As discussed previously, using piecewise linear basis functions also complicates the calculation slightly and the results take longer to compute. We also observed that there was no advantage in using the Galerkin method over the collocation method, and comparing the tables of results between the two methods for piecewise constant basis functions, all errors and convergence rates showed no consistent significant difference. The Galerkin method resulted in a more complex calculation, due to the additional integral the method requires, and hence results in longer computational times. Therefore when calculating results for the direct boundary element method in the next section, we will only consider the simplest and quickest implementation method, that is the collocation method with piecewise constant basis functions.

2.8 Numerical examples for the direct BEM

In this section, we present the results for solving the Helmholtz equation (2.2) with Neumann boundary conditions (2.3b) via the direct BEM, discretising via the collocation method with piecewise constant basis functions. The Neumann BVP is of more interest for us to investigate as the Neumann boundary condition arises naturally in vibro-acoustic problems as a physical quantity. For example, when modelling an object vibrating in an acoustic medium, the acceleration of the object's surface in the normal direction to the boundary is expressed in the form of a Neumann boundary condition in the corresponding acoustic problem [37]. In our numerical examples, we consider the cases when Ω is a unit square and an L-shaped domain. To determine the interior solution to these examples we are required to first calculate the boundary solution $u(\boldsymbol{x})$ for $\boldsymbol{x} \in \Gamma$ from equation (2.23). This equation is discretised via the collocation method with piecewise constant basis functions as described in Section 2.4. This leads to the following BIE

$$\sum_{j=1}^{m} \widehat{u}_j \left(\frac{1}{2}\delta_{i,j} + \int_{E_j} \frac{\partial G_k}{\partial \hat{\mathbf{n}}}(\boldsymbol{x}_i, \boldsymbol{y}) d\Gamma_{\boldsymbol{y}} \right) = \sum_{j=1}^{m} \int_{E_j} G_k(\boldsymbol{x}_i, \boldsymbol{y}) f(\boldsymbol{x}_i) d\Gamma_{\boldsymbol{y}}, \quad (2.44)$$

for $i = 1, 2, ..., m$. Here $\delta_{i,j}$ is the Kronecker delta function defined as

$$\delta_{i,j} = \begin{cases} 1 & \text{if } i = j, \\ 0 & \text{if } i \neq j \end{cases}$$

In equation (2.44), f is the Neumann boundary condition (2.3b) and

$$u(\boldsymbol{x}) = \sum_{j=1}^{m} \widehat{u}_j b_j(\boldsymbol{x}), \quad (2.45)$$

where $\widehat{u}_j$ are the coefficients that need to be determined and b_j are the piecewise constant basis functions given by (2.29). Once the coefficients $\widehat{u}_j$ from (2.44) the boundary solution has been calculated then the interior solution is calculated via (2.25). It is important to note that $u(\boldsymbol{x})$ on the left hand side of equation (2.25) is the interior solution and the u in the term $(D_k u)(\boldsymbol{x})$ on the right hand side of the equation is the boundary solution calculated previously. For the numerical examples we consider we examine the errors and estimated order of convergence (EOC) at different values of the wavenumber

k. We also consider the case when there is a point source within these two domains. The MATLAB code for these examples are available from the following URL:https://github.com/JacobRowbottom/BEM/tree/main/Direct .

2.8.1 Inhomogeneous Neumann BVP

Square domain

We consider solving the homogeneous Helmholtz equation with Neumann boundary conditions via the direct BEM for a unit square domain $\Omega = \{(x_1, x_2) \in \mathbb{R}^2 : 0 \leq x_1 \leq 1, 0 \leq x_2 \leq 1\}$. The boundary conditions are defined as

$$\begin{aligned} &\frac{\partial u}{\partial \hat{\mathbf{n}}}(0, x_2) = 1, \qquad \text{for} \quad 0 \leq x_2 \leq 1, \\ &\frac{\partial u}{\partial \hat{\mathbf{n}}} = 0, \qquad\qquad\qquad\quad \text{elsewhere.} \end{aligned} \tag{2.46}$$

That is to say, there is only a non-zero boundary condition on the left edge of the square and the boundary condition is zero elsewhere. The exact solution to the above problem is $u(\boldsymbol{x}) = \frac{1}{k}\left(\cot(k)\cos(kx_1) + \sin(kx_1)\right)$ and is independent of x_2, where $\boldsymbol{x} = (x_1, x_2)$ is a point inside the domain - see Appendix C.3.

	Results at $k = 1$		Results at $k = 10$		Results at $k = 25$	
m	Error	EOC	Error	EOC	Error	EOC
32	0.0025	-	0.0244	-	0.4548	-
64	8.4609e-04	1.56	0.0082	1.57	0.1192	1.93
128	2.7991e-04	1.60	0.0028	1.55	0.0332	1.84
256	9.1485e-05	1.61	9.13658e-04	1.58	0.0087	1.93
512	2.9639e-05	1.62	3.0998e-04	1.59	0.0022	1.98

Table 2.14: Relative errors and estimated orders of convergence for the direct BEM in a square domain at the point (0.5, 0.5) for different k values.

Figure 2.8 shows the numerical and analytical interior solutions of the BVP above for $k = 1$, $k = 10$ and $k = 25$. We observe that the numerical and analytical solutions are visually identical. Table 2.14 shows the errors and estimated convergence rates for different values of the wavenumber k. We find similar results to the indirect method, with the error increasing as k increases. However, the errors in most cases are larger than for the indirect method examples, but we do achieve considerably less than 1% error for all values of k. The convergence rate is also lower than for the Dirichlet problem with the indirect BEM

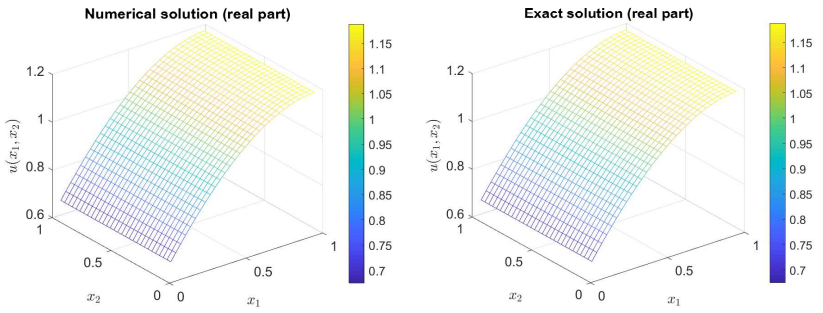

(a) $k = 1$ (b) $k = 1$

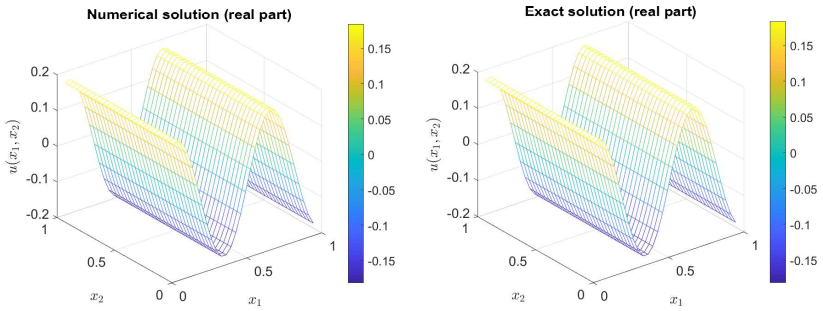

(c) $k = 10$ (d) $k = 10$

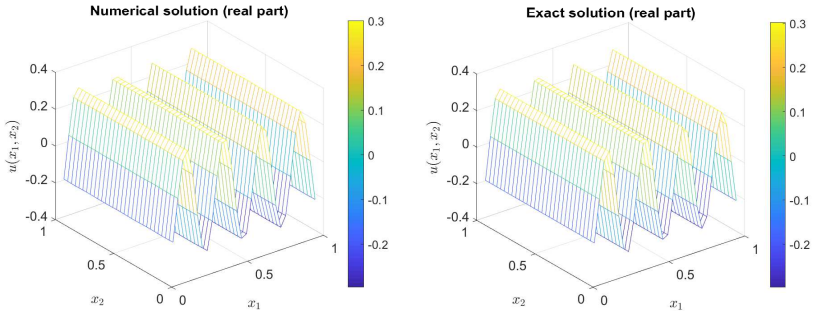

(e) $k = 25$ (f) $k = 25$

Figure 2.8: Comparison between the exact and numerical solutions of the Neumann BVP for the Helmholtz equation in a unit square domain. The numerical solution was calculated using the collocation method based direct BEM with piecewise constant basis functions and $m = 256$ boundary elements.

and appears to have decreased from approximately 2.6 to 1.6, which is most likely due to the change in boundary condition.

L-Shaped domain

We now consider solving the homogeneous Helmholtz equation with Neumann boundary conditions via the direct BEM for the L-shaped domain. We define the boundary conditions as

$$\begin{aligned} &\frac{\partial u}{\partial \hat{\mathbf{n}}}(0, x_2) = 1, \qquad \text{for} \quad 0 \leq x_2 \leq \frac{1}{2}, \\ &\frac{\partial u}{\partial \hat{\mathbf{n}}} = 0, \qquad\qquad\qquad\qquad \text{elsewhere.} \end{aligned} \tag{2.47}$$

Again, we only have a non-zero boundary condition on the left edge of the domain and zero elsewhere. This BVP has no exact solution therefore error results are found by calculating the relative error between two approximate solutions as we double the number of boundary elements via (2.43).

	Results at $k = 1$		Results at $k = 10$		Results at $k = 25$	
m	Error	EOC	Error	EOC	Error	EOC
32	0.0108	-	0.6344	-	0.7467	-
64	0.0035	1.63	0.0762	3.06	0.5721	0.38
128	0.0011	1.67	0.0148	2.36	0.1358	2.07
256	3.7223e-04	1.56	0.0031	2.26	0.0384	1.82
512	1.2031e-04	1.63	6.1242e-04	2.34	0.0098	1.97

Table 2.15: Relative errors and estimated orders of convergence for the direct BEM in an L-shaped domain at the point (0.75, 0.25) for different k values.

Figure 2.9 shows the numerical interior solutions of the BVP for $k = 1$, $k = 10$ and $k = 25$. We notice that the solution is now more complex than in the unit square domain as it depends on both x_1 and x_2. Table 2.15 shows the approximate errors and convergence orders. From this table, we observe that even for $k = 25$ we still eventually obtain small errors below 1% for $m = 512$. In comparison to Table 2.6 for the indirect BEM with the collocation method, we observe that the rate of convergence is more consistent with the direct method and is approximately second order, although the errors are slightly larger than for the indirect BEM in most cases.

2.8.2 Point source excitation with a sound hard boundary

We now consider the numerical solution of the inhomogeneous Helmholtz equation (2.2) with a homogeneous Neumann boundary condition via the direct BEM

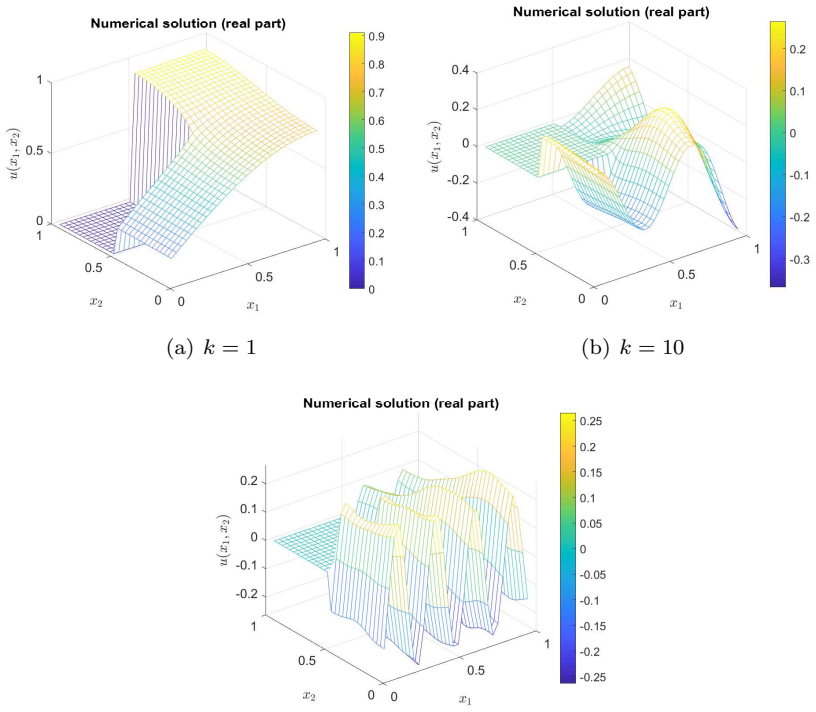

(a) $k = 1$ (b) $k = 10$

(c) $k = 25$

Figure 2.9: Numerical solutions of the Neumann BVP for the Helmholtz equation in an L-shaped domain. The numerical solution was calculated using the collocation method based direct BEM with piecewise constant basis functions and $m = 256$ boundary elements.

for a unit square domain and also an L-shaped domain as depicted in Figure 2.10. For these numerical examples we consider the case when $g(\boldsymbol{x}) = \delta(\boldsymbol{x} - \boldsymbol{x}_0)$ in equation (2.2) and $f = 0$ in (2.3b). Here $\boldsymbol{x}_0 = (x_1^0, x_2^0)$ is the position of the source point inside Ω. The solution to this BVP is discussed in Section 2.1 and may be written as $u = v + G_k$, where v is the solution to a BVP for the homogeneous Helmholtz equation with an inhomogeneous Neumann boundary condition $\frac{\partial v}{\partial \hat{\mathbf{n}}} = -\frac{\partial G_k}{\partial \hat{\mathbf{n}}}$. We numerically solve for v using the direct BEM discretised via the collocation method with piecewise constant basis functions and evaluate G_k directly via (2.5).

An analytical solution to the two-dimensional inhomogeneous Helmholtz problem for a general rectangular domain is given in Appendix C.4. However,

since we are considering a unit square domain, the solution may be expressed more simply as

$$u(\boldsymbol{x}) = 4\sum_{p=0}^{\infty}\sum_{q=0}^{\infty}\frac{\cos(p\pi x_1)\cos(q\pi x_2)\cos\left(p\pi x_1^0\right)\cos\left(q\pi x_2^0\right)}{k^2-\pi^2\left(p^2+q^2\right)}. \tag{2.48}$$

We compare the exact solution to the point source problem with the numerical solution in Figure 2.11, which shows the solutions for a range of different k values resulting from a point source in the centre of the domain at $\boldsymbol{x}^0 = (0.5, 0.5)$. From this figure we observe that the wave oscillates symmetrically outwards from the source point, with an increased oscillation as k increases. We observe a good agreement between the numerical solutions at $m = 256$ and the exact solutions with the sums in (2.48) truncated at $p = q = 200$.

	Results at $k = 1$		Results at $k = 10$		Results at $k = 25$	
m	Error	EOC	Error	EOC	Error	EOC
32	0.0014	-	0.0018	-	0.4357	-
64	4.3055e-04	1.70	0.0023	-0.35	0.1164	1.90
128	1.4831e-04	1.54	0.0012	0.94	0.0317	1.88
256	5.5171e-05	1.52	4.6043e-04	1.38	0.0079	2.00
512	1.7353e-05	1.57	1.6274e-04	1.50	0.0019	2.06

Table 2.16: Relative errors and estimated orders of convergence for the direct BEM in a square domain at the point (0.25, 0.25) with a homogeneous Neumann boundary condition and a point source at (0.5, 0.5) for different k values.

Table 2.16 presents the relative errors and convergence rates for the point source problem in the unit square domain with source point $\boldsymbol{x}_0 = (0.5, 0.5)$. As before, we truncate the sums in (2.48) after $p = q = 200$ terms. From this table we observe similar results to before, that is, the relative error increases as k increases. The order of convergence for $k = 1$ and $k = 10$ seems to be converging to approximately 1.5. However, for $k = 25$ we appear to achieve second order convergence, but with larger errors.

In Figure 2.12 we show the numerical solution for the point source problem in an L-shaped domain with different values of k resulting from a point source at position $\boldsymbol{x}_0 = (0.25, 0.25)$. The solutions appear to be very similar in nature to those for the unit square, but with an obvious loss of symmetry. Table 2.17 presents the relative errors and convergence rates for the point source problem

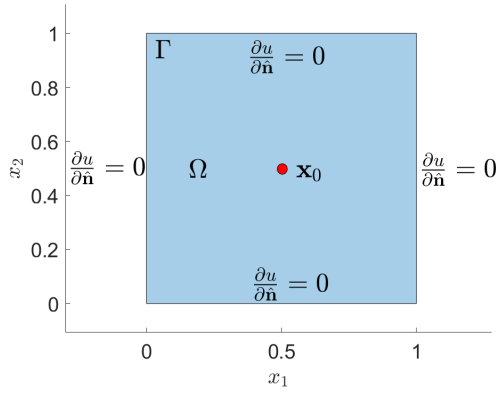

(a) Unit Square

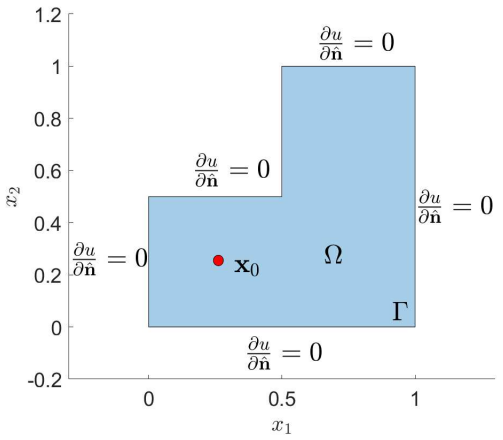

(b) L-shaped domain

Figure 2.10: The unit square and L-shaped BVP for the source point case with homogeneous Neumann boundary conditions. The source points are highlighted by the red circle where $\boldsymbol{x}_0 = (0.5, 0.5)$ for the unit square and $\boldsymbol{x}_0 = (0.25, 0.25)$ for the L-shape.

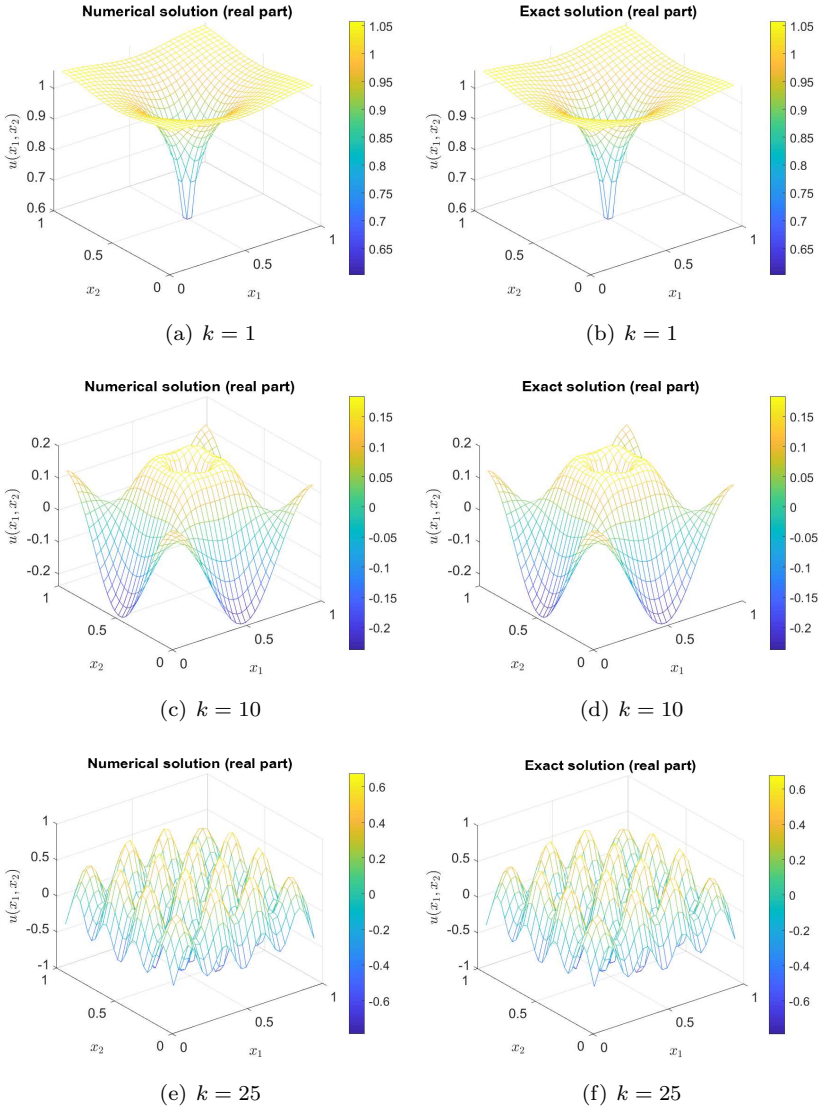

(a) $k = 1$ (b) $k = 1$

(c) $k = 10$ (d) $k = 10$

(e) $k = 25$ (f) $k = 25$

Figure 2.11: Comparison between the exact and numerical solutions of the Neumann BVP for the inhomogeneous Helmholtz equation in a unit square domain with source point $\boldsymbol{x}_0 = (0.5, 0.5)$. The numerical solution was calculated using the collocation method based direct BEM with piecewise constant basis functions and $m = 256$ boundary elements. The exact solution was calculated via (2.48) with the sums truncated at $p = q = 200$.

in the L-shaped domain, where the error results are found by calculating the relative error between two approximate solutions as we double the number of boundary elements via (2.43). From this table, we achieve approximately second order convergence for all cases of k, but with an increase in the error values as we increase k. We also observe that for all cases we achieve less than 1% error when $m = 512$.

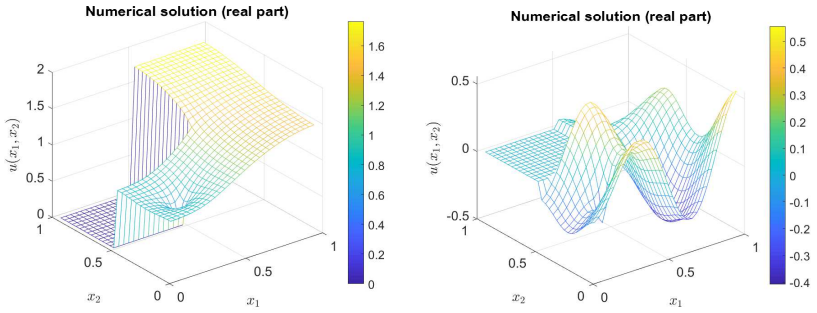

(a) $k = 1$

(b) $k = 10$

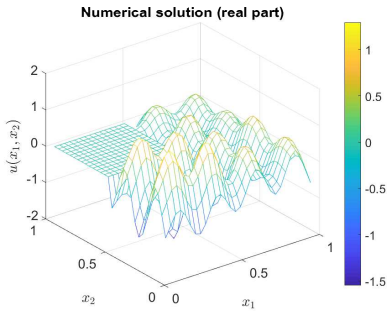

(c) $k = 25$

Figure 2.12: Numerical solutions of the Neumann BVP for the inhomogeneous Helmholtz equation in an L-shaped domain with source point $\boldsymbol{x}_0 = (0.25, 0.25)$. The numerical solution was calculated using the collocation method based direct BEM with piecewise constant basis functions and $m = 256$ boundary elements.

	Results at $k = 1$		Results at $k = 10$		Results at $k = 25$	
m	Error	EOC	Error	EOC	Error	EOC
32	0.0060	-	0.7942	-	0.6533	-
64	0.0026	1.21	0.1062	2.90	0.5142	0.35
128	6.2311e-04	2.06	0.0218	2.28	0.1242	2.05
256	1.5641e-04	1.99	0.0047	2.21	0.0363	1.77
512	4.3511e-05	1.85	9.9229e-04	2.24	0.0094	1.95

Table 2.17: Relative errors and estimated orders of convergence for the direct BEM in an L-shaped domain at the point (0.75, 0.25) with a homogeneous Neumann boundary condition and a point source at (0.25,0.25) for different k values.

2.9 Conclusion

In this chapter, we derived an indirect boundary integral formulation for the two-dimensional BVP for the Helmholtz equation with Dirichlet boundary conditions. We applied the indirect BEM to express the solution as a single layer potential in terms of an unknown layer density σ. We then discretised the resulting BIEs with both the collocation and Galerkin methods, whereby the layer density σ is approximated as a linear combination of basis functions, leading to a linear system of m equations. The methods differ as the collocation method generates an approximate solution by imposing a set of conditions that the integral equation must be solved exactly at a finite number of points in the domain, known as collocation points. Whereas the Galerkin method uses a weak form of the integral equation that is given by multiplying through by each of the basis functions in turn and integrating over the boundary. This involves computing an additional boundary integral compared with the collocation method, resulting in a more complicated implementation. We then solved the resulting BIEs with piecewise constant basis functions as well as piecewise linear basis functions for different domains including a unit circle, unit square and an L-shaped domain. An analysis was conducted by examining the relative error as we double the number of elements and calculating the estimated order of convergence, for different values of k. We found that, in general, as we increased the wavenumber k that the errors increased. We found also that the errors for the L-shaped domain were much larger than for the other domains, and showed a lower order of convergence. However, in this case the errors and convergence orders were estimated calculated using subsequent approximations, whereas for

the other domains we could make use of exact solutions.

A comparison between the two discretisation methods showed that there was no major practical advantage, in terms of accuracy, to using the Galerkin method over the collocation method. However, the Galerkin method resulted in a more complex calculation to implement, due to the additional integral the method requires, and also results in longer computational times. Similarly, when comparing the results between piecewise constant and piecewise linear basis functions we observed that there was no significant difference in the error and the convergence results, and the improvements given by the piecewise linear basis functions were most evident for smooth domains and solutions, which will not be the focus of our work in later chapters. Therefore, when calculating further numerical results using the BEM, we decided to apply the collocation method with piecewise constant basis functions.

In Section 2.3, we derived the BIEs for the two-dimensional Helmholtz BVP via the direct BEM with Neumann boundary conditions. The solution to the BVP can then be expressed in terms of physical quantities. The direct method involves applying Green's identities to derive a boundary integral representation of the Helmholtz equation. Numerical results were computed using the direct BEM discretised using the collocation method with piecewise constant basis functions for a unit square and an L-shaped domain. Experiments were also performed with a point source emitting a wave from inside the domain. This type of problem involves solving the inhomogeneous Helmholtz equation as described in Section 2.1. The error and convergence results exhibited a similar behaviour to the results found using the indirect BEM. That is, the errors increased as k increased. Overall the errors were, in general, slightly larger than for the indirect BEM. The convergence rates were also lower than for the collocation method based indirect BEM on the unit square domain, but higher for the L-shaped domain. In most cases, the convergence appeared to be between first and second order.

Chapter 3

Numerical solution of the wave equation via the convolution quadrature boundary element method

In this chapter, we discuss solving the two-dimensional (in space) wave equation with a Neumann boundary condition via the convolution quadrature boundary element method (CQBEM). We discretise in time via the convolution quadrature method and the spatial discretisation is performed using the direct BEM, as described in Section 2.3. The resulting system of Helmholtz BIEs are solved using the collocation method with piecewise constant basis functions. Numerical experiments are conducted to investigate the solution for an inhomogeneous Neumann initial boundary value problem (IBVP) and also for the case when there is a point source excitation inside the domain together with a homogeneous Neumann boundary condition, for a variety of different domain geometries.

3.1 Integral formulation of the wave equation

Let $\Omega \subset \mathbb{R}^2$ be a finite domain with boundary $\Gamma = \partial\Omega$. We consider the following Neumann IBVP for the two-dimensional inhomogeneous wave equation

$$\Delta\Phi - \frac{1}{c^2}\frac{\partial^2\Phi}{\partial t^2} = P(\boldsymbol{x}, t), \quad \text{in} \quad \Omega \times [0, T], \tag{3.1}$$

with initial conditions

$$\Phi(\cdot, 0) = \partial_t\Phi(\cdot, 0) = 0, \quad \text{in} \quad \Omega, \tag{3.2}$$

and Neumann boundary condition

$$\frac{\partial\Phi}{\partial\hat{\mathbf{n}}} = F \quad \text{on} \quad \Gamma \times (0, T], \tag{3.3}$$

for some $T > 0$. Where Φ is the solution in two-dimensional space $\boldsymbol{x} = (x_1, x_2) \in \Omega$ and time $t > 0$. Here, we assume F and P are real-valued functions of space (in two-dimensions) and time, $c > 0$ is the wave speed and $\hat{\mathbf{n}}$ is the unit outward normal to the boundary. We will consider problems when internal wave sources described by P undergo reflections at rigid boundaries ($F \equiv 0$), or when $P \equiv 0$ and the boundary Γ corresponds to an interface with a vibrating structure that generates an inhomogeneous boundary condition F.

In order to treat the inhomogeneous wave equation (3.1) using a boundary integral formulation, we introduce an incident solution V and a reverberant solution U in the whole of $\mathbb{R}^2$, and write $\Phi = (U + V)|_\Omega$. We assume that V solves the free-space problem

$$\Delta V - \frac{1}{c^2}\partial_t^2 V = \widehat{P}, \quad \text{in} \quad \mathbb{R}^2 \times [0, T], \tag{3.4}$$

where $\widehat{P}$ is an extension of P to the whole of $\mathbb{R}^2$. In this work, we will only consider the spatially localised sources of the form

$$P(\boldsymbol{x}, t) = \delta(\boldsymbol{x} - \boldsymbol{x}_0)P_0(t), \tag{3.5}$$

where $\boldsymbol{x}_0 \in \Omega$ is a source point and $P_0 : [0, T] \to \mathbb{R}$ defines the time-dependence of the source term. Hence $\widehat{P}$ is an extension by zero outside Ω. To find the solution to the free-space problem (3.4) we take the Laplace transform with

respect to t - see Appendix D.2. The resulting equation is

$$\Delta\widetilde{V} - \frac{\zeta^2}{c^2}\widetilde{V} = \delta(\boldsymbol{x} - \boldsymbol{x}_0)\widetilde{P}_0(\zeta). \tag{3.6}$$

Here $\widetilde{V}$ and $\widetilde{P}_0$ represent the Laplace transforms of V and P_0 respectively, with ζ being the Laplace transform parameter. Rewriting (3.6) gives

$$\Delta\widetilde{V} + \left(\frac{i\zeta}{c}\right)^2 \widetilde{V} = \delta(\boldsymbol{x} - \boldsymbol{x}_0)\widetilde{P}_0(\zeta), \tag{3.7}$$

and therefore (3.7) is the inhomogeneous Helmholtz equation (2.2) with wavenumber $k = i\zeta/c$ and $g(\boldsymbol{x}) = \delta(\boldsymbol{x} - \boldsymbol{x}_0)\widetilde{P}_0(\zeta)$. Hence, by linearity, the solution to (3.7) is a scaled fundamental solution to the Helmholtz equation written as

$$\widetilde{V}(\boldsymbol{x}, \zeta) = \widetilde{P}_0(\zeta)G_k(\boldsymbol{x}, \boldsymbol{x}_0), \tag{3.8}$$

where G_k is given by (2.5). Applying the convolution theorem (see Appendix D) then allows us to express the solution to (3.4) as

$$V(\boldsymbol{x}, t) = \int_0^T G(\boldsymbol{x} - \boldsymbol{x}_0, t - \tau)P_0(\tau)d\tau, \tag{3.9}$$

which may be numerically evaluated using an appropriate quadrature rule. Here G is the fundamental solution to the wave equation in two-dimensions given by

$$G(\boldsymbol{x}, t) = \frac{H(t - \|\boldsymbol{x}\|/c)}{2\pi\sqrt{t^2 - \|\boldsymbol{x}\|^2/c^2}}, \tag{3.10}$$

and H is the Heaviside step-function.

We now consider the reverberant solution U. It is easy to see that U must satisfy the homogeneous wave equation, and since $F \equiv 0$ in (3.3), then the boundary condition for U is given by

$$\frac{\partial U}{\partial \hat{\mathbf{n}}} = -\frac{\partial V}{\partial \hat{\mathbf{n}}}. \tag{3.11}$$

The boundary value problem for U therefore takes the same form as (3.1) – (3.3) when $P \equiv 0$ and $F = -\frac{\partial V}{\partial \hat{\mathbf{n}}}$.

For simplicity in future sections, we define the time-domain single and double

layer potential operators, respectively, as

$$(\mathcal{S}\phi)(\boldsymbol{x},t) := \int_0^T \int_\Gamma G(\boldsymbol{x}-\boldsymbol{y},t-\tau)\phi(\boldsymbol{y},\tau)d\Gamma_{\boldsymbol{y}}d\tau, \quad \boldsymbol{x}\in\Omega, \tag{3.12}$$

$$(\mathcal{D}\psi)(\boldsymbol{x},t) := \int_0^T \int_\Gamma \frac{\partial G}{\partial \hat{\mathbf{n}}_{\boldsymbol{y}}}(\boldsymbol{x}-\boldsymbol{y},t-\tau)\psi(\boldsymbol{y},\tau)d\Gamma_{\boldsymbol{y}}d\tau, \quad \boldsymbol{x}\in\Omega, \tag{3.13}$$

where ψ and ϕ are densities. The traces of $\mathcal{S}$ and $\mathcal{D}$ to the boundary Γ are defined by time-domain boundary integral operators:

$$(\mathcal{V}\phi)(\boldsymbol{x},t) := \int_0^T \int_\Gamma G(\boldsymbol{x}-\boldsymbol{y},t-\tau)\phi(\boldsymbol{y},\tau)d\Gamma_{\boldsymbol{y}}d\tau, \quad \boldsymbol{x}\in\Gamma, \tag{3.14}$$

and

$$(\mathcal{K}\psi)(\boldsymbol{x},t) := \int_0^T \int_\Gamma \frac{\partial G}{\partial \hat{\mathbf{n}}_{\boldsymbol{y}}}(\boldsymbol{x}-\boldsymbol{y},t-\tau)\psi(\boldsymbol{y},\tau)d\Gamma_{\boldsymbol{y}}d\tau, \quad \boldsymbol{x}\in\Gamma, \tag{3.15}$$

respectively.

The solution to the wave equation may be represented in a number of different ways in terms of the boundary layer potentials. For example, one may apply the single-layer ansatz, leading to an indirect method for an unknown density function ϕ as follows:

$$\Phi(\boldsymbol{x},t) = (\mathcal{S}\phi)(\boldsymbol{x},t) \quad \text{in} \quad \Omega\times[0,T]. \tag{3.16}$$

As for the Helmholtz equation, one can also apply the double-layer ansatz $\Phi = \mathcal{D}\phi$ instead of (3.16). Alternatively, one can employ a direct representation, known as Kirchoff's formula [73] given by:

$$\Phi(\boldsymbol{x},t) = \left(\mathcal{S}\frac{\partial\Phi}{\partial\hat{\mathbf{n}}}\bigg|_\Gamma\right)(\boldsymbol{x},t) - (\mathcal{D}\Phi|_\Gamma)(\boldsymbol{x},t) \quad \text{in} \quad \Omega\times[0,T]. \tag{3.17}$$

Kirchoff's formula (3.17) is derived from Green's identities similarly to the derivation given in Section 2.3 for the Helmholtz equation. In fact, one can repeat the same steps as in Section 2.3, but using G from (3.10) in place of G_k (2.5) and including an additional integral over the time variable as in (3.12) - (3.15) above. Moving (3.16) and (3.17) from the interior domain Ω to the bound-

ary Γ, one then obtains the following time-domain boundary integral equations

$$\Phi(\boldsymbol{x},t) = (\mathcal{V}\phi)(\boldsymbol{x},t) \quad \text{on} \quad \Gamma \times [0,T], \tag{3.18}$$

$$\left(\frac{1}{2}I + \mathcal{K}\right)\Phi(\boldsymbol{x},t) = \left(\mathcal{V}\frac{\partial \Phi}{\partial \hat{\mathbf{n}}}\bigg|_{\Gamma}\right)(\boldsymbol{x},t) \quad \text{on} \quad \Gamma \times [0,T], \tag{3.19}$$

again using similar arguments to those in sections 2.2 and 2.3. As before, we have made use of the continuity of the Green's function G across Γ to derive (3.18) and the properties of the Dirac delta distribution to derive (3.19) - see Appendix A.1. Similar to (3.16) and (3.17), equation (3.19) is known as a direct boundary integral equation whereas (3.18) is known as an indirect integral equation. As mentioned before, we note that the direct integral equations are expressed in terms of physical quantities, while the indirect integral equations are expressed in terms of unknown densities with no physical interpretation, in general. Therefore proceeding using the direct boundary integral equations is advantageous for engineering applications.

In the remainder of this chapter, we consider solving the IBVP for the wave equation (3.1) - (3.3) by making use of its reformulation as a direct time-domain boundary integral equation (3.19). We next discuss the time-discretisation of (3.19) via the convolution quadrature method and then the spatial discretisation via the BEM with piecewise constant basis functions.

3.2 Time discretisation via CQ

In this section, we outline the semi-discretisation of the BIE (3.19) in time using Lubich's convolution quadrature method [119, 120]. In particular, through the application of CQ we are able to transform the space-time BIE (3.19) into a series of frequency domain problems with complex wavenumbers. We do not recall the theoretical framework here but summarise the application of the method, which is also discussed in [15] in the context of the indirect BEM for the Dirichlet problem. The CQ method approximates convolution integrals of the form

$$y(t) = \int_0^t \kappa(t-\tau)h(\tau)d\tau, \tag{3.20}$$

for a given kernel κ and function h. We note, that the boundary integral operators $\mathcal{V}$ and $\mathcal{K}$ in (3.19) take the form of time convolutions and make use of the

notation

$$\left(\widetilde{\mathcal{V}}(\partial_t)F\right)(\boldsymbol{x},t) = (\mathcal{V}F)(\boldsymbol{x},t), \tag{3.21}$$

$$\left(\widetilde{\mathcal{K}}(\partial_t)\Phi\right)(\boldsymbol{x},t) = (\mathcal{K}\Phi)(\boldsymbol{x},t), \tag{3.22}$$

to emphasise this. Note that $\widetilde{\mathcal{V}}(\partial_t)F$ is standard notation for $(\mathcal{V} * F)$ in the CQ literature [39, 121, 165]. Here $\widetilde{\mathcal{V}}(\zeta)$ and $\widetilde{\mathcal{K}}(\zeta)$ are the Laplace transforms of $\mathcal{V}$ and $\mathcal{K}$ respectively, where ζ is the Laplace transform frequency parameter. That is, $\widetilde{\mathcal{V}}(\zeta) = L_k$ in equation (2.11) and $\widetilde{\mathcal{K}}(\zeta) = M_k$ in equation (2.12) for $k = i\zeta/c$. Explicitly, for $\boldsymbol{x} \in \Gamma$ the Laplace transforms of (3.21) and (3.22) are given by

$$\left(\widetilde{\mathcal{V}}(\zeta)\widetilde{F}\right)(\boldsymbol{x}) = \left(L_k\widetilde{F}\right)(\boldsymbol{x}) = \int_\Gamma G_k(\boldsymbol{x},\boldsymbol{y})\widetilde{F}(\boldsymbol{y},\zeta)d\Gamma_{\boldsymbol{y}}, \tag{3.23}$$

$$\left(\widetilde{\mathcal{K}}(\zeta)u\right)(\boldsymbol{x}) = (M_k u)(\boldsymbol{x}) = \int_\Gamma \frac{\partial G_k}{\partial \hat{\mathbf{n}}_{\boldsymbol{y}}}(\boldsymbol{x},\boldsymbol{y})u(\boldsymbol{y},\zeta)d\Gamma_{\boldsymbol{y}}, \tag{3.24}$$

respectively, where G_k is the fundamental solution to the Helmholtz equation given by (2.5), $\widetilde{F}$ denotes the Laplace transform of F and u is the solution to the Helmholtz equation at wavenumber $k = i\zeta/c$. Note that we have made use of the convolution theorem to derive (3.23) and (3.24) – see Appendix D. It is also important to note that the Laplace transform of Φ (denoted $\widetilde{\Phi}$) is the solution to the Helmholtz equation, $u = \widetilde{\Phi}$ – see equation (3.7).

To discretise the time convolution $\left(\widetilde{\mathcal{K}}(\partial_t)\Phi\right)$ we split the time interval $[0,T]$ into N steps of equal length $\Delta t = T/N$ and compute an approximate solution at the discrete times $t_n = n\Delta t$, for $n = 0, 1, 2, ..., N-1$. The continuous convolution operator $\widetilde{\mathcal{K}}(\partial_t)$ at the discrete times t_n is replaced by the discrete convolution operator

$$(\widetilde{\mathcal{K}}(\partial_t^{\Delta t})\Phi^{\Delta t})(\cdot,t_n) = \sum_{j=0}^{n} w_{n-j}^{\Delta t}(\widetilde{\mathcal{K}})\Phi_j, \tag{3.25}$$

for $n = 0, 1, 2, ..., N-1$, where $\Phi_j = \Phi^{\Delta t}(\cdot, t_j)$ and the superscript Δt is used to denote quantities that have been semi-discretised in time. The convolution weights are defined by their Z-transform

$$\widetilde{\mathcal{K}}\left(\frac{\gamma(z)}{\Delta t}\right) = \sum_{n=0}^{\infty} w_n^{\Delta t}(\widetilde{\mathcal{K}})z^n, \quad |z| < 1. \tag{3.26}$$

The function $\gamma(z)$ is the quotient of the generating polynomials of a multistep method used to discretise in time. The general approximation scheme for a multistep method for a first order ODE $\frac{dy}{dt} = f(t, y)$, whose solution is here (for CQ) assumed to take the form of the function y in equation (3.20), may be approximated via

$$\frac{dy}{dt} \approx \frac{1}{\Delta t} \sum_{j=0}^{m} a_j y(t_{n+j-m}) = \sum_{j=0}^{m} b_j f(t_{n+j-m}, y(t_{n+j-m})), \tag{3.27}$$

in which m is the number of steps, Δt is the time-step size and the coefficients a_j and b_j, for $j = 0, ..., m$, determine the multistep method. By convention $a_0 = 1$, such that $y_{n+1} \approx y(t_{n+1})$ can be conveniently expressed. The quotient of the generating polynomials $\gamma(z)$ is then related to the coefficents in (3.27) via

$$\gamma(z) = \frac{\sum_{j=0}^{m} a_j z^{m-j}}{\sum_{j=0}^{m} b_j^{m-j}}. \tag{3.28}$$

Table 3.1 shows the coefficients of some of the most commonly used A-stable multistep schemes. An A-stable method is one where all solutions to (3.27) tend to zero as $n \to \infty$. In our numerical examples in Section 3.4 we consider both the backward Euler method (BE) and the second order backward difference formula (BDF2).

Method	m	$a_0, ..., a_m$	$b_0, ..., b_m$	$\gamma(z)$
Backward Euler	1	1,-1	1,0	$1 - z$
BDF2	2	$\frac{3}{2}, -2, \frac{1}{2}$	1,0,0	$\frac{1}{2}(z^2 - 4z + 3)$
Trapezium	1	1,-1	$\frac{1}{2}, \frac{1}{2}$	$\frac{2(1-z)}{1+z}$

Table 3.1: Examples of commonly used A-stable multistep methods.

The convolution weights can be calculated via an approximation of Cauchy's integral formula using the trapezodial rule. The approximate convolution weights are then given by a scaled inverse discrete Fourier transform

$$\begin{aligned} w_j^{\Delta t}(\widetilde{\mathcal{K}}) &= \frac{1}{2\pi i} \oint_C \widetilde{\mathcal{K}} \left(\frac{\gamma(z)}{\Delta t} \right) z^{-(j+1)} dz, \\ &\approx \frac{\lambda^{-j}}{\widetilde{N}} \sum_{l=0}^{\widetilde{N}-1} \widetilde{\mathcal{K}}(\zeta_l) e^{2\pi i l j / \widetilde{N}} =: w_j^{\Delta t, \lambda}(\widetilde{\mathcal{K}}), \end{aligned} \tag{3.29}$$

where C is a circular contour centered at the origin of radius $\lambda < 1$ and

$$\zeta_l = \frac{\gamma(\lambda e^{-2\pi i l/\widetilde{N}})}{\Delta t}, \tag{3.30}$$

for $l = 0, 1, 2, ..., \widetilde{N} - 1$. In this work we allow the choices of N, the number of time-steps, and $\widetilde{N}$, the number of frequencies, to be decoupled in order to potentially over-resolve in the Laplace domain for better accuracy as proposed in [26, 120]. Typically we choose $\widetilde{N} = 2N$ as recommended in [120], although for the numerical results in this chapter (Section 3.4) we find that $N = \widetilde{N}$ provides sufficient accuracy and hence do not resolve any further.

We now show that applying the semi-discretisation (3.25), together with an analogous time discretisation procedure for $\left(\widetilde{\mathcal{V}}(\partial_t)F\right)$, in the integral equation (3.19) leads to a system of integral equations for the Helmholtz equation with complex wavenumbers $k_l = i\zeta_l/c$ for $l = 0, 1, 2, ..., \widetilde{N} - 1$. By extending the sum in (3.25) to $j = N - 1$ and substituting the approximate weights (3.29) into a time discretised version of (3.19), we obtain a system of equations for $\Phi^{\Delta t,\lambda}(\boldsymbol{x}, t_n) = \Phi_n^\lambda(\boldsymbol{x})$:

$$\frac{1}{2}\Phi_n^\lambda + \sum_{j=0}^{N-1} w_{n-j}^{\Delta t,\lambda}\left(\widetilde{\mathcal{K}}\right)\Phi_j^\lambda = \sum_{j=0}^{N-1} w_{n-j}^{\Delta t,\lambda}\left(\widetilde{\mathcal{V}}\right)F(\cdot, t_j), \tag{3.31}$$

for $n = 0, 1, ..., N - 1$.

Substituting the definition of $w^{\Delta t,\lambda}$ (3.29) into (3.31), then multiplying by λ^n and applying a discrete Fourier transform with respect to n gives

$$\frac{1}{2}u_l(\boldsymbol{x}) + \left(\widetilde{K}(\zeta_l)u_l\right)(\boldsymbol{x}) = \left(\widetilde{V}(\zeta_l)\widetilde{F}_l\right)(\boldsymbol{x}), \quad \boldsymbol{x} \in \Gamma, \tag{3.32}$$

for $l = 0, 1, ..., \widetilde{N} - 1$, where

$$u_l = \sum_{n=0}^{N-1} \Phi_n^\lambda \lambda^n e^{-2\pi i l n/\widetilde{N}}, \quad \widetilde{F}_l = \sum_{n=0}^{N-1} F(\cdot, t_n)\lambda^n e^{-2\pi i l n/\widetilde{N}},$$

are the Z-transforms of $\Phi^{\Delta t,\lambda}$ and F respectively. Equation (3.32) is of the same form as the direct BIE for the Helmholtz equation (2.24), but with k_l, $\widetilde{\mathcal{V}}$ and $\widetilde{\mathcal{K}}$ in place of k, L_k and M_k respectively - see (3.23) and (3.24). We have thereby transformed the problem of numerically solving the wave equation to a system of Helmholtz problems with complex wavenumbers $k_l = i\zeta_l/c$, for

$l = 0, 1, 2, ..., \widetilde{N} - 1$. This can be reduced to solving only $\widetilde{N}/2 + 1$ Helmholtz problems, since the wavenumbers k_l (an example is shown in Figure 3.1 (a)) occur in symmetric pairs relative to the imaginary axis, and hence the solutions to these pairs of Helmholtz problems are complex conjugates. One can see this by considering the Helmholtz equation $\Delta u + k^2 u = 0$ and so the solution only depends on k^2. The pairs of wavenumbers take the form $k = \pm k_{\mathrm{R}} + i k_{\mathrm{I}}$, where k_{R}, k_{I} denote the real and imaginary parts respectively. This means that $k^2 = (k_{\mathrm{R}}^2 - k_{\mathrm{I}}^2) \pm i(2k_{\mathrm{R}}k_{\mathrm{I}})$ and hence are conjugate pairs. Taking the complex conjugate of the Helmholtz equation we obtain $\Delta \overline{u} + \overline{k^2}\overline{u} = 0$ and thus the solutions for these pairs of wavenumbers occur in conjugate pairs.

Figure 3.1 investigates the effect the parameters $\widetilde{N} = N$ and λ have on the range of complex wavenumbers k_l. Sub-plot (a) shows a range of the complex wavenumbers $k_l = i\zeta_l/c$ for the set of Helmholtz problems obtained using the BDF2 scheme with $N = \widetilde{N} = 256$, $T = 2$, $c = 1$ and $\lambda = \Delta t^{3/N}$. The wavenumbers in sub-plots (b) and (c) are calculated by the BDF2 scheme with $T = 2$ and $c = 1$ as the parameters $N = \widetilde{N}$ and λ are changed. In sub-plot (b), we observe that as we double the number of frequencies from $\widetilde{N} = 256$ to $\widetilde{N} = 512$, the range of wavenumbers approximately doubles. By considering the imaginary part of the wavenumber at the top of the range of wavenumbers, when $\widetilde{N} = 256$ (the wavenumber at $l = N/2 + 1$ with the largest imaginary part), has $\mathrm{Im}(k_{129}) \approx 500$. Whereas the wavenumber at the top when $\widetilde{N} = 512$ is $\mathrm{Im}(k_{257}) \approx 1000$. In [15], Banjai explains that the choice for λ must be chosen small enough to ensure stability and accuracy, but also large enough to avoid numerical instability issues as stated in Theorem 5.5 and Remark 5.1. Banjai shows that the choice of λ is limited by $\lambda = \max(\Delta t^{3/\widetilde{N}}, 10^{-8/\widetilde{N}})$. Therefore, we investigate the range of complex wavenumbers for the case when $\lambda = \Delta t^{3/\widetilde{N}}$ and $\lambda = 10^{-8/\widetilde{N}}$, as shown in sub-plots (b) and (c). Sub-plot (c) shows the same plot as sub-plot (b) but zoomed in on $-250 < \mathrm{Re}(k_l) < 0$, such that the difference between the two choices of λ is noticeable. In this plot we observe only a slight difference between the two sets of wavenumbers as a result of the choice for λ.

In the next section, we describe the spatial discretisation of these Helmholtz problems via the direct BEM.

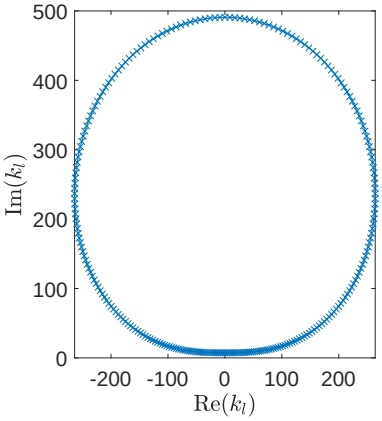

(a)

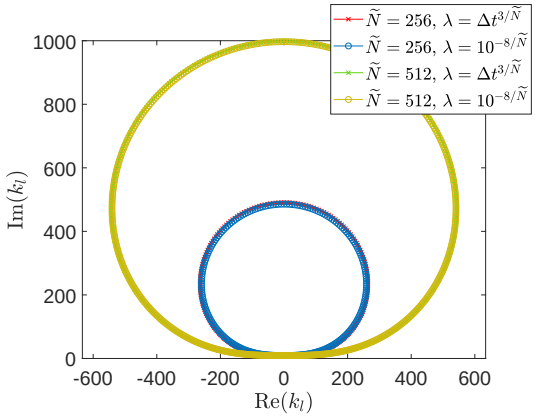

(b)

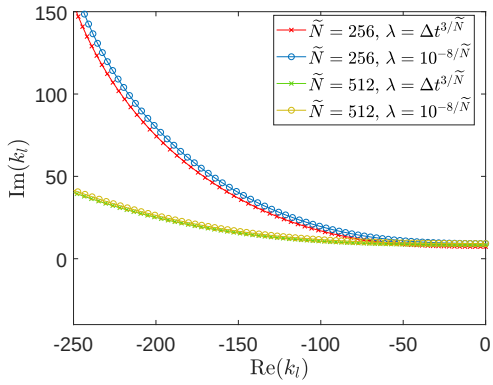

(c)

Figure 3.1: Sub-plot (a) shows a range of complex wavenumbers $k_l = i\zeta_l/c$ for the set of Helmholtz problems obtained using the BDF2 scheme with $N = \widetilde{N} = 256$, $T = 2$, $c = 1$ and $\lambda = \Delta t^{3/N}$. Sub-plot (b) shows a range of complex wavenumbers $k_l = i\zeta_l/c$ for the set of Helmholtz problems obtained using the BDF2 scheme with $T = 2$ and $c = 1$, for different numbers of frequencies $N = \widetilde{N}$ and λ values, as detailed in the legend. Sub-plot (c) shows the same range of complex wavenumbers as plot (b), but focused in on $-250 < \mathrm{Re}(k_l) < 0$.

3.3 Spatial discretisation: BEM

For the spatial discretisation, we employ a piecewise constant collocation boundary element method as discussed in Section 2.4 and divide Γ into M subintervals (or elements) E_m of approximately equal size. For the space-time discrete solution at time t_n, we assume that both the solution of (3.32) u_l and the transformed boundary data $\widetilde{F}_l$, can be approximated by piecewise constant basis functions as follows

$$u_l = \sum_{m=1}^{M} u_{l,m} b_m, \quad \widetilde{F}_l = \sum_{m=1}^{M} \widetilde{F}_{l,m} b_m, \tag{3.33}$$

respectively, where b_m, for $m = 1, 2, ..., M$, are the piecewise constant basis functions defined in (2.29). Again, we note that (3.33) is similar to (2.26) but with the additional frequency index l, since we are finding u_l for a range of frequencies rather than just one. We substitute (3.33) into our integral equations (3.32) and solve for the transformed solution coefficients $u_{l,m}$. The coefficients of the basis expansions of $\widetilde{F}_l$ are simply given by $\widetilde{F}_{l,m} = \widetilde{F}_l(\boldsymbol{x}_m)$, where $\boldsymbol{x}_m$ is the collocation point taken at the centre of the element E_m. The fully discrete system of equations may then be written as

$$\frac{1}{2}\sum_{m=1}^{M} u_{l,m} b_m(\boldsymbol{x}_i) + \sum_{m=1}^{M} u_{l,m} \left(\widetilde{\mathcal{K}}(\zeta_l) b_m\right)(\boldsymbol{x}_i) = \sum_{m=1}^{M} \widetilde{F}_{l,m} \left(\widetilde{V}(\zeta_l) b_m\right)(\boldsymbol{x}_i), \tag{3.34}$$

for $l = 0, 1, ..., \widetilde{N} - 1$, where $\boldsymbol{x}_i$, $i = 1, 2, ..., M$ are the collocation points. As before, we choose these points to be located at the centre of the corresponding boundary element and the functions $\left(\widetilde{\mathcal{V}}(\zeta_l) b_m\right)$ and $\left(\widetilde{\mathcal{K}}(\zeta_l) b_m\right)$ are defined by (3.23) and (3.24), respectively. We note that (3.34) describes the same spatial discretisation method as in Section 2.4, although here the method has been applied to the direct BIE. The numerical solution to the wave equation Φ_j can then be approximated via the trapezoidal rule for evaluating the inverse Z-transform as

$$\Phi_j^{\lambda} = \frac{\lambda^{-j}}{\widetilde{N}} \sum_{l=0}^{\widetilde{N}-1} u_l e^{2\pi i l j/\widetilde{N}}, \tag{3.35}$$

for $j = 0, 1, ..., N - 1$.

The interior solution is calculated by applying the same time and spatial discretisation to (3.17). We obtain the Laplace domain interior solution u_l, at

any point $\boldsymbol{x}$ inside the domain Ω for $l = 0, 1, ..., \widetilde{N} - 1$, as

$$u_l(\boldsymbol{x}) = \left(\widetilde{\mathcal{V}}(\zeta_l)\widetilde{F}_l\right)(\boldsymbol{x}) - \left(\widetilde{\mathcal{K}}(\zeta_l)u_l\right)(\boldsymbol{x}). \tag{3.36}$$

Note here, that u_l is the boundary solution calculated in (3.33) and (3.34). An analogous inverse transform to (3.35) is used to approximate the interior solution $\Phi(\boldsymbol{x}, t)$ from $u_l(\boldsymbol{x})$ at $\boldsymbol{x} \in \Omega$ via

$$\Phi_n^{\lambda}(\boldsymbol{x}) = \frac{\lambda^{-n}}{\widetilde{N}} \sum_{l=0}^{\widetilde{N}-1} u_l(\boldsymbol{x}) e^{2\pi i l n/\widetilde{N}}, \tag{3.37}$$

for $n = 0, 1, ..., N - 1$.

3.4 Numerical results

In this section, we present the results for solving the wave equation (3.1) with Neumann boundary conditions (3.3) via the collocation based direct CQBEM with piecewise constant basis functions in space, as discussed in sections 3.2 and 3.3. We now present a step-by-step guide which lists the steps required to apply the collocation based direct CQBEM with piecewise constant basis functions to the homogeneous two-dimensional wave equation (3.1) with $P \equiv 0$ and Neumann boundary condition (3.3).

1. To begin, we divide the boundary Γ into M boundary elements E_m of approximately equal size and split the time interval $[0, T]$ into N steps of equal length $\Delta t = T/N$. The number of frequencies $\widetilde{N}$ must then be chosen. In the numerical examples we consider in this section, the number of frequencies are chosen to be $\widetilde{N} = N$ as we find it provides sufficient accuracy. However, it is recommended that using $\widetilde{N} = 2N$ frequencies to over-resolve in the Laplace domain can be used to obtain better accuracy as proposed in [26, 120].

2. We then calculate the wavenumbers $k_l = i\zeta_l/c$ for $l = 0, 1, ..., \widetilde{N} - 1$, where ζ_l are determined via (3.30). The coefficients in (3.30) are dependent on which multistep method is used. Table 3.1 provides a summary of the coefficients of some common A-stable multistep methods. In our numerical examples we consider the BE and BDF2.

3. Next, we calculate the transformed Neumann boundary data $\widetilde{F}_l$ from (3.33) where the coefficients $\widetilde{F}_{l,m}$ are determined via

$$\widetilde{F}_{l,m} = \widetilde{F}_l(\boldsymbol{x}_m) \sum_{n=0}^{N-1} F(\boldsymbol{x}_m, t_n) \lambda^n e^{-2\pi i l n/\widetilde{N}}.$$

   Here $\boldsymbol{x}_m$, for $m = 1, 2, ..., M$, are the collocation points chosen to be the centre of the elements and b_m, for $m = 1, 2, ..., M$, are the piecewise constant basis functions defined in (2.29). The parameter λ is given by $\lambda = \max(\Delta t^{3/\widetilde{N}}, 10^{-8/\widetilde{N}})$.

4. We then solve the system of Helmholtz equations (3.34) for the transformed boundary solution coefficients $u_{l,m}$, for each wave number k_l, $l = 0, 1, ..., \widetilde{N} - 1$, and for each collocation point $\boldsymbol{x}_i$, $i = 1, 2, ..., M$. The functions $\left(\widetilde{\mathcal{V}}(\zeta_l) b_m\right)$ and $\left(\widetilde{\mathcal{K}}(\zeta_l) b_m\right)$ are defined by (3.23) and (3.24), respectively.

5. Once the boundary solution $u_{l,m}$ in the frequency domain has been determined. The boundary solution to the wave equation in the time domain is found via the inverse transform given by (3.35).

6. The interior solution in the Laplace domain $u_l(\boldsymbol{x})$ can then be calculated via (3.36), where $\boldsymbol{x}$ is any point inside the domain Ω. Note that u_l in equation (3.36) is the boundary solution calculated in (3.33) and (3.34). The interior solution to the wave equation in the time domain $\Phi(\boldsymbol{x}, t)$ at $\boldsymbol{x} \in \Omega$ is then approximated via the inverse transform to (3.35).

The MATLAB code for these examples are available from the following URL: https://github.com/JacobRowbottom/CQBEM-HYBRID/tree/main/Neumann%20IBVP.

In our numerical examples, we first consider an inhomogeneous Neumann IBVP for the cases when Ω is a unit square and an L shaped domain. We examine the errors and estimated orders of convergence (EOC) for different multistep methods for the time discretisation. We also later consider the case when there is a point source inside a square domain, L-shaped domain and an irregular polygon domain.

3.4.1 Inhomogeneous Neumann IBVP

We consider the results of applying the CQBEM to the homogeneous wave equation (3.1), when $P = 0$, with Neumann boundary condition (3.3) for the

case when Ω is either a unit square or an L-shaped domain, as depicted in Figure 3.2.

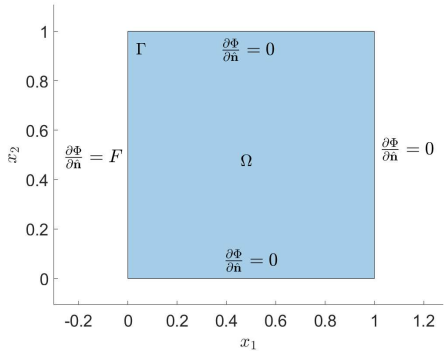

(a) Unit square domain

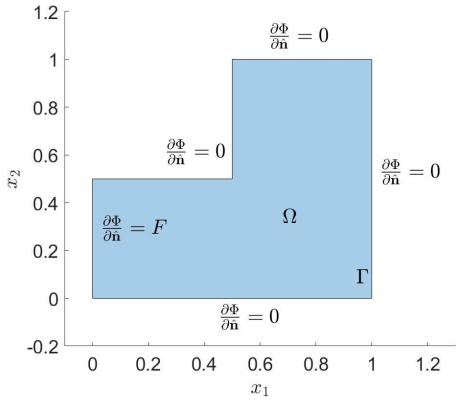

(b) L-shaped domain

Figure 3.2: The Neumann boundary conditions on the square and L-shaped domains.

Square domain

For the unit square example, we consider one-dimensional wave propagation that is only dependent on a single spatial coordinate x_1. A general solution to the one-dimensional wave equation was derived by d'Alembert [78] and is

written as

$$\Phi(\boldsymbol{x},t)=\frac{1}{2}\left(\Phi_0(x_1-ct)+\Phi_0(x_1+ct)\right)+\frac{1}{2c}\int_{x_1-ct}^{x_1+ct}\Phi_0'(s)ds, \tag{3.38}$$

where Φ satisfies the initial conditions

$$\begin{aligned}\Phi(\boldsymbol{x},0)&=\Phi_0(\boldsymbol{x}),\\ \partial_t\Phi(\boldsymbol{x},0)&=\Phi_0'(\boldsymbol{x}),\end{aligned}$$

and Φ_0, Φ_0' are given functions. For our numerical examples, we define the functions Φ_0 and Φ_0' to be zero (to machine precision) in $\Omega\cup\Gamma$, in order to (approximately) satisfy the initial conditions (3.2). We consider the Neumann boundary condition

$$\begin{aligned}F(\boldsymbol{x},t)=&-\alpha(x_1-c(t-t_0))e^{-\alpha(x_1-c(t-t_0))^2}\\ &-\alpha(x_1+c(t+t_0))e^{-\alpha(x_1+c(t+t_0))^2},\end{aligned} \tag{3.39}$$

along the left edge, where $x_1=0$ and zero boundary conditions on all other edges, as shown in Figure 3.2. Here $\boldsymbol{x}=(x_1,x_2)$ and in our numerical examples we choose the wave speed $c=1$. The parameters $t_0>0$ and $\alpha>0$ control the position of the peak of the wave and its bandwidth, respectively. These parameters are chosen carefully to ensure that the initial conditions are approximately satisfied. For our results, we only consider small times so that we do not observe any reflections, in order to compare our results with the exact solution

$$\Phi(\boldsymbol{x},t)=\frac{1}{2}\left(e^{-\alpha(x_1-c(t-t_0))^2}+e^{-\alpha(x_1+c(t+t_0))^2}\right) \tag{3.40}$$

for an infinite domain (in the x_1 direction).

We now analyse the numerical results for the case when the domain is a unit square. For simplicity, we parameterise a point along the boundary $\boldsymbol{x}\in\Gamma$ by the boundary arclength parameter $s\in[0,L)$, where L is the length of the boundary. Similarly the parameterised collocation points $\boldsymbol{x}_i$ are denoted as $s_i\in[0,L)$. Figure 3.3 shows the numerical boundary solution Φ_n, $n=0,1,...,N-1$ and the corresponding exact solution Φ, for $N=256$ time-steps and $M=256$ boundary elements. From this figure we can see that the numerical and exact solutions appear identical by eye, exhibiting the same behaviour as the wave propagates through the domain and along the boundary. The horizontal axis

shows the arclength parameter s along the boundary Γ. Figure 3.4 shows the solution against time at a single interior point $\boldsymbol{x} = (0.5, 0.5)$ for $N = M = 256$. We observe that the numerical solution is matching the exact solution well.

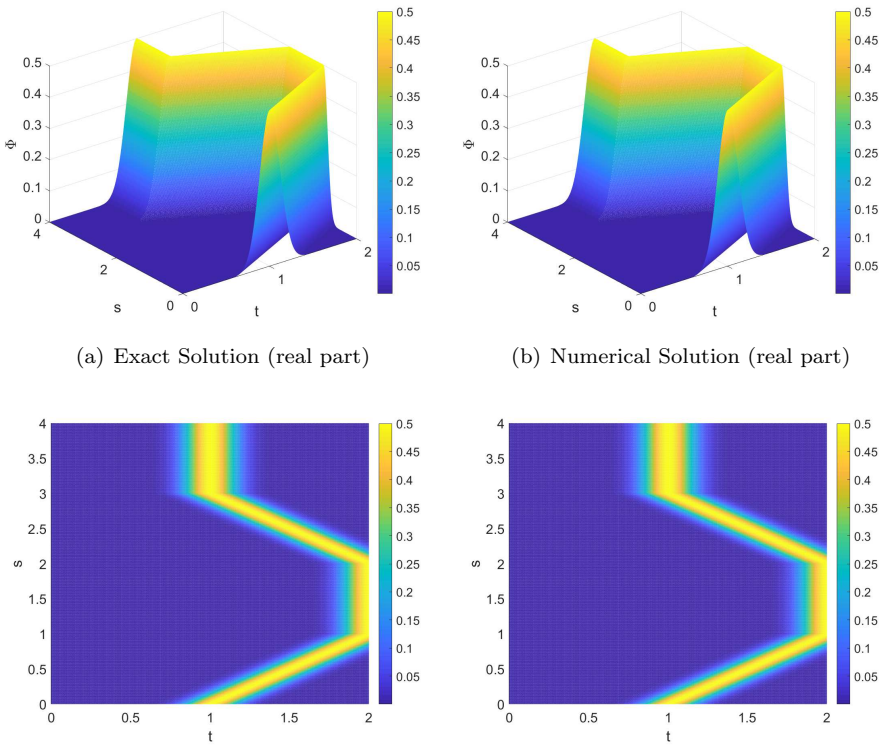

(a) Exact Solution (real part)

(b) Numerical Solution (real part)

(c) Exact Solution (real part)

(d) Numerical Solution (real part)

Figure 3.3: Comparison between the exact and numerical boundary solutions of the Neumann IBVP for the wave equation in a unit square domain along the boundary Γ. The numerical solution was calculated using the collocation based direct CQBEM with piecewise constant basis functions in space and a CQ backward Euler time-stepping method in time with $N = M = 256$.

To investigate the error of the interior solution at $\boldsymbol{x} \in \Omega$ we use the following relative error:

$$\text{Error}(N) = \sqrt{\frac{\sum_{n=0}^{N-1} \left(\Phi(\boldsymbol{x}, t_n) - \Phi_n(\boldsymbol{x})\right)^2}{\sum_{n=0}^{N-1} \left(\Phi(\boldsymbol{x}, t_n)\right)^2}}. \tag{3.41}$$

We choose $\lambda = 10^{-8/\tilde{N}}$, to ensure stability as suggested in [15]. The convergence

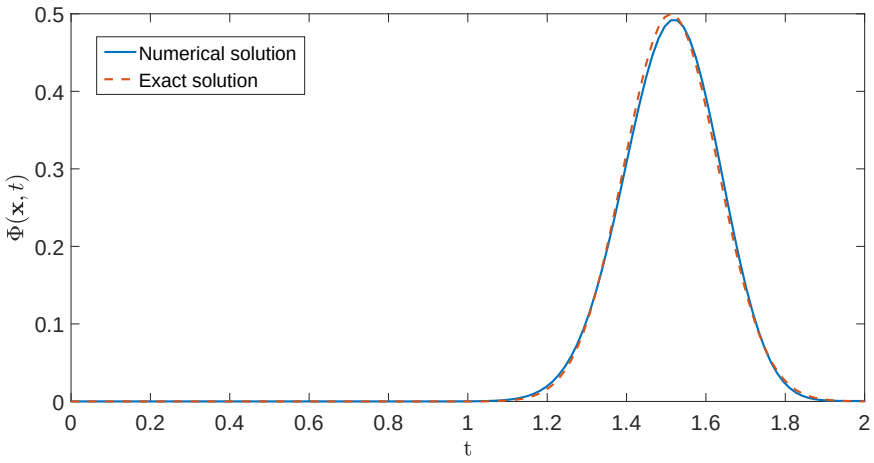

Figure 3.4: Plot of the numerical solution $\Phi_n(\boldsymbol{x})$, versus the exact solution $\Phi(\boldsymbol{x}, t_n)$ for $n = 0, 1, ..., N-1$, at the point $\boldsymbol{x} = (0.5, 0.5)$ inside the unit square domain. The numerical solution was calculated using the collocation based direct CQBEM with piecewise constant basis functions in space and CQ with the backward Euler time-stepping method in time with $N = M = 256$.

rates are estimated by $\log_2(\text{Error}(N/2)/\text{Error}(N))$ and the errors and convergence rates are shown in tables 3.2 and 3.3 for the cases when the parameters are taken as $\alpha = 36$, $t_0 = 0.1$ and for the case when $\alpha = 4096$, $t_0 = 1$ in (3.39). Table 3.2 shows the error and convergence rates for the backward Euler time discretisation. For the case when $\alpha = 36$, $t_0 = 1$, if M is chosen large enough, we observe the expected first order convergence [91] as we double the number of time-steps and boundary elements together. However, when we consider the case with $\alpha = 4096$ and $t_0 = 0.1$ we observe significantly larger errors due to there not being a large enough number of boundary elements and time-steps to model the broadband signal. In Table 3.3, we observe the error and convergence rates obtained by implementing BDF2 time discretisation, therefore as we double the number of time-steps we multiply the number boundary elements by four, in order to obtain the expected second order convergence for the BDF2 time discretisation [91]. For the case when $\alpha = 36$ and $t_0 = 1$, the errors are smaller than those from the backward Euler method and we achieve the expected second order convergence rate. But for the case when $\alpha = 4096$, $t_0 = 0.1$, while the errors are smaller than with backward Euler, we again observe relatively large errors and an inconsistent convergence rate.

		$\alpha = 36,\quad t_0 = 1,\ T = 2$		$\alpha = 4096,\quad t_0 = 0.1,\ T = 1$	
N	M	Error	EOC	Error	EOC
32	4	0.1246	-	2.9893	-
64	8	0.0722	0.79	0.8822	1.76
128	16	0.0460	0.65	0.8325	0.08
256	32	0.0256	0.85	0.7604	0.13
512	64	0.0136	0.91	0.6633	0.20
1024	128	0.0070	0.96	0.5413	0.29

Table 3.2: Relative errors and estimated orders of convergence for the interior solution in the square domain at the point $\boldsymbol{x} = (0.5, 0.5)$ using the backward Euler time discretisation in the CQ method with different choices for the parameters α and t_0 in the Neumann boundary condition (3.39).

		$\alpha = 36,\quad t_0 = 1,\ T = 2$		$\alpha = 4096\quad t_0 = 0.1,\ T = 1$	
N	M	Error	EOC	Error	EOC
64	4	0.0681	-	0.8715	-
128	16	0.0121	2.49	0.7983	0.13
256	64	0.0018	2.75	0.6372	0.33
512	256	4.5453e-04	1.99	0.3884	0.71
1024	1024	1.1602e-04	1.97	0.1465	0.29

Table 3.3: Relative errors and estimated orders of convergence for the interior solution in the square domain at the point $\boldsymbol{x} = (0.5, 0.5)$ using the BDF2 time discretisation in the CQ method with different choices for the parameters α and t_0 in the Neumann boundary condition (3.39).

We next investigate the affect the number frequencies $\widetilde{N}$, the number of time-steps N and the number of boundary elements M have on the interior solution plots. Figure 3.5 shows the numerical solution Φ against time at the interior point $\boldsymbol{x} = (0.5, 0.5)$ for a variety of different frequencies, time-steps and boundary elements. The numerical solutions were calculated using the collocation based direct CQBEM with piecewise constant basis functions in space and a CQ BDF2 time-stepping method in time. Sub-plot (a) shows the numerical solutions computed while fixing the number of boundary elements to $M = 512$, as the number of time-steps $\widetilde{N} = N$ is doubled. We observe that if Δt is large, when $N = 16$ ($\Delta t = 0.0125$), the numerical solution is inaccurate compared to the exact solution observed in Figure 3.4. For $N > 256$, we observe a numerical solution which appears to match the exact solution

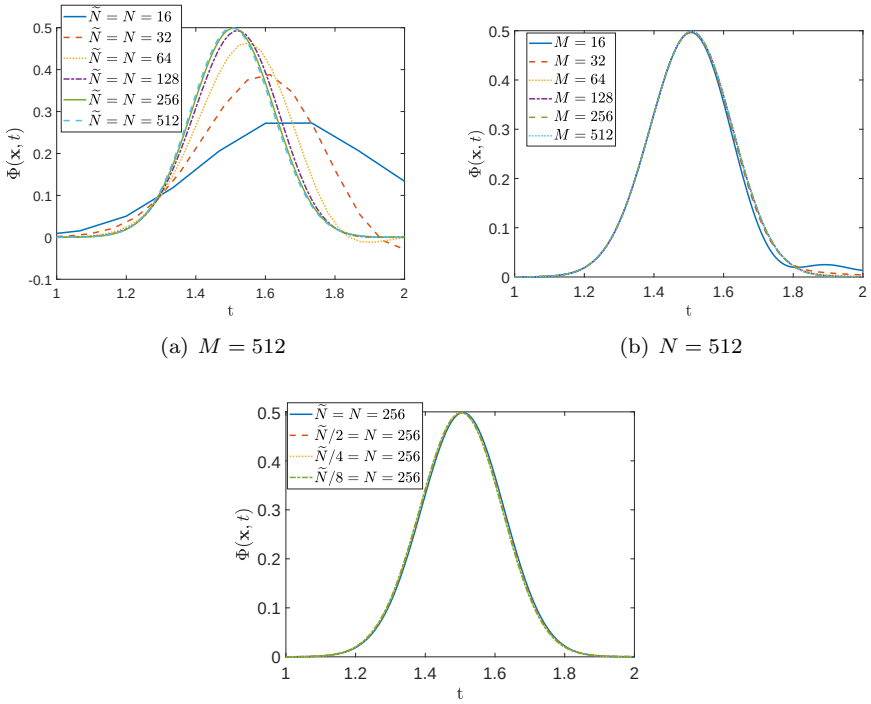

(a) $M = 512$

(b) $N = 512$

(c) $N = M = 256$

Figure 3.5: Plots of the numerical solution $\Phi_n(\boldsymbol{x})$ at the point $\boldsymbol{x} = (0.5, 0.5)$ inside the unit square domain. The numerical solution was calculated using the collocation based direct CQBEM with piecewise constant basis functions in space and CQ with the BDF2 time-stepping method in time. Sub-plot (a) has $M = 512$ boundary elements as the number of time-steps is changed. Sub-plot (b) has $N = \widetilde{N} = 512$ time-steps as the number of boundary elements is changed. Sub-plot (c) has $N = M = 256$ time-steps and boundary elements as the number of frequencies $\widetilde{N}$ is doubled. The solutions are shown for $1 < t < T = 2$ to focus on the late time behaviour since the solution along the boundary is zero (to machine precision) for $t \leq 1$.

well, this corresponds to $\Delta t > 1/128 \approx 0.0078$. In sub-plot (b), the numerical solutions are computed while fixing the number of time-steps and frequencies to $\widetilde{N} = N = 512$ as the number of boundary elements are doubled. From this sub-plot, we observe that for only $M < 32$ do we observe that the numerical solution is inaccurate as the solutions display some slight oscillation towards the tail end of the plots when $t > 1.6$. In sub-plot (c), we fix the number of time-steps and boundary elements to $N = M = 256$, as we double the number

of frequencies, over-resolving in the Laplace domain in each case. In this sub-plot, we observe no difference between the numerical solutions as $\widetilde{N}$ is doubles, which further supports that for $\alpha = 36$ we are not required to over-resolve in order to achieve more accurate results. Comparing sub-plot (a) to sub-plot (b) in Figure 3.5, we notice that the size of Δt has a larger impact on the accuracy of the numerical solution compared to the number of boundary elements.

As a starting point for the choice of the number of boundary elements required, we follow the recommendation of 6-10 boundary elements per wave length as suggested in [129]. In this paper the author discusses that six boundary elements per wavelength, often written concisely as $kh < 1$ where k is the wavenumber and h is the element size, provides sufficient accuracy. The more significantly smaller kh is then the more accurate the solution will be. In Figure 3.5, we observe that $M > 256$ provides sufficient accuracy for the range of wavenumbers that we consider for this problem. However, we find that the choice for the number of time-steps and the number of frequencies required is dependent on the problem we are considering, in particular the choice for α in our Neumann boundary condition (3.39). For the choices $\alpha = 36$ and $t_0 = 1$, we observe that $\widetilde{N} = \widetilde{N} = 256$ time-steps are sufficient enough to model the boundary data and the interior solution accurately. It is also important to note that the choice for α and t_0 in the Neumann boundary data (3.39) must be chosen such that the condition $\text{erf}(\sqrt{\alpha} t_0) \approx 1$ such that the initial conditions are satisfied, where erf is the error function. We also observed that there was no advantage to over-resolving by choosing the number of frequencies independently to the number of time-steps. However, when we investigate the choice for $\alpha = 4096$ and $t_0 = 0.1$ in Tables 3.2 and 3.3, we discovered that a larger number of time-steps and frequencies are required to model the behaviour accurately. This in turn will then require a larger number of boundary elements as the value of wavenumbers will increase as we increase the number of frequencies due to (3.30). This highlights a disadvantage of the CQBEM in modelling broad-band frequency content as the requirement for a alrge number of time-steps and boundary elements results in a longer computational time. This choice of α and t_0 will be investigated further in Section 5.4.1.

We next investigate the bandwidth of the driving force and the interior solution for different choices of the parameters $\widetilde{N}$, N and M. Figure 3.6 shows the logarithm of the boundary data and the interior solution in the Fourier domain against the wavenumber k. The boundary data $\widetilde{F}_l$ is approximated via $\widetilde{F}_l = \sum_{n=0}^{N-1} F(\boldsymbol{x}_m, t_n) \lambda^n e^{-2\pi i l n / \widetilde{N}}$, where F is given by (3.39) when $\alpha = 36$ and

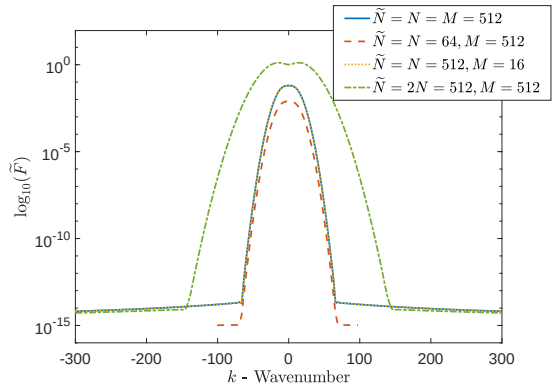

(a) Boundary data

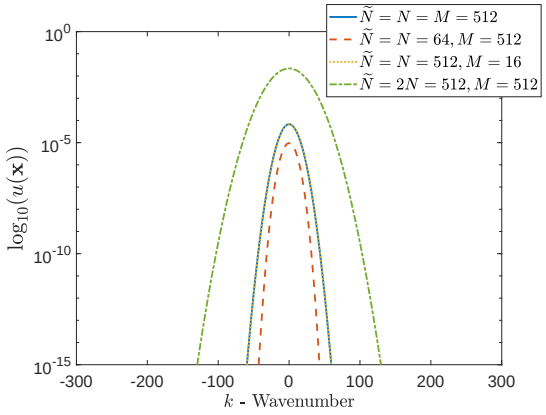

(b) Interior solution

Figure 3.6: Logarithmic plots of the bandwidth of the Neumann boundary condition F and the interior solution $\Phi(\boldsymbol{x})$, at the point $\boldsymbol{x} = (0.5, 0.5)$, in the Fourier domain against the wavenumber k. The Neumann boundary condition F is given by equation (3.39) with $\alpha = 36$ and $t_0 = 1$. The numerical interior solution was calculated using the collocation based direct CQBEM with piecewise constant basis functions in space and CQ with the BDF2 time-stepping method in time. Sub-plot (a) shows the bandwidth of the driving force F. Sub-plot (b) shows the bandwidth of the interior solution $\Phi(\boldsymbol{x})$.

$t_0 = 1$. Here $\boldsymbol{x}_m$ for $m = 1, 2, ..., M$ are the collocation points. The numerical interior solution in the frequency domain $u(\boldsymbol{x})$, was calculated using the collocation based direct CQBEM with piecewise constant basis functions in space and CQ with the BDF2 time-stepping method in time, for $\boldsymbol{x} = (0.5, 0.5)$. In both

sub-plots, we observe that the solutions for all different combinations of parameters decay by a factor in excess of 10^{-8} from their peak value. As well, in both sub-plots, we observe that most solutions have a bandwidth of approximately 70, except for the case when $\widetilde{N} = 2N = 512$ in which the number of frequencies had been doubled. In this case the bandwidth is broader at approximately 140 and therefore as we double the number of frequencies the bandwidth approximately doubles. We notice that changing the number of boundary elements M does not affect the solution in the Fourier domain. However, for the case when we decrease the number of time-steps by a factor of four we observe that the bandwidth is slightly lower with the bandwidth being approximately 40.

L-shaped domain

We now consider solving the homogeneous wave equation (3.1) when $P = 0$, along with the Neumann boundary data (3.39) along the left edge where $x_1 = 0$ and zero boundary data elsewhere, for the case when Ω is an L-shaped domain - see Figure 3.2 (b). Physically this represents a wave pulse originating from the left edge and travelling through the domain and along the boundary. As the wave travels through the narrow half of the domain, it will behave similarly to the wave inside the square domain. Once the wave passes and extends into the wider region of the domain, the wave will travel along the boundary and through the domain, and the solution then depends on both x_1 and x_2. Again we parameterise a position along the boundary $\boldsymbol{x} \in \Gamma$ and the collocation points $\boldsymbol{x}_i$ by the boundary arclength parameter $s \in [0, L)$ and $s_i \in [0, L)$, respectively.

		$\alpha = 36, \quad t_0 = 1, T = 1.5$		$\alpha = 4096, \quad t_0 = 0.1, T = 0.5$	
N	M	Error	EOC	Error	EOC
32	8	0.3229	-	2.8087	-
64	16	0.1922	0.75	0.8329	1.75
128	32	0.0991	0.96	0.7553	0.14
256	64	0.0501	0.98	0.6566	0.20
512	128	0.0249	1.01	0.5328	0.30
1024	256	0.0124	1.06	0.3948	0.43

Table 3.4: Relative errors and estimated orders of convergence for the interior solution in the L-shaped domain at the point $\boldsymbol{x} = (0.25, 0.25)$ using the backward Euler time discretisation in the CQ method with different choices for the parameters α and t_0 in the Neumann boundary condition (3.39).

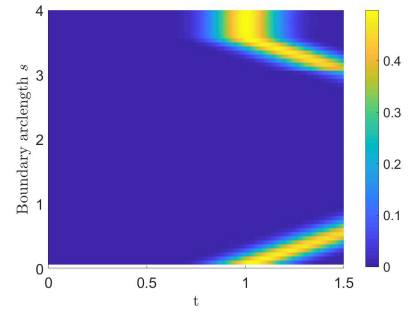

(a) Numerical solution on the boundary Γ.

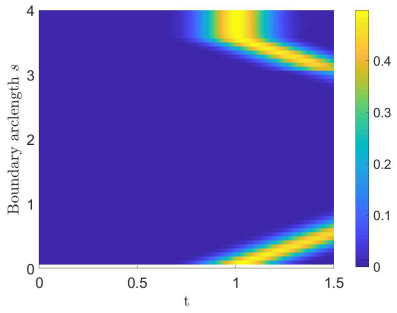

(b) Exact solution on the boundary Γ.

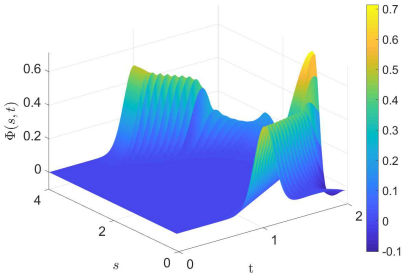

(c) Numerical solution on the boundary Γ.

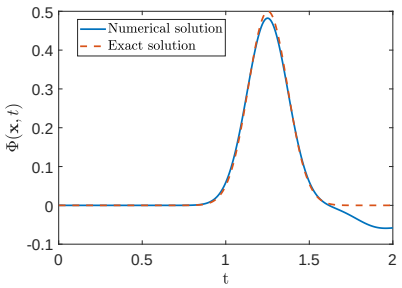

(d) Interior solutions against time, observed at the point $\boldsymbol{x} = (0.25, 0.25)$ in Ω.

Figure 3.7: Numerical solution of the Neumann IBVP for the wave equation with parameters $\alpha = 36$ and $t_0 = 1$ in the Neumann boundary condition (3.39) for an L-shaped domain. Sub-plots (a) and (c) show the numerical solution along the boundary Γ over different time periods and sub-plot (d) depicts the numerical solution observed at an interior point $\boldsymbol{x} = (0.25, 0.25)$ against time. The numerical solution was calculated using the collocation based direct CQBEM with piecewise constant basis functions in space and CQ with the backward Euler time-stepping method in time with $N = M = 256$. Sub-plot (b) shows the exact solution (3.40) along the boundary Γ over time.

Figure 3.7 shows the mesh plots of the numerical boundary solution and the interior solution Φ_n, $n = 0, 1, ..., N-1$ calculated for $N = 256$ time-steps and $M = 256$ boundary elements and compared against the exact solution for the case when $\alpha = 36$ and $t_0 = 1$. In this figure, the exact solution is only valid up until approximately $t = 0.85$ due to wave reflections as well as diffraction from the re-entrant corner at $s = 3$. Initially the wave enters the domain from the left edge and travels along the top edge ($3 < s < 3.5$) up until it reaches the

		$\alpha = 36,\quad t_0 = 1,\ T = 1.5$		$\alpha = 4096,\quad t_0 = 0.1,\ T = 0.5$	
N	M	Error	EOC	Error	EOC
64	8	0.2583	-	0.9533	-
128	32	0.1096	3.12	0.7553	0.38
256	128	0.0306	3.20	0.4772	0.62
512	512	0.0054	2.50	0.2275	1.06
1024	2048	0.0012	2.12	0.0765	1.57

Table 3.5: Relative errors and estimated orders of convergence for the interior solution in the L-shaped domain at the point $\boldsymbol{x} = (0.25, 0.25)$ using the BDF2 time discretisation in the CQ method with different choices for the parameters α and t_0 in the Neumann boundary condition (3.39).

corner ($s = 3$) at $t = 0.5$. From here a diffracted wave travels from the corner at $s = 3$ back into the domain towards the interior point $\boldsymbol{x}$, but does not reach the interior point until $t = 0.5 + \sqrt{0.25^2 + 0.25^2} \approx 0.8536$. However, from sub-plot (d), we do not visibly see these wave contributions in the numerical solution until after $t = 1.5$, even though within the time region $0.85 < t < 1.5$ there are very small diffracted wave contributions in the numerical solution. Therefore, when we calculate the errors in tables 3.4 and 3.5, we calculate up until $T = 1.5$ for $\alpha = 36$ and $t_0 = 1$, but note there are very small diffracted contributions included in the numerical solution, which are not included in the exact solution. For the case when $\alpha = 4096$ and $t_0 = 0.1$ we calculate the error up until $T = 0.5$, and thus avoid the diffracted wave contributions entirely.

Sub plots (a) - (b) of Figure 3.7 show the exact and numerical boundary solution up until $t = 1.5$, which we observe appear identical by eye. Sub-plot (c) shows the complete boundary solution up until $T = 2$. Next, we investigate the errors and convergence rates as we double the number of time-steps for the cases when $\alpha = 36$, $t_0 = 1$ and $T = 1.5$ as well as when $\alpha = 4096$, $t_0 = 0.1$ and $T = 0.5$. Tables 3.4 and 3.5 show the error results and the estimated convergence rates using backward Euler and BDF2 schemes respectively. From these tables we can observe that Table 3.4 shows the expected first order convergence rate for the case when $\alpha = 36$ and $t_0 = 1$, but for the case when $\alpha = 4096$ with $t_0 = 0.1$ the errors are much larger and we do not observe the expected first order convergence rate. In Table 3.5 we again observe smaller errors and a slightly faster convergence rate than the expected second order for the BDF2 method when $\alpha = 36$, $t_0 = 1$ and $T = 1.5$. However, we observe a big loss of

accuracy when $\alpha = 4096$, $t_0 = 0.1$ and $T = 0.5$. When we choose α to be a very large value, we find that in these numerical examples there are not enough time-steps or boundary elements to model the broadband frequency content accurately enough. Therefore a more efficient method is required to calculate the numerical solution for large choices of α.

3.4.2 Response to an interior point source

We consider solving the inhomogeneous wave equation (3.1) when $P(\boldsymbol{x}, t) = P_0(t)\delta(\boldsymbol{x}-\boldsymbol{x}_0)$ with a homogeneous Neumann boundary condition $F \equiv 0$ in (3.3) via CQBEM for a unit square domain, an L-shaped domain and an irregular polygon. We choose P_0 to be a Gaussian pulse of the form

$$P_0(t) = \sqrt{\frac{\alpha}{\pi}}\sin(4\pi t)e^{-\alpha(t-t_0)^2}, \tag{3.42}$$

where $\alpha, t_0 > 0$ are constants that are chosen to be large enough to satisfy the zero initial conditions (3.2) to machine precision.

As described in Section 3.1, the solution to the IBVP (3.1) - (3.3) is written as $\Phi = (U + V)|_\Omega$, where U is the reverberant solution that satisfies the homogeneous wave equation (3.1) when $P = 0$, along with Neumann boundary condition (3.11). The incident solution V then solves the free-space problem (3.4) and is calculated via (3.9), which for this numerical example we write as

$$\begin{aligned} V(\boldsymbol{x}, t) &= \int_0^T G(\boldsymbol{x} - \boldsymbol{x}_0, t-\tau)P_0(\tau)d\tau \\ &= \int_0^T \sqrt{\frac{\alpha}{\pi}}\frac{1}{2\pi}\frac{H(t-\tau-r/c)\sin(4\pi\tau)e^{-\alpha(\tau-t_0)^2}}{\sqrt{(t-\tau)^2 - r^2/c^2}}d\tau, \\ &= \frac{\sqrt{\alpha}}{2\pi^{3/2}}\int_0^{\max(t-r/c,0)}\frac{\sin(4\pi\tau)e^{-\alpha(\tau-t_0)^2}}{\sqrt{(t-\tau)^2 - r^2/c^2}}d\tau, \end{aligned} \tag{3.43}$$

where $r = \|\boldsymbol{x} - \boldsymbol{x}_0\|$. The solution U is then calculated numerically by applying the collocation based CQBEM with piecewise constant basis functions in space, together with either the backward Euler or BDF2 based CQ discretisation in time, as discussed in sections 3.2 and 3.3. Therefore we determine the solutions of a system of Helmholtz problems (3.34) in the frequency domain for a range of complex wavenumbers. To implement the collocation based direct CQBEM with piecewise constant basis functions to calculate the reverberant solution U, we refer the reader to the step-by-step guide listed at the beginning of Section 3.4

but with the following amendments. In this case, the solution of each Helmholtz problem u_l corresponds to the numerical approximation $\widetilde{U}_l$, the Z-transform of U. The boundary data term $\widetilde{F}_l$ in (3.34) is given by the Z-transform of $-\frac{\partial V}{\partial \hat{\mathbf{n}}}$ evaluated at $\zeta = \zeta_l$. The frequency domain interior solution is then calculated by evaluating (3.36). The time-domain boundary and interior solution can then be found via the inverse transforms (3.35) and (3.37), respectively. The MATLAB code for the solving the two-dimensional (in space) inhomogeneous wave equation via the collocation based CQBEM with piecewise constant basis functions in space and CQ discretisation in time are available from the following URL: https://github.com/JacobRowbottom/CQBEM-HYBRID/tree/main/Point%20Source.

In all our numerical experiments in this section, we choose $\alpha = 36$, $t_0 = 1$, $c = 1$ and $T = 2$. To calculate the error at $\boldsymbol{x} \in \Omega$ we use the relative error defined by (3.41) using subsequent interior solutions as we double the number of time steps N. However, as our final solution is of the form $\Phi = U + V$, we calculate the error using only U, the part of the solution obtained via CQBEM. Since we are not comparing the numerical solutions to an exact solution we will not investigate the behaviour of the solutions when choosing $\alpha = 4096$ and $t_0 = 0.1$, as we did in Section 3.4.1, as we have already shown that these choices for α and t_0 lead to a big loss of accuracy when comparing the numerical solutions against an exact solution.

Square domain

N	M	Error	EOC
32	4	-	-
64	8	0.3403	-
128	16	0.2127	4.16
256	32	0.1604	0.61
512	64	0.1096	0.55
1024	128	0.0621	0.82

Table 3.6: Relative errors and estimated orders of convergence for the interior solution in a unit square domain at the point $\boldsymbol{x} = (0.25, 0.25)$ for a source point $\boldsymbol{x}_0 = (0.5, 0.5)$ using the backward Euler time discretisation in the CQ method.

We first consider the case when Ω is a unit square with a source point in the centre at $\boldsymbol{x}_0 = (0.5, 0.5)$ and investigate the interior solution at the point

N	M	Error	EOC
64	4	-	-
128	16	0.8467	-
256	64	0.2415	1.81
512	256	0.0571	2.08
1024	1024	0.0092	2.63

Table 3.7: Relative errors and estimated orders of convergence for the interior solution in a unit square domain at the point $\boldsymbol{x} = (0.25, 0.25)$ for a source point $\boldsymbol{x}_0 = (0.5, 0.5)$ using the BDF2 time discretisation in the CQ method.

$\boldsymbol{x} = (0.25, 0.25)$. Due to the symmetry of the domain, we note that the interior and boundary solutions are symmetric as the point source is chosen to be at the centre. We have computed the errors and estimated convergence rates in tables 3.6 and 3.7. Table 3.6 shows the errors and estimated convergence rates produced using the backward Euler time discretisation in the CQ method. From this table we observe that the errors are decreasing and are tending towards first order convergence. Table 3.7 shows the relative errors and estimated convergence rates obtained from a BDF2 time discretisation in the CQ method. The errors shown are smaller than for the backward Euler method and second order convergence is achieved. We note that, as well as the BDF2 scheme being more accurate than backward Euler, we are also using more boundary elements M with the BDF2 scheme in order to realise the second order convergence rate of the time-stepping scheme. Figures 3.8 and 3.9 show the boundary solution Φ and the interior solutions Φ, U and V, respectively. In Figure 3.9 the reverberant solution U was calculated using the collocation based direct CQBEM with piecewise constant basis functions in space and CQ with the BDF2 time-stepping method in time with $N = M = 512$ and the solution V, which was calculated using numerical integration to evaluate (3.43) via the `integral` command in MATLAB.

We next investigate the impact of changing the number of frequencies $\widetilde{N}$, the number of time-steps N and the number of boundary elements M has on the behaviour of the interior solution Φ. To achieve this we investigate the reverberant solution U and the incident solution V independently. To begin, we consider the reverberant solution U only since it is approximated via the collocation based CQBEM with piecewise constant basis functions in space and BDF2 CQ discretisation in time. Whereas the incident solution V is approximated via the

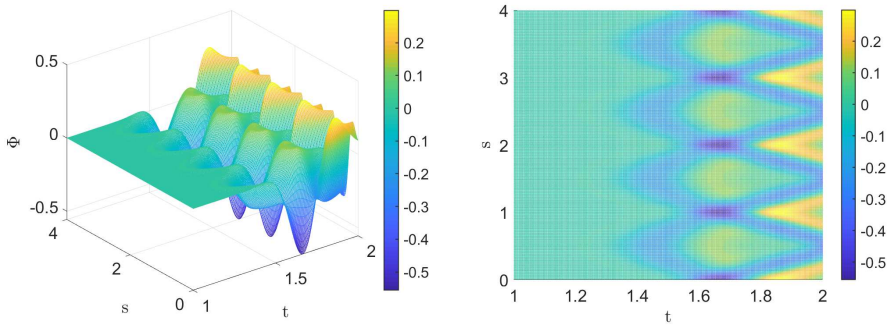

(a) (b)

Figure 3.8: Numerical solution of the Neumann IBVP for the wave equation with a point source excitation at $\boldsymbol{x}_0 = (0.5, 0.5)$ in the centre of a unit square domain. The solutions are observed along the boundary Γ with arclength parameter $s \in [0, 4)$ and were calculated using the collocation based direct CQBEM with piecewise constant basis functions in space and CQ with the BDF2 time-stepping method in time with $N = M = 256$. The solution is shown for $1 < t < T = 2$ to focus on the late time behaviour since the solution along the boundary is zero (to machine precision) for $t \leq 1$.

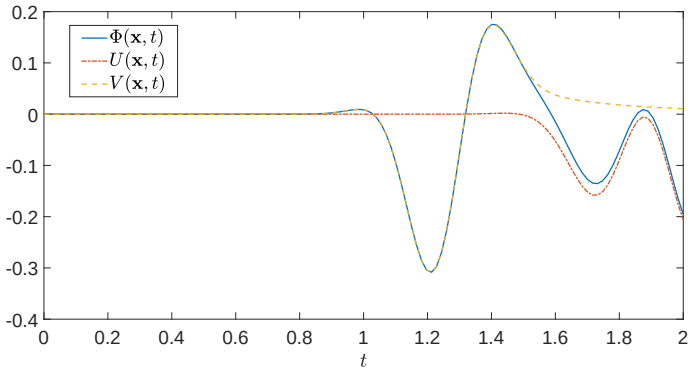

Figure 3.9: Numerical solution for the Neumann IBVP of the wave equation, where the solution $\Phi(\boldsymbol{x}, t) = U(\boldsymbol{x}, t) + V(\boldsymbol{x}, t)$, describes the response to a point source excitation at $\boldsymbol{x}_0 = (0.5, 0.5)$ observed at the point $\boldsymbol{x} = (0.25, 0.25)$ inside a unit square domain, and is plotted against time t. The numerical solution U is calculated using the collocation based direct CQBEM with piecewise constant basis functions in space and CQ with the BDF2 time-stepping method in time with $N = M = 512$. The solution V was calculated using numerical integration, to evaluate (3.43) via the `integral` command in MATLAB.

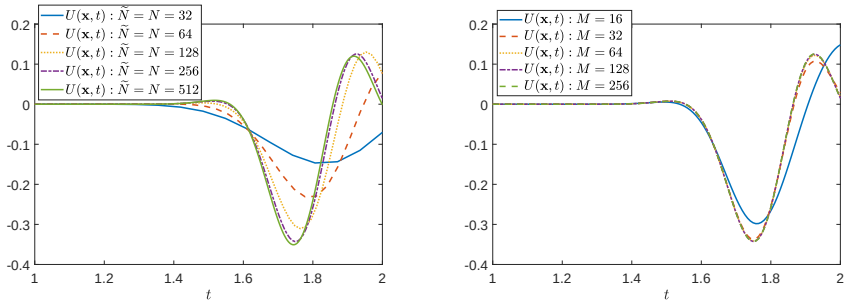

(a) $M = 512$

(b) $N = 512$

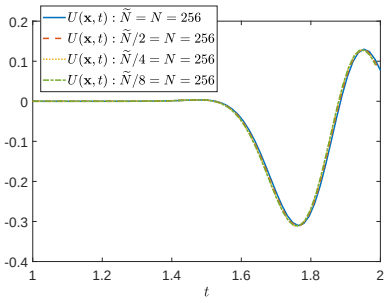

(c) $M = N = 256$

Figure 3.10: Plots of the numerical reverberant solution $U(\boldsymbol{x}, t)$ subject to a point source excitation at $\boldsymbol{x}_0 = (0.5, 0.5)$ observed at the point $\boldsymbol{x} = (0.25, 0.25)$ inside a unit square domain. The numerical solution U was calculated using the collocation based direct CQBEM with piecewise constant basis functions in space and CQ with the BDF2 time-stepping method in time. Sub-plot (a) has a fixed number of $M = 512$ boundary elements as the number of time-steps is changed. Sub-plot (b) has a fixed number of $N = \widetilde{N} = 512$ time-steps as the number of boundary elements is changed. Sub-plot (c) has $N = M = 256$ time-steps and boundary elements as we double the number of frequencies $\widetilde{N}$. The solution is shown for $1 < t < T = 2$ to focus on the late time behaviour since the solution along the boundary is zero (to machine precision) for $t \leq 1$.

`integral` command in MATLAB, which uses a vectorised adaptive quadrature method to approximate (3.43). Therefore the reverberant solution is of more interest for us to investigate. Figure 3.10 shows the numerical reverberant solution U against time subject to a source point excitation at $\boldsymbol{x}_0 = (0.5, 0.5)$ observed at the interior point $\boldsymbol{x} = (0.25, 0.25)$ for different numbers of frequencies, time-steps and boundary elements. The numerical solutions were calculated using the collocation based direct CQBEM with piecewise constant basis functions in

space and a CQ BDF2 time-stepping method in time. Sub-plot (a) shows the numerical solutions computed while fixing the number of boundary elements to $M = 256$ as the number of time-steps $\widetilde{N} = N$ is doubled. Again as was the case for the wave travelling into the domain in Figure 3.5 (a) we observe that if Δt is large the numerical solution is inaccurate. For $N = 256$ and $N = 512$ the solutions appear to match and therefore when $\Delta t < 1/128$ we achieve an accurate solution. In sub-plot (b) the numerical solutions are computed while fixing the number of time-steps and frequencies to $\widetilde{N} = N = 512$ as the number of boundary elements is doubled. From this plot we observe that when $M > 64$ the solutions appear to be accurate and similar to each other. In sub-plot (c) we double the number of frequencies as we fix the number of time-steps and boundary elements. From this plot we observe that there is no significant impact in over-resolving for the case when $\alpha = 36$.

Figure 3.11 then displays the numerical incident solution V against time observed at the interior point $\boldsymbol{x} = (0.25, 0.25)$ subject to a source point excitation at $\boldsymbol{x}_0 = (0.5, 0.5)$. Sub-plot (a) shows the numerical solutions computed while fixing the number of boundary elements to $M = 256$ as the number of time-steps is doubled. We observe that the solutions all behave similarly but as we increase the number of time-steps the line becomes smoother as Δt becomes smaller. Sub-plot (b) shows the numerical solutions computed while fixing the number of time-steps to $N = 256$ as the number of boundary elements is doubled. Again we observe the same increase in accuracy as we double the number of boundary elements. Between Figures 3.10 and 3.11 we notice that the number of time-steps has a much more important impact on the reverberant solution of U and therefore Φ than the incident solution V.

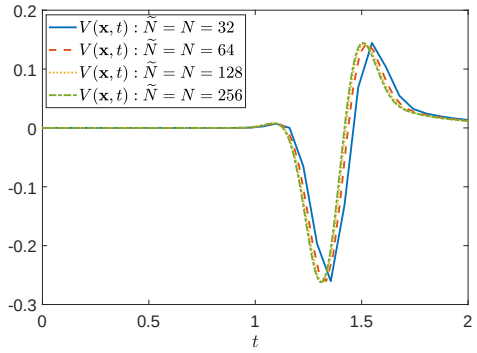

(a) $M = 256$

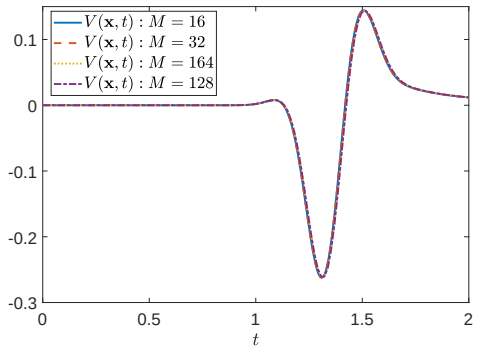

(b) $N = 256$

Figure 3.11: Plots of the numerical incident solution $V(\boldsymbol{x}, t)$ subject to a point source excitation at $\boldsymbol{x}_0 = (0.5, 0.5)$ observed at the point $\boldsymbol{x} = (0.25, 0.25)$ inside a unit square domain. The numerical solution V was calculated using numerical integration, to evaluate (3.43) via the `integral` command in MATLAB. Sub-plot (a) has a fixed number of $M = 256$ boundary elements for all solutions as the number of time-steps is changed. Sub-plot (b) has a fixed number of $N = \widetilde{N} = 256$ time-steps for all solutions as the number of boundary elements is changed.

L-shaped domain

We now consider the L-shaped domain with the source point chosen to be $\boldsymbol{x}_0 = (0.25, 0.25)$ as highlighted by the red dot in Figure 3.12. We investigate the interior solution behaviour at a number of points, labelled $A = (0.1, 0.15)$, $B = (0.5, 0.25)$ and $C = (0.75, 0.75)$ - see Figure 3.12. Figure 3.13 shows

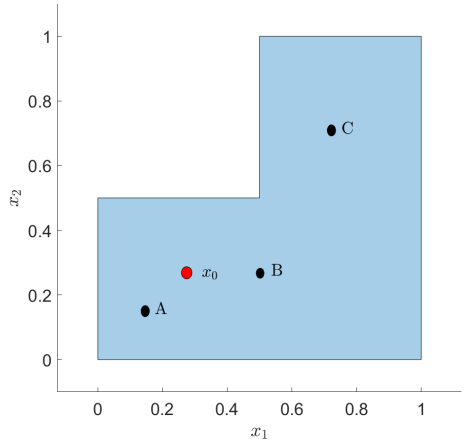

Figure 3.12: The L-shaped domain including the source point and the interior solution points A, B and C.

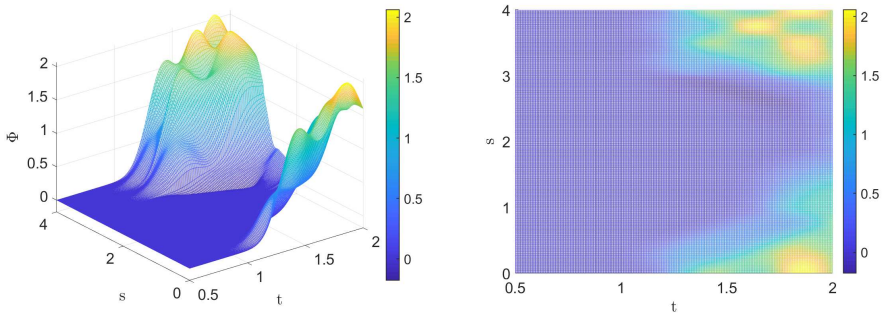

Figure 3.13: Numerical solution of the Neumann IBVP for the wave equation with a point source excitation at $\boldsymbol{x}_0 = (0.25, 0.25)$ in an L-shaped domain. The solutions are observed along the boundary Γ with arclength parameter $s \in [0, 4)$ and were calculated using the collocation based direct CQBEM with piecewise constant basis functions in space and CQ with the BDF2 time-stepping method in time with $N = M = 256$. The solution is shown for $0.5 < t < T = 2$ to focus on the late time behaviour since the solution is zero for $t \leq 0.5$.

the solution Φ along the boundary computed using the collocation based direct CQBEM with piecewise constant basis functions in space and CQ with the BDF2 time-stepping method in time with $N = M = 256$. The plots in Figure 3.14

N	M	Error	EOC
32	8	-	-
64	16	0.1569	-
128	32	0.1096	0.52
256	64	0.0544	1.01
512	128	0.0242	1.17
1024	256	0.0107	1.17

Table 3.8: Relative errors and estimated orders of convergence for the interior solution in the L-shaped domain at the point A for a source point $\boldsymbol{x}_0 = (0.25, 0.25)$ using the backward Euler time discretisation in the CQ method.

N	M	Error	EOC
64	8	-	-
128	32	0.1280	-
256	128	0.0252	2.34
512	512	0.0044	2.52
1024	2048	8.0524e-04	2.45

Table 3.9: Relative errors and estimated orders of convergence for the interior solution in an L-shaped domain at the point A for a source point $\boldsymbol{x}_0 = (0.25, 0.25)$ using the BDF2 time discretisation in the CQ method.

show the interior solutions Φ, U and V at the interior points A, B and C shown in Figure 3.12. The interior solution at point C was calculated for a longer time duration with $T = 2.5$ to show a similar number of reflections as observed at points A and B with $T = 2$. Tables 3.8 and 3.9 show the errors and estimated convergence rates when discretising in time via CQ with the backward Euler and BDF2 methods, respectively. From these tables we observe that BDF2 has smaller errors and to achieve similarly small errors for the backward Euler method we would need to increase the numbers of time-steps and boundary elements further. We observe approximately first order convergence for the backward Euler method shown in Table 3.8 and approximately second order convergence for the BDF2 time-stepping method shown in Table 3.9. Figure 3.14 shows the numerical interior solution at the points A, B and C inside the L-shaped domain. The plots show the full solution Φ, the reverberant solution U, which was calculated using the collocation based direct CQBEM with piecewise constant basis functions in space and CQ with the BDF2 time-

Vertex	x_1	x_2
1	1.0480	0.6993
2	0.2180	1.1720
3	0.0	0.3582
4	0.7680	0.0
5	1.0480	0.2993
Source	0.648	0.5

Table 3.10: Cartesian coordinates of the vertices and the point source for the irregular polygon domain.

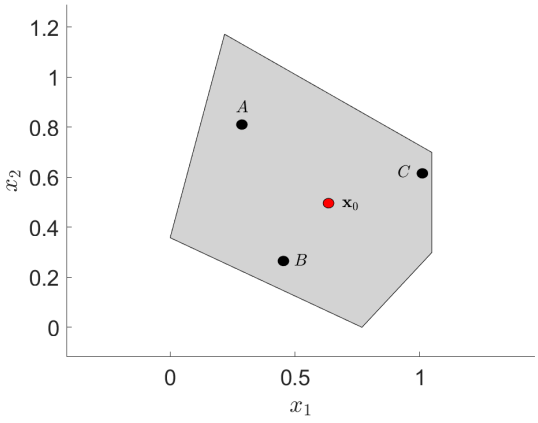

Figure 3.15: The irregular polygon domain.

stepping method in time with $N = M = 512$. The plots also show the solution V, which was calculated using numerical integration to evaluate (3.43) via the `integral` command in MATLAB.

Irregular polygon

We now consider an irregular polygon domain as shown in Figure 3.15, which also lists the vertices and source point coordinates for the domain in Table 3.10. The source point is chosen to be $\boldsymbol{x}_0 = (0.648, 0.5)$ as highlighted by the red dot in Figure 3.15 and we determine the interior solutions Φ, U and V at three different points inside Ω labelled $A = (0.29, 0.8)$, $B = (0.42, 0.275)$ and $C = (0.97, 0.6)$, as shown in Figure 3.15. Figure 3.16 shows the solution Φ along the boundary computed using the collocation based direct CQBEM with piecewise constant basis functions in space and CQ with the BDF2 time-stepping method in time with $N = M = 256$. Comparing to the boundary solutions for the unit square and L-shaped domains shown in Figures 3.8 and 3.13, respectively, the plot here shows the expected loss of symmetry and lack of regularity corresponding to the irregular geometry.

Figure 3.17 shows the numerical interior solution at the points A, B and C. The plots show the full solution Φ, the reverberant solution U, which was calculated using the collocation based direct CQBEM with piecewise constant basis functions in space and CQ with the BDF2 time-stepping method in time with $N = M = 512$. The plots also show the solution V, which was calculated

N	M	Error	EOC
32	8	-	-
64	16	0.4011	-
128	32	0.3449	0.22
256	64	0.2298	0.59
512	128	0.1479	0.64
1024	256	0.0905	0.71

Table 3.11: Relative errors and estimated orders of convergence for the interior solution in the irregular polygon domain at the point B for a source point $\boldsymbol{x}_0 = (0.648, 0.5)$ using the backward Euler time discretisation in the CQ method.

N	M	Error	EOC
64	8	-	-
128	32	0.5042	-
256	128	0.0801	2.65
512	512	0.0192	2.06
1024	2048	0.0065	1.56

Table 3.12: Relative errors and estimated orders of convergence for the interior solution in the irregular polygon domain at the point B for a source point $\boldsymbol{x}_0 = (0.648, 0.5)$ using the BDF2 time discretisation in the CQ method.

using numerical integration to evaluate (3.43) via the `integral` command in MATLAB. Tables 3.11 and 3.12 show the errors and convergence rates when discretising in time via CQ with the backward Euler and BDF2 methods, respectively. The errors are larger than those for the L-shaped domain, but we still observe smaller errors using the BDF2 time discretisation compared against the backward Euler method for the irregular polygon domain. Again, this is due to the errors being calculated using more boundary elements M and the BDF2 scheme being more accurate. The BDF2 method achieves its expected convergence rate of second order and we expect the backward Euler method to achieve first order convergence when using more boundary elements and time-steps.

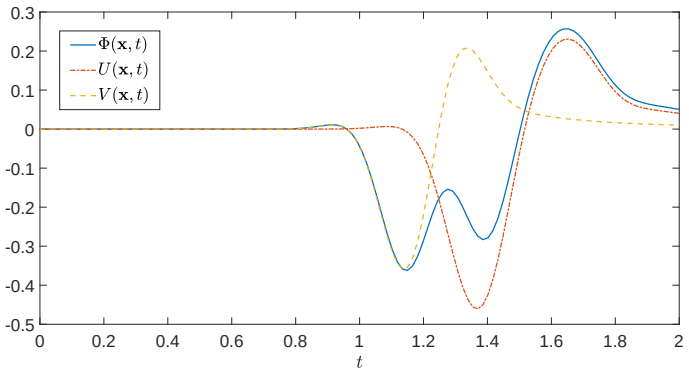

(a) Numerical solution at point A.

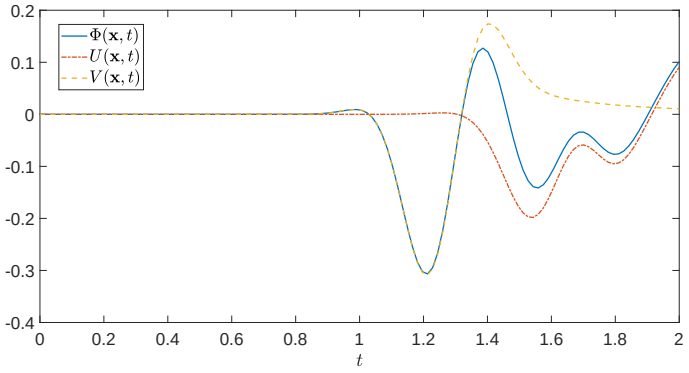

(b) Numerical solution at point B.

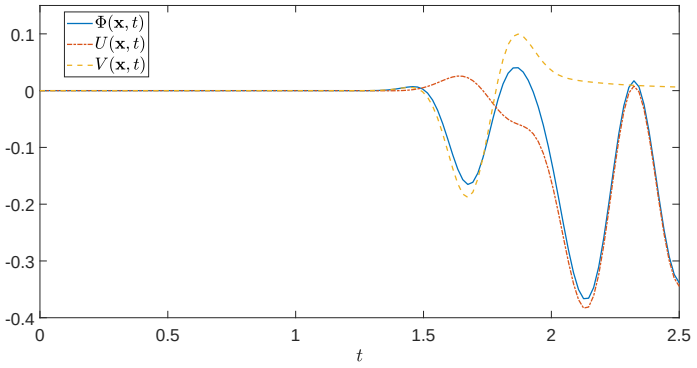

(c) Numerical solution at point C.

Figure 3.14: Plots of the numerical solution of the Neumann IBVP for the wave equation with a point source excitation at $\boldsymbol{x}_0 = (0.25, 0.25)$ observed at the points A, B and C in the L-shaped domain - see Figure 3.12. The reverberant solution U was calculated using the collocation based direct CQBEM with piecewise constant basis functions in space and CQ with the BDF2 time-stepping method in time with $N = M = 512$. The solution V was calculated using numerical integration to evaluate (3.43) via the `integral` command in MATLAB.

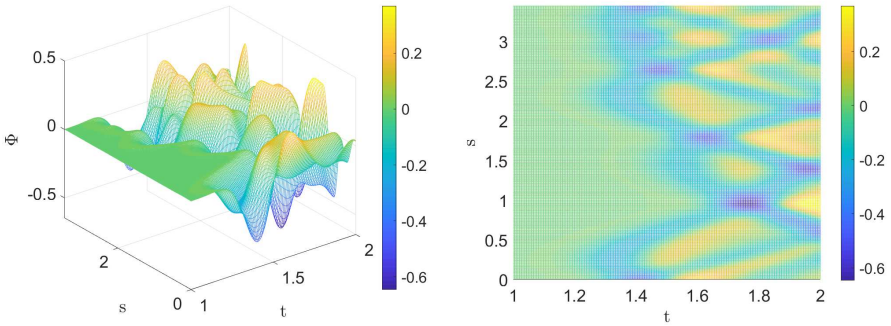

(a) (b)

Figure 3.16: Numerical solution of the Neumann IBVP for the wave equation with a point source excitation at $\boldsymbol{x}_0 = (0.648, 0.5)$ in an irregular polygon domain. The solutions are observed along the boundary Γ with arclength parameter $s \in [0, 3.45)$ and were calculated using the collocation based direct CQBEM with piecewise constant basis functions in space and CQ with the BDF2 time-stepping method in time with $N = M = 256$. The solution is shown for $1 < t < T = 2$ to focus on the late time behaviour since the solution is zero for $t \leq 1$.

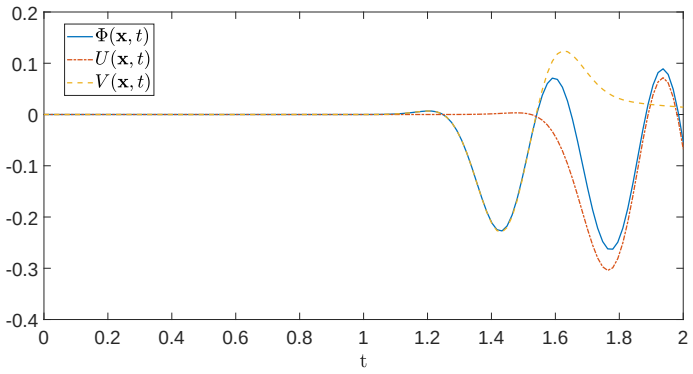

(a) Numerical solution at point A.

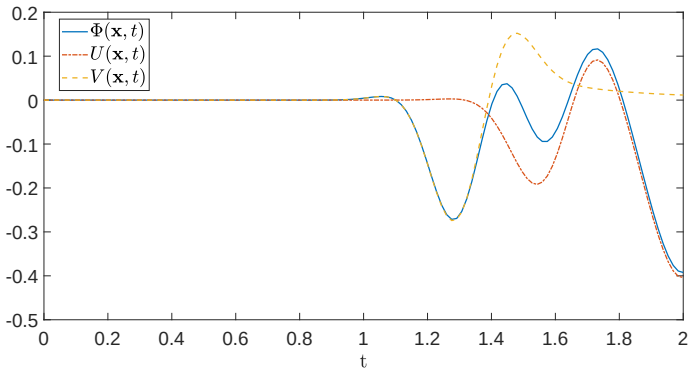

(b) Numerical solution at point B.

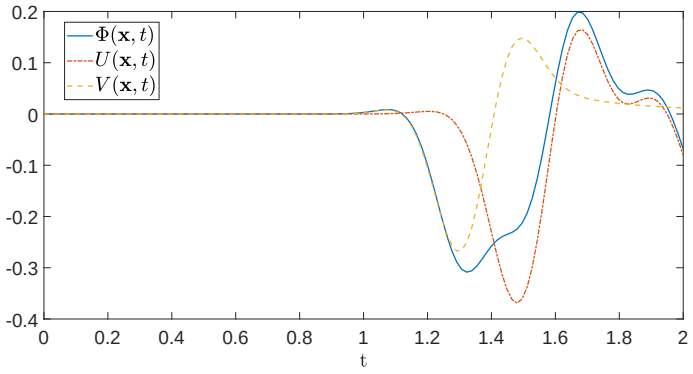

(c) Numerical solution at point C.

Figure 3.17: Plots of the numerical solution of the Neumann IBVP for the wave equation with a point source excitation at $\boldsymbol{x}_0 = (0.648, 0.5)$ observed at the points A, B and C in the irregular polygon domain - see Figure 3.15. The reverberant solution U was calculated using the collocation based direct CQBEM with piecewise constant basis functions in space and CQ with the BDF2 time-stepping method in time with $N = M = 512$. The solution V was calculated using numerical integration to evaluate (3.43) via the `integral` command in MATLAB.

3.5 Conclusion

In this chapter, we described a method to calculate the numerical solution for a time-domain boundary integral formulation of the two-dimensional wave equation. The method uses convolution quadrature for the time discretisation and a direct collocation boundary element method with piecewise constant basis functions for the spatial discretisation. We showed that this problem can be reformulated as the solution of $\widetilde{N}/2+1$ Helmholtz problems with complex wavenumbers. Firstly, we numerically solved the homogeneous wave equation with Neumann boundary conditions for the case when a wave function was travelling into both a unit square and an L-shaped domain. We calculated the errors and estimated convergence rates when applying different time-stepping methods in the CQ time discretisation. The two methods employed were the backward Euler method and the second order backwards difference formula (BDF2). The results showed that both time-stepping methods eventually achieved their expected convergence rates and the errors calculated via the BDF2 method were smaller. However, this was in part due to the error results being computed with larger numbers of spatial boundary elements than the results presented for backward Euler method. The errors for the L-shaped domain were slightly larger than those calculated for the unit square domain. The errors computed for both domains were compared to an analytical solution for the IBVP for different choices of the α and t_0 parameters in the boundary condition (3.39). We observed that when we chose $\alpha = 36$ we achieved small errors and the expected convergence rate. However, when we chose $\alpha = 4096$, to provide a broadband signal, we observed a big loss of accuracy as there were not enough time-steps and boundary elements to model the broadband signal accurately.

We then numerically solved the inhomogeneous wave equation for the case when there was a point source excitation in a unit square, an L-shaped domain and an irregular polygon. The solution is of the form $\Phi = U + V$ as discussed in Section 3.1, where U is the numerical solution to the IBVP for the homogeneous wave equation with an inhomogeneous Neumann boundary condition calculated via the direct CQBEM. The function V is the solution to the inhomogeneous wave equation in free-space. We considered the case when the source term on the right hand side of the wave equation takes the form $P(\boldsymbol{x}, t) = \delta(\boldsymbol{x} - \boldsymbol{y})P_0(t)$, where P_0 is a Gaussian pulse time profile. The error and estimated convergence rates were then calculated for the CQ method with the backward Euler and the BDF2 time-stepping methods. The results achieved the expected convergence

rates for both time discretisation methods, and in general the errors for the BDF2 method were smaller than those calculated using the backward Euler method.

Chapter 4

High frequency approximation of the Helmholtz equation via DEA

In this chapter, we discuss approximating the solution of the two-dimensional Helmholtz equation at high frequencies via Dynamical Energy Analysis (DEA). The solutions to the Helmholtz equation can be represented in the infinite frequency limit as a superposition of plane waves whose amplitude A in a particular direction can be expressed in terms of a wave energy density ρ. We introduce a boundary integral operator that models the transport of these wave energy densities through phase-space. The resulting boundary density can then be projected into the domain. A Petrov-Galerkin discretization of the phase-space boundary integral equation for transporting wave energy densities in two-dimensional domains is detailed. We then consider a variety of numerical experiments in different domain geometries and investigate the convergence properties and the solution behaviour.

4.1 From waves to rays

In this section, we discuss the process of writing the solution to the Helmholtz equation at high frequencies in terms of ray trajectories. We recall the inhomogeneous Helmholtz equation from Section 2.1

$$\Delta u(\boldsymbol{x}) + k^2 u(\boldsymbol{x}) = g(\boldsymbol{x}), \tag{4.1}$$

where $k = \omega/c$ is the wavenumber and g defines a source term within $\Omega \subset \mathbb{R}^2$. Here $\boldsymbol{x} = (x_1, x_2) \in \Omega \subset \mathbb{R}^2$ is the spatial coordinate at which we calculate the solution u. When considering a high frequency, $\omega \gg 1$, we assume that the solution to the Helmholtz equation can be well described by the Wentzel–Kramers–Brillouin (WKB) ansatz [88]:

$$u(\boldsymbol{x}) = e^{i\omega S(\boldsymbol{x})} \sum_{\kappa=0}^{\infty} a_\kappa(\boldsymbol{x})(i\omega)^{-\kappa}, \tag{4.2}$$

where S is the phase of a plane wave solution and a_κ are the amplitude coefficients corresponding to each term in the expansion $\kappa = 0, 1, \ldots$. Substituting the leading order ($\kappa = 0$) term of (4.2) into the homogeneous Helmholtz equation (4.1) when $g = 0$, leads to

$$\begin{aligned} \Delta(a_0 e^{i\omega S}) + \frac{\omega^2}{c^2} a_0 e^{i\omega S} &= 0, \\ \implies \left(a_0 \left(\frac{1}{c^2} - |\nabla S|^2 \right) \omega^2 + (2\nabla a_0 \cdot \nabla S + a_0 \Delta S) i\omega + \Delta a_0 \right) e^{i\omega S} &= 0. \end{aligned}$$

For large values of ω we omit terms of $\mathcal{O}(\omega^0)$. Considering terms of order ω^2 leads to the Eikonal equation and collecting terms of order ω yields the transport equation, respectively, as follows:

$$|\nabla S| = \frac{1}{c}, \tag{4.3}$$

$$2\nabla A \cdot \nabla S + A \Delta S = 0. \tag{4.4}$$

Here we have relabelled a_0 to A as the amplitude for convenience. The Eikonal equation (4.3) is a part of a class of PDEs known as the Hamilton-Jacobi equations [161] and is a non-linear time independent PDE. The transport equation (4.4) is a linear equation for A with variable coefficients given by the gradient and Laplacian of S. The two equations are independent of ω and are therefore

more efficient than solving the Helmholtz equation directly when ω is very large.

The solution to the Eikonal equation can be found via the method of characteristics. This leads to the following ODE system

$$\begin{aligned} \frac{d\boldsymbol{x}}{dt} &= \nabla_{\boldsymbol{p}}\mathcal{H}(\boldsymbol{x},\boldsymbol{p}) = c\frac{\boldsymbol{p}}{|\boldsymbol{p}|}, \\ \frac{d\boldsymbol{p}}{dt} &= -\nabla_{\boldsymbol{x}}\mathcal{H}(\boldsymbol{x},\boldsymbol{p}) = -|\boldsymbol{p}|\nabla c, \end{aligned} \tag{4.5}$$

with Hamiltonian $\mathcal{H}(\boldsymbol{x},\boldsymbol{p}) = c|\nabla S| = c|\boldsymbol{p}| = \mathcal{E}$, where $\mathcal{E}$ is the total energy of the system. We consider the case of a fixed constant energy, which we arbitrarily set as $\mathcal{E} \equiv 1$ and therefore we can write

$$|\boldsymbol{p}| = \frac{1}{c}. \tag{4.6}$$

The equations in the ODE system (4.5) are known as the ray equations [161] and by solving (4.5) we obtain solutions $S\left(\boldsymbol{x}(t),\boldsymbol{p}(t)\right)$ along ray trajectories in phase-space $\boldsymbol{X} = (\boldsymbol{x},\boldsymbol{p})$, where $\boldsymbol{x}$ is the position of the ray and $\boldsymbol{p}$ the momentum variable, also known as the slowness vector.

In the above, we have derived the frequency domain versions of the Eikonal and transport equations instead of the time-dependent versions. Time-harmonic solutions to the wave equation can also be written in the form $\Phi(\boldsymbol{x},t) = \widetilde{A}(\boldsymbol{x},t)e^{i\omega\widetilde{S}(\boldsymbol{x},t)}$ where $\widetilde{S}(\boldsymbol{x},t)$ satisfies the time-dependent Eikonal equation and $\widetilde{A}(\boldsymbol{x},t)$ satisfies the time-dependent transport equation [161]. Recall from Section 2.1 that the time-harmonic solution and the frequency domain solution are related via $\Phi(\boldsymbol{x},t) = u(\boldsymbol{x})e^{i\omega t}$ where $u(\boldsymbol{x}) = A(\boldsymbol{x})e^{i\omega S(\boldsymbol{x})}$ satisfies the Helmholtz equation. The time-dependent amplitude $\widetilde{A}$ and phase $\widetilde{S}$ are therfore connected to the frequency domain amplitude and phase via $\widetilde{A}(\boldsymbol{x},t) = A(\boldsymbol{x})$ and $\widetilde{S}(\boldsymbol{x},t) = S(\boldsymbol{x}) + t$, meaning that in the time-harmonic case the amplitude is time-independent.

The solution to the transport equation in (4.5) is driven by the phase solution S from the Eikonal equation. The solutions to the ray equations (4.5) in phase-space are determined uniquely via a set of initial conditions. However, the projection onto position $\boldsymbol{x}$ space leads to the multi-valued phase solutions. It is therefore advantageous to solve the transport equation in phase-space instead. We are interested in the long-time evolution of the Hamiltonian system for approximating the solution to the Helmholtz equation. We therefore write the system in terms of a general density distribution f in phase-space $\boldsymbol{Y} = (\boldsymbol{x}',\boldsymbol{p}')$.

The density distribution follows a phase-space conservation law known as the Liouville equation [161]

$$\frac{\partial f}{\partial t}(\boldsymbol{Y},t)+\frac{\partial \boldsymbol{Y}}{\partial t}\cdot\nabla_{\boldsymbol{Y}} f(\boldsymbol{Y},t)=0. \tag{4.7}$$

The phase-space density f may then be written as

$$f(\boldsymbol{Y},t)=\sum_{j=1}^{R}\widetilde{A}_j^2(\boldsymbol{x},t)\delta(\boldsymbol{p}-\nabla\widetilde{S}_j(\boldsymbol{x},t)), \tag{4.8}$$

which solves (4.7) if $\widetilde{S}_j$ and $\widetilde{A}_j$ satisfy the time-dependent Eikonal and transport equations, respectively, and where R is the number of plane waves, so the density f corresponds to the squares of the amplitudes $\widetilde{A}_j$ for rays travelling in a direction defined by $\widetilde{S}_j$. The method of characteristics leads to an expression for the solution of (4.7) in terms of a Frobenius-Perron (FP) operator $\mathcal{L}^\tau$ written as

$$\mathcal{L}^\tau[f](\boldsymbol{X})=\int\delta(\boldsymbol{X}-\phi^\tau(\boldsymbol{Y}))f(\boldsymbol{Y},0)d\boldsymbol{Y}. \tag{4.9}$$

The FP operator describes the evolution through time τ of a density f along the solution trajectories of the Hamiltonian system defined by the ray equations (4.5). The solutions of the Hamiltonian system define trajectories in phase-space and may be written in the form $\boldsymbol{X}(\tau)=\phi^\tau(\boldsymbol{X}(0))$, where ϕ^τ is the associated flow map. However, for the frequency domain problems we consider, we are interested in the stationary density ρ accumulated in the long-time limit of the dissipative FP operator [45] given by

$$\rho(\boldsymbol{X})=\lim_{T\to\infty}\int_0^T\int w(\boldsymbol{Y},\tau)\delta(\boldsymbol{X}-\phi^\tau(\boldsymbol{Y})f(\boldsymbol{Y},0)d\boldsymbol{Y}d\tau, \tag{4.10}$$

for a given initial density distribution $f(\boldsymbol{Y},0)$ and dissipative factor w. Typically, w will take the form of an exponential decay along ray trajectories.

4.2 Propagating phase-space densities via boundary integral operators

In this section we outline the underlying model for propagating phase-space densities along ray trajectories within bounded domains $\Omega\subset\mathbb{R}^2$ using the Frobenius-Perron operator (4.9). In some examples we consider transporting

densities through multiple sub-domains which may be considered as subdivisions of the domain Ω, we denote these sub-domains $\Omega_i, i = 1, ..., \varrho$, where ϱ is the number of sub-domains. We assume that the wave speed c is constant throughout all sub-domains. We define the phase-space coordinates $\boldsymbol{Y}_j = (s'_j, p'_j)$ on the boundary of Ω_j, denoted $\Gamma_j, j = 1, ..., \varrho$, where s'_j is the arclength parameter along the boundary and $p'_j = \sin(\theta'_j)/c$ denotes the component of the momentum vector that is tangential to the boundary Γ_j at s'_j. Note that θ'_j is the angle formed between the outgoing ray trajectory and the unit normal vector to Γ_j pointing inwards, as shown in Figure 4.1. The boundary flow map $\phi_{i,j}(s'_j, p'_j) = (\phi_s(s'_j, p'_j), \phi_p(s'_j, p'_j))$ describes the flow from s'_j on the boundary of Ω_j in the direction θ'_j to $(\phi_s(s'_j, p'_j), \phi_p(s'_j, p'_j))$, where $\phi_s(s'_j, p'_j)$ is the position on the boundary of the domain Ω_i and $\phi_p(s'_j, p'_j) = \sin\left(\theta'_i(s'_j, p'_j)\right)/c$ is the corresponding tangential momentum. Likewise, θ_i is the angle formed between outgoing ray trajectory and unit normal pointing inwards from Γ_i at $\phi_s(s'_j, p'_j)$.

The phase-space densities are transported through Ω using a modified form of the FP operator (4.9), in which the continuous flow map ϕ^τ is replaced by the discrete boundary map $\phi_{i,j}$ as described above and depicted in Figure 4.1. Thus the FP operator can be written as a local boundary integral operator $\mathcal{B}_j$, which describes the transport of a density ρ from the phase-space on boundary Γ_j to the next boundary intersection with Γ_i via

$$\mathcal{B}_j[\rho](\boldsymbol{X}_i) := \int_{-c^{-1}}^{c^{-1}} \int_{\Gamma_j} w_{i,j}(\boldsymbol{Y}_j) T(\boldsymbol{X}_i, \boldsymbol{Y}_j) \rho(\boldsymbol{Y}_j) d\boldsymbol{Y}_j, \tag{4.11}$$

where

$$T(\boldsymbol{X}_i, \boldsymbol{Y}_j) = e^{-\mu_j D(\boldsymbol{X}_i, \boldsymbol{Y}_j)} \delta\left(s_i - \phi_s(s'_j, p'_j)\right) \delta\left(p_i - \phi_p(s'_j, p'_j)\right). \tag{4.12}$$

Here $\boldsymbol{X}_i = (s_i, p_i) \in \Gamma_i \times (-c^{-1}, c^{-1})$ for $i = 1, 2, ..., \varrho$, and $w_{i,j}$ is a weighting factor which takes into account absorption factors at boundaries as well as reflection/transmission coefficients. The coefficient $\mu_j > 0$ is used to include dissipation as the ray travels through Ω_j and $D(\boldsymbol{X}_i, \boldsymbol{Y}_j)$ represents the Euclidean distance between s'_j and the solution point s_i. The global boundary integral operator $\mathcal{B} = \sum_j \mathcal{B}_j$ is then found by taking the sum over each sub domain Ω_j that shares a common edge with Ω_i, including Ω_i itself [12]. The stationary boundary density induced by an initial boundary density ρ_0 can be obtained

from a Neumann series [76] via

$$\rho = \sum_{n=0}^{\infty} \mathcal{B}^n[\rho_0] = (I - \mathcal{B})^{-1}[\rho_0], \tag{4.13}$$

where $\mathcal{B}^n$ represents n iterates of the operator $\mathcal{B}$.

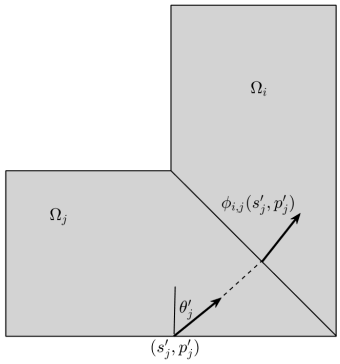

Figure 4.1: The boundary map $\phi_{i,j}(s'_j, p'_j)$ taking the phase-space coordinate $\boldsymbol{Y}_j = (s'_j, p'_j)$ on the boundary to $\phi_{i,j}(s'_j, p'_j) = (\phi_s(s'_j, p'_j), \phi_p(s'_j, p'_j))$, which corresponds to the next intersection with a boundary edge where the ray undergoes either transmission or a specular reflection.

We now discuss the projection of the boundary density (4.13) into the interior domain via the Hamiltonian ODE system (4.5). Our derivations are given for the case of a single domain Ω with boundary Γ, but extend directly to the case of multiple sub-domains where the domain Ω would simply be replaced by any Ω_j, $j = 1, ..., \varrho$ with boundary Γ_j. We first introduce local coordinates in a neighbourhood of the boundary Γ by extending the phase-space coordinates $\boldsymbol{X} = (s, p)$ of a particle on Γ to the full four-dimensional phase-space coordinates of the particle in Ω as $\mathcal{X} = (x_\parallel, x_\perp, p_\parallel, p_\perp)^T$. We denote a position $\boldsymbol{x}_\Gamma = (x_\parallel, x_\perp)$ such that along the boundary Γ, $x_\parallel = s$ and $x_\perp = 0$ correspond to the position parallel and perpendicular to the boundary, respectively. We then denote the local momentum vector $\boldsymbol{p}_\Gamma = (p_\parallel, p_\perp)$ where $p_\parallel = p = |\boldsymbol{p}_\Gamma| \sin(\theta)$ is the component parallel to the boundary and $p_\perp = |\boldsymbol{p}_\Gamma| \cos(\theta)$ is perpendicular to the boundary. The phase-space coordinates of a particle tracing out a ray

trajectory are then given by

$$\frac{d\mathcal{X}}{dt} = \begin{bmatrix} \frac{\partial \mathcal{H}}{\partial p_\parallel} & \frac{\partial \mathcal{H}}{\partial p_\perp} & -\frac{\partial \mathcal{H}}{\partial x_\parallel} & -\frac{\partial \mathcal{H}}{\partial x_\perp} \end{bmatrix}^T. \tag{4.14}$$

Recall from Section 4.1 that the Hamiltonian is $\mathcal{H} = c|\boldsymbol{p}_\Gamma| = c\sqrt{p_\parallel^2 + p_\perp^2} = 1$, and so (4.14) can be written as

$$\frac{d\mathcal{X}}{dt} = \frac{c}{|\boldsymbol{p}_\Gamma|} \begin{bmatrix} p_\parallel \\ p_\perp \\ 0 \\ 0 \end{bmatrix}. \tag{4.15}$$

We now introduce $\rho_{4D}(\mathcal{X}) \in [0, \infty)$ as the stationary boundary density in Ω with respect to the local coordinate system $\mathcal{X}$. The relationship between the restriction of ρ_{4D} to Γ and the stationary boundary density $\rho(s, p)$ is given by fixing coordinates on the fixed energy surface $\mathcal{H} = \mathcal{E} = 1$ to find the boundary density ρ.

We next introduce the following change of variables

$$s = x_\parallel, \qquad t = \frac{\boldsymbol{p}_\Gamma \cdot (\boldsymbol{x}_\Gamma - \boldsymbol{x}_0)}{c|\boldsymbol{p}_\Gamma|}, \qquad p = p_\parallel, \qquad \mathcal{E} = c\sqrt{p_\parallel^2 + p_\perp^2},$$

where $\boldsymbol{x}_0 \in \Gamma$ is the initial position of the ray expressed in the same coordinate system as $\boldsymbol{x}_\Gamma$. The change of variables for t is unapparent and we will therefore discuss it in more detail now. We begin with the $\frac{dx_\parallel}{dt} = \frac{cp_\parallel}{|\boldsymbol{p}_\Gamma|}$ entry from (4.15) and multiply both the numerator and denominator by $p_\parallel$ to obtain

$$\frac{dx_\parallel}{dt} = \frac{cp_\parallel^2}{p_\parallel |\boldsymbol{p}_\Gamma|}. \tag{4.16}$$

Next, we recall that $|\boldsymbol{p}_\Gamma| = \sqrt{p_\parallel^2 + p_\perp^2}$ and replace $p_\parallel^2$ with $|\boldsymbol{p}_\Gamma|^2 - p_\perp^2$ in (4.16). We then split the fraction into two terms leading to

$$\begin{aligned} \frac{dx_\parallel}{dt} &= \frac{c|\boldsymbol{p}_\Gamma|}{p_\parallel} - \frac{p_\perp}{p_\parallel}\left(\frac{cp_\perp}{|\boldsymbol{p}_\Gamma|}\right), \\ &= \frac{c|\boldsymbol{p}_\Gamma|}{p_\parallel} - \frac{p_\perp}{p_\parallel}\frac{\partial x_\perp}{\partial t}. \end{aligned} \tag{4.17}$$

To obtain the second line of equation (4.17) we use the result $\frac{dx_\perp}{dt} = \frac{cp_\perp}{|\boldsymbol{p}_\Gamma|}$ from (4.15). We now integrate (4.17) with respect to t, noting that we treat $p_\parallel$, $p_\perp$ as constants due to (4.15). We obtain an equation for $x_\parallel$ given by

$$x_\parallel = \frac{c|\boldsymbol{p}_\Gamma|}{p_\parallel} t - \frac{p_\perp}{p_\parallel} x_\perp + \text{constant}. \tag{4.18}$$

Applying the initial conditions when $t = 0$ and recalling that the initial position of the ray is $\boldsymbol{x}_\Gamma(0) = \boldsymbol{x}_0$, we determine the constant to be

$$\text{constant} = p_\parallel x_\parallel(0) + p_\perp x_\perp(0) = \boldsymbol{p}_\Gamma \cdot \boldsymbol{x}_0. \tag{4.19}$$

We substitute the integration constant (4.19) into (4.18) and rearrange for t to obtain

$$t = \frac{\boldsymbol{p}_\Gamma \cdot (\boldsymbol{x}_\boldsymbol{\Gamma} - \boldsymbol{x}_0)}{c|\boldsymbol{p}_\Gamma|},$$

which is the expression for t in the change of variables introduced earlier.

The Jacobian matrix for this change of variables is then

$$J = \begin{bmatrix} \frac{\partial x_\parallel}{\partial s} & \frac{\partial x_\parallel}{\partial t} & \frac{\partial x_\parallel}{\partial p} & \frac{\partial x_\parallel}{\partial \mathcal{E}} \\ \frac{\partial x_\perp}{\partial s} & \frac{\partial x_\perp}{\partial t} & \frac{\partial x_\perp}{\partial p} & \frac{\partial x_\perp}{\partial \mathcal{E}} \\ \frac{\partial p_\parallel}{\partial s} & \frac{\partial p_\parallel}{\partial t} & \frac{\partial p_\parallel}{\partial p} & \frac{\partial p_\parallel}{\partial \mathcal{E}} \\ \frac{\partial p_\perp}{\partial s} & \frac{\partial p_\perp}{\partial t} & \frac{\partial p_\perp}{\partial p} & \frac{\partial p_\perp}{\partial \mathcal{E}} \end{bmatrix} = \begin{bmatrix} 1 & \frac{cp_\parallel}{|\boldsymbol{p}_\Gamma|} & 0 & 0 \\ 0 & \frac{cp_\perp}{|\boldsymbol{p}_\Gamma|} & 0 & 0 \\ 0 & 0 & 1 & 0 \\ 0 & 0 & -\frac{p_\parallel}{p_\perp} & \frac{\mathcal{E}}{c^2 p_\perp} \end{bmatrix} \tag{4.20}$$

and it follows that $\det(J) = 1$. The integration over $\mathcal{X}$ is then equivalent to integrating over the new variables

$$\iiiint dx_\parallel dx_\perp dp_\parallel dp_\perp = \iiiint ds dt dp d\mathcal{E},$$

and therefore $\rho_{4D}(x_\parallel, x_\perp, p_\parallel, p_\perp) = \rho_{4D}(s, t, p, \mathcal{E})$.

The stationary boundary density is then related to $\rho_{4D}(s, t, p, \mathcal{E})$ by restricting to a fixed energy $c|\boldsymbol{p}_\Gamma| = \mathcal{E} = 1$, which gives the stationary boundary density $\rho(s, p)$ as follows

$$\rho(s, p)\delta(c|\boldsymbol{p}_\Gamma| - 1) = \rho_{4D}(s, 0, p, \mathcal{E}). \tag{4.21}$$

Note also that $\rho_{4D}(s, t, p, \mathcal{E}) = \rho_{4D}(\boldsymbol{x}, \boldsymbol{p})$, where $\boldsymbol{x}(s) = (x_1(s), x_2(s)) \in \Omega$ are the Cartesian coordinates of $s \in \Gamma$ and $\boldsymbol{p} = (p_1, p_2)$ are the Cartesian coordinate components of the corresponding momentum vector. In the latter case, we note

that $\rho_{4D}(\boldsymbol{x},\boldsymbol{p})$ extends directly to any $\boldsymbol{x}\in\Omega$, not just local to $s\in\Omega$.

The stationary interior density $\rho_\Omega(\boldsymbol{x})$ at $\boldsymbol{x}\in\Omega$ is defined as

$$\begin{aligned}\rho_\Omega(\boldsymbol{x}) &= \iint \rho_{4D}(\boldsymbol{x},\boldsymbol{p})d\boldsymbol{p},\\ &= \iint e^{-\mu D(\boldsymbol{x},s)}\rho_{4D}(s,0,p,\mathcal{E}(\boldsymbol{p}))d\boldsymbol{p},\\ &= \iint e^{-\mu D(\boldsymbol{x},s)}\rho(s,p)\delta(c|\boldsymbol{p}|-1)|\boldsymbol{p}|d|\boldsymbol{p}|d\Theta.\end{aligned} \tag{4.22}$$

In the above, we change the Cartesian momentum vector $\boldsymbol{p}$ to polar coordinates via $d\boldsymbol{p}=dp_1dp_2=|\boldsymbol{p}|d|\boldsymbol{p}|d\Theta$. We implement the Dirac delta property (A.4) with $g(|\boldsymbol{p}|)=c|\boldsymbol{p}|-1$, so then we may write $\delta(c|\boldsymbol{p}|-1)=\frac{\delta(|\boldsymbol{p}|-1/c)}{c}$. By then applying the property (A.3) we obtain the interior stationary density as

$$\rho_\Omega(\boldsymbol{x})=\frac{1}{c^2}\int_0^{2\pi} e^{-\mu D(\boldsymbol{x},s)}\rho(s,p)d\Theta, \tag{4.23}$$

where $\Theta\in[0,2\pi)$ is the polar angle parametrising trajectories approaching $\boldsymbol{x}$ from $s(\boldsymbol{x},\Theta)\in\Gamma$. The notation for the distance D is used again, albeit here, the distance D is used to represent the Euclidean distance between the solution point $\boldsymbol{x}\in\Omega$ and the boundary position $s\in\Gamma$.

4.3 Discretisation

In this section we discuss a direction preserving discretisation of the local boundary operator (4.11) using a Petrov-Galerkin projection in order to numerically solve for the stationary density ρ via (4.13). This discretisation was first introduced in [11]. We discuss how to simplify the corresponding integrals for the case of polygonal sub-domains Ω_j, $j=1,2,...,\varrho$, that we will consider in our numerical experiments.

We recall the Galerkin method from Section 2.5 in which we considered a BIE of the form $Av=B$, where A, v and B were combinations of linear operators and functions depending on whether the indirect or the direct method was used, as detailed in Table 2.1. The Galerkin method imposes the following

$$\sum_{j=1}^{M}\phi_j\langle Ab_j,b_i\rangle=\langle B,b_i\rangle,$$

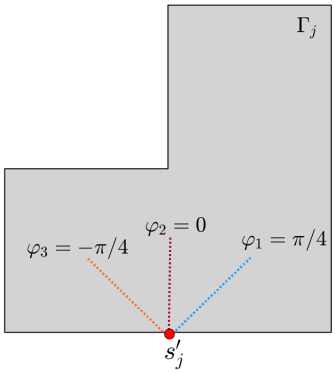

Figure 4.2: The local direction coordinates $\varphi_\kappa \in (-\pi/2, \pi/2)$, $\kappa = 1, 2, 3$ given by the global directions $\Psi_\beta = 2\pi(\beta - 1)/\Lambda$ for $\beta = 1, 2, ..., 8$ when $\Lambda = 8$ for the case when Ω is an L-shaped domain. The map between local and global directions is of the form $\varphi_\kappa = \alpha - \Psi_{\kappa+1}$ for $\kappa = 1, 2, 3$, where the constant α relates to the global direction that corresponds to the inward normal vector at s'_j. For this example, when the ray is travelling from the bottom edge, $\alpha = \pi/2$.

for $i = 1, 2, ..., M$, where M is the number of boundary elements. Here b_i are test functions, b_j are basis functions and ϕ_j, $j = 1, 2, ..., M$, are the unknown basis coefficients to be determined. In the Galerkin method, the test and basis functions are chosen to be the same. In our numerical experiments in sections 2.7 and 2.8, b_i and b_j were chosen to be either piecewise constant or piecewise linear basis functions. Later, the stationary density ρ is discretised such that the standard Galerkin approach is applied to the space variable. In this case, the basis and test functions are both the same scaled piecewise constants. For the momentum variable, the Petrov-Galerkin method is considered, in which the test and basis functions are chosen to be in different spaces. The test function is denoted by χ_i and the basis function as b_j. The basis functions for the momentum variable are chosen to be Dirac delta generalised functions and the test functions are chosen to be piecewise constants. Therefore imposing the Petrov-Galerkin method to the BIE $Av = B$, results in the following

$$\sum_{j=1}^{M} \phi_j \langle Ab_j, \chi_i \rangle = \langle B, \chi_i \rangle, \tag{4.24}$$

for $i = 1, 2, ..., M$.

Now we discuss discretising the boundary operator (4.11). We begin by dividing the boundary Γ_j into elements $E^j_{m'}$ for $m' = 1, 2, ..., M_j$ and we define a set of global ray directions $\Psi_\beta \in [0, 2\pi)$, where $\beta = 1, 2, ..., \Lambda$, defined anticlockwise relative to the positive x_1-axis. Here we choose $\Psi_\beta = 2\pi(\beta - 1)/\Lambda$. We also perform the boundary element subdivision in such a way that any two sub-domains sharing a common edge will have identical boundary elements along the common edge. Furthermore, we set up the subdivision such that $E^j_{m'}$ does not extend over any of the vertices of the polygon Γ_j. We now define $\varphi_{\kappa'}(s'_j) \in (-\pi/2, \pi/2)$, $\kappa' = 1, 2, ..., R_{m'}$ to be the local ray directions at $s'_j \in \Gamma_j$. The local directions correspond to the subset of the global directions that are directed into Ω_j at s'_j and have been re-labelled according to the angle they make with the interior normal vector at s'_j - see Figure 4.2 for further details.

We now approximate the stationary density ρ on $\Gamma_j \times (-c^{-1}, c^{-1})$ using a finite dimensional approximation of the form

$$\rho(s'_j, p'_j) \approx \sum_{m'=1}^{M_j} \sum_{\kappa'=1}^{R_{m'}} \rho_{(j,m',\kappa')} \widehat{b}_{m'}(s'_j) \delta\left(p'_j - \widetilde{p}_{\kappa'}(s'_j)\right), \tag{4.25}$$

where $\widetilde{p}_{\kappa'}(s'_j) = \sin\left(\varphi_{\kappa'}(s'_j)\right)/c$ and

$$\widehat{b}_{m'}(s'_j) = \begin{cases} |E^j_{m'}|^{-1/2} & \text{for } s'_j \in E^j_{m'}, \\ 0 & \text{otherwise,} \end{cases} \tag{4.26}$$

with $|E^j_{m'}| = \text{diam}(E^j_{m'})$. For $m' = 1, 2, ..., M_j$, $\widehat{b}_{m'}$ defines an orthonormal basis of piecewise constant functions with respect to the standard L^2 inner product, $\int_{E^j_{m'}} \widehat{b}_{m'}(s'_j)^2 ds'_j = 1$. We apply a standard Galerkin projection onto our basis in the position variable s'_j.

For the momentum variable, we choose a set of test functions that are orthogonal in the L^2 inner product to $\delta(p'_j - \widetilde{p}_{\kappa'}(s'_j))$ for $\kappa' = 1, 2, ..., R_{m'}$. Therefore, the test functions can be chosen as the set of characteristic functions $\chi_{\kappa'}(p'_j)$ given by

$$\chi(p'_j) = \begin{cases} 1 & \text{if } \theta'_j \in I_{\kappa'}, \\ 0 & \text{otherwise.} \end{cases} \tag{4.27}$$

Here $I_{\kappa'}$ are subdivisions of the local direction range

$$(-\pi/2, \pi/2) = \bigcup_{\kappa'=1}^{R_{m'}} I_{\kappa'}$$

such that

$$\begin{aligned} I_1 &= (-\pi/2, \varphi_1 + \Delta\varphi_1/2], \\ I_{R_{m'}} &= (\varphi_{R_{m'-1}} + \Delta\varphi_{R_{m'-1}}/2, \pi/2), \end{aligned}$$

and

$$I_{\kappa'} = (\varphi_{\kappa'-1} + \Delta\varphi_{\kappa'-1}/2, \varphi_{\kappa'} + \Delta\varphi_{\kappa'}/2], \quad \kappa' = 2, 3, ..., R_{m'} - 1,$$

where $\Delta\varphi_{\kappa'} = \varphi_{\kappa'+1} - \varphi_{\kappa'}$, see Figure 4.3. Therefore we have the property

$$\begin{aligned} \int_{-c^{-1}}^{c^{-1}} \delta(p'_j - \widetilde{p}_{\kappa'}(s'_j))\chi_\kappa(p'_j)dp'_j = 1, \quad \text{if} \quad \kappa' = \kappa, \\ \int_{-c^{-1}}^{c^{-1}} \delta(p'_j - \widetilde{p}_{\kappa'}(s'_j))\chi_{\kappa'}(p'_j)dp'_j = 0, \quad \text{otherwise.} \end{aligned} \tag{4.28}$$

A Petrov-Galerkin projection of the operator $\mathcal{B}_j$ (4.11) on to the basis and test function combination described above for s'_j and p'_j leads to a matrix B defined by

$$\begin{aligned} &B_{I,J} = \\ &\int_{-\frac{1}{c}}^{\frac{1}{c}} \int_{\Gamma_i} \left(\int_{-\frac{1}{c}}^{\frac{1}{c}} \int_{\Gamma_j} w_{i,j}(\boldsymbol{Y}_j) T(\boldsymbol{X}_i, \boldsymbol{Y}_j) \widehat{b}_{m'}(s'_j) \delta(p'_j - \widetilde{p}_\kappa(s'_j)) ds'_j dp'_j \right) \\ &\times \widehat{b}_m(s_i)\chi_\kappa(p_i) ds_i dp_i, \end{aligned} \tag{4.29}$$

with I and J denoting the multi-indices $I = (i, m, \kappa)$ and $J = (j, m', \kappa')$. We enforce the Dirac δ property (A.3) twice (see equation (4.12)) to evaluate the integrals with respect to s_i and p_i. This leads to the simplified form

$$B_{I,J} = \int_{-\frac{1}{c}}^{\frac{1}{c}} \int_{\Gamma_j} e^{-\mu_j D(\phi_{i,j}(\boldsymbol{Y}_j),\boldsymbol{Y}_j)} w_{i,j}(\boldsymbol{Y}_j) \widehat{b}_{m'}(s'_j) \delta(p'_j - \widetilde{p}_\kappa(s'_j)) \widehat{b}_m(s_i) \chi_\kappa(p_i) ds'_j dp'_j. \tag{4.30}$$

We now substitute the spatial basis (4.26) into (4.30) to give

$$B_{I,J} = \int_{E^j_{m'}} \frac{w_{i,j}(\widetilde{p}_\kappa(s'_j)) e^{-\mu_j D_i(s'_j)}}{|E^i_m|^{1/2} |E^j_{m'}|^{1/2}} \chi_\kappa(p_i) ds'_j, \tag{4.31}$$

where the notation $D_i(s'_j)$ is the Euclidean distance between $s'_j \in \Gamma_j$ and $s_i(s'_j, \widetilde{p}_{\kappa'}(s'_j)) \in \Gamma_i$. We have therefore reduced the four-dimensional integration to a single integral over the boundary element $E^j_{m'} \subset \Gamma_j$ as a result of the spatial basis and the properties of the Dirac delta generalised function. We have also assumed that the weight function $w_{i,j}$ is independent of $s'_j \in E^j_{m'}$ and can either define locally constant damping at boundaries or direction only dependent reflection/transmission coefficients [45].

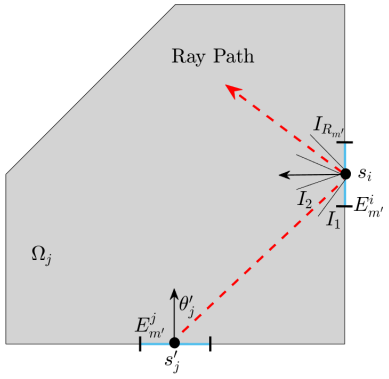

Figure 4.3: An illustration of the case when the entries of the discretised boundary matrix $B_{I,J}$ are non-zero for a reflected ray, when $i = j$. The ray is initially positioned at s'_j travelling at a local direction θ'_j, it arrives at the boundary element E^i_m and the local direction of the reflected ray must fall within the local direction sub-interval I_κ.

The calculation of the matrix element $B_{I,J}$ is therefore relatively simple, since the two basis functions are locally constant and will be zero unless the direction $\theta_i \in I_\kappa$ and $s_i \in E^i_m$, meaning that the majority of the matrix elements will be zero. The case when the matrix elements are non-zero is illustrated in Figure 4.3 and the calculation only involves the integral of the exponential term $e^{-\mu_j D_i(s'_j)}$ over the element $E^j_{m'}$ and multiplication by the pre-factor $w_{i,j}(\widetilde{p}_\kappa(s'_j))\widehat{b}_{m'}(s'_j)\widehat{b}_m(s_i) = w_{i,j}(\widetilde{p}_\kappa(s'_j))(|E^j_{m'}||E^i_m|)^{-1/2}$. For polygonal boundaries, the Euclidean distance function $D_i(s'_j)$ is linear in $s'_j \in E^j_{m'}$ and hence the integral in the equation (4.31) can be performed analytically with relative ease. The only issue that arises is when $s_i(s'_j, \widetilde{p}_\kappa(s'_j))$ coincides with one of the vertices, and the integral must be sub-divided at the corresponding value of s'_j.

Once the boundary operator $\mathcal{B}$ has been calculated in (4.31), then the coefficients ρ_J in (4.25) can be calculated by solving the linear system $\boldsymbol{\rho} = (I - B)^{-1}\boldsymbol{\rho}_0$, which corresponds to the discretised form of equation (4.13). Here $\boldsymbol{\rho}$ and $\boldsymbol{\rho}_0$ represent the coefficients of the expansions of ρ and ρ_0, respectively, when projected onto the finite dimensional basis. The entries of the source vector $\boldsymbol{\rho}_0$ corresponding to an initial density ρ_0 are given using the property (4.28) and the definition of the spatial basis functions (4.26) via

$$\begin{aligned}[\boldsymbol{\rho}_0]_J &= \int_{\Gamma_j \times (-c^{-1}, c^{-1})} \rho_0(s'_j, p'_j)\widehat{b}_{m'}(s'_j)\chi_{\kappa'}(p'_j)dY_j \\ &= \frac{1}{|E^j_{m'}|^{1/2}} \int_{E^j_{m'}} \int_{I_{\kappa'}} \rho_0(s'_j, p'_j)dp'_j ds'_j.\end{aligned} \tag{4.32}$$

Once $\boldsymbol{\rho}$ has been computed and substituted into (4.25), then the interior density ρ_Ω can be approximated using (4.23) as follows

$$\rho_\Omega(\boldsymbol{x}) \approx$$
$$\frac{1}{c^2} \sum_{m'=1}^{M_j} \sum_{\kappa'=1}^{R_{m'}} \rho_J \int_0^{2\pi} e^{-\mu_j D(\boldsymbol{x}, s'_j(\boldsymbol{x},\Theta))} \delta\left(p'_j(\boldsymbol{x},\Theta) - \widetilde{p}_{\kappa'}\left(s'_j(\boldsymbol{x},\Theta)\right)\right) \widehat{b}_{m'}(s'_j(\boldsymbol{x},\Theta))d\Theta. \tag{4.33}$$

Equation (4.33) can be simplified further by rewriting the term $\delta(p'_j(\boldsymbol{x}, \boldsymbol{\Theta}) - \widetilde{p}_{\kappa'}(s'_j(\boldsymbol{x},\Theta)))$ as

$$\delta(p'_j(\boldsymbol{x}, \boldsymbol{\Theta}) - \widetilde{p}_{\kappa'}(s'_j(\boldsymbol{x},\Theta))) = \frac{c\delta(\theta'_j(\boldsymbol{x},\Theta) - \varphi_{\kappa'})}{\cos(\theta'_j(\boldsymbol{x},\Theta))} = \frac{c\delta(\Theta - \Psi_\beta)}{\cos(\theta'_j(\boldsymbol{x},\Theta))}, \tag{4.34}$$

via the property (A.5) of the Dirac delta. In (4.34) Ψ_β is the global direction

corresponding to the local direction $\varphi_{\kappa'}$, which arises in the term $\widetilde{p}_{\kappa'}(s'_j(\boldsymbol{x},\Theta)) = \sin(\varphi_{\kappa'}(s'_j(\boldsymbol{x},\Theta)))/c$. The dependence on s'_j in $\varphi_{\kappa'}$ relates to the differences in the local direction set on each edge of Γ_j, and is independent of s'_j along a given edge of Γ_j. To apply the Dirac delta property (4.34) to (4.33) we first divide the integral into a set of sub-integrals, split at the angles Θ where $s'_j(\boldsymbol{x},\Theta)$ corresponds to a vertex of Γ_j. The second equality in (4.34) is due to the fact that the mapping between local and global directions is a switch of orientation (multiplication by -1) and then a translation by a local edge dependent constant. The denominator in (4.34) is calculated from the derivative of $p'_j(\boldsymbol{x},\Theta) = \sin(\theta'_j(\boldsymbol{x},\Theta))$ with respect to θ'_j [45]. The global ray summation result for the interior density is then given by

$$\rho_\Omega(\boldsymbol{x}) \approx \frac{1}{c}\sum_{\beta=0}^{\Lambda} \frac{e^{-\mu_j D(\boldsymbol{x},s'_j(\boldsymbol{x},\Psi_\beta))}\rho_J(\boldsymbol{x},\Psi_\beta)}{|E^j_{m'}(\boldsymbol{x},\Psi_\beta)|^{1/2}\cos(\theta'_j(\boldsymbol{x},\Psi_\beta))}. \tag{4.35}$$

Note that the integral in (4.33) only results in a non-zero value when Θ corresponds with a direction from the global direction set and therefore the double sum over boundary elements and local directions is reduced to a single summation over global directions Ψ_β, $\beta = 1, 2, ..., \Lambda$. The boundary position s'_j and local direction θ'_j can be determined from the solution point $\boldsymbol{x}$ and ray direction Ψ_β.

4.4 Numerical results

In this section, we approximate the boundary integral operator $\mathcal{B}_j$ via the Petrov-Galerkin discretisation (4.31), which transports wave energy densities between intersections with the boundary Γ_j, $j = 1, 2, ..., \varrho$. We then apply the ray summation (4.35) to evaluate the projection of these phase-space densities into Ω. We investigate the errors and estimated convergence rates for a number of examples, including for the case when there is a line source propagating into either a unit square or an L-shaped domain. We also consider the case when there is a source point inside the domain for either a unit square, an L-shape or an irregular shaped polygon. The following is a step-by-step guide for implementing DEA to approximate the Helmholtz equation in two-dimensions as described in Sections 4.1 - 4.3.

1. We begin by defining s'_j as the arclength parameter along the boundary

Γ_j, $j = 1, 2, ..., \varrho$, and the momentum $p'_j = \sin(\theta'_j)/c$. The variable θ'_j is the angle formed between the outgoing ray trajectory and the unit normal vector to Γ_j and c is the wave speed which is chosen to be a constant value. Next we divide the boundary Γ_j, $j = 1, 2, ..., \varrho$, into elements $E^j_{m'}$ for $m' = 1, 2, ..., M_j$ and we define a set of global ray directions $\Psi_\beta \in [0, 2\pi)$, where $\beta = 1, 2, ..., \Lambda$, defined anticlockwise relative to the positive x_1-axis. In our numerical examples we choose $\Psi_\beta = 2\pi(\beta - 1)/\Lambda$.

2. Next we approximate the stationary density vector $\boldsymbol{\rho}_0$ via (4.32), where ρ_0 is the initial density of the given problem.

3. Next we determine the matrix entries of the boundary integral operator $\mathcal{B}$ which has been discretised using the Petrov-Galerkin projection given by (4.31). The Euclidean distance between $s'_j \in \Gamma_j$ and $s_i(s'_j, \widetilde{p}_{\kappa'}(s'_j)) \in \Gamma_i$ is given by $D_i(s'_j)$. The weight function $w_{i,j}$ is independent of $s'_j \in E^j_{m'}$ and can either define locally constant damping at boundaries or direction only dependent reflection/transmission coefficients, in the numerical results to follow these are defined for each problem. The characteristic function $\chi(p'_j)$ as part of the momentum variable discretisation is defined by (4.27).

4. Once the boundary operator $\mathcal{B}$ has been calculated in (4.31), then the coefficients ρ_J in (4.25) can be calculated by solving the linear system $\boldsymbol{\rho} = (I - B)^{-1}\boldsymbol{\rho}_0$, which corresponds to the discretised form of equation (4.13). Here $\boldsymbol{\rho}$ and $\boldsymbol{\rho}_0$ represent the coefficients of the expansions of ρ and ρ_0, respectively, when projected onto the finite dimensional basis.

5. Finally, the interior density $\rho_\Omega(\boldsymbol{x})$ is a summation of all global rays given by (4.35). Where ρ_J was determined via the previous step. The boundary position s'_j and local direction θ'_j can be determined from the solution point $\boldsymbol{x}$ and ray direction Ψ_β.

The MATLAB code for these examples are available from the following URL: https://github.com/JacobRowbottom/DEA.

4.4.1 Constant line source

Square domain

We consider a unit square domain Ω with sound-hard reflections at the boundary. Since the unit square consists of only one sub-domain, we simply write

the phase-space boundary coordinates as (s, p) and $\boldsymbol{x}_s$ denotes the Cartesian coordinates of the arclength parameter s. We enforce a spatially constant line source defined by

$$\rho_0(s,p) = \begin{cases} \delta(p-\xi)\cos(\xi) & \text{for } \boldsymbol{x}_s = 0, \\ 0 & \text{otherwise,} \end{cases} \tag{4.36}$$

along the left edge, propagating rays into the domain directed at angle $\xi \in (-\pi/2, \pi/2)$. The angle ξ is the angle between the interior normal vector and the ray leaving the boundary.

We first consider the case when $\xi = 0$, i.e. the source is directed perpendicularly to the edge. Physically this represents a very simple problem, since the rays only bounce between the source edge on the left and the opposite edge on the right, and are always directed perpendicular to these edges. Therefore the ray density will simply be constant along these two edges and will be zero on the remaining two edges. We choose the damping coefficient $\mu = \pi/2$ and then the interior ray density ρ_Ω may be calculated at $\boldsymbol{x} = (x_1, x_2) \in \Omega$ via a geometric series [74] over the reflection order, as derived in Appendix E for a rectangle of length l in the x_1 coordinate here applied with $l = 1$ to give

$$\rho_\Omega(\boldsymbol{x}) = \frac{e^{-\mu x_1} + e^{-\mu(2-x_1)}}{1 - e^{-2\mu}}. \tag{4.37}$$

Figure 4.4 shows the exact solution for the interior ray density ρ_Ω and the numerical solution $\widehat{\rho}_\Omega$, which is approximated via (4.35). The solutions were calculated at $N_{\boldsymbol{x}} = 3638$ interior points $\boldsymbol{x}_i$, $i = 1, 2, ..., N_{\boldsymbol{x}}$, which are taken to be the centroids of a triangle mesh generated by the Distmesh package [147] for MATLAB with mesh spacing 0.025. The calculation of $\widehat{\rho}_\Omega$ was computed by choosing the global direction set to be $\Psi_\beta = 2\pi(\beta - 1)/\Lambda$ for $\beta = 1, ..., \Lambda$, which will also be the case for all future calculations of $\widehat{\rho}_\Omega$. The choice of Ψ_β can be made dependent on the given problem or geometry, but our choice for Ψ_β is based on a simple equispaced subdivision of directions that include $\Psi_1 = 0$, which corresponds to the source direction in this example. From Figure 4.4 we observe the predicted behaviour of the rays bouncing between the left and right edges meaning the solution is independent of x_2. We also notice that the numerical solution matches the exact solution accurately, which is also

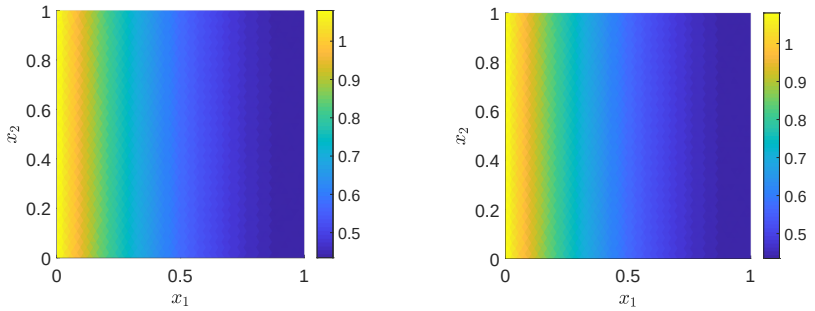

(a) Numerical solution $\widehat{\rho}_\Omega$ (b) Exact solution ρ_Ω

Figure 4.4: The numerical and exact solutions for the interior density inside a unit square domain in the case when there is a constant line source travelling into the domain in the direction $\xi = 0$ from the left edge. The numerical interior density $\widehat{\rho}_\Omega$ was calculated via DEA using $M = 256$ boundary elements and with $\Lambda = 32$ global directions. Both solutions were evaluated at $N_{\boldsymbol{x}} = 3638$ interior points.

supported by the error results in Table 4.1.

$\Lambda/2$	Error
4	1.4737e-16
8	1.4736e-16
16	1.4736e-16
32	1.4736e-16
64	1.4736e-16
128	1.4736e-16
256	1.4736e-16

Table 4.1: Relative mean errors for the interior density inside a unit square domain for the case when there is a constant line source travelling into the domain in the direction $\xi = 0$ from the left edge. We investigate the errors as we double the number of global directions Λ. The numerical interior density was calculated using $M = 256$ boundary elements and evaluated at $N_{\boldsymbol{x}} = 3638$ interior points.

Table 4.1 shows the relative error as we increase the number of degrees of freedom in the momentum approximation on a given boundary element, which for our direction set is $\Lambda/2 - 1$, since just under half of the global direction set will be directions propagating within the unit square domain from any given

edge. The error is calculated via the relative mean error:

$$\text{Error} = \frac{\sum_{i=1}^{N_{\boldsymbol{x}}} |\widehat{\rho}_{\Omega}(\boldsymbol{x}_i) - \rho_{\Omega}(\boldsymbol{x}_i)|}{\sum_{i=1}^{N_{\boldsymbol{x}}} \rho_{\Omega}(\boldsymbol{x}_i)}. \tag{4.38}$$

We find that even when the direction basis contains only four directions $\Psi_1 = 0$, $\Psi_2 = \pi/2$, $\Psi_3 = \pi$ and $\Psi_4 = 3\pi/2$, we still achieve machine precision accuracy when approximating ρ_{Ω}. This is because the exact solution for ρ on the boundary Γ lies in the approximation space, since it takes only a constant value on each edge and propagates only in the directions Ψ_1 and Ψ_3.

	$\Lambda = 8$		$\Lambda = 16$		$\Lambda = 32$	
M	Error	EOC	Error	EOC	Error	EOC
20	-	-	-	-	-	-
40	0.0528	-	0.0358	-	0.0358	-
80	0.0289	0.87	0.0170	1.07	0.0170	1.07
160	0.0152	0.93	0.0086	0.98	0.0086	0.98
320	0.0079	0.94	0.0039	1.14	0.0039	1.14
640	0.0039	1.02	0.0020	0.96	0.0020	0.96

Table 4.2: Relative mean errors and estimated orders of convergence for the interior density inside a unit square domain for the case when there is a constant line source travelling into the domain in the direction $\xi = -3\pi/8$. We investigate the errors and convergence rates as the number of boundary elements M is doubled when $\Lambda = 8$, 16 and 32 global directions. The numerical interior density was calculated via DEA and was evaluated at $N_{\boldsymbol{x}} = 3638$ interior points.

We also consider the case when the source is travelling into the domain from the left edge (4.36) at an angle $\xi = -3\pi/8$. For this example the rays do not simply travel between the left and right edges but instead reflect on all boundary edges giving a more complex solution as shown in Figure 4.5(a). Figure 4.5(a) displays the numerical solution for the interior density $\widehat{\rho}_{\Omega}$ which is approximated via (4.35) using the Dirac delta basis with Ψ_β for $\Lambda = 64$ global directions. The solution was calculated at $N_{\boldsymbol{x}} = 3638$ interior points $\boldsymbol{x}_i$, $i = 1, 2, ..., N_{\boldsymbol{x}}$, which are again taken to be the centroids of a Distmesh triangle mesh with mesh spacing 0.025. From this figure, we observe the rays reflecting from all edges of the domain with the density ρ_{Ω} decaying as the rays move away from the source edge on the left. Sub-plot (b) shows the interior density for the case when ξ is not included in the direction set, Ψ_β for $\Lambda = 8$. In this sub-plot, we observe that the interior density does not display the expected behaviour as shown in

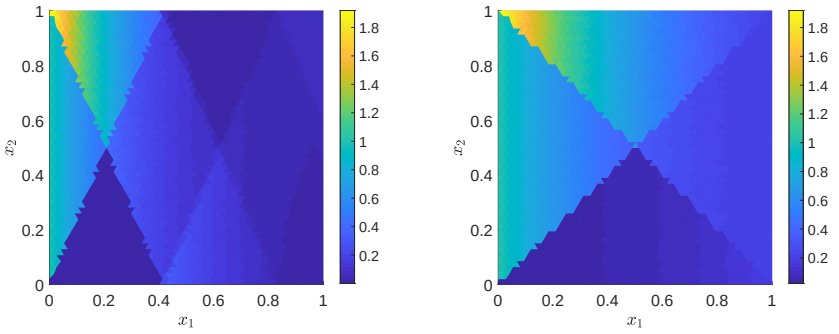

(a) $\Lambda = 64$ (b) $\Lambda = 8$

Figure 4.5: The numerical solution for the interior density inside a unit square domain in the case when there is a constant line source travelling into the domain in the direction $\xi = -3\pi/8$ from the left edge. The numerical interior density $\widehat{\rho}_\Omega$ was calculated via DEA using $M = 160$ boundary elements and with $\Lambda = 64$ global directions in sub-plot (a) and with $\Lambda = 8$ global directions in sub-plot (b). The interior density was evaluated at $N_{\boldsymbol{x}} = 3638$ interior points.

sub-plot (a) instead we observe that the rays travelling from the left edge do not bounce along the top and bottom edges of the domain but travel from corner to corner, because the direction the true direction of $-3\pi/8$ is mapped to the next direction within the global set, which here is $\xi = -\pi/4$ when $\Lambda = 8$. Next we investigate the error results for the approximate interior density $\widehat{\rho}_\Omega$ at a fixed set of global directions when $\Lambda = 8$, $\Lambda = 16$ and $\Lambda = 32$ as we double the number of boundary elements M. Table 4.5 shows the respective errors and estimated orders of convergence for these choices for Λ. The errors are calculated using subsequent interior densities $\widehat{\rho}_\Omega$ as we double M. We write this error of the mean interior density as follows

$$\text{Error}(M) = \frac{\left|\sum_{i=1}^{N_{\boldsymbol{x}}} \widehat{\rho}_M(\boldsymbol{x}_i) - \sum_{i=1}^{N_{\boldsymbol{x}}} \widehat{\rho}_{2M}(\boldsymbol{x}_i)\right|}{\sum_{i=1}^{N_{\boldsymbol{x}}} \widehat{\rho}_{2M}(\boldsymbol{x}_i)}, \tag{4.39}$$

where $\widehat{\rho}_M$ is the approximation of $\widetilde{\rho}_\Omega$ calculated using M boundary elements compared to the result $\widehat{\rho}_{2M}$, which approximates $\widetilde{\rho}_\Omega$ at double the number of boundary elements $2M$. The estimated convergence rate was calculated via $\log_2(\text{Error}(M/2)/\text{Error}(M))$. We can deduce that for the case when we have $\Lambda = 8$ global directions, the angle $\xi = 3\pi/8$ is not included in the global direction

set Ψ_β, $\beta = 1, 2, ..., \Lambda$. However for the cases when $\Lambda = 16$ and 32, we observe the same error results since $\Psi_4 = 3\pi/8$ when $\Lambda = 16$ and $\Psi_7 = 3\pi/8$ when $\Lambda = 32$, and hence $\xi = 3\pi/8$ is included in the set of global directions for both cases. Due to the simple geometry of Ω and the choice of our direction set we observe that if $3\pi/8$ is included in the direction set then all reflected ray directions are also included in the global direction set. This results in a better accuracy than when $\Lambda = 8$ and all cases of Λ demonstrate approximately first order convergence in the number of boundary elements M, as shown in Table 4.2.

L-shaped domain

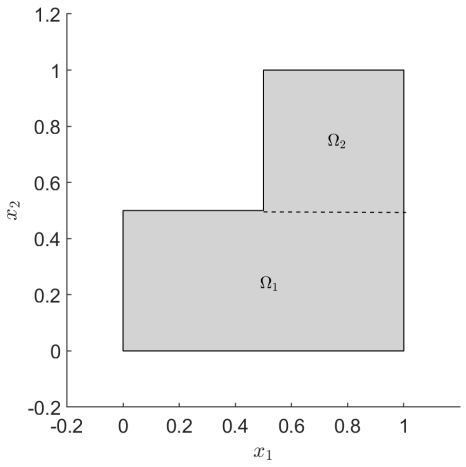

Figure 4.6: The L-shaped domain.

We now consider an L-shaped domain Ω with sound-hard reflections at the boundary. The domain is divided into two sub-domains as shown in Figure 4.6, such that we have $\Omega = \Omega_1 \cup \Omega_2$, since the L-shape is non-convex. We enforce a spatially constant line source defined by (4.36) along the left edge in the first sub-domain Ω_1, propagating rays into the domain directed at an angle $\xi \in (-\pi/2, \pi/2)$.

We first consider the case when $\xi = 0$, which physically represents the rays bouncing between the source edge on the left and the opposite edge on the right in Ω_1 only, and there should be no propagation into Ω_2. Figure 4.7 shows

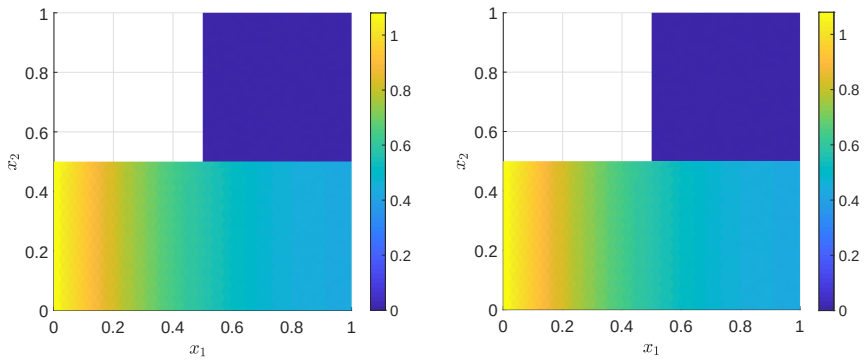

(a) Numerical solution $\widehat{\rho}_\Omega$ (b) Exact solution ρ_Ω

Figure 4.7: The numerical and exact solutions for the interior density inside the L-shaped domain in the case when there is a constant line source travelling into the domain at an angle $\xi = 0$ from the far left edge. The numerical interior density $\widehat{\rho}_\Omega$ was calculated via DEA using $M = 256$ boundary elements and with $\Lambda = 8$ global directions. Both solutions were evaluated at $N_{\boldsymbol{x}} = 1820$ interior points in Ω_1 and $N_{\boldsymbol{x}} = 900$ points in Ω_2.

the exact interior density ρ_Ω calculated via (4.37) in Ω_1, and zero in Ω_2 as well as the numerical interior ray density $\widehat{\rho}_\Omega$ calculated via DEA using $\Lambda = 8$ global directions. Both the exact and the numerical interior ray densities were evaluated at $N_{\boldsymbol{x}} = 1820$ interior points in Ω_1 and $N_{\boldsymbol{x}} = 900$ points in Ω_2, that were taken to be the centroids of a Distmesh triangle mesh with spacing 0.025, as before. The damping coefficient was again taken to be $\mu = \pi/2$. From the figure, we observe the predicted physical behaviour of the rays reflecting between the two side edges of sub-domain Ω_1 and zero in Ω_2, with both the exact and numerical interior densities appearing identical.

We now investigate the relative error of the numerical interior ray density $\widehat{\rho}_\Omega$ in sub-domain Ω_1 only, since the interior density in Ω_2 is zero. We compute the relative error in sub-domain Ω_1 via (4.38) as we double the number of global directions Λ for a fixed number of boundary elements $M = 256$. Table 4.3 shows the relative error computed this way against $\Lambda/2$, since only (approximately) half of the directions Ψ_β, $\beta = 1, 2, ..., \Lambda$, will propagate within the domain from any given edge as before. The error is calculated using $N_{\boldsymbol{x}} = 1820$ interior points that are the centroids of a triangle mesh with spacing 0.025. As before

we achieve machine precision for all error calculations, even for the coarse discretisation with $\Lambda/2 = 4$, since the exact solution on the boundary Γ lies in the approximation space due to the boundary density being a constant value on each edge and propagating only in the directions Ψ_1 and Ψ_3.

$\Lambda/2$	Error
4	1.0179e-16
8	1.0179e-16
16	1.0179e-16
32	1.0179e-16
64	1.0179e-16
128	1.0179e-16
256	1.0179e-16

Table 4.3: Relative mean errors for the interior density inside the L-shaped domain for the case when there is a constant line source travelling into the domain in the direction $\xi = 0$. We investigate the errors as we double the number of global directions Λ. The numerical interior density was calculated using $M = 256$ boundary elements and evaluated at $N_{\boldsymbol{x}} = 1820$ interior points.

We also consider the case when the left edge is a line source (4.36) propagating at an angle of $\xi = 3\pi/8$. Figure 4.8 shows the interior density calculated via DEA for this problem with $\Lambda = 128$ global directions and plotted at $N_{\boldsymbol{x}} = 7320$ interior points in Ω_1 and $N_{\boldsymbol{x}} = 3638$ points in Ω_2, which in both cases are generated from the centroids of a Distmesh triangular mesh with mesh spacing 0.0125. From this figure, we observe a higher density of ray trajectories close to the source edge in Ω_1 before the damping becomes more evident and the density is then lower throughout the rest of the domain, in particular in Ω_2. We now have a non-zero interior density in sub-domain Ω_2, whereas for the case when $\xi = 0$ we only observed a zero value for the interior density in Ω_2 due to the optical shadowing effect.

We investigate the relative error results for the approximate interior density $\widehat{\rho}_\Omega$. We calculate the interior density using $\Lambda = 16$ global directions such that the angle $\xi = 3\pi/8$ is included in the global direction set. Therefore the results show an accurate representation of the ray trajectories inside the domain. Table 4.4 shows the estimated convergence rate and the mean errors of the numerical interior density $\widehat{\rho}_\Omega$ as we double the number of boundary elements M. The mean errors were calculated in each sub-domain individually using subsequent mean errors as the number of boundary elements is doubled via (4.39). From this

table, we observe approximately first order convergence in both sub-domains with both sets of errors being similar.

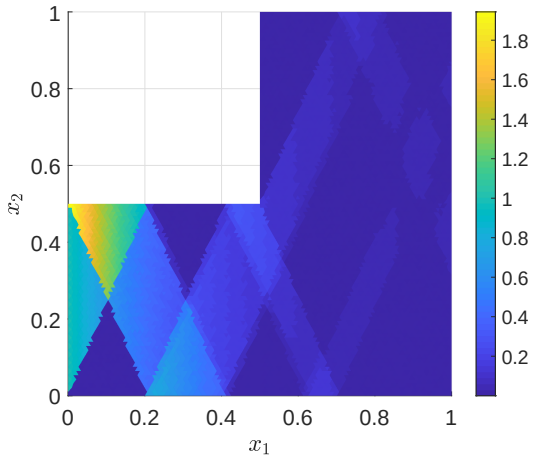

Figure 4.8: The numerical solution for the interior density inside the L-shaped domain in the case when there is a constant line source travelling into the domain in the direction $\xi = -3\pi/8$ from the far left edge. The numerical interior density $\widehat{\rho}_\Omega$ was calculated via DEA using $M = 160$ boundary elements and with $\Lambda = 128$ global directions. The interior density was evaluated at $N_{\boldsymbol{x}} = 7320$ points in Ω_1 and $N_{\boldsymbol{x}} = 3638$ points in Ω_2.

	Ω_1			Ω_2		
M	M_1	Error	EOC	M_2	Error	EOC
40	30	0.0411	-	20	0.0672	-
80	60	0.0245	0.75	40	0.0278	1.27
160	120	0.0122	1.01	80	0.0110	1.34
320	240	0.0062	0.98	160	0.0060	0.91
640	480	0.0023	1.49	320	0.0026	1.21

Table 4.4: Relative mean errors for the interior density inside the L-shaped domain in the case when there is a constant line source travelling into the domain in the direction $\xi = -3\pi/8$. We investigate the errors and convergence in each sub-domain individually as we double the number of boundary elements M with a fixed number of global directions $\Lambda = 16$. The numerical interior density was evaluated at $N_{\boldsymbol{x}} = 7320$ points in Ω_1 and $N_{\boldsymbol{x}} = 3638$ points in Ω_2.

4.4.2 Response to an interior point source

In this section, we consider the numerical interior density $\widehat{\rho}_\Omega$ for the case when there is a point source inside either a unit square, an L-shape or an irregular polygon. We now describe how the initial density ρ_0 is obtained for a source point $\boldsymbol{x}_0 \in \Omega$ propagating ray trajectories in all directions. We begin by recalling that the ray density ρ is given by the square amplitudes of a plane decomposition of the solution to the Helmholtz equation (2.2) as

$$\rho(\boldsymbol{x}, \boldsymbol{p}) = |u(\boldsymbol{x})|^2 \delta(\boldsymbol{p} - \boldsymbol{p}_0).$$

The slowness or momentum vector $\boldsymbol{p}_0$ corresponds to the direction arriving from $\boldsymbol{x}_0$. Replacing u with the high frequency asymptotic formula for the fundamental solution of the Helmholtz equation (2.5), taken from [74], yields the initial density

$$\begin{aligned} \rho_0(\boldsymbol{x}, \boldsymbol{p}) &= \left| \frac{i}{4} H_0^{(1)} \left(k \left\| \boldsymbol{x} - \boldsymbol{x}_0 \right\| \right) \right|^2 \delta(\boldsymbol{p} - \boldsymbol{p}_0) \\ &\underset{\mathrm{Re}(k) \gg 1}{\approx} \frac{e^{-2\mathrm{Im}(k) \| \boldsymbol{x} - \boldsymbol{x}_0 \|} \delta(\boldsymbol{p} - \boldsymbol{p}_0)}{8\pi |k| \left\| \boldsymbol{x} - \boldsymbol{x}_0 \right\|}. \end{aligned} \tag{4.40}$$

The energy density in the high frequency limit decays in all directions due to the $\left\| \boldsymbol{x} - \boldsymbol{x}_0 \right\|^{-1}$ term.

In what follows, we consider examples where Ω is either treated as a single domain or divided into two sub-domains $\Omega = \Omega_1 \cup \Omega_2$. For the former case, we omit the index j to denote the number of sub-domains and consider only a single domain Ω with boundary Γ, for simplicity. To obtain the source density ρ_0 along the boundary Γ, we set

$$\rho_0(\boldsymbol{x}, \boldsymbol{p}) = \rho_0(s, p) \delta(c|\boldsymbol{p}| - 1), \tag{4.41}$$

where s parameterises Γ and p denotes the momentum component tangential to Γ at s - see (4.21). We will use local coordinates on the boundary $\boldsymbol{p} = (p_\parallel, p_\perp)$, where $p_\parallel$ and $p_\perp$ are the components of the momentum vector parallel and perpendicular to Γ, respectively. If we also denote $\boldsymbol{p}_0 = (p_\parallel^0, p_\perp^0)$ then $\delta(\boldsymbol{p} - \boldsymbol{p}_0) = \delta(p_\parallel - p_\parallel^0) \delta(p_\perp - p_\perp^0)$ and one obtains using property (A.5) that

$$|\boldsymbol{p}_0| \delta(p_\parallel - p_\parallel^0) \delta(p_\perp - p_\perp^0) = c p_\perp^0 \delta(p_\parallel - p_\parallel^0) \delta(c|\boldsymbol{p}| - 1). \tag{4.42}$$

We note that $p = p_{\parallel}$ and $p_{\perp}^{0} = |\boldsymbol{p}_0| \cos(\theta_0)$. Then, combining (4.42) with (4.40) and (4.41) leads to the initial boundary density on Γ written as

$$\rho_0(s,p) = \frac{c\cos(\theta_0)e^{-\mu D(\boldsymbol{x}_0,s)}\delta(p-p_0)}{8\pi|k|D(\boldsymbol{x}_0,s)}, \tag{4.43}$$

where we have replaced $p_{\parallel}^{0}$ by p_0 and $\mathrm{Im}(k)$ by μ.

The extension to multidomains when $\Omega = \Omega_1 \cup \Omega_2$ is straight forward and gives the initial boundary density as

$$\rho_0(s_j', p_j') = \frac{c\cos(\theta_0)e^{-\mu D(\boldsymbol{x}_0,s_j')}w_{1,j}(s_j',p_j')\delta(p_j'-p_0)}{8\pi|k|D(\boldsymbol{x}_0,s_j')}, \tag{4.44}$$

assuming that $\boldsymbol{x}_0 \in \Omega_1$ and where $p_0 = \sin(\theta_0)/c$ is the tangential momentum of the ray emerging from s_j' that arrived from $\boldsymbol{x}_0$, and $\theta_0 \in (-\pi/2, \pi/2)$. For domains which are divided into two sub-domains such as the L-shape, the initial density ρ_0 will only be non-zero along the edges that are directly illuminated by the point source rays [11]. Therefore we can write $w_{1,j}$ in equation (4.44) as

$$w_{1,j}(s_j',p_j') = \begin{cases} 1 & \text{if } j=1 \text{ and } s_j' \text{ is on a free edge,} \\ A(p_j') & \text{if } j=1 \text{ and } s_j' \text{ is on the inner edge connecting to } \Omega_2, \\ B(p_j') & \text{if } j=2 \text{ and } s_j' \text{ is on the inner edge connecting to } \Omega_1, \\ 0 & \text{otherwise.} \end{cases} \tag{4.45}$$

We define a free edge as an edge not connected to another sub-domain and A, B denote the reflection and transmission probabilities for rays in Ω_1 arriving at the shared edge between Ω_1 and Ω_2. Here we choose $A(p_j') \equiv 0$ and $B(p_j') \equiv 1$, corresponding to pure transmission with $c = 1$ for $j = 1, 2$, as shown in Figure 4.9(a). Sub-plot (b) shows the problem set up for the source point problem for the case when the domain is a L-shape consisting of two sub-domains. The lines and arrows show the trajectories of the rays from the source point $\boldsymbol{x}_0$, highlighted by the red circle, travelling towards the boundary. For all numerical examples to follow we choose with $\mu = \pi/2$.

Square domain

We first consider the case when Ω is a unit square domain with the point source chosen to be in the centre at $\boldsymbol{x}_0 = (0.5, 0.5)$. Figure 4.10 shows the numerical

interior density $\widehat{\rho}_\Omega$ with $M = 256$ boundary elements, $\Lambda = 512$ global directions and plotted at $N_{\boldsymbol{x}} = 3638$ interior points using a Distmesh internal mesh with spacing 0.025. The figure shows that the interior solutions vary between lighter and darker regions with the lighter regions being more locally concentrated near the source point, physically representing a higher ray density.

We estimate the relative error using (4.39) with subsequent approximate interior densities $\widehat{\rho}_\Omega$, although here we double the number of boundary elements M and the number of directions Λ in the global direction set. Table 4.5 shows the error evaluated using $N_{\boldsymbol{x}} = 14632$ interior points. From this table, we observe that the errors decrease as we increase the number of elements and directions, eventually achieving small errors that are less than 1% with a convergence rate between first and second order.

Λ	M	Mean Error	EOC
8	10	-	-
16	20	0.0165	-
32	40	0.0137	0.27
64	80	0.0046	1.57
128	160	0.0010	2.06

Table 4.5: Relative mean errors for the interior density inside a unit square domain for the case when there is a point source at $\boldsymbol{x}_0 = (0.5, 0.5)$. We investigate the errors and convergence as we double the number of boundary elements M and the number of global directions Λ. The numerical interior density was averaged over $N_{\boldsymbol{x}} = 7320$ interior points.

L-shaped domain

We now consider the L-shaped domain, $\Omega = \Omega_1 \cup \Omega_2$ as shown in Figure 4.6, with a point source located at $\boldsymbol{x}_0 = (0.25, 0.25)$. We calculate the relative error via (4.39) using subsequent interior densities $\widehat{\rho}_\Omega$ as we double both the number of boundary elements M and the number of directions Λ in the global direction set. Table 4.6 shows the relative error calculated using $N_{\boldsymbol{x}} = 3638$ interior points in Ω_1 and $N_{\boldsymbol{x}} = 1796$ in interior points in Ω_2, the points were chosen to be the centroids of a Distmesh triangular mesh with mesh spacing 0.0175 and M_1 and M_2 denote the number of boundary elements on the sub-domains Ω_1 and Ω_2, respectively. From this table we observe that in both sub-domains as we increase the number of boundary elements and directions the mean error decreases and we achieve approximately first order convergence. Figure 4.11 shows the approximate interior density solution computed with a total of $M = 256$ boundary elements with $M_1 = 192$ in Ω_1 and $M_2 = 128$ in Ω_2, as well as $\Lambda = 256$ global directions and $N_{\boldsymbol{x}} = 7320$ interior points in Ω_1 and $N_{\boldsymbol{x}} = 3638$ points in Ω_2. From this figure we observe the rays are more concentrated around the source point as the density is concentrated more strongly in sub-domain Ω_1 than in sub-domain Ω_2. We also observe a shaded region inside sub-domain Ω_2 from the left edge to the top edge of sub-domain Ω_2. This is due to the fact that the rays travelling from the source point never directly intersect with these edges and only rays which have reflected from other edges will enter this region.

		Ω_1			Ω_2		
Λ	M	M_1	Error	EOC	M_2	Error	EOC
8	8	6	-	-	4	-	-
16	16	12	0.0157	-	8	0.1989	-
32	32	24	0.0112	0.49	16	0.0611	1.70
64	64	48	0.0060	0.90	32	0.0224	1.45
128	128	96	0.0028	1.10	24	0.0083	1.43

Table 4.6: Relative mean errors for the interior density inside an L-shaped domain for the case when there is a point source at $\boldsymbol{x}_0 = (0.25, 0.25)$. We investigate the errors and convergence in each sub-domain individually as we double the number of boundary elements M and number of global directions Λ. The numerical interior density was averaged over $N_{\boldsymbol{x}} = 7320$ interior points in Ω_1 and $N_{\boldsymbol{x}} = 3638$ points in Ω_2.

Irregular polygon

We now consider the irregular shaped polygon domain Ω as shown in Figure 3.15, with a source point $\boldsymbol{x}_0 = (0.648, 0.5)$. The Cartesian coordinates of the vertices and source point are also given in Table 3.10. Figure 4.12 shows the interior density approximation $\widehat{\rho}_\Omega$ calculated via DEA with $\Lambda = 256$ global directions, $M = 256$ boundary elements and with $N_{\boldsymbol{x}} = 11003$ interior points that are the centroids of the triangular mesh with mesh spacing 0.0125.

Table 4.7 shows the mean errors calculated via (4.39) using subsequent approximations for the interior density with $N_{\boldsymbol{x}} = 1820$ as we double the number of boundary elements M and the number of global directions. From this table, we observe that we eventually achieve small errors as we increase the number of boundary elements and directions with a varying convergence rate between approximately first and second order. Typically, when considering a domain such as the irregular polygon, one could potentially expect larger errors compared to the square and L-shaped domain because the true reflection directions are not necessarily included in the direction basis set. Comparing the results in tables 4.5 to 4.7 we actually observe similar errors for the irregular polygon results in Table 4.7, but it is difficult to compare directly since the M and Λ combinations are not the same. All relative errors are also significantly less than 1% for $\Lambda \geq 64$ global directions.

Λ	M	Mean Error	EOC
8	5	-	-
16	10	0.0223	-
32	20	0.0375	-0.75
64	40	0.0076	2.30
128	80	0.0023	1.72

Table 4.7: Relative errors for the interior density inside an irregular polygon domain for the case when there is a point source at $\boldsymbol{x}_0 = (0.648, 0.5)$. We investigate the errors and convergence as we double the number of boundary elements M and number of global directions Λ. The numerical interior density was averaged over $N_{\boldsymbol{x}} = 3791$ interior points.

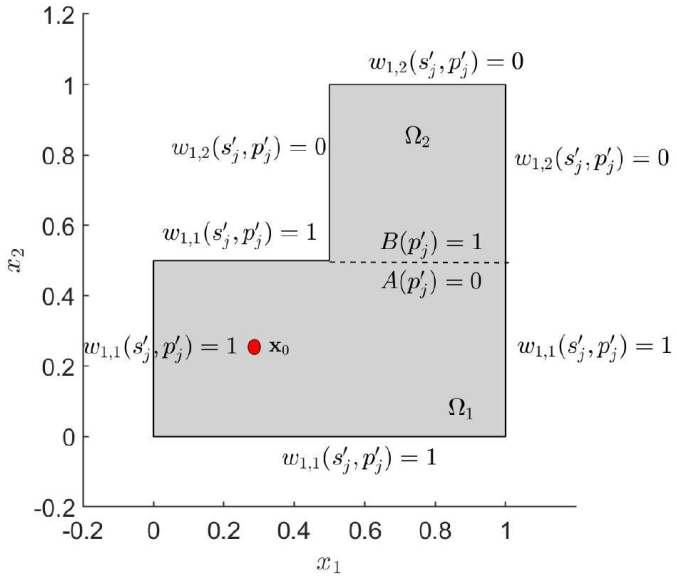

(a)

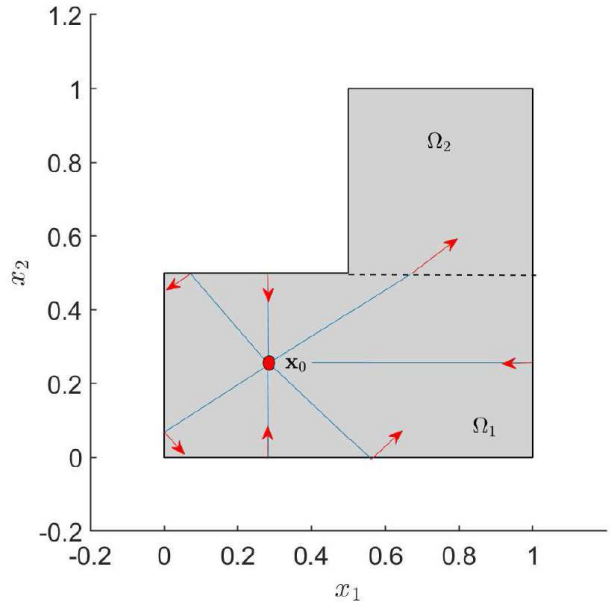

(b)

Figure 4.9: Sub-plot (a) shows the weight function $w_{1,j}$ on the L-shaped domain which has been divided into two sub-domains with the source point $\boldsymbol{x}_0 = (0.25, 0.25)$, highlighted by the red circle. Sub-plot (b) shows the schematic of the point source to the boundary.

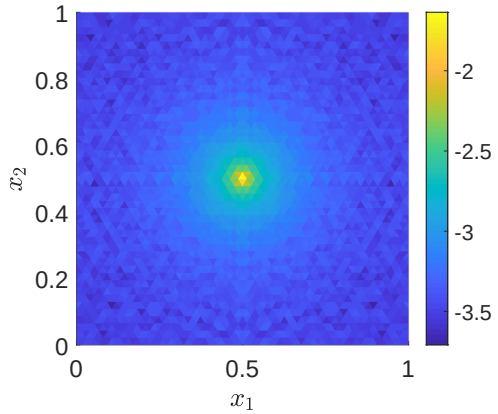

Figure 4.10: The numerical solution of the interior density inside a unit square domain for the case when there is a point source at $\boldsymbol{x}_0 = (0.5, 0.5)$. The numerical interior density $\widehat{\rho}_\Omega$ was calculated via DEA using $M = 256$ boundary elements and with $\Lambda = 512$ global directions. The interior density was evaluated at $N_{\boldsymbol{x}} = 3638$ interior points.

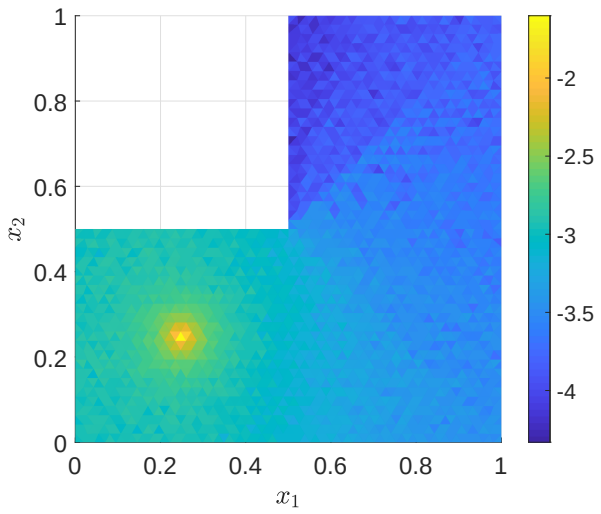

Figure 4.11: The numerical solution of the interior density inside an L-shaped domain for the case when there is a point source at $\boldsymbol{x}_0 = (0.25, 0.25)$. The numerical interior density $\widehat{\rho}_\Omega$ was calculated via DEA using a total of $M = 256$ boundary elements with $M_1 = 192$ in Ω_1 and $M_2 = 128$ in Ω_2 and with $\Lambda = 256$ global directions. The interior density was evaluated at $N_{\boldsymbol{x}} = 7320$ points in Ω_1 and $N_{\boldsymbol{x}} = 3638$ points in Ω_2.

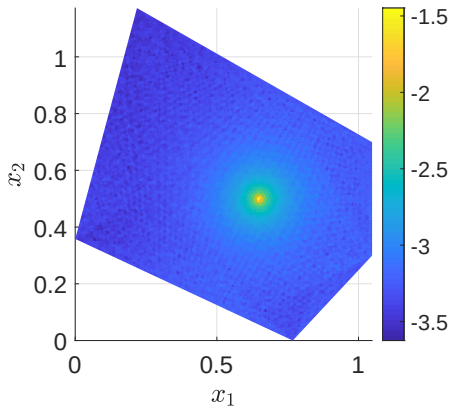

Figure 4.12: The numerical solution of the interior density inside the irregular polygon domain for the case when there is a point source at $\boldsymbol{x}_0 = (0.648, 0.5)$. The numerical interior density $\widehat{\rho}_\Omega$ was calculated via DEA using $M = 256$ boundary elements and with $\Lambda = 256$ global directions. The interior density was evaluated at $N_{\boldsymbol{x}} = 11003$ interior points.

4.5 Conclusion

In this chapter, we have discussed the approximation of the Helmholtz equation by representing the solutions as a superposition of plane waves, whose amplitude A in a particular direction can be expressed in terms of a wave energy density ρ. We introduced a boundary integral operator, that is a modified version of the Frobenius-Perron operator, which forms part of a phase-space boundary integral equation that can be solved for the energy density ρ on the boundary. The resulting boundary density can then be projected into the domain. We then applied a Petrov-Galerkin discretisation of the phase-space boundary integral equation, which is used to model the transport of wave energy densities along a finite set of global directions through phase-space. One advantage of this discretisation is that it reduces the arising four-dimensional integral to a single integral over a boundary element that is simple to calculate without needing to resort to numerical integration. The evaluation of the interior solution is then reduced to a finite sum over the global direction set.

Numerical experiments were undertaken for which we considered a line source travelling from the left edge of both a unit square and an L-shaped domain. We achieved machine accuracy in both domains when the source was travelling perpendicularly to the edge. The direction of the source was then changed to $\xi = -3\pi/8$, which resulted in small errors when the error was computed relative to subsequent solutions as we double the number of boundary elements, but we still obtained first order convergence. The errors were compared, coinciding with and above, the smallest number of directions when choosing the number of global directions such that the angle ξ was included within the direction set. Once $\xi = -3\pi/8$ was included within the direction set, increasing the number of directions further had no effect on the error. We then considered experiments when there was a point source inside a unit square, an L-shape and an irregular polygon shaped domain. We investigated the relative errors as we doubled the number of boundary elements and the number of directions and we achieved small errors in all cases as well as a convergence rate between first and second order.

Chapter 5

Hybrid methods for the wave equation

In this chapter, we solve the two-dimensional wave equation via two newly proposed hybrid methods. These hybrid methods employ a convolution quadrature method for the time discretisation, which leads to a system of $\widetilde{N}$ Helmholtz problems with complex wavenumbers, in the frequency domain. For a range of wavenumbers that will be considered low frequency content, the Helmholtz problems will be solved numerically using a piecewise constant collocation BEM for the spatial discretisation, as discussed in Chapter 3. For a range of wavenumbers that will be considered as the high frequency content, the Helmholtz problems will be replaced by one of two alternative high frequency approximations. The first of these high frequency approximations will be based on a plane-wave approximation for which the amplitudes are approximated via DEA with a Petrov-Galerkin discretization, as discussed in Chapter 4. The phase terms will then be approximated by matching the solutions calculated via BEM and an expression for the plane-wave approximation, as discussed in more detail in Section 5.3.2. The second high frequency approximation that we propose is to use an incident illumination approximation where only the direct contribution of the source term on the boundary is considered, and reflected contributions are assumed to play an insignificant role. Numerical experiments are then performed investigating both hybrid methods for the cases when the wave problems are driven by either a plane wave travelling into the domain or a point source inside the domain. Error and convergence rates will be explored as well as investigat-

ing the importance of the choice of frequency value where we switch between applying the BEM and a high frequency approximation.

5.1 Convolution quadrature for the wave equation: recap

Let $\Omega \subset \mathbb{R}^2$ be a finite domain with boundary $\Gamma = \partial\Omega$. We consider the Neumann IBVP for the inhomogeneous wave equation from Chapter 3:

$$\Delta\Phi - \frac{1}{c^2}\frac{\partial^2\Phi}{\partial t^2} = P(\boldsymbol{x}, t), \quad \text{in} \quad \Omega \times [0, T], \tag{5.1}$$

with initial conditions

$$\Phi(\cdot, 0) = \partial_t\Phi(\cdot, 0) = 0, \quad \text{in} \quad \Omega, \tag{5.2}$$

and Neumann boundary condition

$$\frac{\partial\Phi}{\partial\hat{\mathbf{n}}} = F \quad \text{on} \quad \Gamma \times (0, T], \tag{5.3}$$

for some $T > 0$. Here, we assume F and P are real-valued functions of space and time, $c > 0$ is the wave speed and $\hat{\mathbf{n}}$ is the unit outward normal to the boundary. As before, we will consider problems when internal wave sources described by P undergo reflections at rigid boundaries ($F \equiv 0$), or when $P \equiv 0$ and the boundary Γ corresponds to an interface with a vibrating structure that generates an inhomogeneous boundary condition F.

We consider solving the IBVP of the wave equation (5.1) when $P \equiv 0$ with initial conditions (5.2) together with an inhomogeneous boundary condition (5.3) by reformulating it as a direct boundary integral equation

$$\Phi(\boldsymbol{x}, t) = \left(\mathcal{S}\frac{\partial\Phi}{\partial\hat{\mathbf{n}}}\bigg|_\Gamma\right)(\boldsymbol{x}, t) - (\mathcal{D}\Phi|_\Gamma)(\boldsymbol{x}, t) \quad \text{in} \quad \Omega \times [0, T]. \tag{5.4}$$

Here $\mathcal{S}$ and $\mathcal{D}$ are given by (3.12) and (3.13), respectively. Moving (5.4) from the interior domain Ω to the boundary Γ, one then obtains the following direct time-domain boundary integral equation

$$\left(\frac{1}{2}I + \mathcal{K}\right)\Phi(\boldsymbol{x}, t) = \left(\mathcal{V}\frac{\partial\Phi}{\partial\hat{\mathbf{n}}}\bigg|_\Gamma\right)(\boldsymbol{x}, t) \quad \text{on} \quad \Gamma \times [0, T]. \tag{5.5}$$

Here $\mathcal{V}$ and $\mathcal{K}$ are the traces of $\mathcal{S}$ and $\mathcal{D}$ on to Γ, that are given by (3.14) and (3.15), respectively. Following the same steps as in Chapter 3, we employ the BDF2 time-stepping CQ method for the semi-discretisation in time of the BIE (5.5). The result is a system of boundary integral equations for the Helmholtz equation given by

$$\frac{1}{2}u_l(\boldsymbol{x}) + \left(\widetilde{\mathcal{K}}(\zeta_l)u_l\right)(\boldsymbol{x}) = \left(\widetilde{\mathcal{V}}(\zeta_l)\widetilde{F}_l\right)(\boldsymbol{x}), \quad \boldsymbol{x} \in \Gamma, \tag{5.6}$$

where

$$u_l = \sum_{n=0}^{N-1} \Phi_n^{\lambda} \lambda^n e^{-2\pi i l n/\widetilde{N}}, \quad \widetilde{F}_l = \sum_{n=0}^{N-1} F(\cdot, t_n)\lambda^n e^{-2\pi i l n/\widetilde{N}},$$

are the Z-transforms of $\Phi^{\Delta t,\lambda}$ and F respectively, and $\Phi_n^{\lambda} = \Phi^{\Delta t,\lambda}(\cdot, n\Delta t)$ denotes the solution of (5.5) after it has been semi-discretised in time using CQ - see (3.31). In addition, $\widetilde{V}(\zeta_l)$ and $\widetilde{K}(\zeta_l)$ are the single and double layer boundary integral operators (3.23) and (3.24), respectively. The index l runs over a set of complex wavenumbers $k_l = \zeta_l/c$ for $l = 0, 1, ..., \widetilde{N} - 1$, as shown in Figure 3.1. In the numerical experiments we consider in this chapter, we choose the number of time-steps to typically be $N = \widetilde{N}/2$, where $\widetilde{N}$ are the number of frequencies. Here, we allow the choice of N and $\widetilde{N}$ to be independent, as before, in order to potentially over-resolve in the Laplace domain for better accuracy as proposed in [26, 120].

Once we have computed the Helmholtz solutions u_l for $l = 0, 1, ..., \widetilde{N} - 1$, the discrete solution to the wave equation Φ_l can then be approximated via a trapezoidal rule for the inverse Z-transform given by (3.35). The interior solution is also calculated by applying the same time and spatial discretisation to (5.4). The Laplace domain interior solution u, at any point $\boldsymbol{x}$ inside the domain is given by (3.36). An analogous inverse transform is used to calculate the interior solution $\Phi(\boldsymbol{x}, t)$ from $u(\boldsymbol{x})$ via the transform given by (3.37).

In the next section we briefly describe the spatial discretisation of these Helmholtz problems via the BEM as discussed previously in Section 3.3, as well as discussing the use of a high-frequency approximation for cases when $\mathrm{Re}(k_l)$ is large relative to a typical length scale of the domain Ω.

5.2 Hybrid methods framework

For the spatial discretisation we either employ a piecewise constant collocation BEM to (5.6) as shown previously in Section 3.3 for the low frequency approximation, or for the high frequency region (to be specified in terms of $\mathrm{Re}(k_l)$), we employ a high-frequency approximation (HFA). We specify a threshold k^* for which we employ the BEM when $|\mathrm{Re}(k_l)| \leq k^*$ and let $\eta \leq \widetilde{N}/2$ be the minimal integer valued index of the minimal $|\mathrm{Re}(k_l)| > k^*$, which is the region for which we apply the high frequency approximation - see Figure 5.1. We note that the indexing $l = 0, 1, ..., \widetilde{N} - 1$ starts from $\mathrm{Re}(k_0) = 0$ at the bottom of the loop and runs clockwise. Therefore we specify the location of the wavenumber k_η to be within the lower left quarter of the loop of possible k_l values. As before in Section 3.2, we are only required to solve $\widetilde{N}/2 + 1$ Helmholtz problems since the wavenumbers k_l, $l = 0, 1, ..., \widetilde{N} - 1$ occur in symmetric pairs of the form $k_l = \pm\mathrm{Re}(k_l) + i\mathrm{Im}(k_l)$, for $l = 0, 1, ..., \widetilde{N}/2$.

The first HFA will be provided by a plane-wave approximation in which the plane-wave amplitudes are determined using the DEA method described in Chapter 4. The phases are constructed by performing a matching of the high frequency approximation with the BEM results at the highest frequencies for which the BEM is applied, as discussed later in Section 5.3.2. The second HFA we consider is an incident illumination approximation where only the direct contribution of the source term on the boundary is included and reflected contributions are assumed to play an insignificant role. This approximation therefore relies on there being sufficient decay before any reflections occur. For wavenumbers which have a very large imaginary part, we expect that the incident illumination approximation will be a reasonable approach since the magnitude of $\mathrm{Im}(k_l)$ determines the decay rate of the plane waves as they propagate. The DEA numerical approach will be able to go beyond the incident illumination model in terms of the reflection order, but will introduce additional sources of error due to the numerical discretisation procedures.

At low frequencies, we employ a piecewise constant collocation boundary element method as discussed in Sections 2.4 and 3.3, in which we divide the boundary Γ into M subintervals (or elements) E_m of approximately equal size. Recall that approximating the solution with piecewise constants b_m, $m = 1, 2, ..., M$

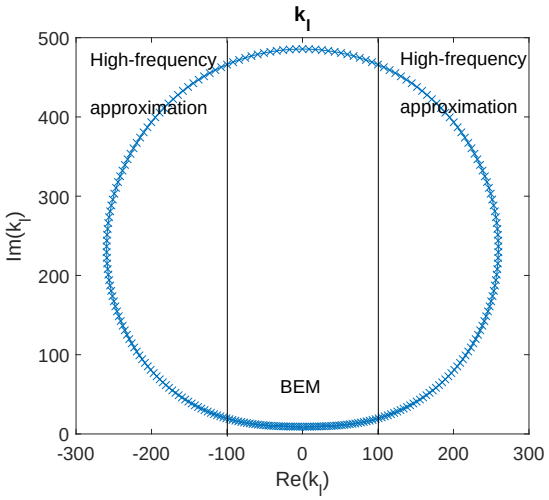

Figure 5.1: Example of a hybrid method implementation with the threshold $k^* = 100$ chosen to be the wavenumber where the method switches from the BEM to a high frequency approximation.

(2.29) via (3.33) leads to the system of equations

$$\frac{1}{2}\sum_{m=1}^{M} u_{l,m} b_m(\boldsymbol{x}_i) + \sum_{m=1}^{M} u_{l,m}\left(\widetilde{\mathcal{K}}(\zeta_l) b_m\right)(\boldsymbol{x}_i) = \sum_{m=1}^{M} \widetilde{F}_{l,m}\left(\widetilde{V}(\zeta_l) b_m\right)(\boldsymbol{x}_i), \quad (5.7)$$

for $\{l = 0, 1, ..., \widetilde{N}/2 : |\mathrm{Re}(k_l)| \leq k^*\}$, where $\boldsymbol{x}_i$, $i = 1, 2, ..., M$ are the collocation points. The collocation point $\boldsymbol{x}_i$ is chosen to be at the centre of the corresponding boundary element E_i.

In the following section, we discuss how the transformed boundary solution $u_{l,m}$ in the high frequency region can be calculated using the two HFAs discussed above.

5.3 High frequency approximations

We consider two high frequency approximations for solving the set of Helmholtz problems (5.6) for $\{l = 0, 1, ..., \widetilde{N}/2 : |\mathrm{Re}(k_l)| > k^*\}$. Firstly we recall that the solution to the Helmholtz equation (2.2) at high frequencies may be well

described as a plane-wave superposition solution of the form

$$u(\boldsymbol{x}) = \sum_{\kappa=1}^{R} A_\kappa(\boldsymbol{x}, \omega) e^{i\omega S_\kappa(\boldsymbol{x})}, \tag{5.8}$$

where $\omega = \mathrm{Re}(ck)$. The amplitude terms A_κ are approximated using DEA as described in Chapter 4, by making use of the following relationship between the stationary phase-space density ρ and the phases S_κ via

$$\rho(\boldsymbol{x}, \boldsymbol{p}) = \sum_{\kappa}^{R} A_\kappa^2(\boldsymbol{x}, \omega) \delta(\boldsymbol{p} - \nabla S_\kappa(\boldsymbol{x})), \tag{5.9}$$

see also (4.8) for the equivalent statement in the time-dependent case. Here $\boldsymbol{p} \in \mathbb{R}^2$ is the momentum vector that satisfies $|\boldsymbol{p}| = c^{-1}$. For a plane wave that has direction relative to the x_1 axis defined by the angle Θ, then $c\boldsymbol{p} = (\cos(\Theta), \sin(\Theta))$. Therefore the phase-space density ρ is equal to the superposition of squares of the amplitudes A_κ corresponding to rays travelling in directions defined by S_κ. The approximation of the phase terms S_κ in our plane-wave superposition solution (5.8) will be calculated by setting the solution calculated via the BEM (3.33) equal to the expression (5.8) at $l = \eta - 1$ and $l = \eta$, in which the amplitude terms have been determined from DEA, and the phase terms are the only unknowns in the expression to be determined. The calculation of the phase terms S_κ will be described in more detail in Section 5.3.2.

5.3.1 DEA approximation of the amplitudes

In this section, we briefly recall the DEA method from Chapter 4 and give an overview of the approach in terms of its implementation within a hybrid method. We define the phase-space coordinates $\boldsymbol{X} = (s, p)$ on the boundary of Ω, where s is the arclength parameter along the boundary Γ and p denotes the component of the momentum vector that is tangential to Γ at s. The phase-space densities are transported through Ω using a modified form of the FP operator (4.9), written as a boundary integral operator $\mathcal{B}$, which describes the transport of a density ρ from the phase-space on the boundary Γ to the next boundary intersection with Γ via

$$\mathcal{B}[\rho](\boldsymbol{X}) := \int w(\boldsymbol{Y}) \delta(\boldsymbol{X} - \phi(\boldsymbol{Y})) \rho(\boldsymbol{Y}) d\boldsymbol{Y}. \tag{5.10}$$

Here the map ϕ is the boundary map for Γ that transports a phase-space boundary coordinate $\boldsymbol{Y} = (s', p')$ along a ray path starting from the position specified by s' and travelling in the direction specified by p' until reaching Γ. The boundary map $\phi(\boldsymbol{Y}) = (\phi_s(\boldsymbol{Y}), \phi_p(\boldsymbol{Y}))$ has position $\phi_s(\boldsymbol{Y})$, which is determined from the intersection of the ray with the boundary and has tangential slowness $\phi_p(\boldsymbol{Y})$ corresponding to a specular reflection of the incoming ray once it reaches the boundary. The term w is a weighting factor containing a damping term and is defined as

$$w(\boldsymbol{Y}) = e^{-2\mathrm{Im}(k_l)D(\phi(\boldsymbol{Y}),\boldsymbol{Y})}, \tag{5.11}$$

where $D(\phi(\boldsymbol{Y}), \boldsymbol{Y})$ represents the Euclidean distance between $\phi_s(\boldsymbol{Y})$ and s' on Γ.

The stationary boundary density ρ resulting from an initial boundary density ρ_0 is given via

$$\rho = \sum_{n=0}^{\infty} \mathcal{B}^n[\rho_0] = (I - \mathcal{B})^{-1}[\rho_0], \tag{5.12}$$

where $\mathcal{B}^n$ denotes n iterates of the operator $\mathcal{B}$. The initial density term ρ_0 is related to the amplitude of the prescribed boundary condition $\widetilde{F}_l$ for the frequency domain Helmholtz problem - see (5.6). The details of this relation are given in Section 5.4 for each of the numerical examples considered.

As in Chapter 4, we approximate the density ρ by solving a finite dimensional approximation of (5.12). We implement the Petrov-Galerkin discretisation scheme detailed in Section 4.3, meaning that the spatial approximation by piecewise constant basis functions is consistent with that applied for the BEM at low frequencies. We divide the boundary Γ into elements E_m for $m = 1, 2, ..., M$ and define a set of global ray directions $\Theta_\beta \in [0, 2\pi)$, where $\beta = 1, 2, ..., \Lambda$, defined anticlockwise relative to the positive x_1-axis. Here we choose $\Theta_\beta = 2\pi(\beta - 1)/\Lambda$. Furthermore, we set up the subdivision such that E_m does not extend over any of the vertices of the polygon Γ. We now define $\theta_\kappa(s) \in (-\pi/2, \pi/2)$, $\kappa = 1, 2, ..., R_m$ to be the local ray directions at $s \in E_m$, for any $m = 1, 2, ..., M$. The local directions correspond to the subset of the global directions that are directed into Ω at s and have been re-labelled according to the angle they make with the interior normal vector at s as described in Section 4.3 and depicted in Figure 4.2. We approximate the stationary density

ρ on $\Gamma \times (-c^{-1}, c^{-1})$ using a finite dimensional approximation of the form

$$\rho(s,p) \approx \sum_{m=1}^{M} \sum_{\kappa=1}^{R_m} \rho_{(m,\kappa)} \widehat{b}_m(s) \delta\left(p - \widetilde{p}_\kappa(s)\right), \tag{5.13}$$

where $\widetilde{p}_\kappa(s) = \sin\left(\theta_\kappa(s)\right)/c$ and $\widehat{b}_m$ defines an orthonormal basis of piecewise constant functions (4.26) with respect to the standard L^2 inner product, $\int_{E_m} (\widehat{b}_m(s))^2 ds = 1$. As detailed in Section 4.3, for the momentum variable we choose a set of test functions that are orthogonal in the L^2 inner product to $\delta(p - \widetilde{p}_\kappa(s))$ for $\kappa = 1, 2, ..., R_m$. The test functions are the set of characteristic functions χ_κ given by (4.27), satisfying (4.28) as described in Section 4.3.

A Petrov-Galerkin projection of the operator $\mathcal{B}$ (5.10) on to the basis and test function combination described in Section 4.3 and summarised above leads to a matrix B defined by

$$\begin{aligned} B_{I,J} &= \int_\Gamma \int_{-c^{-1}}^{c^{-1}} w(\boldsymbol{Y}) \widehat{b}_{m'}(s') \widehat{b}_m(\phi_s(\boldsymbol{Y})) \delta(p' - \widetilde{p}_{\kappa'}(s')) \chi_\kappa(\phi_p(\boldsymbol{Y})) d\boldsymbol{Y}, \\ &= \int_\Gamma w(s', \widetilde{p}_{\kappa'}(s')) \widehat{b}_{m'}(s') \widehat{b}_m(\phi_s(s', \widetilde{p}_{\kappa'}(s'))) \chi_\kappa(\phi_p(s', \widetilde{p}_{\kappa'}(s'))) ds', \\ &= \frac{1}{|E_{m'}|^{1/2}} \int_{E_{m'}} w(s', \widetilde{p}_{\kappa'}(s')) \widehat{b}_m(\phi_s(s', \widetilde{p}_{\kappa'}(s'))) \chi_\kappa(\phi_p(s', \widetilde{p}_{\kappa'}(s'))) ds', \end{aligned} \tag{5.14}$$

where $I = (m, \kappa)$ and $J = (m', \kappa')$. Therefore the two-dimensional integral in (5.14) (that has already been simplified from a four-dimensional integral of the form (4.29)) has been reduced to a single integral over the boundary element $E_{m'} \subset \Gamma$ due to the spatial basis and the properties of the Dirac δ distributions arising in equations (5.10) and (5.13). The calculation when the matrix elements are non-zero only involves the integral of the exponential term (5.11) over the element $E_{m'}$ with a multiplication of the pre-factor $(|E_m||E_{m'}|)^{-1/2}$.

The coefficients of the expansion (5.13) can be found by solving the linear system $\boldsymbol{\rho} = (I - B)^{-1} \boldsymbol{\rho}_0$, which corresponds to the discretised form of equation (5.12). Here $\boldsymbol{\rho}_0$ and $\boldsymbol{\rho}$ represent the coefficients of the expansions of ρ_0 and ρ, respectively, when projected onto the finite dimensional basis. Note that the invertibility of $I - B$ is a consequence of the fact that for A-stable CQ time discretisations, we have $\mathrm{Im}(k_l) > 0$ for all $l = 0, 1, ..., \widetilde{N} - 1$ and hence the damping term (5.11) will ensure that the leading eigenvalue of the matrix B is smaller than 1 in absolute value. The entries of the source vector $\boldsymbol{\rho}_0$

corresponding to an initial density ρ_0 are given using the property (4.28) and orthonormality of the spatial basis via

$$\begin{aligned}[\boldsymbol{\rho}_0]_J &= \int_\Gamma \int_{-c^{-1}}^{c^{-1}} \rho_0(s,p)\widehat{b}_m(s)\chi_\kappa(p)d\boldsymbol{X}, \\ &= \frac{1}{|E_m|^{1/2}} \int_{E_m} \int_{I_\kappa} \rho_0(s,p)dpds,\end{aligned} \tag{5.15}$$

where I_κ are a set of subintervals that satisfy $\cup_{\kappa=1}^{R_m} I_\kappa = (-\pi/2, \pi/2)$ for $\kappa = 1, 2, ..., R_m$ as discussed in Section 4.3.

5.3.2 Wave matching approximation of the phase terms

We now discuss how to determine the phase terms S_κ in (5.8), given that the amplitudes A_κ for each direction κ have been found by combining (5.9) and (5.12), and choosing the directions in the sum over κ in (5.9) to correspond to those of the discretisation represented in (5.13). A new methodology is required to determine the unknown phase terms S_κ. We propose a method that reconstructs the phase terms from a full wave solution calculated via BEM at the maximal frequency before we switch to the high frequency formulation and also at the lowest frequency at which we apply the high frequency formulation. These frequency values are denoted $\omega_{\eta-1} = \mathrm{Re}(ck_{\eta-1})$ and $\omega_\eta = \mathrm{Re}(ck_\eta)$, respectively. We apply both the BEM and DEA to obtain a set of equations of the form

$$u_l(\boldsymbol{x}) = \sum_{\kappa=1}^{R} A_\kappa(\boldsymbol{x}, \omega_l) e^{i\omega_l(\sin(\theta_\kappa)s/c + \gamma_\kappa^l)}, \tag{5.16}$$

for $l = \eta - 1$ and also for $l = \eta$. The left hand side of (5.16) is provided by the solutions calculated from the BEM and $\boldsymbol{x} \in \Gamma$ are the Cartesian coordinates corresponding to the arclength value s.

Before proceeding any further, we now discuss the representation of the phase terms in (5.16) as the linear function $S_\kappa(\boldsymbol{x}) = \sin(\theta_\kappa)s/c + \gamma_\kappa^l$. This stems from the fact that the wave speed c is assumed to be constant. We reintroduce from Section 4.2 a position vector $\boldsymbol{x}_\Gamma = (x_\parallel, x_\perp)$ such that along the boundary Γ, $x_\parallel = s$ and $x_\perp = 0$ correspond to the position parallel and perpendicular to the boundary, respectively. We further recall the local momentum vector $\boldsymbol{p}_\Gamma = (p_\parallel, p_\perp)$, where $p_\parallel = p = \sin(\theta)/c$ is the component parallel to the boundary and $p_\perp = \cos(\theta)/c$ is perpendicular to the boundary, where θ is the angle formed

between the ray direction and the inward normal vector to Γ at s. The phase term $\delta(\boldsymbol{p} - \nabla S_\kappa(\boldsymbol{x}))$ from (5.9) can then be rewritten as

$$\delta(\boldsymbol{p}_\Gamma - \nabla S_\kappa(\boldsymbol{x}_\Gamma)) = \delta\left(p_\parallel - \frac{\partial S_\kappa}{\partial x_\parallel}\right)\delta\left(p_\perp - \frac{\partial S_\kappa}{\partial x_\perp}\right). \tag{5.17}$$

Substituting (5.17) into (5.9), the delta generalised functions specify that the phase-space density ρ is non-zero when $\frac{\partial S_\kappa}{\partial x_\parallel} = p_\parallel$ and $\frac{\partial S_\kappa}{\partial x_\perp} = p_\perp$, and so ∇S_κ is independent of $\boldsymbol{x}_\Gamma$. In general, after integration, we obtain the following expression for the phase term S_κ:

$$\begin{aligned} S_\kappa(\boldsymbol{x}_\Gamma) &= p_\parallel x_\parallel + p_\perp x_\perp + \gamma_\kappa^l, \\ &= \frac{\sin(\theta_\kappa)}{c} s + \gamma_\kappa^l, \end{aligned} \tag{5.18}$$

on the boundary Γ. The constants γ_κ^l, $\kappa = 1, 2, ..., R$, $l = \eta$, $\eta + 1$ are the unknowns to be determined by imposing (5.16) at a set of points s on Γ. The variables θ_κ, $\kappa = 1, 2, ..., R$ are the local angles with respect to the unit normal introduced in the previous section. To calculate the undetermined constants γ_κ^l we calculate the solutions to the Helmholtz problems using the BEM at the frequencies $\omega_{\eta-1}$ and ω_η, which correspond to a pair of frequencies where we switch from using the BEM in the low frequency region to using DEA in the high frequency region. The choice of $\omega_{\eta-1}$ and ω_η will be studied numerically later on.

The phase reconstruction procedure must be performed at more than one frequency due to the non-uniqueness of the phase solution at a single frequency owing to the periodicity of the plane waves. The phase terms at $\omega_{\eta-1}$ and ω_η may then be related via

$$\gamma_\kappa^{\eta-1} + \frac{\sin(\theta_\kappa)s}{c} + \frac{2\pi\nu}{\omega_{\eta-1}} = \gamma_\kappa^\eta + \frac{\sin(\theta_\kappa)s}{c} + \frac{2\pi\nu}{\omega_\eta}. \tag{5.19}$$

Solving (5.19) for $\nu \in \mathbb{Z}$ allows us to recover a unique set of phase constants γ_κ via

$$\gamma_\kappa = \gamma_\kappa^l + \frac{2\pi\nu}{\omega_l}, \tag{5.20}$$

for either $l = \eta - 1$ or $l = \eta$. Once γ_κ are known we calculate the solutions to the Helmholtz problems using (5.16) for all frequencies with absolute value larger than $|\omega_{\eta-1}|$.

The calculation of $\gamma_\kappa^{\eta-1}$ (and γ_κ^η) will be dependent on the numerical exam-

ple we are considering. In our numerical examples we only consider polygonal domains and therefore the values for γ_κ^η will need to be calculated for each edge separately since each edge will have a different subset of the global directions Θ_β, $\beta = 1, 2, ..., \Lambda$, associated to it and hence the γ_κ^η values will be different on each edge. We generate a system of M equations of the form (5.16) by choosing $\boldsymbol{x} = \boldsymbol{x}_i$ for $i = 1, 2, ..., M$ as the collocation points from the BEM approximation in (5.16). The next task is to determine how many of the amplitudes A_κ are non-zero at every collocation point $\boldsymbol{x}_i$ on a given edge, since this provides a reduction in the number of phase constants γ_κ^l that we need to recover. The system of equations (5.16) can then be solved as a linear system

$$u_l(\boldsymbol{x}_i) = \sum_{\kappa=1}^{R} A_\kappa(\boldsymbol{x}_i, \omega_l) e^{i\omega_l(\sin(\theta_l)s_i/c)} v_\kappa^l, \tag{5.21}$$

for $i = 1, 2, ..., M$, $l = \eta - 1$ or $l = \eta$ and where s_i is the arc-length parameter for the point $\boldsymbol{x}_i$. The unknowns $v_\kappa^l = e^{i\omega_l \gamma_\kappa^l}$ may be determined using the Moore-Penrose pseudo-inverse to obtain the least squares solution. Once each v_κ^l term has been found, one can directly calculate the phase constants via $\gamma_\kappa^l = -i \log(v_\kappa^l)/\omega_l$.

To summarise this new methodology described above, the following is a list of steps on how to implement it.

1. The new methodology requires us to solve (5.21) for the unknown coefficients γ_κ, that arise due to the reconstruction of the phase information S_κ as a linear function. This is solved at two frequencies denoted $\omega_{\eta-1} = \mathrm{Re}(ck_{\eta-1})$ and $\omega_\eta = \mathrm{Re}(ck_\eta)$, whereby ω_η is the maximal frequency before we switch from using the BEM to the HFA.

2. We calculate the left hand side term of equation (5.21) $u_l(\boldsymbol{x}_i)$ via the BEM, at the collocation points $\boldsymbol{x}_i$, for $i = 1, 2, ..., M$, for $\omega_{\eta-1}$ and ω_η.

3. Next we must determine the amplitudes A_κ. The amplitudes are computed via (5.9) where ρ is calculated by applying DEA on the Helmholtz equation at $\omega_{\eta-1}$ and ω_η, at both at every collocation point $\boldsymbol{x}_i$ on a given edge, as described in Section 5.3.1.

4. Then we solve (5.21) for v_κ^l for either $l = \eta$ or $l = \eta - 1$. Once each v_κ^l term has been found, we directly calculate the phase constants via $\gamma_\kappa^l = -i \log(v_\kappa^l)/\omega_l$.

5. Due to the non-uniqueness of the phase solution we then find γ_κ via (5.20) where ν is found by rearranging (5.19) as

$$\nu == \frac{\omega_{\eta-1}\omega_\eta(\gamma_\kappa^\eta - \gamma_\kappa^{\eta-1})}{2\pi(\omega_\eta - \omega_{\eta-1})}.$$

5.3.3 Simple high frequency approximation

In this section, we describe a simple high-frequency approximation [SHFA] based on the observation that the wavenumbers k_l in the high frequency range typically have large imaginary part. The dissipative factor (5.11) appearing in the operator $\mathcal{B}$ will then damp out all contributions except those from very short ray trajectories, meaning that the approximation $\rho \approx \rho_0$ will be reasonably good. In this case there is no need to perform any DEA calculations and the solution for a wavenumber k_l with a large enough imaginary part can be approximated by simply rescaling the Z-transformed boundary data $\widetilde{F}_l$. In particular we set

$$u_l(\boldsymbol{x}) = \frac{\widetilde{F}_l(\boldsymbol{x})}{ik_l \cos(\theta_0(\boldsymbol{x}))}, \tag{5.22}$$

where $\theta_0(\boldsymbol{x})$ defines the direction of the source term at $\boldsymbol{x} \in \Gamma$ relative to the normal direction. For example, for a point source from $\boldsymbol{x}_0 \in \Omega$, then

$$\cos(\theta_0(\boldsymbol{x})) = \frac{\hat{\mathbf{n}} \cdot (\boldsymbol{x} - \boldsymbol{x}_0)}{\|\boldsymbol{x} - \boldsymbol{x}_0\|}.$$

For a boundary value problem with boundary data related to a plane wave entering the domain from one or more edges, then the angle θ_0 can be found directly from the plane wave direction.

In the next section, we will present numerical results produced using the hybrid methods described above for both the interior and the boundary solutions in a variety of different examples.

5.4 Numerical results

In this section, we consider numerically solving the wave equation (5.1) with Neumann boundary conditions (5.3) via the two hybrid methods introduced in this chapter. We first consider an inhomogeneous Neumann IBVP for the cases when Ω is a unit square or an L-shaped domain and the boundary data

corresponds to a plane wave travelling into the domain. We also later consider the case when there is a point source inside either a square domain or an irregular polygon domain. We now present a step-by-step guide of how to implement the hybrid methods to determine the interior solution of the wave equation.

1. To begin, we divide the boundary Γ into M boundary elements E_m of approximately equal size and split the time interval $[0, T]$ into N steps of equal length $\Delta t = T/N$. We then chose the number of frequencies $\widetilde{N}$, in the numerical results we investigate the affect of potentially over-resolve in the Laplace domain for better accuracy by allowing the choice of N and $\widetilde{N}$ to be independent Therefore we typically choose $\widetilde{N} = 2N$.

2. We then choose the cut-off frequency k^* at which we switch from the BEM to a high frequency approximation. For the frequencies evaluated via the BEM, the choice for the the number of boundary elements should be chosen such that there is a good level of accuracy up to the BEM cut-off frequency. This follows on the rule of thumb described earlier in Section 3.4 in which at least six boundary elements per wavelength as discussed by [129].

3. We then calculate the wavenumbers $k_l = \zeta_l i$ for $l = 0, 1, ..., \widetilde{N} - 1$, where $\zeta_l =$ are calculated via the BDF2 time-stepping method.

4. Next we calculate the transformed Neumann boundary data $\widetilde{F}_l$ to be implemented into the CQBEM solutions for where the coefficients $\widetilde{F}_{l,m}$ are determined via

$$\widetilde{F}_{l,m} = \widetilde{F}_l(\boldsymbol{x}_m) \sum_{n=0}^{N-1} F(\boldsymbol{x}_m, t_n) \lambda^n e^{-2\pi i l n/\widetilde{N}}.$$

5. For the low frequency region we employ a piecewise constant collcoation BEM in order to determine the transformed boundary solution $u_{l,m}$ for $\{l = 0, 1, ..., \widetilde{N}/2 : |\mathrm{Re}(k_l)| \leq k^*\}$, for $m = 1, 2, ..., M$. This requires to solve the system of equations of the form (5.7) where b_m, $m = 1, 2, ..., M$ are the piecewise constant basis functions given by(2.29) and $\boldsymbol{x}_i$, $i = 1, 2, ..., M$ are the collocation points. The functions $\left(\widetilde{\mathcal{V}}(\zeta_l) b_m\right)$ and $\left(\widetilde{\mathcal{K}}(\zeta_l) b_m\right)$ are defined by (3.23) and (3.24), respectively.

6. Next we solve the set of Helmholtz problems (5.6) in the high frequency

region via either the DEA or the SHFA for the high frequency approximation .

(a) To employ the SHFA one must simply approximate equation (5.22) for $\{l = 0, 1, ..., \widetilde{N}/2 : |\mathrm{Re}(k_l)| > k^*\}$ where $\widetilde{F}_l$ is approximated as before.

(b) For the DEA approximation for the high frequency approximation, we must first reformulate the boundary data F_l in to terms of a source term ρ such that it can be input into the calculation of DEA approximation. The reformulation of the boundary data is described in more detail for each problem we consider. Next, we must calculate the unknown constants γ as part of the wave matching approximation of the hybrid method in equation (5.16) as described in Section 5.3.2. Once γ has been calculated the boundary solution is calculated via (5.16), where the amplitudes A_κ are provided by the DEA approximation described in Section 5.3.1.

7. Once the boundary solution u_l has been computed for all wavenumbers. The boundary solution to the wave equation in the time domain is found via the inverse transform given by (3.35).

8. The interior solution in the Laplace domain $u_l(\boldsymbol{x})$ can then be calculated via (3.36), where $\boldsymbol{x}$ is any point inside the domain Ω. Note that u_l in equation (3.36) is the boundary solution calculated in (3.33) and (3.34). The interior solution to the wave equation in the time domain $\Phi(\boldsymbol{x}, t)$ at $\boldsymbol{x} \in \Omega$ is then approximated via the inverse transform to (3.35).

The MATLAB code for these examples are available from the following URL: https://github.com/JacobRowbottom/CQBEM-HYBRID.

5.4.1 Plane wave boundary data

We consider the results of applying the two hybrid methods to the homogeneous wave equation (5.1), when $P = 0$, with Neumann boundary condition (5.3) for the case when Ω is either a unit square or an L-shaped domain, as depicted in

Figure 5.2. We define our Neumann boundary condition (5.3) to be

$$F(\boldsymbol{x},t)=\begin{cases} W(x_2\sin(\Theta_0)-ct) & \text{if } x_1=0,\\ W(x_1\cos(\Theta_0)-ct) & \text{if } x_2=0 \text{ and } \Theta_0>0,\\ 0 & \text{otherwise,}\end{cases} \tag{5.23}$$

where $\Theta_0 \in [0,\pi/2)$ is a direction relative to the positive x_1 axis. Here $\boldsymbol{x} = (x_1,x_2)$ and the angle Θ_0 is in general distinct from the global direction set Θ_β, $\beta = 1,2,...,\Lambda$. However, for accuracy reasons, we choose Θ_0 to correspond to one of the global directions. The choice of the global direction set can be made in a problem specific manner, and therefore this choice does not indicate a limitation of the method. We consider the case when the function W takes the form of the normal derivative of a Gaussian pulse written as

$$W(x) = -\alpha(x+ct_0)(n_1\cos(\Theta_0)+n_2\sin(\Theta_0))e^{-\alpha(x+ct_0)^2}, \tag{5.24}$$

for $x \in \mathbb{R}$ and where $\hat{\mathbf{n}} = (n_1,n_2)$ are the entries of the unit normal vector $\hat{\mathbf{n}}$. The parameters $t_0 > 0$ and $\alpha > 0$ control the position of the peak of the Gaussian pulse and its bandwidth, respectively. These parameters are chosen carefully to ensure that the initial conditions are approximately satisfied and the pulse has decayed sufficiently at $t = 0$. In this section we only consider regular geometric domains and directions Θ_0 for the boundary condition, as illustrated in Figure 5.2, such that we will only need to use $\Lambda = 8$ global directions in the DEA implementation in order to include all possible propagation directions.

We now discuss how the Neumann boundary condition is implemented in the DEA scheme by writing it in the form of the square modulus of a plane wave solution to the Helmholtz equation, which is then used to determine the initial density ρ_0. Here we will denote $\frac{\partial u_l}{\partial \hat{\mathbf{n}}} = \widetilde{F}_l$ as the Z-transform of F, where F is the Neumann boundary condition (5.23). Recall that the solution may be approximated (at high frequencies) as a plane-wave superposition of the form (5.8) as follows:

$$u_l(\boldsymbol{x}) \approx \sum_{\beta=1}^{R} A_\kappa(\boldsymbol{x},\omega_l)e^{i\omega_l(x_1\cos(\Theta_\beta)+x_2\sin(\Theta_\beta))/c}, \tag{5.25}$$

where $\boldsymbol{x} \in \Gamma$ and Θ_β are the global angles relative to the x_1 axis. Differentiating (5.25) with respect to the unit normal will either be with respect to x_1 if we

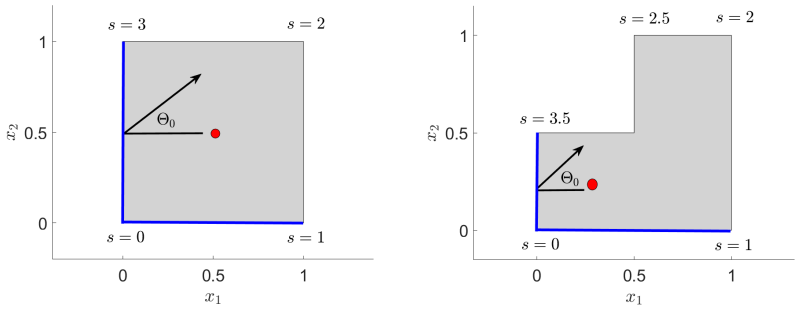

(a) Unit square domain

(b) L-shaped domain

Figure 5.2: The domains considered in the numerical experiments for solving the homogeneous wave equation (5.1), when $P = 0$, with Neumann boundary condition (5.23) showing the value of the boundary arclength s at each vertex, the propagation direction Θ_0 for the plane wave boundary data and the interior evaluation point as a red dot. The bold boundary lines indicate the positions where the plane wave may enter the domain and therefore provide the inhomogeneous boundary data.

differentiate along the left edge of the domain or with respect to x_2 if we consider differentiating along the bottom edge of the domain, as shown in Figure 5.2. By first considering differentiating (5.25) along the left edge with respect to x_1 and considering a boundary condition generated by a single plane wave ($R = 1$) travelling at an angle Θ_0, we obtain the following

$$\frac{\partial u_l}{\partial \hat{\mathbf{n}}}(\boldsymbol{x}) = ik_l \cos(\Theta_0) A(\boldsymbol{x}, \omega_l) e^{i\omega_l (x_1 \cos(\Theta_0) + x_2 \sin(\Theta_0))/c}. \tag{5.26}$$

Substituting the approximation of $u_l(\boldsymbol{x})$ from (5.25) into (5.26) gives

$$\frac{\partial u_l}{\partial \hat{\mathbf{n}}}(\boldsymbol{x}) = ik_l \cos(\Theta_0) u_l(\boldsymbol{x}). \tag{5.27}$$

Now rearranging (5.27) and taking the absolute value squared we obtain an expression for $|u_l(\boldsymbol{x})|^2$ follows as

$$|u_l(\boldsymbol{x})|^2 = \frac{\left|\frac{\partial u_l}{\partial \hat{\mathbf{n}}}(\boldsymbol{x})\right|^2}{|k_l|^2 |\cos(\Theta_0)|^2}. \tag{5.28}$$

An analogous procedure can be applied for the case when we differentiate (5.25)

with respect to x_2 along the bottom edge, which leads to

$$|u_l(\boldsymbol{x})|^2 = \frac{\left|\frac{\partial u_l}{\partial \hat{\mathbf{n}}}(\boldsymbol{x})\right|^2}{|k_l|^2|\sin(\Theta_0)|^2}. \tag{5.29}$$

We note that for the case when $\Theta_0 = 0$, this corresponds to the plane wave travelling from the left edge only and the boundary data along the bottom edge is assumed to be homogeneous. We may write $|u_l(\boldsymbol{x})|^2$ more concisely as follows

$$|u_l(\boldsymbol{x})|^2 = \begin{cases} \left|\frac{\partial u_l}{\partial \hat{\mathbf{n}}}(\boldsymbol{x})\right|^2 / \left(|k_l|^2|\cos(\Theta_0)|^2\right) & \text{if } x_1 = 0, \\ \left|\frac{\partial u_l}{\partial \hat{\mathbf{n}}}(\boldsymbol{x})\right|^2 / \left(|k_l|^2|\sin(\Theta_0)|^2\right) & \text{if } x_2 = 0 \text{ and } \Theta_0 > 0, \\ 0 & \text{otherwise.} \end{cases} \tag{5.30}$$

Note that here $\frac{\partial u_l}{\partial \hat{\mathbf{n}}} = \widetilde{F}_l$, for $\left\{l = 0, 1, ..., \widetilde{N}/2 : |\mathrm{Re}(k_l| > k^*\right\}$. The source term ρ_0 is then calculated via

$$\rho_0(s, p) = |u_l(\boldsymbol{x})|^2 \delta(p - p_0), \tag{5.31}$$

where $p_0 = \sin(\theta_0)/c$ and θ_0 is the local direction (corresponding to the global direction Θ_0) of the plane wave inducing the boundary data, relative to the normal vector to Γ at position s and, as before, s is the arclength representation of $\boldsymbol{x} \in \Gamma$.

Square domain

We now present the numerical results for the case when Ω is a unit square as shown in Figure 5.2 (a). For all cases in this section, we let the wave speed $c = 1$. We first investigate solving the IBVP for the case when $\alpha = 36$, $t_0 = 1$ and $\Theta_0 = 0$ in (5.24), such that we can perform an error analysis from the results and compare against the error results computed via CQBEM in Section 3.4.1. Note that the boundary data (5.23) is equivalent to (3.39) in the case $\Theta_0 = 0$ along the edge where $x_1 = 0$. The second part of the boundary data (3.39) propagates to the left away from Ω with an initial peak position at $x_1 = -ct_0$ and we always choose t_0 sufficiently large so that the boundary data is zero to machine precision throughout Ω at $t = t_0$. The error of the time-dependent

interior solution is calculated via

$$\text{Error}(N) = \sqrt{\frac{\sum_{n=0}^{N-1} \left(\Phi(\boldsymbol{x}, t_n) - \Phi_n(\boldsymbol{x})\right)^2}{\sum_{n=0}^{N-1} \left(\Phi(\boldsymbol{x}, t_n)\right)^2}}, \tag{5.32}$$

and the convergence rates are estimated by $\log_2(\text{Error}(N/2)/\text{Error}(N))$. We compare the numerical solution Φ_n against the exact solution $\Phi(\boldsymbol{x}, t_n)$ given by

$$\Phi(\boldsymbol{x}, t) = \frac{1}{2} e^{-\alpha(x_1 - c(t-t_0))^2} \tag{5.33}$$

for an infinite domain (in the x_1 - direction). We consider only early times such that we do not observe any reflections and the solution matches (5.33). Note also that (5.33) is equivalent to (3.40) if we omit the second left-propagating term in (3.40) that travels away from Ω and therefore has no effect on Φ for $\boldsymbol{x} \in \Omega$.

Figure 5.3 shows a comparison between the exact and numerical interior solutions $\Phi_n(\boldsymbol{x})$, $n = 0, 1, ..., N-1$ at $\boldsymbol{x} = (0.5, 0.5)$. We apply a high frequency approximation whenever $|\text{Re}(k_l)| > 80$ and apply $M = 512$ boundary elements to provide a good level of accuracy up to the BEM cut-off frequency. The plots compare the results of using the SHFA with the DEA based plane wave approximation up to $T = 2$, as well as computing the interior solution at all frequencies via the CQBEM approximation. These approximations were all compared with the exact solution for a total of $N = \widetilde{N} = 512$ time-steps. From this figure, we observe that all numerical solutions match the behaviour of the exact solution well by eye. Even with a large number of Helmholtz problems (237 of the 257 problems) being approximated via a high frequency method, the hybrid methods solutions match well for the case when α is reasonably low.

Table 5.1 shows the error results and convergence rates for the interior solution calculated via the DEA and SHFA based hybrid methods, in which the high frequency approximations are implemented whenever $|\text{Re}(k_l)| > 80$. The table shows that both hybrid methods have almost identical error results and convergence rates as well as achieving the desired second order convergence for BDF2 based CQ. In comparison to the error results and convergence rates calculated using CQBEM for all frequencies shown in Table 3.3, we can determine that the results from Table 5.1 are almost identical. Therefore for the low choice of α we can deduce that the hybrid methods can numerically solve this example accurately. We note that for the case when $N = 64$, the numerical solution was

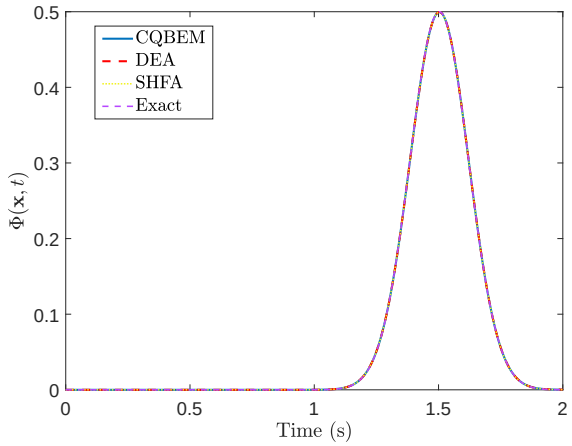

Figure 5.3: Interior solution to the wave equation at $\boldsymbol{x} = (0.5, 0.5)$ inside a unit square with boundary data (5.24) and parameters $\Theta_0 = 0$, $\alpha = 36$, $t_0 = 1$, with $M = 512$ boundary elements and $N = \widetilde{N} = 512$ time-steps. The high frequency approximations are applied whenever $|\mathrm{Re}(k_l)| > 80$.

computed fully via CQBEM, since $|\mathrm{Re}(k_l)| \leq 80$ for all $l = 0, 1, ..., \widetilde{N} - 1$ here.

			DEA		SHFA	
N	M	η	Error	EOC	Error	EOC
64	4	-	0.0681	-	0.0681	-
128	16	23	0.0121	2.49	0.0121	2.49
256	64	24	0.0018	2.75	0.0018	2.75
512	256	25	4.5863e-04	1.97	4.5454e-04	1.99
1024	1024	26	1.1835e-04	1.95	1.1836e-04	1.94

Table 5.1: Errors and convergence rates for the interior solution on the unit square domain observed at the point $\boldsymbol{x} = (0.5, 0.5)$ for the case when the boundary data are given by (5.24) with parameters $\Theta_0 = 0$, $\alpha = 36$, $t_0 = 1$ and $T = 2$. The interior solutions were calculated numerically using the DEA and SHFA based hybrid CQ schemes, whereby the high frequency approximations were applied whenever $|\mathrm{Re}(k_l)| > 80$.

We now investigate solving the IBVP for the case when $\alpha = 36$, $t_0 = 1$ and $\Theta_0 = \pi/4$ in (5.24). Figure 5.4 shows a comparison between the numerical interior solutions at the point $\boldsymbol{x} = (0.5, 0.5)$. We apply a high frequency approximation whenever $|\mathrm{Re}(k_l)| > 80$, with $N = \widetilde{N} = 512$ time-steps and $M = 512$ boundary elements. The plots compare the results of approximating

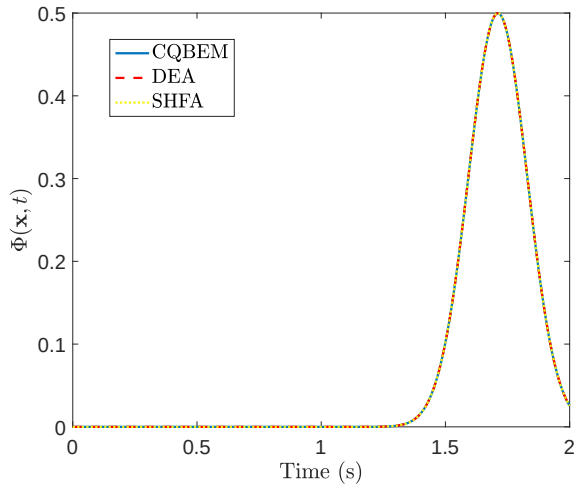

Figure 5.4: Interior solution to the wave equation at $\boldsymbol{x} = (0.5, 0.5)$ inside a unit square with boundary data (5.24) and parameters $\Theta_0 = \pi/4$, $\alpha = 36$, $t_0 = 1$, with $N = \widetilde{N} = 512$ time-steps and $M = 512$ boundary elements. The high frequency approximations are applied whenever $|\mathrm{Re}(k_l)| > 80$.

the high frequency Helmholtz solutions via either the DEA or SHFA approximations. Here we compare the numerical results against a numerical solution calculated using CQBEM. From this figure, we observe that all numerical solutions behave identically by eye. This is supported further by the error and convergence results in Table 5.2. The errors in Table 5.2 were computed using (5.32), but with subsequent interior solutions as we double the number of time-steps in place of the exact solution. From this table, we observe that both hybrid methods achieve similar error results that are eventually less than 1% error when $N = \widetilde{N} = M = 1024$, with the SHFA method obtaining a slightly smaller error. The convergence rates are larger than the expected second order convergence for the BDF2 based CQ, but we expect that as we increase the number of time-steps and boundary elements further, the rates will eventually converge to second order.

We now present the numerical results when $\alpha = 4096$, $t_0 = 0.1$ and $\Theta_0 = 0$ in (5.24), in order to obtain a broadband signal. For this example we can compare our numerical results against the exact solution given by (5.33) up to time $T = 1$, such that we do not observe any reflections.

Figure 5.5 shows a comparison between the exact and numerical interior

			DEA		SHFA	
N	M	η	Error	EOC	Error	EOC
64	4	-	-	-	-	-
128	16	23	1.1614	-	1.1614	-
256	64	24	0.1762	2.72	0.1762	2.72
512	256	25	0.0148	3.57	0.0148	3.41
1024	1024	26	0.0021	2.82	0.0018	3.04

Table 5.2: Errors and convergence rates for the interior solution on the unit square domain observed at the point $\boldsymbol{x} = (0.5, 0.5)$ for the case when the boundary data are given by (5.24) with parameters $\Theta_0 = \pi/4$, $\alpha = 36$, $t_0 = 1$ and $T = 2$. The interior solutions were calculated numerically using the DEA and SHFA based hybrid CQ schemes, whereby the high frequency approximations were applied whenever $|\mathrm{Re}(k_l)| > 80$.

solutions at $\boldsymbol{x} = (0.5, 0.5)$. We apply a high frequency approximation whenever $|\mathrm{Re}(k_l)| > 350$ and employ $M = 1024$ boundary elements to provide a good level of accuracy up to the BEM cut-off wavenumber $k^* = 350$. The plots compare the results of using the SHFA and the DEA based plane wave approximations with the exact solution up to $T = 1$, for $N = \widetilde{N}/2 = 4096$ time-steps. In this case both high frequency approximations produce identical looking results matching the exact solution. Figure 5.6 shows the solution along the boundary using both the DEA and SHFA high frequency approximations. We observe that the two solutions are visually identical over the entire boundary and the plots show the Gaussian pulse moving over the left edge of the square ($3 < s < 4$) at around $t = t_0 = 0.1$ and then travelling along the upper and lower edges.

Figure 5.8 shows the Z-transformed boundary solution u_l. The left sub-plot (a) shows the absolute value of u_l at $l = \eta$, where we switch from using the BEM and instead use one of the high frequency approximations. We compare the values calculated using the BEM to the solutions calculated using the high frequency approximations. We observe that the main differences between the three methods are along the upper ($2 < s < 3$) and lower ($0 < s < 1$) edges where the high frequency approximations give zero and the BEM does not. This is because the high frequency approximations of u_l omit waves tangential to the boundary. The right sub-plot (b) shows a zoomed in panel focusing on the values along the right edge ($1 < s < 2$). We notice that the difference between DEA and the SHFA is that the DEA approximation includes reflected wave contributions along the right edge, but the SHFA does not. We also

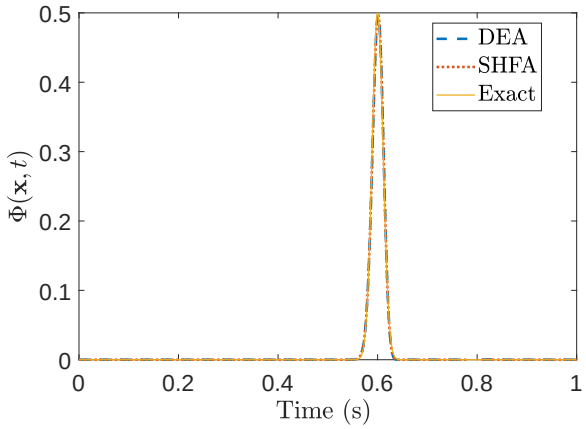

Figure 5.5: Interior solution to the wave equation at $\boldsymbol{x} = (0.5, 0.5)$ inside a unit square with boundary data (5.24) and parameters $\Theta_0 = 0$, $\alpha = 4096$, $t_0 = 0.1$, with $M = 1024$ boundary elements and $N = \widetilde{N}/2 = 4096$ time-steps. The high frequency approximations are applied whenever $|\mathrm{Re}(k_l)| > 350$.

notice that the BEM appears to be double that of the DEA approximation and oscillates more. This is due to the contributions of the diffracted waves being included in the BEM, but not in DEA. The bottom sub-plot (c) shows a plot of $\mathrm{Re}(u_l)$ computed using the DEA based approximation for $|\mathrm{Re}(k_l)| > 350$ for wavenumbers close to $\mathrm{Re}(k_l) = k^* = 350$. Along the top edge ($2 < s < 3$), the value of $\mathrm{Re}(u_l)$ jumps to zero when we switch from the BEM to the DEA approximation as would be expected from the upper left sub-plot (a). Along the rest of the boundary, the solutions from the two methods match up very well demonstrating the success of the phase reconstruction process outlined in Section 5.3.2.

Figure 5.7 shows the logarithm of the boundary data and the interior solution in the Fourier domain against k the wavenumber. The transformed boundary data $\widetilde{F}_l$ is approximated via $\widetilde{F}_l = \sum_{n=0}^{N-1} F(\cdot, t_n)\lambda^n e^{-2\pi i l n/\widetilde{N}}$ where F is given by (5.23) with $\alpha = 4096$, $t_0 = 0.1$ and $\Theta_0 = 0$. The interior solution was calculated using the DEA based hybrid CQ scheme, whereby the high frequency approximation was applied whenever $|\mathrm{Re}(k_l)| > 350$, for $\widetilde{N}/2 = N = 4096$, $M = 1024$. In this figure, we observe that the two solutions decay by a factor of 10^{-8} from their peak values at approximately $k = 680$ for the driving force and approximately $k = 560$ for the interior solution, which in comparison to

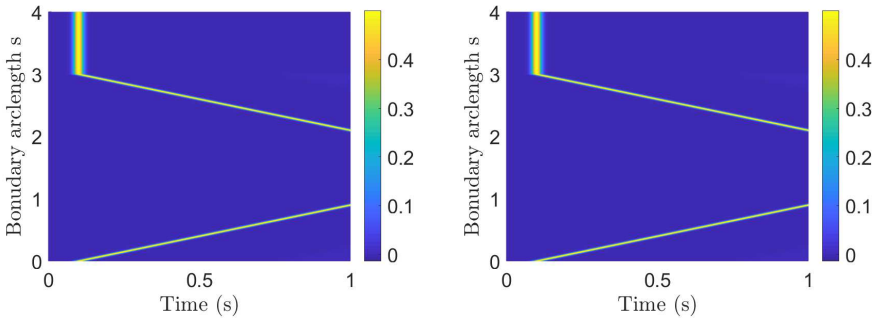

(a) DEA (b) SHFA

Figure 5.6: Solution to the wave equation along the boundary of a unit square domain with boundary data (5.24) and parameters $\Theta_0 = 0$, $\alpha = 4096$, $t_0 = 0.1$, with $M = 1024$ boundary elements and $N = \widetilde{N}/2 = 4096$ time-steps. The high frequency approximations (a) DEA and (b) SHFA are applied whenever $|\mathrm{Re}(k_l)| > 350$.

Figure 3.6 displays both a significantly more broadband solution and boundary condition. This is a consequence of increasing the parameter α from 36 to 4096.

In Table 5.3 we investigate the relative errors and convergence rates of the interior solutions observed at the point $\boldsymbol{x} = (0.5, 0.5)$, calculated via both hybrid methods, as we double the number of time-steps $N = \widetilde{N}/2$ and increase the number of boundary elements M by a factor of four. The interior solutions were calculated for the parameters $\Theta_0 = 0$, $\alpha = 4096$ and $t_0 = 0.1$, with the high frequency approximations being implemented whenever $|\mathrm{Re}(k_l)| > 350$. Here η corresponds to the index $l = \eta$ of the first wavenumber in the list k_l, $l = 1, 2, ..., \widetilde{N}$ such that $|\mathrm{Re}(k_l)|$ exceeds k^* - see also page 156 -157. The relative errors were computed via (5.32) using the exact solution (5.33) up until $T = 1$. From the table we observe that both hybrid methods produce identical results and convergence rates. On the last row of the table we achieve errors of less than 1% as there are enough boundary elements to model the highly oscillatory behaviour, and we also observe a convergence rate close to the expected second order.

In the problems considered so far, we have demonstrated that the hybrid approaches can both provide accurate results, but owing to the choice of wavenumber threshold, whether it be $k^* = 80$, for when $\alpha = 36$ and $t_0 = 1$ or $k^* = 350$

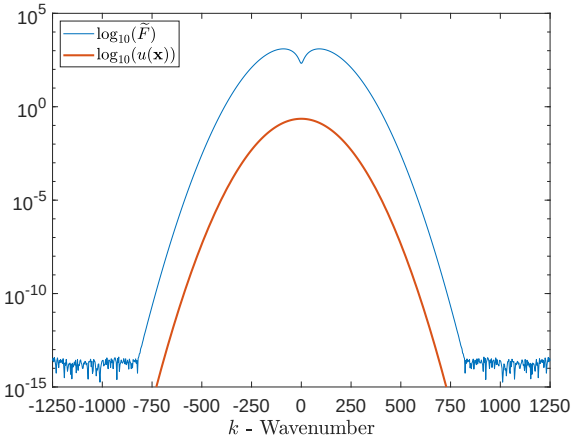

Figure 5.7: Logarithmic plots of the bandwidth of the Neumann boundary condition F and the interior solution $\Phi(\boldsymbol{x})$ observed at the point $\boldsymbol{x} = (0.5, 0.5)$ in the Fourier domain against the wavenumber k. The Neumann boundary condition F is given by equations (5.23) - (5.24) with $\alpha = 4096$, $t_0 = 0.1$ and $\Theta_0 = 0$. The numerical interior solution was calculated using the DEA based hybrid CQ scheme, whereby the high frequency approximation was applied whenever $|\mathrm{Re}(k_l)| > 350$ for parameters for $\widetilde{N}/2 = N = 4096$, $M = 1024$ and $\Lambda = 8$.

				DEA		SHFA	
$\widetilde{N}$	N	M	η	Error	EOC	Error	EOC
1024	512	4	101	0.4518	-	0.4518	-
2048	1024	16	108	0.4629	-0.04	0.4629	-0.04
4096	2048	64	111	0.1372	1.75	0.1372	1.75
8192	4096	256	112	0.0142	3.27	0.0142	3.27
16384	8192	1024	112	0.0026	2.45	0.0026	2.45

Table 5.3: Errors and convergence rates for the interior solution in the unit square domain observed at the point $\boldsymbol{x} = (0.5, 0.5)$ for the case when the boundary data are given by (5.24) with parameters $\Theta_0 = 0$, $\alpha = 4096$, $t_0 = 0.1$ and $T = 1$. The wavenumber threshold is chosen to be$k^* = 350$. The interior solutions were calculated numerically using the DEA and SHFA based hybrid CQ schemes whereby the high frequency approximations were applied whenever $|\mathrm{Re}(k_l)| > 350$.

when $\alpha = 4096$ and $t_0 = 0.1$, we find that the computational cost saving relative to using CQBEM is relatively modest. The corresponding full CQBEM calculation would take approximately 5 times longer than the DEA based hy-

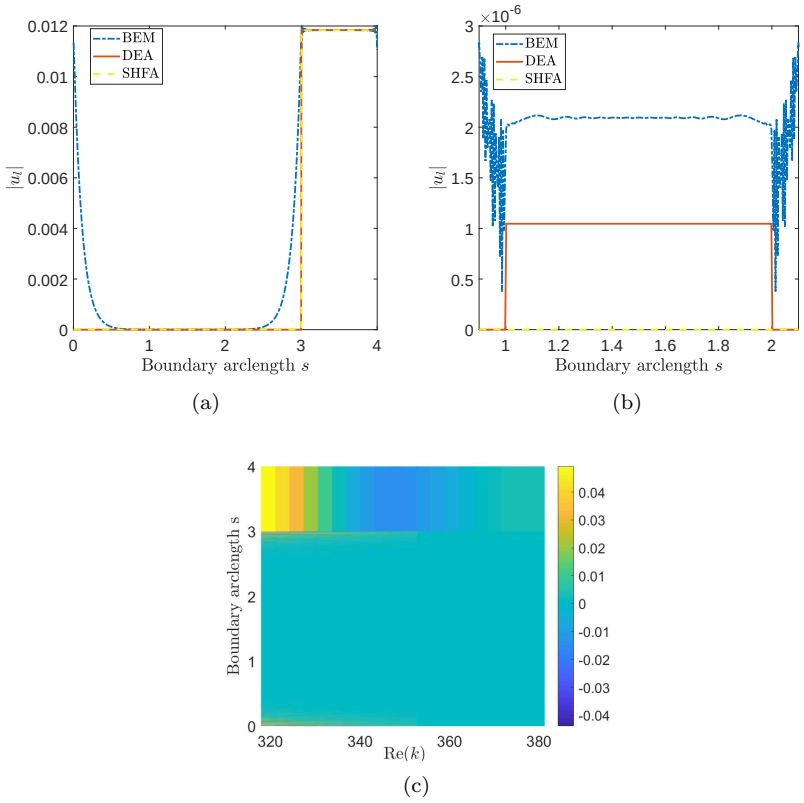

Figure 5.8: The Z-transformed boundary solution u_l on the unit square with boundary data (5.24) and parameters $\Theta_0 = 0$, $\alpha = 4096$, $t_0 = 0.1$, with $M = 1024$ boundary elements and $N = \widetilde{N}/2 = 4096$ time-steps. The left sub-plot (a) shows $|u_l|$ for $l = \eta$, which corresponds to the wavenumber k_η where we switch between using the BEM and a high frequency approximation. The right sub-plot (b) shows the same result as plot (a), but zoomed in along the right edge ($1 < s < 2$). The bottom sub-plot (c) shows $\mathrm{Re}(u_l)$ computed using the DEA based hybrid CQ scheme along the boundary of the square for a range of wavenumbers in the vicinity of $\mathrm{Re}(k) = k^* = 350$.

brid calculation and around 6 times longer than the SHFA based calculation when $N = 4096$, but the cost saving improves as N increases. This is true for the SHFA in particular since the cost is approximately $\mathcal{O}(1)$ in N, the same as for the high frequency approximation introduced in [133] for exterior wave problems.

In Table 5.4 we investigate the effect of lowering the wavenumber threshold

k^* with final time $T = 1$ in the range where the exact solution is valid. However we keep the number of time-steps fixed, overresolving for each case with $\widetilde{N} = 2N$, and investigate the error as we decrease the number of boundary elements together with k^*, since the minimal wavelength that we need to resolve in the BEM increases. From this table, we determine that lowering the wavenumber threshold from $k^* = 350$ to $k^* = 175$ increases the error from 1.7% to 6.2% and that as the threshold continues to be lowered, the error increases further, although we observe a significant decrease in the computational time.

In Table 5.5, we investigate further the effect of lowering the wavenumber threshold k^* with final time $T = 1$ in the range where the exact solution is valid. We now consider the effect of increasing the number of frequencies $\widetilde{N}$ by overresolving in the Laplace domain [26] to a greater degree that is approximately inversely proportionate to the factor by which we decrease k^*. In this case we observe that although the number of Helmholtz problems to be solved increases overall, the number solved using the BEM remains approximately the same. We find that reducing the wavenumber threshold to $k^* = 175$ does not have a significant effect on the error, but again we observe a significant decrease in computational time. Decreasing the threshold further gives improvements in computational efficiency, but at the cost of more significant increases to the error. We note also that the phase reconstruction process involved in the DEA based solution fails when the wavenumber threshold is reduced to $k^* = 45$, leading to significantly larger errors than for the SHFA. For the larger choices of wavenumber threshold considered, the performance of the DEA and SHFA based schemes was very similar, but with the DEA approach requiring more computational resources as would be expected. The computational times listed in the tables are using non-optimised MATLAB codes.

We now investigate the same IBVP as discussed previously, but now we consider the case when the plane wave boundary data enters the domain at an angle of $\Theta_0 = \pi/4$. Figure 5.9 shows the boundary solution versus time calculated using DEA for the high frequency approximation in sub-plot (a) and using the SHFA in sub-plot (b). We observe that these boundary solutions appear visually identical. They both depict the Gaussian pulse entering along the lower and left edges of the square ($0 < s < 1$ and $3 < s < 4$) at the bottom left corner ($s = 0 = 4$) around $t = t_0 = 0.1$ and then travelling along those edges until reaching the corners of the right and top edges ($s = 1$ and $s = 3$) at around $t \approx 0.81$s, where there are slight wave reflections heading back along the lower and left edges, but the majority of the wave propagation continues

$\widetilde{N}$	N	M	k^*	η	DEA Error	DEA time	SHFA Error	SHFA time
4096	2048	1024	350	111	0.01664	13.0h	0.01608	10.5h
4096	2048	512	175	56	0.0620	1.5h	0.0408	1.35h
4096	2048	256	90	29	0.2336	1h	0.0663	42 mins
4096	2048	128	45	15	0.1196	35 mins	0.1176	20 mins
4096	2048	64	25	8	0.2546	25 mins	0.1617	9.8 mins

Table 5.4: Errors and computation times for the DEA and SHFA based hybrid CQ schemes on the unit square domain for $T = 1$ when lowering the choice of wavenumber threshold k^*. As the maximal BEM wavenumber is decreased, there is also a proportionate decrease in the number of boundary elements while fixing the number of time-steps and frequencies.

$\widetilde{N}$	N	M	k^*	η	DEA Error	DEA time	SHFA Error	SHFA time
4096	2048	1024	350	111	0.01664	13.0h	0.01608	10.5h
8192	2048	512	175	112	0.01817	2.6h	0.01778	1.4h
16382	2048	256	90	115	0.03340	1.5h	0.03383	48 mins
32768	2048	128	45	115	0.4632	48 mins	0.06427	23 mins
65536	2048	64	25	128	0.4272	28 mins	0.09393	14 mins

Table 5.5: Errors and computation times for the DEA and SHFA based hybrid CQ schemes on the unit square domain for $T = 1$ when lowering the choice of wavenumber threshold k^*. As the maximal BEM wavenumber is decreased, there is also a proportionate decrease in the number of boundary elements together with an increase in the number of Helmholtz problems solved overall.

along the right and top edges. In sub-plot (c) we compare the interior solutions at the point $\boldsymbol{x} = (0.5, 0.5)$ computed using the DEA and SHFA high frequency approximations with the parameters $\Theta_0 = 0$, $\alpha = 4096$ and $t_0 = 0.1$. In this figure we observe that both solutions behave identically.

Figure 5.10 shows the Z-transformed boundary solution u_l. The left sub-plot (a) shows the absolute value at $l = \eta$ and in this plot we notice that there is no visual difference between the BEM solution and the high frequency approximations since there are no edges where the wave direction is tangential to the boundary. Hence, the hybrid methods perform better here than for the case when $\Theta_0 = 0$. Sub-plot (b) is a zoomed in section of sub-plot (a) focusing on the right and top edges ($1 < s < 3$) where we observe a difference between the approximations. In particular, the SHFA prediction is zero as it does not include any reflected wave contributions. The DEA solution shows a smooth

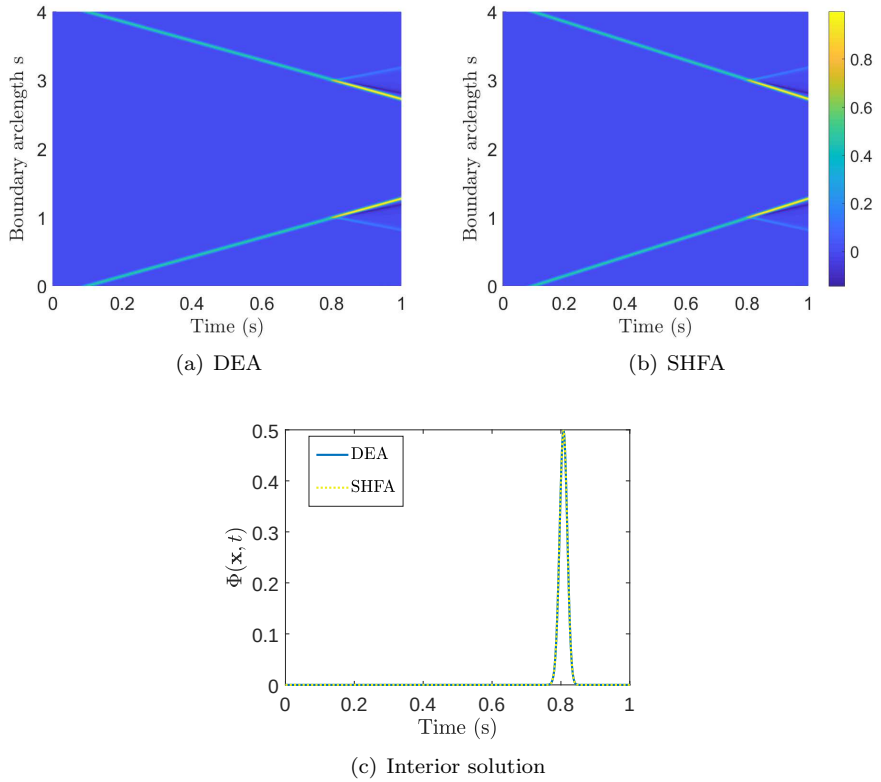

(a) DEA (b) SHFA

(c) Interior solution

Figure 5.9: Solutions to the wave equation for a unit square domain with boundary data (5.24) and parameters $\Theta_0 = \pi/4$, $\alpha = 4096$, $t_0 = 0.1$, with $M = 1024$ boundary elements and $N = \widetilde{N}/2 = 4096$ time-steps. The high frequency approximations in all cases are applied whenever $|\mathrm{Re}(k_l)| > 350$. The sub-plots (a) and (b) show the solution along the boundary computed via the DEA based and the SHFA based hybrid methods, respectively. Sub-plot (c) shows the interior solution observed at the point $\boldsymbol{x} = (0.5, 0.5)$ calculated via both hybrid methods.

continuation of the solution across the edges whereas the BEM solution exhibits a small jump and oscillation close to the bottom-right ($s = 1$) and top-left ($s = 3$) vertices, before continuing as a smooth solution along the top and right edges. The discrepancy is a result of the DEA not including contributions from diffracted waves. The bottom sub-plot (c) shows $\mathrm{Re}(u_l)$ for wavenumbers close to $k^* = 350$ for which the solution is only shown along the bottom edge since it is the most dominant region of the solution. The solution is computed using the

DEA based approximation above the threshold $k^* = 350$, and using the BEM otherwise. We again observe that the solutions from the two methods match up very well, demonstrating the success of the phase reconstruction process outlined in Section 5.3.2.

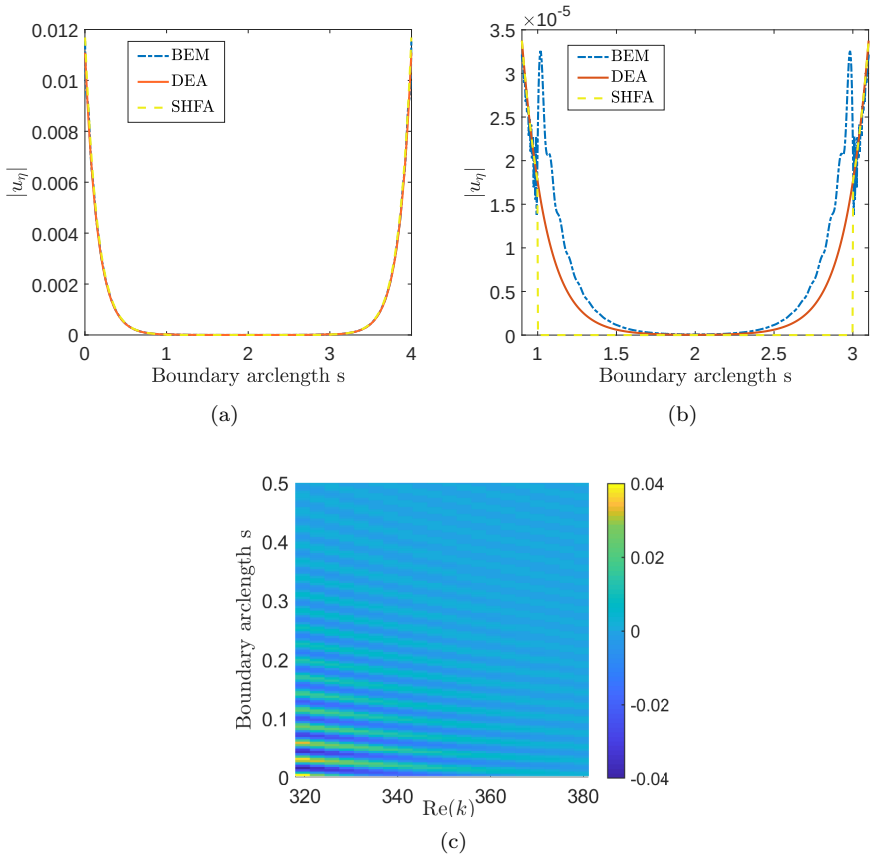

Figure 5.10: The Z-transformed boundary solution u_l on the unit square domain with boundary data (5.24) and parameters $\Theta_0 = \pi/4$, $\alpha = 4096$, $t_0 = 0.1$, with $M = 1024$ boundary elements and $N = \widetilde{N}/2 = 4096$ time-steps. The left sub-plot (a) shows $|u_l|$ for $l = \eta$, which corresponds to the wavenumber k_η where we switch between using the BEM and a high frequency approximation. The right sub-plot (b) shows the same result as plot (a) but zoomed in along the right and top edges ($1 < s < 3$). The bottom sub-plot (c) shows $\mathrm{Re}(u_l)$ computed using the DEA based hybrid CQ scheme along the bottom edge ($0 < s < 0.5$) for a range of wavenumbers in the vicinity of $\mathrm{Re}(k) = k^* = 350$.

Tables 5.6 and 5.7 investigate the relative errors and convergence rates of

the interior solutions, observed at the point $\boldsymbol{x} = (0.5, 0.5)$, calculated via both hybrid methods with parameters $\Theta_0 = \pi/4$, $\alpha = 4096$ and $t_0 = 0.1$, with the high frequency approximations implemented whenever $|\mathrm{Re}(k_l)| > 350$. The errors were computed via (5.32), but using subsequent interior solutions as we double the number of time-steps. Table 5.6 investigates the error as we double the number of time-steps $N = \widetilde{N}/2$ and we increase the number of boundary elements M by a factor of four. From this table, we observe that the errors and convergence rates for both methods are approximately the same, although we note that the SHFA will have a faster calculation time due to the additional discretisation in DEA. The errors in this table do not show an error below 1% since there are not enough boundary elements in the interior solution when $M = 256$ to model the highly oscillatory behaviour. We then investigated further by fixing the number of boundary elements at $M = 1024$ and doubling the number of time-steps in Table 5.7. In this table, we observe the expected second order convergence rate for BDF2 based CQ schemes and errors smaller than 1% for both methods. Again the errors for both methods are approximately equal when comparing against subsequent interior solutions.

				DEA		SHFA	
$\widetilde{N}$	N	M	η	Error	EOC	Error	EOC
1024	512	4	101	-	-	0.0606	-
2048	1024	16	108	1.9917	-	1.9918	-
4096	2048	64	111	1.3707	0.54	1.3707	0.54
8192	4096	256	112	0.4821	1.51	0.4821	1.51
16384	8192	1024	112	0.0445	3.44	0.0445	3.44

Table 5.6: Errors and convergence rates for the interior solution on the unit square domain observed at the point $\boldsymbol{x} = (0.5, 0.5)$ for the case when the boundary data are given by (5.24) with parameters $\Theta_0 = \pi/4$, $\alpha = 4096$, $t_0 = 0.1$ and $T = 1$. The interior solutions were calculated numerically using the DEA and SHFA based hybrid CQ schemes whereby the high frequency approximations were applied whenever $|\mathrm{Re}(k_l)| > 350$.

When to implement either the DEA based or SHFA based hybrid method the choice of k^* is dependent on the choices for the parameters α and t_0 in the Neumann boundary condition (5.23). For a broadband signal such as when $\alpha = 4096$, the method requires a large number of time-steps and may also be required to be potentially over-resolved by choosing the number of frequencies independently. If the interior solution plot appears to include additional os-

				DEA		SHFA	
$\widetilde{N}$	N	M	η	Error	EOC	Error	EOC
256	128	1024	80	-	-	-	-
512	256	1024	92	0.5919	-	0.5919	-
1024	512	1024	101	0.3769	0.65	0.3769	0.65
2048	1024	1024	108	0.1455	1.37	0.1455	1.37
4096	2048	1024	111	0.0397	1.87	0.0397	1.87
8192	4096	1024	112	0.0100	2.80	0.0100	2.80
16384	8192	1024	112	0.0025	2.00	0.0025	2.00

Table 5.7: Errors and convergence rates for the interior solution on the unit square domain observed at the point $\boldsymbol{x} = (0.5, 0.5)$ for the case when the boundary data are given by (5.24) with parameters $\Theta_0 = \pi/4$, $\alpha = 4096$, $t_0 = 0.1$ and $T = 1$. The interior solutions were calculated numerically using the DEA and SHFA based hybrid CQ schemes whereby the high frequency approximations were applied whenever $|\mathrm{Re}(k_l)| > 350$.

cillations or appears noisy, then the model may require more time-steps and frequencies to model the highly oscillatory behaviour. The choice of k^* is important for this choice of α as it determines the number of boundary elements required for the BEM to provide sufficient accuracy for the Helmholtz problems calculated for the low frequency region. For our choices of α and t_0 in this work we have followed the suggestion from Marburg in [130] and ensured that there are six boundary elements per wavelength. For different choices of Θ_0 one may require to include more ray directions Λ. In the numerical results we included we our choices of Θ_0 were chosen such that we could choose $\Lambda = 8$and hence our global direction set would include the angle Θ_0 to ensure high accuracy, resulting in a faster computational time. To improve accuracy one may increase the choice of k^* such that more wavenumbers are calculated via the BEM as part of the low frequency region. However one must ensure that there are enough boundary elements chosen to provide a good level of accuracy up to the BEM cut-off frequency. To understand if the phase matching was constructed successfully one can investigate the behaviour of the $\mathrm{Re}(u_l)$ along the boundary in the vicinity of the cut off wavenumber chosen. The solutions calculated via the BEM and those calculated via a HFA should appear smooth as they cross over the switch frequency. If one can clearly view a discrepancy between the two methods then perhaps more refined discretisations are required or the phase reconstruction has been performed incorrectly.

L-shaped domain

We now present the numerical results for solving the same IBVP as above for the case when Ω is an L-shaped domain as shown in Figure 5.2 (b). The DEA approximation process needs to be modified for non-convex domains such as the L-shape and we implement the DEA approximation on a sub-divided version of the domain where each of the (two) sub-domains is convex as shown in Figure 5.11. In this case the sub-division was implemented by introducing an (artificial) internal interface connecting the vertices at $s = 1$ and $s = 3$ to form two convex quadrilateral sub-domains. The extension of the DEA approximation to multi-domains is discussed in more detail in Chapter 4. The sub-domains in Figure 5.11 are set up where Ω_1 is the quadrilateral with vertices 1, 2, 5 and 6 and sub-domain Ω_2 is quadrilateral with the vertices 2, 3, 4 and 5. For this example the amplitudes are calculated for each sub-domain but we must omit any amplitudes associated with the internal interface from the DEA result and reorder the amplitudes such that they are consistent with the low frequency BEM calculations before integrating into the CQ algorithm, that is that the amplitudes are ordered for the domain Ω with vertices 1, 2, 3, 4, 5, 6. The internal interface will have identical boundary elements for each sub-domain along this edge. We would like to note that there is no computational advantage in the difference between the subdividing of the L-shape domain shown in Figures 4.6 and 5.11. The subdivision of Figure 4.6 was a conscious choice such that the interior density for the problem where a spatially constant line source travels into the domain perpendicular to the left edge provided a more visually informative plot.

We first investigate the case when $\alpha = 36$, $t_0 = 1$ and $\Theta_0 = 0$ in (5.24), such that we can perform an error analysis for the results and compare against the error results for CQBEM reported in Section 3.4.1. For this case we can also compare the numerical solutions with the same exact solution (5.33) as before, but only consider short time periods where there are no reflections or diffraction from the reentrant corner at $s = 3$.

Figure 5.12 shows the numerical interior solutions observed at the point $\boldsymbol{x} = (0.25, 0.25)$ calculated via the CQBEM, as well as the DEA and SHFA based hybrid methods, and compared against the exact solution for $N = \widetilde{N} = 512$ time-steps and $M = 512$ boundary elements. The high frequency approximations are applied whenever $|\mathrm{Re}(k_l)| > 80$. From this figure, we observe that all numerical solutions match well until $t = 1.5$. However, we note that for

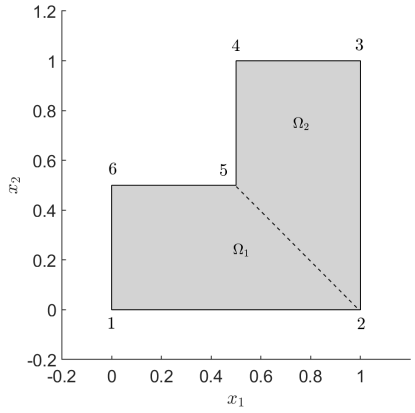

Figure 5.11: The L-shaped domain $\Omega = \Omega_1 \cup \Omega_2$ with the vertices numbered. Here sub-domain Ω_1 is the quadrilateral with vertices 1,2,5 and 6 and sub-domain Ω_2 is quadrilateral with the vertices 2, 3, 4 and 5. The internal interface is the dashed edge connecting vertices 2 and 5.

			DEA		SHFA	
N	M	η	Error	EOC	Error	EOC
64	8	-	0.2583	-	0.2583	-
128	32	23	0.1096	3.12	0.1096	3.12
256	128	24	0.0305	3.21	0.0306	3.20
512	512	25	0.0054	2.50	0.0054	2.50
1024	2048	26	0.0026	1.05	0.0026	1.05

Table 5.8: Errors and convergence rates for the interior solution on the L-shaped domain observed at the point $\boldsymbol{x} = (0.25, 0.25)$ for the case when the boundary data are given by (5.24) with parameters $\Theta_0 = 0$, $\alpha = 36$, $t_0 = 1$ and $T = 1.5$. The interior solutions were calculated numerically using the DEA and SHFA based hybrid CQ schemes whereby the high frequency approximations were applied whenever $|\mathrm{Re}(k_l)| > 80$.

$t > 0.85$, the numerical solutions contain contributions due to diffraction from the reentrant corner at $s = 3$ and therefore the exact solution is not valid after this time - see the results for the L-shaped domain reported in Section 3.4.1 for further details. For $t > 1.5$ the diffracted contributions are noticeable in the numerical solution. For a low switch frequency $k^* = 80$, the majority of Helmholtz problems are being treated with a high frequency approximation as shown in Figure 5.13 which shows that 464 out of the 512 Helmholtz problems are being

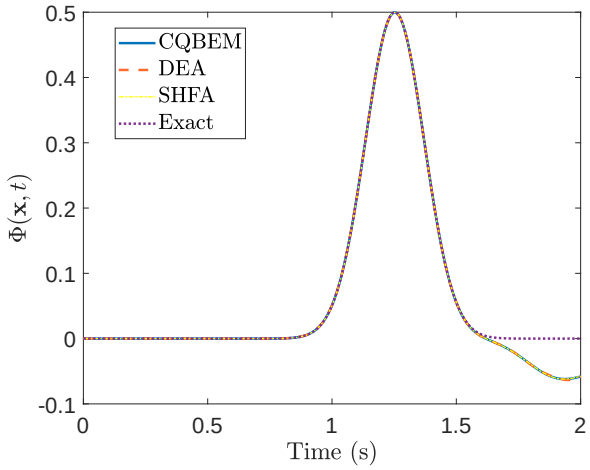

Figure 5.12: Interior solution to the wave equation at $\boldsymbol{x} = (0.25, 0.25)$ inside the L-shaped domain with boundary data (5.24) and parameters $\Theta_0 = 0$, $\alpha = 36$, $t_0 = 1$, with $N = \widetilde{N} = 512$ time-steps and $M = 512$ boundary elements. The high frequency approximations are applied whenever $|\mathrm{Re}(k_l)| > 80$.

computed via a high frequency approximation. The solution computed via the hybrid methods behaves identically to those computed using the CQBEM. This observation is further supported by the error results and convergence rates found in Table 5.8, for which we calculate the error up until $T = 1.5$ so that we can compare against the exact solution, but note that there are small contributions due to diffraction included in the numerical solution.

First, comparing the DEA and SHFA hybrid methods against each other we determine that both have identical errors (to the quoted number of digits) that are small, and similar convergence rates that vary between first and second order. By comparing the results from Table 5.8 with the results computed via the CQBEM in Table 3.5, we observe that the errors are similar until the case $N = 1024$ when the CQBEM error is smaller. This is due to the additional error introduced by the high frequency approximations since the majority of the Helmholtz problems are treated with the high frequency approximation and the results could be improved by increasing the choice of the threshold k^*. However, such an increase would also incur additional computational costs. For the case when we have $N = \widetilde{N} = 512$ frequencies, only fifty of these Helmholtz problems are approximated using the BEM. Even for this low frequency switch value, we still observe low errors from the hybrid methods.

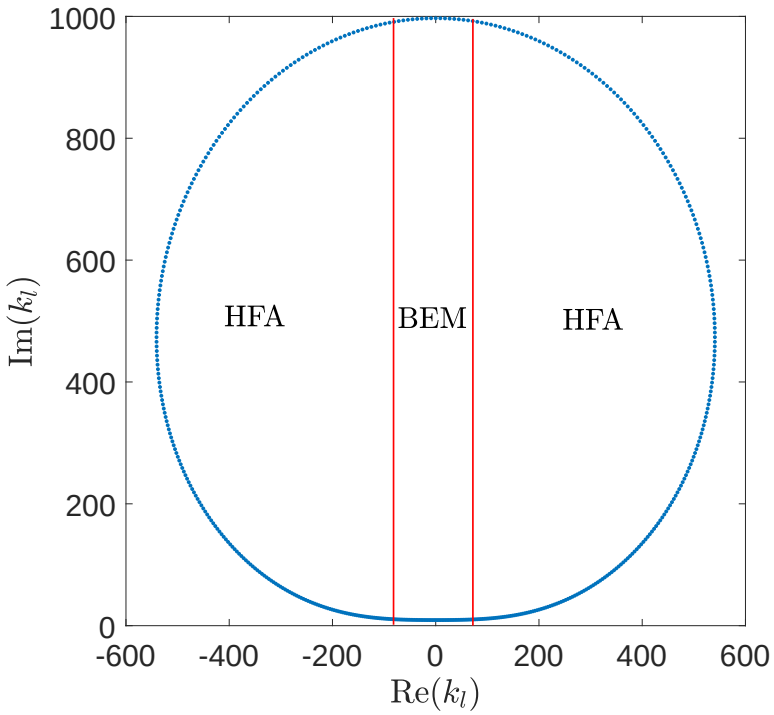

Figure 5.13: The range of complex wavenumbers $k_l = i\zeta_l/c$ for the set of Helmholtz problems obtained using the BDF2 scheme with $\widetilde{N} = N = M = 512$, $T = 2$, $c = 1$ and $\lambda = 10^{-8/\widetilde{N}}$. The threshold $k^* = 80$ is chosen to be the wavenumber where the hybrid method switches from the BEM to a high frequency approximation.

We now consider the case when $\alpha = 36$, $t_0 = 1$ and $\Theta_0 = \pi/4$ in (5.24). Figure 5.14 shows the numerical interior solutions observed at the point $\boldsymbol{x} = (0.25, 0.25)$ calculated using CQBEM, as well as the DEA and SHFA based hybrid methods for $N = \widetilde{N} = 512$ time-steps and $M = 512$ boundary elements. The high frequency approximations are implemented whenever $|\mathrm{Re}(k_l)| > 80$. From the figure, we observe that the numerical solutions are all behaving similarly by eye. Even with a large number of Helmholtz problems being approximated via a high frequency method, the solution matches well for the case when α is reasonably low. Table 5.9 shows the error and convergence rates for this problem, where the errors are calculated via (5.32) using subsequent solutions as we double the number of time-steps. From this table we observe that again

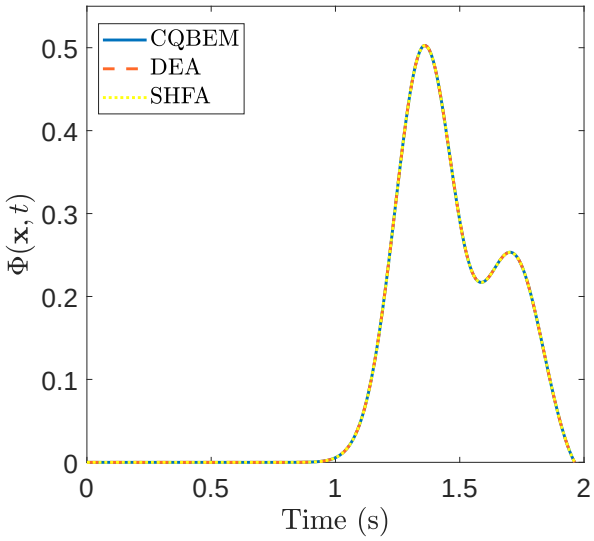

Figure 5.14: Interior solution to the wave equation at $\boldsymbol{x} = (0.25, 0.25)$ inside the L-shaped domain with boundary data (5.24) and parameters $\Theta_0 = \pi/4$, $\alpha = 36$, $t_0 = 1$, with $N = \widetilde{N} = 512$ time-steps and $M = 512$ boundary elements. The high frequency approximations are applied whenever $|\mathrm{Re}(k_l)| > 80$.

both methods behave very similarly obtaining small errors, which are eventually smaller than 1%, and achieve approximately a second order convergence rate.

			DEA		SHFA	
N	M	η	Error	EOC	Error	EOC
64	8	-	-	-	-	-
128	32	23	0.3040	-	0.3040	-
256	128	24	0.0747	2.02	0.0747	2.02
512	512	25	0.0110	2.76	0.0111	2.75
1024	2048	26	0.0019	2.53	0.0019	2.55

Table 5.9: Errors and convergence rates for the interior solution on the L-shaped domain observed at the point $\boldsymbol{x} = (0.25, 0.25)$ for the case when the boundary data are given by (5.24) with parameters $\Theta_0 = \pi/4$, $\alpha = 36$, $t_0 = 1$ and $T = 2$. The interior solutions were calculated numerically using the DEA and SHFA based hybrid CQ schemes whereby the high frequency approximations were applied whenever $|\mathrm{Re}(k_l)| > 80$.

We now present the numerical results when $\alpha = 4096$, $t_0 = 0.1$ and $\Theta_0 = 0$

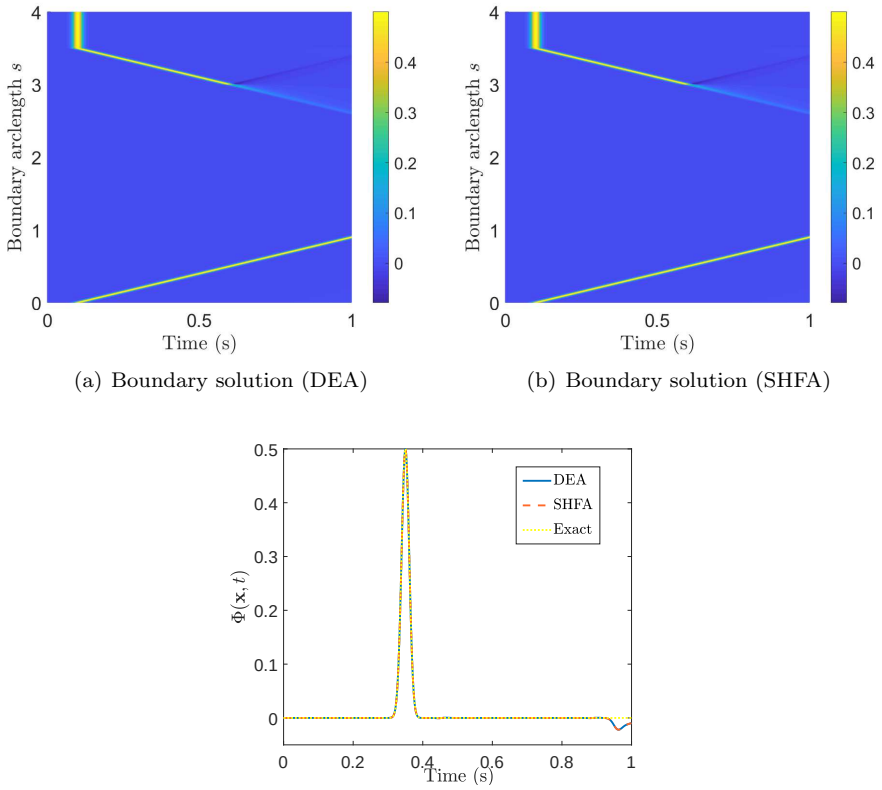

(a) Boundary solution (DEA)

(b) Boundary solution (SHFA)

(c) Interior solution

Figure 5.15: Solutions to the wave equation for an L-shaped domain with boundary data (5.24) and parameters $\Theta_0 = 0$, $\alpha = 4096$, $t_0 = 0.1$, with $M = 1024$ boundary elements and $N = \widetilde{N}/2 = 4096$ time-steps. The high frequency approximations in all cases are applied whenever $|\mathrm{Re}(k_l)| > 350$. The sub-plots (a) and (b) show the solution along the boundary computed via the DEA based and the SHFA based hybrid methods, respectively. Sub-plot (c) shows the interior solution observed at the point $\boldsymbol{x} = (0.25, 0.25)$ calculated via both hybrid methods and compared to the exact solution.

in (5.24), in order to obtain a broadband signal. For this example we can compare our numerical results against the exact solution given by (5.33) up to the time $t = 0.5$ so that we do not observe any reflections at the solution point $\boldsymbol{x} = (0.25, 0.25)$. Figure 5.15 (a) - (b) shows the solution along the boundary computed using the DEA and SHFA based hybrid methods, respectively, with $M = 1024$ boundary elements and $N = \widetilde{N}/2 = 4096$ time-steps. We observe

that the DEA and SHFA based approaches give visually identical solutions over the entire boundary. The plots show the Gaussian pulse moving over the left edge of the L-shape ($3.5 < s < 4$) at around $t = t_0 = 0.1$ and then travelling along the upper and lower edges. At around $t = 0.6$, we observe a reflection of the pulse, which partially travels back along the upper edge from the corner at $s = 3$, but with the majority of the pulse continuing along the boundary where $2.5 < s < 3$. Along the lower edge the pulse instead simply continues along the boundary. Figure 5.15 (c) shows a comparison between the exact and numerical interior solutions at $\boldsymbol{x} = (0.25, 0.25)$. We again apply a high frequency approximation whenever $|\mathrm{Re}(k_l)| > 350$ and use $N = \widetilde{N}/2 = 4096$ time-steps and $M = 1024$ boundary elements. We observe that both high frequency approximations produce identical looking results up to $t = 0.9$. For $t > 0.9$ we observe that the numerical solutions deviate from the exact solution because the numerical solutions include contributions due to corner diffraction from the reenterant corner at $s = 3$ and therefore the exact solution is not valid, as discussed in more detail in Section 3.4.1.

Figure 5.16 shows the Z-transformed boundary solution u_l. The left sub-plot (a) shows the absolute value at $l = \eta$. The values of $|u_\eta|$ calculated using the BEM are compared to both of the proposed high frequency approximations. The main difference between the three methods occurs along the left-upper ($3 < s < 3.5$) and lower ($0 < s < 1$) edges where the high frequency approximations give zero and the BEM does not, since both high frequency approximations of u_l omit waves tangential to the boundary. In sub-plot (b) we highlight that the main difference between DEA and the SHFA is apparent on the lower part of the right hand edge when $1 < s < 1.5$. The BEM and DEA approaches include reflected wave contributions, but the SHFA does not. These results are consistent with those for the unit square, however in this problem we also observe an optically shaded region when $x_2 \geq 0.5$, which corresponds to the upper right quadrant of the L-shape where the high frequency approximations are zero (between $1.5 < s < 3$). Near the edges of the shadowed region, when $s = 1.5$ and $s = 3$, we observe deviations between the BEM and the high frequency approximations where the diffracted contributions are most dominant. Sub-plot (c) shows $\mathrm{Re}(u_l)$ for wavenumbers close to the wavenumber threshold $k^* = 350$ computed using the DEA approximation when $|\mathrm{Re}(k_l)| > 350$ and the BEM otherwise. The plot focuses on the left ($3.5 < s < 4$) and left-upper edges ($3 < s < 3.5$). The value of $\mathrm{Re}(u_l)$ jumps to zero on the left-upper edge when we switch from the BEM to the DEA approximation as would be expected from

sub-plot (a). For wavenumbers $\mathrm{Re}(k) > 350$ along the boundary $3 < s < 3.5$ we observe no phase change in the DEA approximation. This is expected since the wave is travelling parallel to the boundary and therefore the solution will be constant because the amplitude is zero. Again, we observe that the solutions from the DEA and the BEM methods match up very well around the threshold $k^* = 350$ along the left edge, demonstrating that the phase reconstruction is working well.

In Table 5.10 we investigate the relative errors and convergence rates of the interior solutions observed at the point $\boldsymbol{x} = (0.25, 0.25)$ calculated via both hybrid methods as we double the number of time-steps $N = \widetilde{N}/2$ and increase the number of boundary elements M by a factor of four. The interior solutions were calculated for the parameters $\Theta_0 = 0$, $\alpha = 4096$ and $t_0 = 0.1$, with the high frequency approximations being implemented whenever $|\mathrm{Re}(k_l)| > 350$. The relative errors were computed via (5.32) against the exact solution (5.33) up until $T = 0.5$, since for the L-shaped domain the solution after $t = 0.5$ contains contributions due to reflections as well as diffraction from the reentrant corner at $s = 3$, and therefore the exact solution is not valid after this time. From the table we observe that both methods give approximately the same error and convergence results with both methods obtaining less than 1% error with $N \geq 4096$ time-steps and $M = 512$ boundary elements. We also eventually achieve approximately second order convergence for the BDF2 based CQ scheme when we choose M large enough to accurately model up to the threshold wavenumber $k^* = 350$.

				DEA		SHFA	
$\widetilde{N}$	N	M	η	Error	EOC	Error	EOC
1024	512	8	101	0.2898	-	0.2898	-
2048	1024	32	108	0.1836	0.66	0.1836	0.66
4096	2048	128	111	0.0433	2.08	0.0433	2.08
8192	4096	512	112	0.0037	3.55	0.0037	3.55
16384	8192	2048	112	5.0609e-4	2.87	5.0609e-4	3.55

Table 5.10: Errors and convergence rates for the interior solution on the L-shaped domain observed at the point $\boldsymbol{x} = (0.25, 0.25)$ for the case when the boundary data are given by (5.24) with parameters $\Theta_0 = 0$, $\alpha = 4096$, $t_0 = 0.1$ and $T = 0.5$. The interior solutions were calculated numerically using the DEA and SHFA based hybrid CQ schemes whereby the high frequency approximations were applied whenever $|\mathrm{Re}(k_l)| > 350$.

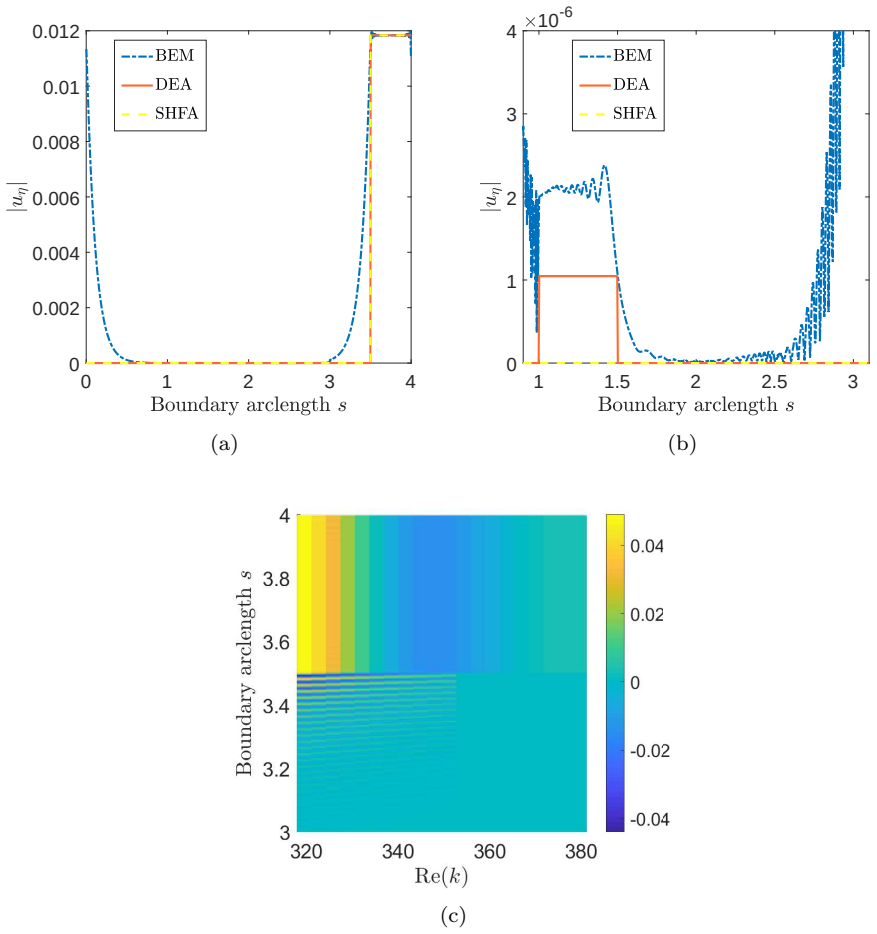

Figure 5.16: The Z-transformed boundary solution u_l on the L-shaped domain with boundary data (5.24) and parameters $\Theta_0 = 0$, $\alpha = 4096$, $t_0 = 0.1$, with $M = 1024$ boundary elements and $N = \widetilde{N}/2 = 4096$ time-steps. The left sub-plot (a) shows $|u_l|$ for $l = \eta$, which corresponds to the wavenumber k_η where we switch between using the BEM and a high frequency approximation. Sub-plot (b) shows a zoomed in version of plot (a) along the right and upper edges ($1 < s < 3$). The bottom sub-plot (c) shows Re(u_l) computed using the DEA based hybrid CQ scheme along the upper and left edges of the left part of the L-shape ($3 < s < 4$) for a range of wavenumbers in the vicinity of Re(k) = $k^* = 350$.

Table 5.11 demonstrates the effect of lowering the wavenumber threshold k^* with final time $T = 0.5$. As for the unit square, we investigate the error as we

lower the threshold k^* and increase the number of frequencies $\widetilde{N}$ by overresolving in the Laplace domain [26], allowing us to decrease the number of boundary elements M. Note that the number of Helmholtz problems solved using the BEM remains approximately unchanged. We find again that reducing the wavenumber threshold from $k^* = 350$ to $k^* = 175$ makes only a small difference to the error but gives a significant decrease in the computational time, and decreasing further gives more moderate improvements in computational efficiency whilst causing more significant increases in the error. In this case the phase reconstruction process does not fail until we reduce the wavenumber threshold to $k^* = 25$ (compared to $k^* = 45$ for the unit square), leading to significantly larger errors than for the SHFA. For the larger choices of wavenumber threshold considered, the performance of the DEA and SHFA based schemes was again very similar, but with the DEA approach requiring more computational resources as before.

$\widetilde{N}$	N	M	k^*	η	DEA Error	DEA time	SHFA Error	SHFA time
4096	2048	1024	350	56	0.01612	7.3h	0.01611	5.3h
8192	2048	512	175	56	0.02125	2.0h	0.01887	46mins
16382	2048	256	90	58	0.05513	1.0h	0.05429	20 mins
32768	2048	128	45	58	0.1173	47 mins	0.1145	11 mins
65536	2048	64	25	64	0.4740	41 mins	0.1552	6.5 mins

Table 5.11: Errors and computation times for the DEA and SHFA based hybrid CQ schemes on the L-shaped domain for $T = 0.5$ when lowering the choice of wavenumber threshold k^*. As the maximal BEM wavenumber is decreased, there is also a proportionate decrease in the number of boundary elements together with an increase in the number of Helmholtz problems solved overall.

We now investigate the same IBVP as discussed previously, but consider the case when the plane wave boundary data enters the domain at an angle of $\Theta_0 = \pi/4$. Figure 5.17 (a) - (b) shows the solution along the boundary computed using the DEA and SHFA based hybrid methods, respectively, with the parameters $\Theta_0 = \pi/4$, $\alpha = 4096$, $t_0 = 0.1$, with $M = 1024$ boundary elements and $N = \widetilde{N}/2 = 4096$ time-steps. The boundary solutions in sub-plots (a) - (b) appear identical and show the Gaussian pulse entering along the lower and left edges of the L-shaped domain ($0 < s < 1$ and $3.5 < s < 4$) at the origin, ($s = 0 = 4$) at around $t = t_0 = 0.1$. The pulse then travels along those edges until we observe some small amplitude reflections when the wave reaches the top of the left edge at $s = 3.5$, but most of the wave continues along the left

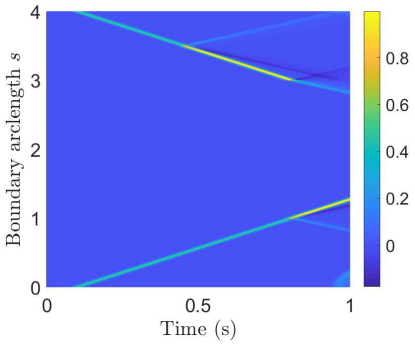

(a) Boundary solution (DEA)

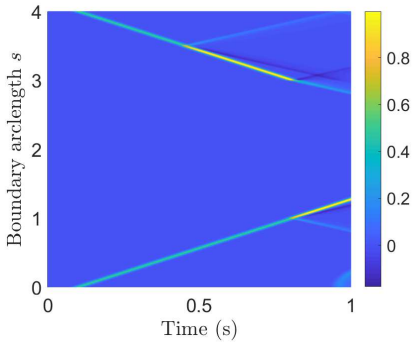

(b) Boundary solution (SHFA)

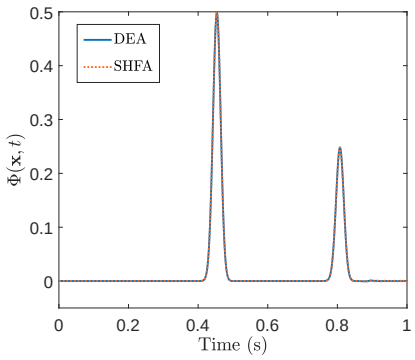

(c) Interior solution

Figure 5.17: Solutions to the wave equation for an L-shaped domain with boundary data (5.24) and parameters $\Theta_0 = \pi/4$, $\alpha = 4096$, $t_0 = 0.1$, with $M = 1024$ boundary elements and $N = \widetilde{N}/2 = 4096$ time-steps. The high frequency approximations in both cases are applied whenever $|\mathrm{Re}(k_l)| > 350$. The sub-plots (a) and (b) show the solution along the boundary computed via the DEA and SHFA based hybrid methods, respectively. Sub-plot (c) shows the interior solution observed at the point $\boldsymbol{x} = (0.25, 0.25)$ calculated via both hybrid methods.

most upper edge ($3.5 < s < 3$). We also observe some interference, indicated by the darker blue lines, which follows the pulse up along the left most upper edge. When the pulse reaches the reenterant corner at $s = 3$ we again observe that the majority of the pulse continues to travel along the upper most left edge ($2.5 < s < 3$) with some small amplitude reflections indicated by the lighter blue lines, as well as some interference. Similarly along the bottom edge the wave continues to travel until it reaches the bottom right vertex ($s = 1$) where

we observe some small amplitude reflection back along the bottom edge, but the majority of the wave continues up along the right edge ($1 < s < 2$). In sub-plot (c), we observe that the interior solution at $\boldsymbol{x} = (0.25, 0.25)$ is visually identical for each of the methods.

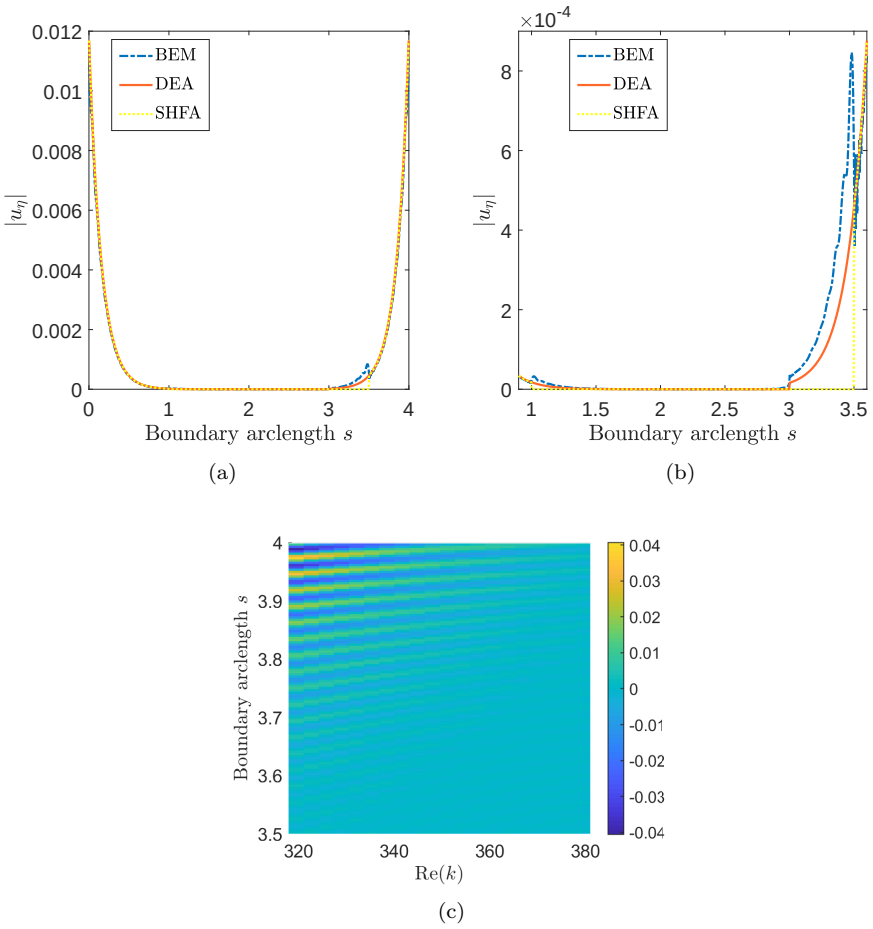

Figure 5.18: The Z-transformed boundary solution u_l on the L-shaped domain with boundary data (5.24) and parameters $\Theta_0 = \pi/4$, $\alpha = 4096$, $t_0 = 0.1$, with $M = 1024$ boundary elements and $N = \widetilde{N}/2 = 4096$ time-steps. The left sub-plot (a) shows $|u_l|$ for $l = \eta$, which corresponds to the wavenumber k_η where we switch between using the BEM and a high frequency approximation. Sub-plot (b) shows the same result as plot (a), but zoomed in along the right and upper edges ($1 < s < 3$). Sub-plot (c) shows $\mathrm{Re}(u_l)$ computed using the DEA based hybrid CQ scheme along the left edge of the L-shape ($3.5 < s < 4$) for a range of wavenumbers in the vicinity of $\mathrm{Re}(k) = k^* = 350$.

Figure 5.18 (a) - (b) shows the Z-transformed boundary solution $|u_l|$ at $l = \eta$. For this problem as we are considering $\Theta_0 = \pi/4$, there is no optically shaded region, but we do expect to see a diffracted contribution originating from the re-entrant corner where $s = 3$ that is not captured by the high frequency approximations. In this case there are also no edges where the wave direction is tangential to the boundary and hence the agreement between the BEM solution and the high frequency approximations is better than for $\Theta_0 = 0$. We observe the main difference between the models in sub-plot (b), which is zoomed in between the left-upper edge ($3 < s < 3.5$) and the lower part of the right edge ($1 < s < 1.5$) where the SHFA prediction is zero due to not including the reflected wave contributions. The DEA solution shows a smooth continuation across all edges, whereas the BEM solution exhibits some oscillation close to the bottom-right vertex ($s = 1$) and along the entire left-upper edge ($3 < s < 3.5$). The bottom sub-plot (c) shows $\mathrm{Re}(u_l)$ for wavenumbers close to k_η, where $\mathrm{Re}(k_\eta) \approx 350$. The solution is only shown for the left-most edge ($3.5 < s < 4$) where the solution $\mathrm{Re}(u_l)$ is more dominant in comparison along to the rest of the boundary. The solution is computed using the DEA based approximation for $|\mathrm{Re}(k_l)| > 350$, and using the BEM otherwise. We observe that the solutions from the two methods match up very well, once again demonstrating the success of the phase reconstruction process.

				DEA		SHFA	
$\widetilde{N}$	N	M	η	Error	EOC	Error	EOC
1024	512	8	101	-	-	-	-
2048	1024	32	108	1.5715	-	1.5715	-
4096	2048	128	111	0.8745	0.85	0.8745	0.85
8192	4096	512	112	0.4669	0.91	0.4669	0.91
16384	8192	2048	112	0.0501	3.22	0.0445	3.39

Table 5.12: Errors and convergence rates for the interior solution on the L-shaped domain observed at the point $\boldsymbol{x} = (0.25, 0.25)$ for the case when the boundary data are given by (5.24) with parameters $\Theta_0 = \pi/4$, $\alpha = 4096$, $t_0 = 0.1$ and $T = 1$. The interior solutions were calculated numerically using the DEA and SHFA based hybrid CQ schemes whereby the high frequency approximations were applied whenever $|\mathrm{Re}(k_l)| > 350$.

Tables 5.12 and 5.13 investigate the relative errors and convergence rates of the interior solutions, observed at the point $\boldsymbol{x} = (0.25, 0.25)$, calculated via the DEA and SHFA hybrid methods with parameters $\Theta_0 = \pi/4$, $\alpha = 4096$,

$t_0 = 0.1$ and $T = 1$, with the high frequency approximations being implemented whenever $|\mathrm{Re}(k_l)| > 350$. The errors were computed via (5.32), but using subsequent interior solutions as we double the number of time-steps. Table 5.12 investigates the error as we double the number of time steps $N = \widetilde{N}/2$ and increase the number of boundary elements M by a factor of four. From this table, we observe that the errors and convergence rates for both methods are approximately the same, until the final row when $N = 8192$ where the SHFA has a slightly lower error. However, both methods do not show an error below 1% since there are not enough boundary elements when $M = 512$ to model the highly oscillatory behaviour when $|\mathrm{Re}(k_l)| \approx 350$. We therefore investigated further by fixing the number of boundary elements at $M = 1024$ and doubling the number of time-steps in Table 5.13. In this table, we observe the expected second order convergence rate and errors smaller than 1% for both methods. Again the errors for both methods are approximately equal when comparing against subsequent interior solutions.

				DEA		SHFA	
$\widetilde{N}$	N	M	η	Error	EOC	Error	EOC
256	128	1024	80	-	-	-	-
512	256	1024	92	0.4338	-	0.4338	-
1024	512	1024	101	0.2346	0.89	0.2346	0.89
2048	1024	1024	108	0.0789	1.57	0.0789	1.57
4096	2048	1024	111	0.0209	1.92	0.0209	1.92
8192	4096	1024	112	0.0053	1.98	0.0053	1.98
16384	8192	1024	112	0.0013	2.03	0.0013	2.03

Table 5.13: Errors and convergence rates for the interior solution on the L-shaped domain observed at the point $\boldsymbol{x} = (0.25, 0.25)$ for the case when the boundary data are given by (5.24) with parameters $\Theta_0 = \pi/4$, $\alpha = 4096$, $t_0 = 0.1$ and $T = 1$. The interior solutions were calculated numerically for fixed $M = 1024$ using the DEA and SHFA based hybrid CQ schemes whereby the high frequency approximations were applied whenever $|\mathrm{Re}(k_l)| > 350$.

5.4.2 Response to an interior point source

In this section we consider solving the wave equation for the case when there is a point source inside either a unit square or an irregular shaped polygon, as shown in Figure 5.19, which also depicts the source point $\boldsymbol{x}_0$. The point source excitation is of the form $P(\boldsymbol{x}, t) = \delta(\boldsymbol{x} - \boldsymbol{x}_0)P_0(t)$, where we choose the temporal

source profile to be a Gaussian pulse either of the form (3.42) or as follows

$$P_0(t) = \sqrt{\frac{\alpha}{\pi}} e^{-\alpha(t-t_0)^2}. \tag{5.34}$$

The parameters $t_0 > 0$ and $\alpha > 0$ control the peak position and bandwidth of the Gaussian pulse, respectively.

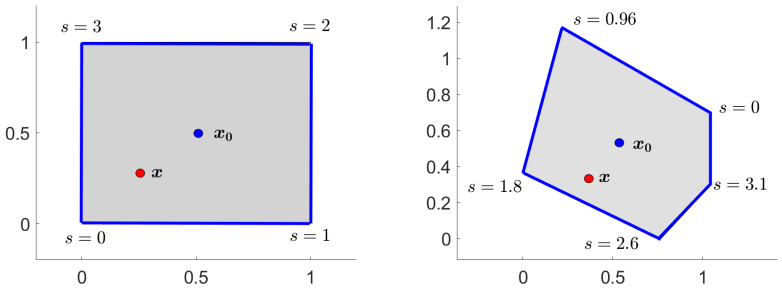

(a) Unit square domain (b) Irregular polygon domain

Figure 5.19: Set-up of the numerical experiments for the case when there is a point source excitation. This figure shows the domains considered, the source point $\boldsymbol{x}_0$ and the interior point $\boldsymbol{x}$ at which the solution is evaluated.

As described in Chapter 3, the solution to the IBVP (5.1) - (5.3) is written as $\Phi = (U + V)|_\Omega$, where U is the reverberant solution that satisfies the homogeneous wave equation (5.1) when $P = 0$, along with Neumann boundary condition (3.11) and V solves the free-space problem (3.4). The boundary condition (3.11) is implemented into the DEA scheme by writing it in the form of the square modulus of the solution to the Helmholtz equation, which is then used to determine the initial density ρ_0. The DEA initial boundary density ρ_0 corresponding to a point source excitation is then given by

$$\rho_0(s,p) = c\cos(\theta_0)|\widetilde{V}_l(\boldsymbol{x} - \boldsymbol{x}_0)|^2 e^{-2\mathrm{Im}(k_l)\|\boldsymbol{x}-\boldsymbol{x}_0\|}\delta(p - p_0), \tag{5.35}$$

where $k_l = i\zeta_l/c$, $p_0 = \sin(\theta_0)/c$ and $\widetilde{V}_l$ is the Z-transform of V. The angle θ_0 defines the direction of the outgoing ray at position s on Γ relative to the normal direction at s. In particular, it is the direction given by a specular reflection at s after arriving from $\boldsymbol{x}_0$. The initial density (5.35) therefore represents the square amplitude of the Z-transformed Dirichlet boundary data transported along the direction corresponding to a specular reflection at s on Γ after arriving from

$\boldsymbol{x}_0$. The exponential term represents the energy decay between leaving $\boldsymbol{x}_0$ and arriving at s, and we have used $\boldsymbol{x}$ to represent the Cartesian coordinates corresponding to the arclength position s. The $c\cos(\theta_0)$ pre-factor is a consequence of projecting the density in Ω induced by the point source onto the boundary Γ [42]. Applying the CQ discretisation to the convolution (3.9) provides an expression for $|\widetilde{V}_l|^2$ in (5.35) as follows

$$\begin{aligned} |\widetilde{V}_l(\boldsymbol{x}-\boldsymbol{x}_0)|^2 &= |G_{k_l}(\boldsymbol{x}-\boldsymbol{x}_0)|^2 \left|\widetilde{P}_0^l\right|^2, \\ &\approx \frac{\left|\widetilde{P}_0^l\right|^2}{8\pi|k_l|\,\|\boldsymbol{x}-\boldsymbol{x}_0\|}, \end{aligned} \tag{5.36}$$

where $\widetilde{P}_0^l$ is the Z-transform of P_0 for $l = 0, 1, ..., \widetilde{N}-1$. Here we have implemented a high frequency asymptotic formula for the $H_0^{(1)}(k\,\|\boldsymbol{x}\|)$ term, which arises in the Green's function G_{k_l}, and can be derived from the formulae given in Section 8.451 of [74]. In particular, we find

$$|H_0^{(1)}(k\,\|\boldsymbol{x}\|)|^2 \underset{|k|\gg 1}{\approx} \frac{2}{\pi|k|\,\|\boldsymbol{x}\|}.$$

Square domain

We first consider the case when Ω is a unit square with the source point in the centre at $\boldsymbol{x}_0 = (0.5, 0.5)$. We choose $c = 1$ for simplicity and investigate the examples where $P_0(t)$ is given by (3.42) with parameters $\alpha = 36$ and $t_0 = 1$, such that we can compare results against those computed via CQBEM in Section 3.4.2. This choice ensures $P_0(0)$ is zero to double precision meaning that the initial conditions (5.2) will be satisfied. Figure 5.20 (a) shows the numerical interior solution observed at $\boldsymbol{x} = (0.25, 0.25)$ calculated using both the SHFA and the DEA based hybrid methods. These interior solutions are compared against a solution which has been computed using the CQBEM. The discretisation parameters are chosen as $N = \widetilde{N}/2 = 512$ time-steps, $M = 512$ boundary elements, $\Lambda = 128$ global directions and $\lambda = 10^{-8/\widetilde{N}}$. A high frequency approximation is applied whenever $|\mathrm{Re}(k_l)| > 80$. The plots compare approximations of the reverberant solution U, which is equivalent to the full solution Φ with the contribution of the direct source excitation removed, calculated using both hybrid methods and the CQBEM for $T = 2$. In addition, the solid line shows a plot of Φ for completeness. From this figure we observe that all numerical solutions of U appear identical by eye. For this problem it is reasonable to compare the

interior solutions against the CQBEM solution since when $\alpha = 36$, we only require $M = 256$ boundary elements to model the oscillatory behaviour accurately and therefore the computation time is reasonable. However, the computation times for the hybrid methods are still faster. Sub-plot (b) shows the solution Φ along the boundary computed using the DEA based hybrid method with the same discretisation parameters that were used for the interior solution in sub-plot (a). The DEA and SHFA based approaches give visually identical solutions over the entire boundary and so just one of the plots is shown for brevity. In this figure we observe the expected symmetry, with identical solutions along all four edges of the square. We also observe the expected physical behaviour since the Gaussian pulse reaches the centre of each edge ($s = 0.5, 1.5, 2.5, 3.5$) first and then spreads across to the corners, after which time the peaks represent reflected waves propagating in a regular and symmetric fashion. In comparison to the boundary solution calculated using the CQBEM shown in Figure 3.8, we observe that the boundary solution shown in 5.20 (b) also matches the CQBEM calculation well, as expected.

Table 5.14 shows the error results and convergence rates for the interior solution calculated via the DEA and SHFA based hybrid methods, in which the high frequency approximations are implemented whenever $|\mathrm{Re}(k_l)| > 80$. This table uses the same parameters as before, with a fixed discretisation of $\Lambda = 180$ global directions and we investigate the errors and convergence rates as we double the number of time-steps and increase the number of boundary elements by a factor of four. The errors are computed using (5.32) with subsequent interior solutions as we double the number of time-steps. From the table we observe that the DEA and SHFA based hybrid methods have identical error results and convergence rates. In comparison to the error results and convergence rates calculated using CQBEM, as shown in Table 3.7, we can determine that the results from Table 5.1 are identical. Therefore for the this choice of α the hybrid methods can numerically solve this example as accurately as CQBEM but with faster computations.

We next investigate examples with temporal profile (5.34) and parameters $\alpha = 4096$, $t_0 = 0.1$ in order to obtain a broadband signal. This choice also ensures $P_0(0)$ is zero to double precision meaning that the initial conditions (5.2) will be satisfied. Figure 5.21 (a) shows the numerical interior solution observed at $\boldsymbol{x} = (0.25, 0.25)$ calculated using both the SHFA and the DEA based hybrid methods. Most of the plotted lines represent the reverberant solution U, which is equivalent to the full solution Φ with the contribution of

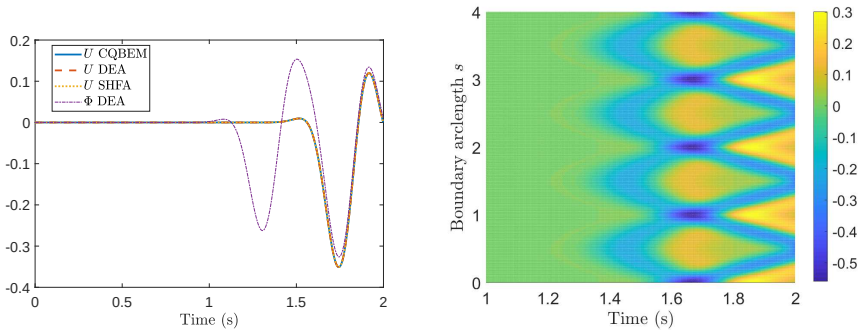

(a) (b)

Figure 5.20: Solution to the wave equation for a unit square domain driven by a point source located at the centre $\boldsymbol{x}_0 = (0.5, 0.5)$ with temporal profile (3.42) and parameters $\alpha = 36$ and $t_0 = 1$. The discretisation parameters are chosen as $M = 512$ boundary elements, $\Lambda = 128$ global directions, $\lambda = 10^{-8/\widetilde{N}}$ and $N = \widetilde{N}/2 = 512$ time-steps. The left-hand plot (a) shows either the interior solution Φ or the reverberant solution U observed at the point $\boldsymbol{x} = (0.25, 0.25)$. Sub-plot (b) shows the solution along the boundary of the unit square domain calculated via the DEA based hybrid CQ scheme. The solution is shown for $1 < t < T = 2$ to focus on the late time behaviour, since the solution is zero for $t \leq 1$. In both hybrid methods, the high frequency approximations are applied whenever $|\mathrm{Re}(k_l)| > 80$.

				DEA		SHFA	
$\widetilde{N}$	N	M	η	Error	EOC	Error	EOC
128	64	4	-	-	-	-	-
256	128	16	23	0.8467	-	0.8467	-
512	256	64	24	0.2415	1.81	0.2415	1.81
1024	512	256	25	0.0571	2.08	0.0571	2.08
2048	1024	1024	26	0.0092	2.63	0.0092	2.63

Table 5.14: Errors and convergence rates for the reverberant solution U at the point $\boldsymbol{x} = (0.25, 0.25)$ for a unit square domain driven by a point source located at the centre $\boldsymbol{x}_0 = (0.5, 0.5)$ with temporal profile (3.42) and parameters $\alpha = 36$, $t_0 = 1$, $T = 2$ and $\Lambda = 180$ global directions. The interior solutions were calculated numerically using the DEA and SHFA based hybrid CQ schemes whereby the high frequency approximations were applied whenever $|\mathrm{Re}(k_l)| > 80$.

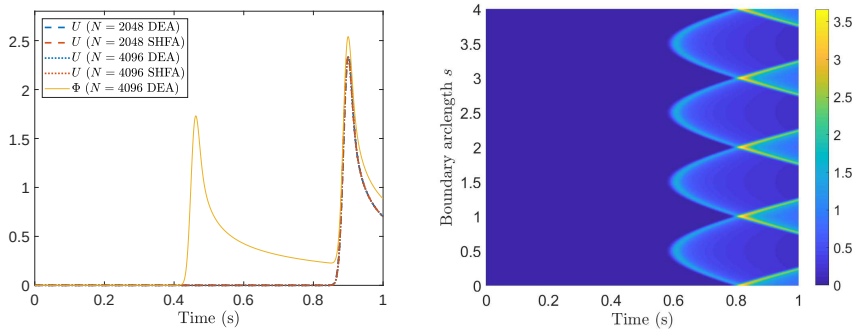

(a) (b)

Figure 5.21: Solution to the wave equation for a unit square domain driven by a point source located at the centre $\boldsymbol{x}_0 = (0.5, 0.5)$ with temporal profile (5.34) and parameters $\alpha = 4096$ and $t_0 = 0.1$. The discretisation parameters are chosen as $M = 1024$ boundary elements, $\Lambda = 180$ global directions and $\lambda = 10^{-8/\widetilde{N}}$. The left-hand plot (a) shows either the interior solution Φ or the reverberant solution U observed at the point $\boldsymbol{x} = (0.25, 0.25)$ for $N = \widetilde{N}/2$ time-steps for as specified in the legend. Sub-plot (b) shows the solution along the boundary of the unit square domain for $N = \widetilde{N}/2 = 4096$ using the DEA based hybrid CQ scheme. In both hybrid methods, the high frequency approximations are applied whenever $|\mathrm{Re}(k_l)| > 350$.

the direct source excitation removed, calculated using both hybrid methods for $T = 1$. The solid line shows a plot of Φ for completeness. The high frequency approximations are implemented whenever $|\mathrm{Re}(k_l)| > 350$ and we employ $M = 1024$ boundary elements to provide a good level of accuracy up to the BEM cut-off wavenumber k_η. We observe that both high frequency approximations produce identical looking results. Figure 5.21 (b) shows the solution Φ along the boundary computed using the DEA based hybrid method when discretising using $M = 1024$ boundary elements, $N = \widetilde{N}/2 = 4096$ time-steps and $\Lambda = 180$ global directions. The DEA and SHFA based approaches give visually identical solutions over the entire boundary and so just one of the plots is shown for brevity. In this figure we observe the expected symmetry, with identical solutions along all four edges of the square. We also observe the expected physical behaviour since the Gaussian pulse reaches the centre of each edge ($s = 0.5, 1.5, 2.5, 3.5$) first and then spreads across to the corners as in Figure 5.20 (b).

Figure 5.22 shows the Z-transformed boundary solution u_l corresponding to

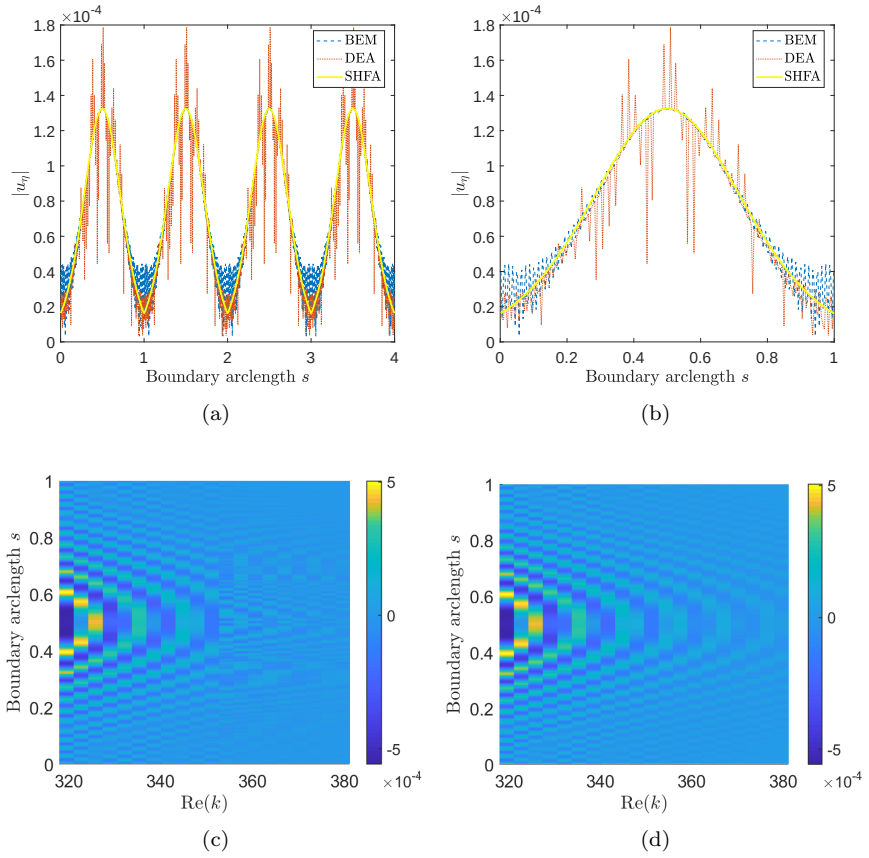

Figure 5.22: The Z-transformed boundary solution u_l on the boundary of a unit square domain driven by a point source located at the centre $\boldsymbol{x}_0 = (0.5, 0.5)$ with temporal profile (5.34) and parameters $\alpha = 4096$ and $t_0 = 0.1$. The discretisation parameters are chosen to be $M = 1024$ boundary elements, $N = \widetilde{N}/2 = 4096$ time-steps, $\Lambda = 180$ global directions and $\lambda = 10^{-8/\widetilde{N}}$. Sub-plots (a) - (b) show $|u_l|$ for $l = \eta$, which corresponds to the wavenumber k_η where we switch between using the BEM and a high frequency approximation. Sub-plot (b) is a zoomed in section along the bottom edge ($0 < s < 1$) only. Sub-plots (c) and (d) show $\mathrm{Re}(u_l)$ computed using the DEA and SHFA based hybrid CQ schemes, respectively. The results are shown for a range of wavenumbers near to the case $l = \eta$, which approximately corresponds to $\mathrm{Re}(k) = 350$.

the parameters $t_0 = 0.1$, $\alpha = 4096$ and discretising using $M = 1024$ boundary elements, $N = \widetilde{N}/2 = 4096$ time-steps and $\Lambda = 180$ global directions. The sub-plots (a) - (b) show $|u_l|$ at $l = \eta$ calculated using the BEM as well as

the proposed high frequency approximations. In sub-plot (a) we observe the solution is symmetric along all four edges of the square. In sub-plot (b), we investigate the solutions focused along the bottom edge ($0 < s < 1$) of the square only, to observe the solutions more clearly instead of showing all four symmetrically repeated copies. In this sub-plot, the BEM solution oscillates rapidly and has a noisy appearance, particularly near the corners. The SHFA result has a smooth slowly varying appearance in comparison as a consequence of the SHFA not including any reflected waves. However, the DEA result does include the reflected wave contributions but loses accuracy due to difficulties relating to phase reconstruction when the amplitudes approximated by the full wave BEM simulation are rapidly oscillating. Recall that one of the fundamental assumptions of the plane wave solution ansatz (5.8) is that the amplitude is slowly varying. One reason that this assumption is less valid here is due to the fact that the solution is now a superposition of circular waves that we are approximating by a superposition of plane waves. The result is that the DEA based scheme underestimates the oscillation amplitude near the corners and an overestimates on either side of the peak at the centre of the edge. These inaccuracies are further shown in sub-plots (c) and (d), which present the DEA and SHFA based hybrid method approximations of $\mathrm{Re}(u_l)$, respectively along the bottom edge, for wavenumbers close to k_η where $\mathrm{Re}(k_\eta) \approx 350$. In these plots we can see a difference in the results when $\mathrm{Re}(k) \approx 350$, where we switch between the BEM and a high frequency approximation. In sub-plot (c), the solution for $\mathrm{Re}(k) > 350$ appears to be corrupted by noise, which is most visible around the middle of the edge at $s = 0.5$. In sub-plot (d) for SHFA, the solution suffers from the omission of wave interference patterns, which is most evident close to the corners at $s = 0$ and $s = 1$.

Although we observed some limitations of the high frequency approximations in Figure 5.22, there does not appear to be any significant differences between the methods in the time-dependent solution, as shown in Figure 5.21. We therefore investigate further by repeating the analysis with the same parameters but using a lower threshold $k^* = 90$ for switching between the BEM and a high frequency approximation. We choose the discretisation parameters to be $N = \widetilde{N}/2 = 4096$ time-steps, $M = 256$ boundary elements and $\Lambda = 180$ global directions. The results are shown in Figure 5.23. Sub-plot (a) depicts the time-dependent interior reverberant solutions U for the DEA and SHFA based hybrid methods for the case when the threshold is $k^* = 90$ compared to the reverberant solutions when $k^* = 350$ taken from Figure 5.21 and discretised with $M = 1024$

boundary elements. The solid line shows a plot of Φ for completeness. From this figure, we observe that the peak of the pulse at $t = 0.9$ for U when $k^* = 90$ is smaller than when $k^* = 350$. In addition, for the DEA based hybrid method we observe some oscillation in the time region $0.6 < t < 0.8$ suggesting that there are some inaccuracies in the numerical solution for this choice of k^*. In sub-plots (b) - (d) we again observe the same limitations with the high frequency approximations. Sub-plot (b) shows the absolute value of the boundary solution u_l at $l = \eta$, along the bottom edge of the square, calculated using the BEM, DEA and SHFA approximations. Sub-plots (c) and (d) show the DEA and SHFA based hybrid method approximations of $\mathrm{Re}(u_l)$ for wavenumbers close to k_η where $|\mathrm{Re}(k_\eta)| \approx 90$. In these plots we observe that the inaccuracies are even more noticeable with both methods displaying the same discrepancies as before. Sub-plot (e) shows $\mathrm{Re}(u_l)$ for wavenumbers close to k_η where $|\mathrm{Re}(k_\eta)| \approx 90$, where u_l was computed using the BEM for all values of k. Comparing sub-plots (c) and (d) to sub-plot (e), we observe how inaccurate the DEA solution is in comparison to the BEM solution when the cut-off frequency is chosen to low. We also observe the SHFA behaving similarly to the BEM solution.

We next investigate the behaviour of the solution by changing the number of global directions, Λ, in the DEA based hybrid method. Until this point in the results for $\alpha = 4096$, we have only performed calculations with a fixed number of global directions $\Lambda = 180$. We now repeat the analysis above with the same parameters, $t_0 = 0.1$ and $\alpha = 4096$, but investigate the solutions with $\Lambda = 90$ and $\Lambda = 360$, while implementing the switch from the BEM to the DEA based high frequency approximation whenever $|\mathrm{Re}(k_\eta)| > 350$. Figure 5.24 shows the results computed using $N = \widetilde{N}/2 = 4096$ time-steps and $M = 1024$ boundary elements. Sub-plot (a) shows either the interior solution Φ or the reverberant solution U observed at the point $\boldsymbol{x} = (0.25, 0.25)$ using different choices of Λ for the number of global directions as specified in the legend. From this plot, we observe that there is no clear difference between the choices. Sub-plot (b) shows the absolute value of the boundary solution u_l at $l = \eta$ calculated using the DEA based approximation for different choices of Λ along the bottom edge only ($0 < s < 1$). Again, we observe the DEA solutions lose accuracy even if we increase the number of directions. The sub-plots (c) and (d) show the DEA approximations of $\mathrm{Re}(u_l)$ for wavenumbers close to k_η where we consider wavenumbers, $\mathrm{Re}(k_\eta) \approx 350$ with $\Lambda = 90$ and $\Lambda = 360$, respectively. We observe that by increasing the number of directions Λ in the global set, there is no significant difference. In comparison to Figure 5.22 (c), we observe similar

behaviour in the appearance of noise being most visible around the middle of the edge at $s = 0.5$. We now calculate the relative errors up to $T = 1$ using (5.32) with subsequent solutions U for time-steps $N = \widetilde{N}/2 = 4096$ and $N = \widetilde{N}/2 = 2048$ with a fixed number of boundary elements $M = 1024$. The error calculated when $\Lambda = 90$ is 0.0198 , the error when $\Lambda = 180$ is 0.0194 and the error when $\Lambda = 360$ is 0.0240. Therefore, as we increase the number of directions, from $\Lambda = 90$ to $\Lambda = 180$ there is a slight increase in accuracy, which is not visible by eye from the time-domain interior solutions in Figure 5.24 (a). However, once we double the number of directions again, the error increases slightly.

In the DEA based scheme to model the point source, the number of ray directions Λ required to ensure an accurate solution is much larger than in the case with the plane-wave boundary data. However, as mentioned in the results above, the DEA based scheme for point sources suffers from poor accuracy as the method was unable to accurately represent circular waves without using a large number of ray directions Λ that would remove any advantage in the computational run time compared to implementing the CQBEM. Therefore the recommendation for implementing the SHFA based scheme is now discussed. As mentioned previously at the end of the square domain results in Section 5.4.1, the choice of k^* is dependent on the choices for the parameters α and t_0 in the Neumann boundary condition (5.23). For the point source case, this is dependent on the choices for α and t_0 in the temporal profile (5.34). For a broadband signal such as was the case when $\alpha = 4096$ the method requires a large number of time-steps and may also be required to be over-resolved by choosing the number of frequencies independently. One must still ensure that there are enough boundary elements as suggested in [130] up to the cut-off frequency to ensure sufficient accuracy for the solutions calculated via the BEM. If the interior solution plot appears to include additional oscillations or appears noisy, then the model may require more time-steps and frequencies to model the highly oscillatory behaviour. To improve accuracy one may increase the choice of k^* such that more wavenumbers are calculated via the BEM as part of the low frequency region. Again to better understand if the phase matching was constructed successfully one can investigate the behaviour of the $\mathrm{Re}(u_l)$ along the boundary in the vicinity of the cut off wavenumber chosen. The solutions calculated via the BEM and those calculated via a HFA should appear smooth as they cross over the switch frequency. If one can clearly view a discrepancy between the two methods then perhaps more refined discretisations are required

or the phase reconstruction has been performed incorrectly.

Irregular polygon domain

We now consider the case when the domain is an irregular polygon as shown in Figure 5.19 (b), taking the source point to be $\boldsymbol{x}_0 = (0.648, 0.5)$. We choose $c = 1$ as before and initially consider the temporal profile to be (3.42) with parameters $\alpha = 36$ and $t_0 = 1$ so that we can compare against the results from Section 3.4.2. Figure 5.25 (a) shows the numerical interior solution at $\boldsymbol{x} = (0.42, 0.275)$ and compares the results of using the DEA and SHFA based hybrid methods and a solution computed using the CQBEM up to $T = 2$. In this sub-plot, most of the plotted lines represent the reverberant solution U except the solid line, which shows a plot of the full solution Φ. We apply a high frequency approximation whenever $|\mathrm{Re}(k_l)| > 80$ with $M = 512$ boundary elements, $N = \widetilde{N}/2 = 512$ time-steps and $\Lambda = 180$ global directions. We again observe that both hybrid methods produce identical looking results, which are similar to the CQBEM solution. Figure 5.25 (b) shows the solution Φ along the boundary computed using the DEA based hybrid method with the same parameter choices as before. In comparison to the results for the unit square shown in Figure 5.20, the plot here shows the expected loss of symmetry and lack of regularity corresponding to the irregular geometry. In comparison to the boundary solution calculated using CQBEM shown in Figure 3.16, we observe that the boundary solution also matches those from the DEA and SHFA based hybrid methods.

				DEA		SHFA	
$\widetilde{N}$	N	M	η	Error	EOC	Error	EOC
128	64	8	-	-	-	-	-
256	128	32	23	0.5042	-	0.5042	-
512	256	128	24	0.0801	2.65	0.0801	2.65
1024	512	512	25	0.0192	2.06	0.0192	2.06
2048	1024	2048	26	0.0065	1.56	0.0065	1.56

Table 5.15: Errors and convergence rates for the reverberant solution U at the point $\boldsymbol{x} = (0.42, 0.275)$ for an irregular polygon domain driven by a point source located at $\boldsymbol{x}_0 = (0.648, 0.5)$ with temporal profile (5.34) and parameters $\alpha = 36$, $t_0 = 1$, $T = 2$ and $\Lambda = 180$ global directions. The interior solutions were calculated numerically using the DEA and SHFA based hybrid CQ schemes whereby the high frequency approximations were applied whenever $|\mathrm{Re}(k_l)| > 80$.

Table 5.15 shows the error results and convergence rates for the interior solution calculated via the DEA and SHFA based hybrid methods, in which the high frequency approximations are implemented whenever $|\mathrm{Re}(k_l)| > 80$. This table uses the same parameters as before, with a fixed discretisation of $\Lambda = 180$ global directions and we investigate the error and convergence rates as we double the number of time-steps and increase the boundary elements by a factor of four. The errors are computed using (5.32) with subsequent interior solutions as we double the number of time-steps. From the table we notice that the DEA and SHFA based methods again have identical error results and convergence rates, as was the case for the unit square in Table 5.14. In comparison to the error results and convergence rates calculated using CQBEM, as shown in Table 3.12, we can determine that the results are also identical. Therefore for the this choice of α the hybrid methods can numerically solve this example as accurately as CQBEM, but with faster computation times.

We next investigate the results on the irregular polygon domain for the case when P_0 is chosen to be (5.34) with the parameters $\alpha = 4096$ and $t_0 = 0.1$. Again, the source point is chosen to be at $\boldsymbol{x}_0 = (0.648, 0.5)$ and $c = 1$. Figure 5.26 (a) shows the numerical interior solution at $\boldsymbol{x} = (0.42, 0.275)$, comparing the results of using the SHFA with the DEA based hybrid methods up to $T = 1$. The plot shows the reverberant solutions U and also the full solution Φ represented by the solid line. We apply a high frequency approximation whenever $|\mathrm{Re}(k_l)| > 350$ with $M = 1024$ boundary elements and $\Lambda = 180$ global directions. We again observe that both high frequency approximations produce identical looking results. Figure 5.26 (b) shows the solution Φ along the boundary computed using the DEA based hybrid methods with the same parameter choices as before, with $N = \widetilde{N}/2 = 4096$. Compared to the boundary solution for the unit square shown in Figure 5.21 (b), the plot here shows the expected loss of symmetry and lack of regularity corresponding to the irregular geometry. One can relate the position of the initial wavefront reaching Γ shown in Figure 5.26 (b) to the geometry shown in Figure 5.19 (b), where the vertices appear as cusp points in the initial wavefront at $s = 0, 0.96, 1.8, 2.6$ and 3.1.

Figure 5.27 shows the Z-transformed boundary solution u_l corresponding to the same parameter choices as for Figure 5.26. Sub-plot (a) shows $|u_l|$ at $l = \eta$ calculated using the BEM as well as both of the proposed high frequency approximations. We observe similar behaviour as for the unit square domain, in which the BEM solution has a noisy appearance owing to the highly oscillatory interference patterns, particularly close to the vertices and along the

two shorter edges ($s > 2.6$). The SHFA result again has a smooth and slowly varying appearance corresponding to the fact that the SHFA does not include reflected wave contributions. The DEA result also corresponds to the previous observations for the unit square and includes some of the oscillations seen in the BEM result, but to a poor level of accuracy with the same root causes as before. The issues present in both the DEA and SHFA approximations are also shown in the sub-plots (b) and (c), respectively, which show plots of $\mathrm{Re}(u_l)$ for wavenumbers close to $\mathrm{Re}(k) = 350$. In sub-plot (b) for DEA, we see the influence of the spurious noise in the DEA result, particularly for the shorter edges when $s > 2.6$. In sub-plot (c) for the SHFA, the omission of wave interference patterns can be observed, particularly in the vicinity of the vertex at $s = 0.96$, but this deficiency also appears to be less noticeable than for the unit square.

We repeat the investigation of the effect of lowering the wavenumber threshold to $k^* = 90$, as we did for the unit square domain and the results are shown in Figure 5.28. We choose the discretisation parameters to be $N = \widetilde{N}/2 = 4096$ time-steps, $M = 256$ boundary elements and $\Lambda = 180$ global directions. Sub-plot (a) depicts the time-dependent interior reverberant solutions U for the DEA and SHFA based hybrid methods for the case when the threshold is $k^* = 90$ compared to the reverberant solutions when $k^* = 350$ taken from Figure 5.26 using the same discretisation parameters but with $M = 1024$ boundary elements instead. The solid line shows a plot of Φ for completeness. From this figure, we observe that the reverberant solutions computed using both hybrid methods with $k^* = 90$ have additional oscillations after the initial peak, but the oscillations are more dominant in the solution computed via the DEA based hybrid method. In sub-plots (b) - (d) we again observe the same limitations with the high frequency approximations. Sub-plot (b) shows the absolute value of the boundary solution u_l at $l = \eta$ calculated using the BEM, DEA and SHFA approximations. Sub-plots (c) and (d) show the DEA and SHFA based hybrid approximations of $\mathrm{Re}(u_l)$ for wavenumbers close to $|\mathrm{Re}(k)| = 90$. In these plots we observe that the inaccuracies are even more noticeable for $k^* = 90$, with both methods displaying the same shortcomings as before.

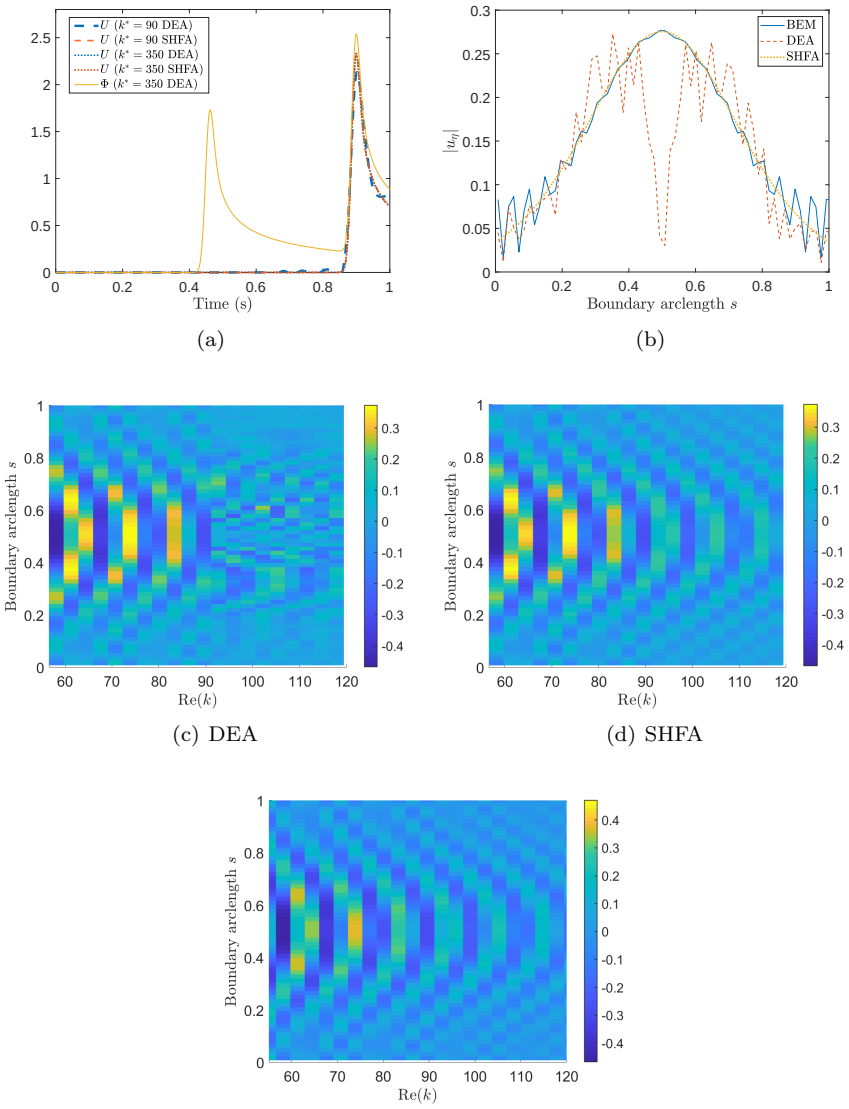

(a) (b)

(c) DEA (d) SHFA

(e) BEM

Figure 5.23: (a): Solution to the wave equation for a unit square domain driven by a point source located at the centre $\boldsymbol{x}_0 = (0.5, 0.5)$ with temporal profile (5.34) and parameters $\alpha = 4096$ and $t_0 = 0.1$. Plot (a) shows the interior solution Φ or the reverberant solution U at $\boldsymbol{x} = (0.25, 0.25)$ for different thresholds k^*. Solutions calculated with a threshold of $k^* = 90$ used $M = 256$ boundary elements, whereas the solutions calculated using a threshold of $k^* = 350$ used $M = 1024$ boundary elements. (b) - (e): The Z-transformed boundary solution u_l on the boundary of the unit square driven by the point source excitation used for plot (a). Sub-plot (b) shows $|u_l|$ for $l = \eta$, which corresponds to the wavenumber k_η where we stop using the BEM and instead use a high frequency approximation. Sub-plots (c) - (e) show $\mathrm{Re}(u_l)$ computed using either the DEA or SHFA based hybrid CQ schemes, or fully using the BEM. The results are shown for a range of wavenumbers in the vicinity of $l = \eta$, which approximately corresponds to $\mathrm{Re}(k) = 90$. Discretisation parameters: $N = \widetilde{N}/2 = 4096$ time-steps, $\Lambda = 180$ global directions and $\lambda = 10^{-8/\widetilde{N}}$.

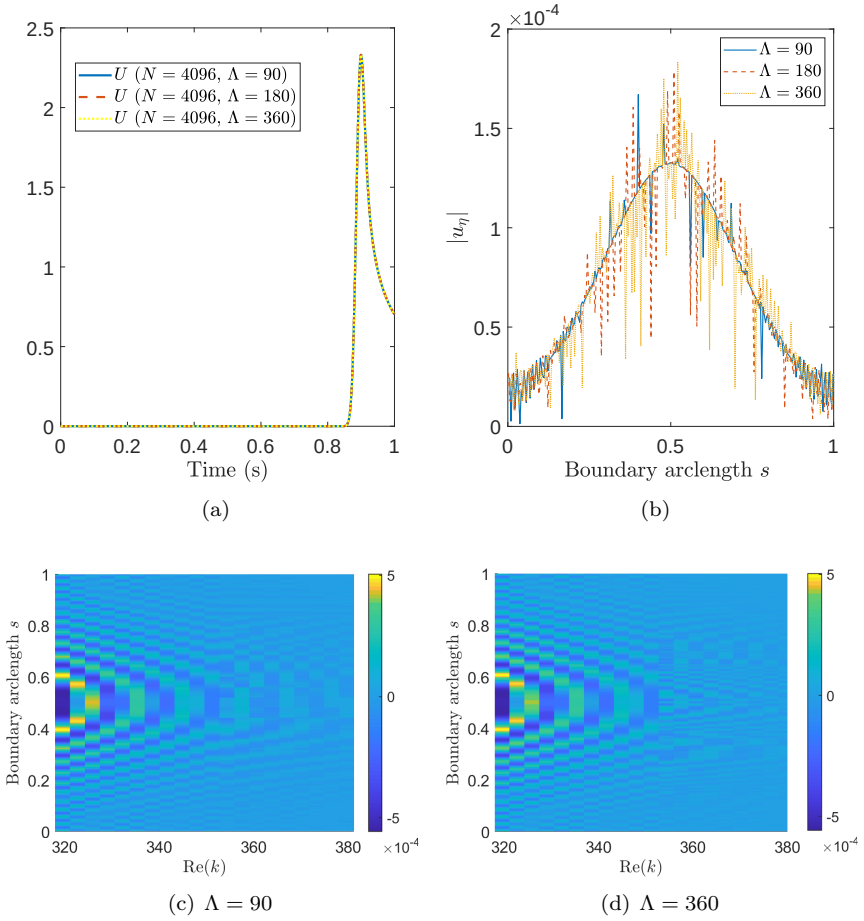

Figure 5.24: (a): Solution to the wave equation for a unit square domain driven by a point source located at the centre $\boldsymbol{x}_0 = (0.5, 0.5)$ with temporal profile (5.34) and parameters $t_0 = 0.1$ and $\alpha = 4096$. Plot (a) shows the reverberant solution U at $\boldsymbol{x} = (0.25, 0.25)$ for different numbers of global directions Λ, as specified by the legend. (b) - (d): The Z-transformed boundary solution u_l on the boundary of the unit square driven by the point source excitation used for plot (a). Sub-plots (c) and (d) show $\mathrm{Re}(u_l)$ computed using the DEA based hybrid CQ scheme for $\Lambda = 90$ and $\Lambda = 360$, respectively. The results are shown for a range of wavenumbers in the vicinity of $l = \eta$, which approximately corresponds to $\mathrm{Re}(k) = 350$. Discretisation parameters: $M = 1024$ boundary elements, $N = \widetilde{N}/2 = 4096$ time-steps and $\lambda = 10^{-8/\widetilde{N}}$.

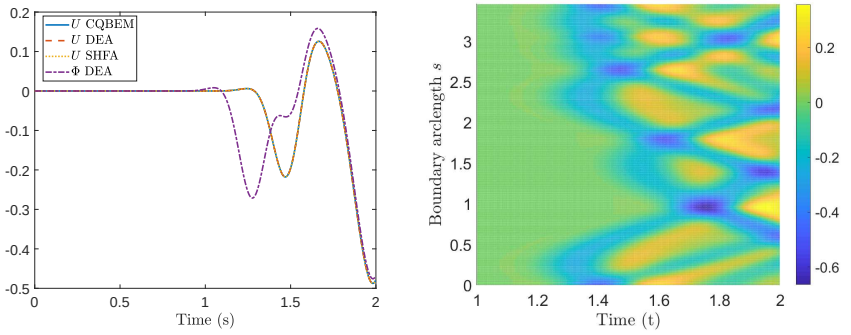

(a) (b)

Figure 5.25: Solution to the wave equation for the irregular polygon domain driven by a point source located at $\boldsymbol{x}_0 = (0.648, 0.5)$ with temporal profile (3.42) and parameters $\alpha = 36$ and $t_0 = 1$. The discretisation parameters are chosen as $N = \widetilde{N}/2 = 512$ time-steps, $M = 512$ boundary elements, $\Lambda = 180$ global directions and $\lambda = 10^{-8/\widetilde{N}}$. The left-hand plot (a) shows either the interior solution Φ or the reverberant solution U observed at the point $\boldsymbol{x} = (0.42, 0.275)$. Sub-plot (b) shows the solution along the boundary of the irregular polygon domain computed using the DEA based hybrid CQ scheme. The solution is shown for $1 < t < T = 2$ to focus on the late time behaviour since the solution is zero for $t \leq 1$. In both hybrid methods, the high frequency approximations are applied whenever $|\mathrm{Re}(k_l)| > 80$.

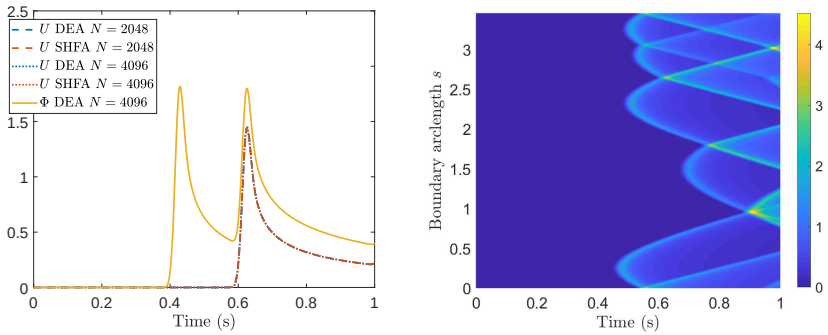

(a) (b)

Figure 5.26: Solution to the wave equation for the irregular polygon domain driven by a point source located at $\boldsymbol{x}_0 = (0.648, 0.5)$ with temporal profile (5.34) and parameters $\alpha = 4096$ and $t_0 = 0.1$. The discretisation parameters are chosen as $M = 1024$ boundary elements, $\Lambda = 180$ global directions and $\lambda = 10^{-8/\widetilde{N}}$. The left-hand plot (a) shows either the interior solution Φ or the reverberant solution U observed at the point $\boldsymbol{x} = (0.42, 0.275)$ for $N = \widetilde{N}/2$ time-steps as specified in the legend. Sub-plot (b) shows the solution along the boundary of the irregular polygon domain for $N = \widetilde{N}/2 = 4096$ using the DEA based hybrid CQ scheme. In both hybrid methods, the high frequency approximations are applied whenever $|\mathrm{Re}(k_l)| > 350$.

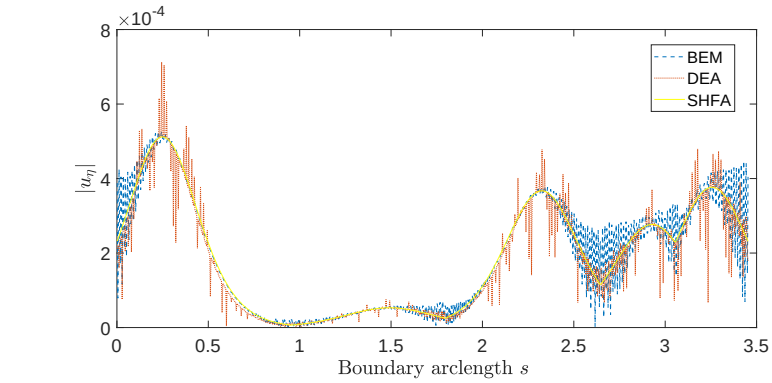

(a)

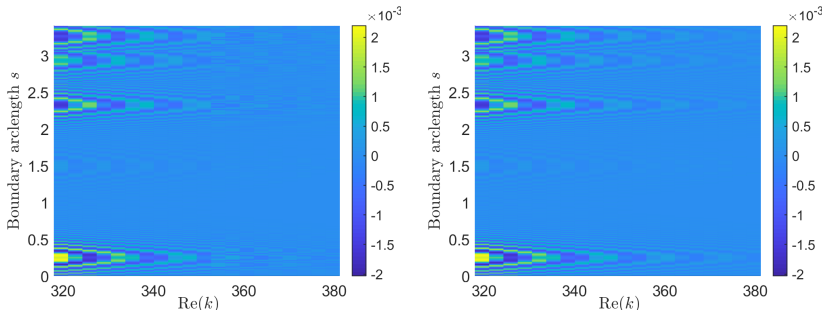

(b) DEA (c) SHFA

Figure 5.27: The Z-transformed boundary solution u_l on the boundary of the irregular polygon domain driven by a point source located at $\boldsymbol{x}_0 = (0.648, 0.5)$ with temporal profile (5.34) and parameters $\alpha = 4096$ and $t_0 = 0.1$. Sub-plot (a) shows $|u_l|$ for $l = \eta$, which corresponds to the wavenumber k_η where we switch between using the BEM and a high frequency approximation. Sub-plots (c) and (d) show $\mathrm{Re}(u_l)$ computed using the DEA and SHFA based hybrid CQ schemes, respectively. The results are shown for a range of wavenumbers near to the case $l = \eta$, which approximately corresponds to $\mathrm{Re}(k) = 350$. Discretisation parameters are chosen to be $M = 1024$ boundary elements, $N = \widetilde{N}/2 = 4096$ time-steps, $\Lambda = 180$ global directions and $\lambda = 10^{-8/\widetilde{N}}$.

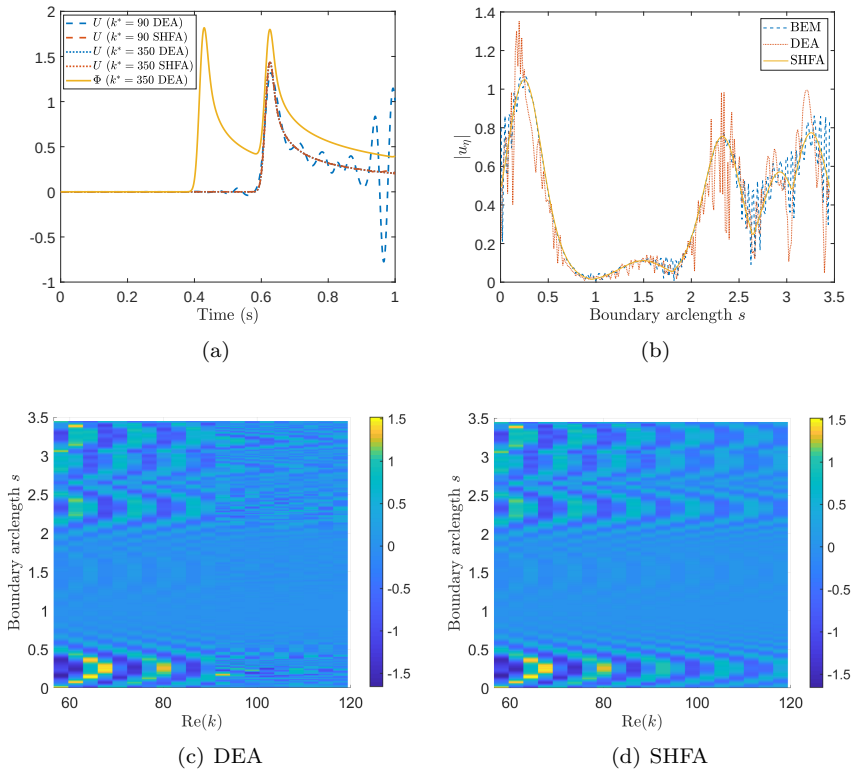

(a) (b)

(c) DEA (d) SHFA

Figure 5.28: (a): Solution to the wave equation for a irregular polygon domain driven by a point source located at $\boldsymbol{x}_0 = (0.648, 0.5)$ with temporal profile (5.34) and parameters $\alpha = 4096$ and $t_0 = 0.1$. Plot (a) shows either the interior solution Φ or the reverberant solution U at $\boldsymbol{x} = (0.97, 0.6)$ for different thresholds k^*. Solutions calculated with a threshold of $k^* = 90$ used $M = 256$ boundary elements, whereas the solutions calculated using a threshold of $k^* = 350$ used $M = 1024$ boundary elements. (b) - (d): The Z-transformed boundary solution u_l on the boundary of the irregular polygon driven by the point source excitation used for plot (a). Sub-plot (b) shows $|u_l|$ for $l = \eta$, which corresponds to the wavenumber where we stop using the BEM and instead use a high frequency approximation, when $k^* = 90$. The lower sub-plots (c) and (d) show $\mathrm{Re}(\Phi_l)$ computed using the DEA and SHFA based hybrid CQ schemes, respectively. The results are shown for a range of wavenumbers in the vicinity of $l = \eta$, which approximately corresponds to $\mathrm{Re}(k) = 90$. Discretisation parameters: $N = \widetilde{N}/2 = 4096$ time-steps, $\Lambda = 180$ global directions and $\lambda = 10^{-8/\widetilde{N}}$.

5.5 Conclusion

We have introduced two hybrid CQ based discretisations of the wave equation for interior acoustic Neumann problems with broadband boundary data or source terms. The CQ method was applied to reformulate the time-domain wave problem into a series of frequency domain Helmholtz problems with complex-valued wavenumbers, in which the boundary data and solutions are connected to those of the original time-dependent problem through the Z-transform. The hybrid methods used alternative approaches for approximating the solution of the Helmholtz problems, dependent on the frequency, or more specifically the magnitude of the real part of the wavenumber. For a specified low frequency region, we applied a direct piecewise constant collocation BEM for the discretisation of the Helmholtz problems, while for the remaining (high) frequency region we developed two high frequency approximation methods, both of which are based on a plane wave decomposition of the acoustic field on the boundary. The first approach was based on dynamical energy analysis, which is used to numerically approximate the plane-wave amplitudes. The phases were then reconstructed by matching the BEM solution to the plane wave ansatz at the maximal frequency where we apply the BEM and the minimal frequency where we apply the plane wave ansatz. The second approach that we used was a simple high frequency approximation (SHFA) method based on applying the Neumann-to-Dirichlet map for plane waves to the given boundary data. This approach is only valid if reflected wave contributions are negligible, which can often be the case for CQ discretisations if the imaginary part of the wavenumber is relatively large leading to high levels of dissipation. We then performed numerical experiments to demonstrate the effectiveness of both hybrid approaches for the cases of plane wave boundary data and excitation by an interior point source. In both situations the hybrid methods were able to provide faster computations than using the conventional CQBEM. However, the DEA based scheme for point sources suffered from poor accuracy as the method was unable to accurately represent circular waves without using a large number of ray directions that would remove any efficiency gains. A promising direction for further work in this case could be to use an image-source type method for the high frequency approximation, in which the solution would be expressed more efficiently as a series of circular waves.

Comparing the DEA and SHFA high frequency approximations against each other, we determine that in terms of computational efficiency and simplicity of

implementation then the SHFA is highly preferable since it can be implemented at low cost within a single line of code. It also has the advantageous property that when refining Δt alone and fixing constant the maximal frequency at which a BEM calculation is performed, then the computational cost of the method overall then scales as $\mathcal{O}(1)$ [133]. The DEA approach is in theory able to provide better approximations that include reflected wave contributions. However, we found that these improvements did not always make any significant improvement to the time-domain result and that when we used a lower threshold wavenumber k^* for switching from BEM to the high frequency approximation, then DEA often performed worse owing to inaccuracies introduced in the phase reconstruction process, in particular for the interior point source case. Since the DEA approach also results in a greater computational run time, due to requiring a large number of discretised directions when considering larger models, then we conclude that the accuracy gains from including higher order reflections in the hybrid CQ schemes here do not typically provide sufficient improvements to choose DEA over the SHFA based scheme. One significant reason for this appears to be the large imaginary parts of the wavenumbers within the BDF2 based CQ method that provide a strong damping effect within the DEA calculations, making the reflected wave/ray contributions relatively small.

Chapter 6

Conclusions and further work

In this thesis we have introduced two new hybrid CQ based discretisations for numerically solving the wave equation when the solution includes broadband frequency content. After undergoing a thorough investigation of the literature on numerical methods used to solve the wave equation in Chapter 1, it was decided that the CQ method would be applied to the time-domain wave problem. The CQ method provides a simple way to obtain a stable time stepping scheme using the Laplace transform of the kernel function and aside from stability its main advantage, when applied to the wave equation, is that it avoids having to evaluate the convolution kernel in the time-domain by instead solving a simplified system of frequency domain boundary integral equations for the Helmholtz equation. The boundary data and solutions are then connected to those of the original time-dependent problem via the Z-transform. The hybrid methods proposed alternative approaches for the approximation of the Helmholtz problems, dependent on the frequency, or more specifically the magnitude of the real part of the wavenumber. For a specified low frequency region, we applied the BEM for the discretisation of the Helmholtz problems. However, as we discussed in Chapter 2, to model rapidly oscillating waves requires a large number of boundary elements and results in a large computational cost to obtain a reasonable level of accuracy (say 1% relative error). Therefore for the high frequency problems we developed two high frequency approximation methods, both of which are based on a plane wave decomposition of the acoustic field on the boundary.

The first approach is based on dynamical energy analysis, which is used to numerically approximate the plane-wave amplitudes. DEA uses a linear integral operator for transporting densities along ray trajectories in phase-space, between intersections with the boundary of a domain or sub-domain. A Petrov-Galerkin discretisation is applied to the operator in which the directivity is modelled using a finite global set of Dirac delta distributions that can simulate highly directive problems to high accuracy. The phases were reconstructed by matching the BEM solution to the plane wave ansatz at the maximal frequency where we apply the BEM and the minimal frequency where we apply the plane wave ansatz. The second approach that we proposed was a simple high frequency approximation (SHFA) method based on applying the Neumann-to-Dirichlet map for plane waves to the given boundary data. This approach is only valid if reflected wave contributions are negligible, which can often be the case for CQ discretisations if the imaginary part of the wavenumber is relatively large leading to high levels of dissipation.

We now summarise the conclusions of each chapter in this thesis, before discussing some possible further research directions related to the newly proposed hybrid methods.

6.1 Conclusions

In Chapter 2, we first considered solving the Helmholtz equation via the indirect BEM such that the solution is represented via a single layer potential in terms of an unknown layer density σ. We then compared two discretisation methods, the collocation method and the Galerkin method, which were used to discretise the BIE resulting from applying the indirect BEM to the Helmholtz problem. Furthermore, for each discretisation method we also investigated the solution to the Helmholtz problems when using either piecewise constant basis functions or linear basis functions. An analysis was conducted by examining the relative errors and calculating the estimated order of convergence as we increased the wavenumber, physically representing more oscillatory behaviour. We found that, in general, as we increased the wavenumber k that the errors increased. A comparison between the two discretisation methods showed that there was no significant difference, in terms of accuracy, when using the Galerkin method compared to the collocation method. However, the implementation of the Galerkin method results in a more complex calculation due to the additional

integral that the method requires, leading to longer computational times. Similarly, when comparing the results between constant and linear basis functions we observed that there was no significant difference in the errors obtained or the convergence results. The improvements given by the linear basis functions were most evident for smooth domains, which are not the focus of the work in the later chapters of this thesis.

Next in Chapter 2, we derived the BIEs for solving the two-dimensional Helmholtz BVP via the direct BEM with Neumann boundary conditions. The direct BEM expresses the solution in terms of physical quantities. The numerical experiments were performed using the collocation method with constant basis functions. The error and convergence results exhibited a similar behaviour to the results found using the indirect BEM. That is, the errors increased as k increased. Overall the errors were, in general, slightly larger than for the indirect BEM and in most cases, and the convergence rate appeared to be between first and second order.

In Chapter 3, we applied the CQBEM to calculate the numerical solution for a time-domain boundary integral formulation of the two-dimensional wave equation. The CQBEM used a convolution quadrature method for the time discretisation and a direct collocation boundary element method with piecewise constant basis functions for the spatial discretisation. The CQ method reformulates the time-domain wave problem as a system of Helmholtz problems with complex wavenumbers. For our numerical experiments, we considered the homogeneous wave equation with Neumann boundary conditions for the case when a wave propagates into either a unit square and an L-shaped domain. We investigated the errors and estimated convergence rates when applying different multistep methods in the CQ time discretisation. The two methods employed were the backward Euler method and the second order backwards difference formula (BDF2). The results showed that both multistep methods eventually achieved their expected convergence rates and the errors calculated via the BDF2 method were smaller. When considering problems which had no analytical solutions, the error results were estimated from subsequent approximations.

We also considered the case when there is a point source excitation inside the domain. We investigated the errors and estimated convergence rates when using either the backward Euler or the BDF2 time-stepping methods in the CQ approach for the time discretisation. The results showed the expected convergence rates for the time discretisation methods, and in general the errors for the BDF2 method were again smaller than those calculated using the backward

Euler method. We concluded Chapter 3 by discussing how the CQBEM would not be efficient for broadband signal, since the numerical simulations would require a large number of time-steps and boundary elements to model the high frequency content.

In Chapter 4 we considered other options to model the high frequency wave components. We decided that geometrical optics methods, such as ray tracking methods, were not a viable option since the methods become inefficient when considering frequency domain wave problems in bounded domains. We then considered frequency domain approaches such as SEA and DEA. It was decided that a DEA approach would be more advantageous because some of the SEA assumptions are removed, which provides flexibility to apply to different problems without a loss of accuracy. We approximated the Helmholtz equation by representing the solutions as a superposition of plane waves, whose amplitude in a particular direction can be expressed in terms of a wave energy density. We introduced a phase-space boundary integral operator, that is a modified version of the Frobenius-Perron operator, such that the resulting boundary wave energy density can be propagated through the domain. We then applied a Petrov-Galerkin discretisation of the phase-space boundary integral operator. Numerical experiments were undertaken for which we considered a line source travelling from the left edge of either a unit square and an L-shaped domain. We achieved machine accuracy in both domains when the source was travelling perpendicularly to the edge. The direction of the source was then changed to an angle of $3\pi/8$ with respect to the unit normal of the edge, which also resulted in small errors. We then considered experiments when there was a point source in the domain of a unit square, an L-shape or an irregular shaped polygon. We investigated the mean errors as we doubled the number of boundary elements and the number of directions and we achieved small errors in all cases as well as a convergence rate between first and second order.

In Chapter 5, we introduced two novel hybrid CQ based discretisations of the wave equation for interior acoustic Neumann problems with broadband boundary data or source terms. As discussed at the beginning of this chapter, these methods involve applying a CQ method to reformulate the time-domain wave problem into a series of frequency domain Helmholtz problems with complex-valued wavenumbers. The hybrid methods propose alternative approaches for the approximation of the Helmholtz problems, whereby at lower frequencies we use a BEM and at higher frequencies we use a plane-wave approximation. The first hybrid approach applied DEA to numerically approximate the plane-wave

amplitudes. The phases were reconstructed by matching the BEM solution to the plane wave ansatz at the maximal frequency where we apply the BEM and the minimal frequency where we apply the plane wave ansatz. The second approach that we proposed was a SHFA method based on applying the Neumann-to-Dirichlet map for plane waves to the given boundary data.

We then performed numerical experiments to demonstrate the effectiveness of both hybrid approaches for the cases of plane wave boundary data and excitation by an interior point source. In both situations the hybrid methods were able to provide faster computations than using the CQBEM with similar accuracy, including when we considered plane wave boundary data with a low bandwidth. However, when we considered the broadband behaviour, the DEA based scheme for point sources suffered from poor accuracy owing to its inability to accurately represent circular waves without using a large number of ray directions that would remove any efficiency gains. Comparing the DEA and SHFA based hybrid methods against each other, the SHFA based hybrid approach has a simpler implementation and is more computationally efficient than the DEA based scheme. Although the DEA approach is able to provide better approximations that include reflected wave contributions, these improvements did not typically make any significant improvement to the time domain result. Furthermore, when using lower threshold frequencies for switching from BEM to the high frequency approximation, DEA often performed worse owing to inaccuracies introduced in the phase reconstruction process.

6.2 Further work

We now discuss further research ideas related to the newly proposed hybrid methods.

6.2.1 Extension to non-convex geometry

In our numerical examples, we consider calculating the interior solution to the inhomogeneous wave equation subject to a source propagating inside the domain via the hybrid methods in Section 5.4.2. In these numerical problems we did not consider domains that are divided into more than one sub-domain in the DEA model and only considered the unit square and irregular polygon domains. When we consider a domain with multiple sub-domains in DEA, the direct source contribution from the fundamental solution to the free-space problem

is included but must be manually added in the source sub-domain. This can be resolved by also solving the BEM problem in each sub-domain separately as well as implementing the high frequency approximations separately for each sub-domain.

6.2.2 Three-dimensional geometry

In our numerical examples throughout this work we only considered solving the two-dimensional acoustic wave equation. To fully implement the hybrid methods for modelling more realistic scenarios, extending the proposed methods to model three-dimensional domains would be crucial. For the low frequency content, an application of a collocation based CQBEM for numerically solving three-dimensional transient acoustic problems was considered in [133] for large scale domains. The acoustic wave equation is reformulated as a boundary integral representation with the same single and double layer potentials, but now the Green's function is the three-dimensional free-space fundamental solution to the wave equation instead of the two-dimensional one. For the spatial discretisation, the BEM now divides the domain into two-dimensional boundary surface elements instead of the one-dimensional boundary elements, which will result in a longer computational run time and increased storage. For the high frequency content, we refer to [10] in which the DEA was extended to model three-dimensional domains by propagating wave energy densities through tetrahedral meshes. The energy densities to be computed are transported along ray trajectories through tetrahedral mesh elements using the finite dimensional approximation of a ray transfer operator. An orthonormal piecewise-constant basis approximation was applied for the spatial discretisation and orthonormal Zernike polynomials were applied for the direction coordinate discretisation. Therefore the hybrid methods could be extended to three-dimensional domains by considering the research we have discussed above.

6.2.3 Alternative high frequency approximations

For the high frequency content in the hybrid methods, we could consider other high frequency approximations to compare against the current models proposed in this work. An overview of some high frequency approximations can be found in [161] and in Section 1.3 of this work, in which we discuss different mathematical models based on geometrical optics. Geometrical optics approximations are asymptotic approximations obtained when the frequency tends to infinity. Some

general geometrical optics methods which could be considered include wave front methods, moment methods, full phase-space methods and the Hamilton–Jacobi method. However a promising alternative high frequency approximation to the DEA method for point source problems, such as those considered here, is the image source method [152, 166]. The image source method is based on a set of image sources, which is a mirror image of the original sound source created by the surface. The image-sources are then reflected against all the surfaces again and this process is repeated until a termination condition is satisfied, resulting in accurate solutions. However, if it becomes necessary to calculate many reflections, then the computational run time would rapidly increase. In the context of a BDF2 based CQ scheme, the (typically) large imaginary parts of the wavenumbers considered will probably mean that only a moderate number of reflections must be accounted for though.

6.2.4 Higher-order basis functions

The CQBEM used to solve the Helmholtz problems within the low frequency region uses a collocation based BEM with piecewise constant basis functions for the spatial discretisation. Further work could be undertaken to investigate using higher order basis functions for the spatial discretisation, such as high order polynomial basis functions. Although high order methods have not received a lot of interest recently in room acoustics, an overview of BEM discretisation methods can be found in the literature review of [82].

6.2.5 Alternative time-stepping schemes

The hybrid approaches that we consider in this work solve Helmholtz problems in a low frequency region via the collocation based CQBEM with piecewise constant basis functions in space and a BDF2 based CQ method in time. In our numerical examples in Section 3.4, we compared error and convergence rates for a variety of problems using a collocation based CQBEM with piecewise constant basis functions in space and either a backward Euler or BDF2 method for the time discretisation. In our future work one could consider applying alternative time-stepping methods such as high-order Runge-Kutta methods, which have been implemented by Banjai and co-authors for a variety of wave problems [16, 17, 18] and have shown excellent stability properties.

Appendices

Appendix A

Green's functions and the Dirac delta

A.1 The Dirac generalised function δ

The shifted Dirac generalised function delta, $\delta_a(x) = \delta(x-a)$, $x, a \in \mathbb{R}$, has the following properties

$$\delta_a(x) = 0, \quad \text{if} \quad x \neq a, \tag{A.1}$$

$$\int_{-\infty}^{\infty} \delta_a(x)dx = 1, \tag{A.2}$$

$$\int_{-\infty}^{\infty} \delta_a(x)f(x)dx = f(a). \tag{A.3}$$

The latter of these properties (A.3) is known as the sifting property and holds for all continuous and bounded functions f. When composed with a function g, then δ_a satisfies

$$\int_{-\infty}^{\infty} f(x)\delta\left(g(x)\right)dx = \sum_i \frac{f(x_i)}{|g'(x_i)|}, \tag{A.4}$$

$$\delta(g(x)) = \sum_i \frac{\delta(x-x_i)}{|g'(x_i)|}, \tag{A.5}$$

where x_i are the roots of $g(x) = 0$ and $\delta = \delta_0$ is known simply as the Dirac generalised function delta. Finally, extending to multiple dimensions and letting

$\boldsymbol{x} = (x_1, x_2, ..., x_n)$ and $\boldsymbol{a} = (a_1, a_2, ..., a_n)$, then

$$\delta_{\boldsymbol{a}}(\boldsymbol{x}) = \delta_{a_1}(x_1)\delta_{a_2}(x_2)...\delta_{a_n}(x_n). \tag{A.6}$$

Physically, $\delta_{\boldsymbol{a}}(\boldsymbol{x})$ corresponds to a unit impulse located at $\boldsymbol{x} = \boldsymbol{a}$. Note that properties (A.1) to (A.3) extend directly to the multidimensional case by replacing x with $\boldsymbol{x}$, a with $\boldsymbol{a}$ and integrating over $\mathbb{R}^n$ instead of $\mathbb{R}$.

A.2 Green's functions

A free space Green's function in two dimensions $G(\boldsymbol{x}, \boldsymbol{y})$ is a solution to an inhomogeneous differential equation of the form

$$\mathcal{L}G(\boldsymbol{x}, \boldsymbol{y}) = \delta(\boldsymbol{x} - \boldsymbol{y}), \tag{A.7}$$

where $\mathcal{L}$ is a regular n^{th} order linear differential operator, $\boldsymbol{x}, \boldsymbol{y} \in \mathbb{R}^2$ and $\delta(\boldsymbol{x} - \boldsymbol{y})$ is the Dirac generalised function delta. A particular solution to the linear differential equation $\mathcal{L}u(\boldsymbol{x}) = f(\boldsymbol{x})$, with forcing term f, is then given by

$$u(\boldsymbol{x}) = \iint_{\mathbb{R}^2} G(\boldsymbol{x}, \boldsymbol{y}) f(\boldsymbol{y}) d\boldsymbol{y}. \tag{A.8}$$

It is easy to check that (A.8) is a solution of $\mathcal{L}u = f$ by applying $\mathcal{L}$ to both sides as follows

$$\mathcal{L}u(\boldsymbol{x}) = \iint_{\mathbb{R}^2} \mathcal{L}G(\boldsymbol{x}, \boldsymbol{y}) f(\boldsymbol{y}) d\boldsymbol{y} = \iint_{\mathbb{R}^2} \delta(\boldsymbol{x} - \boldsymbol{y}) f(\boldsymbol{y}) d\boldsymbol{y} = f(\boldsymbol{x}),$$

and using the delta function property (A.3). Physically, $G(\boldsymbol{x}, \boldsymbol{y})$ represents the response of the system $\mathcal{L}u = f$ at $\boldsymbol{x}$ to a unit impulse at $\boldsymbol{y}$. The Green's function is continuous and has continuous derivatives with respect to $\boldsymbol{x}$ up to order $n-2$ for all values of $\boldsymbol{x}$ and $\boldsymbol{y}$.

We are interested in the free space Green's functions for the two-dimensional Laplace equation (2.2) when $k = 0$, the Helmholtz equation (2.2) and the wave equation (3.1). The free space Green's function for the Laplace equation is given by [100]

$$G_0(\boldsymbol{x}, \boldsymbol{y}) := \frac{1}{2\pi} \ln(\|\boldsymbol{x} - \boldsymbol{y}\|), \tag{A.9}$$

and satisfies

$$\Delta G_0(\boldsymbol{x}, \boldsymbol{y}) = \delta(\boldsymbol{x} - \boldsymbol{y}). \tag{A.10}$$

The free space Green's function for the Helmholtz equation is given by [100]

$$G_k(\boldsymbol{x}, \boldsymbol{y}) := -\frac{i}{4} H_0^{(1)} \left(k \left\| \boldsymbol{x} - \boldsymbol{y} \right\| \right), \tag{A.11}$$

where $H_0^{(1)}$ is the zeroth order Hankel function of the first kind, and G_k, satisfies

$$\Delta G_k(\boldsymbol{x}, \boldsymbol{y}) + k^2 G_k(\boldsymbol{x}, \boldsymbol{y}) = \delta(\boldsymbol{x} - \boldsymbol{y}). \tag{A.12}$$

The free space Green's function for the wave equation is given by [100]

$$G(\boldsymbol{x}, t) := \frac{H(t - \left\| \boldsymbol{x} \right\| / c)}{2\pi \sqrt{t^2 - \left\| \boldsymbol{x} \right\|^2 / c^2}}, \tag{A.13}$$

where H is the Heaviside step-function

$$H(x) = \begin{cases} 0 & x < 0 \\ & \\ 1 & x > 0 \end{cases}. \tag{A.14}$$

Then G satisfies

$$\left(\Delta - \frac{1}{c} \frac{\partial^2}{\partial t^2} \right) G(\boldsymbol{x} - \boldsymbol{y}, t - \tau) = \delta(\boldsymbol{x} - \boldsymbol{y}) \delta(t - \tau),$$

and represents the response to a unit impulse at time $t = \tau$, located at $\boldsymbol{x} = \boldsymbol{y}$.

Appendix B

Evaluation of some integrals containing the Green's function for the Laplace equation

In this appendix we determine exact formulae for the following boundary integrals that arise after implementing the singularity subtraction procedure for the Helmholtz equation outlined in Section 2.6. In particular, we consider evaluating the boundary integral from equation (2.40):

$$\int_{E_j} \ln\left(\|\boldsymbol{x}-\boldsymbol{y}\|\right) b_j(\boldsymbol{y}) d\Gamma_{\boldsymbol{y}}, \tag{B.1}$$

for the case when $\boldsymbol{x} \in E_j$. Here the boundary Γ was divided into n elements E_j for $j = 1, 2, ..., n$, $\boldsymbol{x} = (x_1, x_2)$ and $\boldsymbol{y} = (y_1, y_2)$ are points along E_j. The basis functions b_j are either piecewise constants defined by (2.29) or piecewise linears defined by (2.31). For simplicity, we parameterise $\boldsymbol{x}$ and the integration point $\boldsymbol{y}$ by an arclength parameter which we denote as $s(\boldsymbol{x}) \in [0, L)$ and $t(\boldsymbol{y}) \in [0, L)$, respectively, where L is the total boundary length. We will consider evaluating (B.1) for both a circle and a polygon domain.

B.1 Polygon domain

B.1.1 Piecewise constant basis function

For the case when the domain is a polygon, and b_j are piecewise constant basis functions the boundary integral (B.1) simplifies to

$$\int_{E_j} \ln(|s(\boldsymbol{x}) - t(\boldsymbol{y})|) d\Gamma_{\boldsymbol{y}} = (|s(\boldsymbol{x}) - t(\boldsymbol{y})|) \left(\ln(|s(\boldsymbol{x}) - t(\boldsymbol{y})|) - 1\right)\Big|_{E_j}. \quad \text{(B.2)}$$

Here we have made use of the fact that $b_j(\boldsymbol{y}) = 1$ for $\boldsymbol{y} \in E_j$ and that for a straight line elements as on a polygon, $\|\boldsymbol{x} - \boldsymbol{y}\| = |s(\boldsymbol{x}) - t(\boldsymbol{y})|$, where $s, t \in [0, L)$ are arclength parameters with the same origin as introduced previously.

B.1.2 Piecewise linear basis function

For piecewise linear basis functions, we denote h by the size of element E_j and set $t_j = t(\boldsymbol{y}_j)$ for $j = 1, 2, ..., n$, as the boundary node connecting E_j and E_{j+1}, as shown in Figure 2.2. The boundary integral (B.1) with piecewise linear basis functions (2.31) for $j = 1, 2, ..., n$, may be written as

$$\begin{aligned} &\int_{E_j} \ln(|s(\boldsymbol{x}) - t(\boldsymbol{y})|) \frac{(t(\boldsymbol{y}) - t_{j-1})}{h} d\Gamma_{\boldsymbol{y}} \\ &+ \int_{E_{j+1}} \ln(|s(\boldsymbol{x}) - t(\boldsymbol{y})|) \frac{(t_{j+1} - t(\boldsymbol{y}))}{h} d\Gamma_{\boldsymbol{y}}. \end{aligned} \quad \text{(B.3)}$$

Note that the periodicity of the boundary curve Γ means that $E_{n+1} = E_1$. We now just consider the first integral term over element E_j in equation (B.3). We rewrite the integral by adding and subtracting the term $(s(\boldsymbol{x})/h) \ln(|s(\boldsymbol{x}) - t(\boldsymbol{y})|)$ to the integral as follows

$$\int_{E_j} \ln(|s(\boldsymbol{x}) - t(\boldsymbol{y})|) \frac{(t(\boldsymbol{y}) - t_{j-1} + s(\boldsymbol{x}) - s(\boldsymbol{x}))}{h} d\Gamma_{\boldsymbol{y}}.$$

We then split the above expression into two integrals

$$\begin{aligned} &\frac{(s(\boldsymbol{x}) - t_{j-1})}{h} \int_{E_j} \ln(|s(\boldsymbol{x}) - t(\boldsymbol{y})|) d\Gamma_{\boldsymbol{y}} \\ &- \int_{E_j} \frac{(s(\boldsymbol{x}) - t(\boldsymbol{y}))}{h} \ln(|s(\boldsymbol{x}) - t(\boldsymbol{y})|) d\Gamma_{\boldsymbol{y}}. \end{aligned} \quad \text{(B.4)}$$

By considering the first integral of (B.4), since the integration point is with respect to $\boldsymbol{y}$, the evaluation of the integral is given analytically by (B.2) and then, multiplied by the factor of $(s(\boldsymbol{x}) - t_{j-1})/h$, written as

$$\begin{aligned}&\frac{(s(\boldsymbol{x}) - t_{j-1})}{h} \int_{E_j} \ln(|s(\boldsymbol{x}) - t(\boldsymbol{y})|) d\Gamma_{\boldsymbol{y}} \\ &= \frac{(s(\boldsymbol{x}) - t_{j-1})}{h} \left[|s(\boldsymbol{x}) - t(\boldsymbol{y})| \left(\ln(|s(\boldsymbol{x}) - t(\boldsymbol{y})|) - 1\right)\right]\Big|_{E_j}.\end{aligned} \tag{B.5}$$

For the second integral in (B.4) we investigate the behaviour of the integral as $s(\boldsymbol{x}) \to t(\boldsymbol{y})$. If the integral is finite, then a numerical approximation method can be used to evaluate the integral. We investigate using L'Hopitals rule [104], which states that if

$$\lim_{x \to a} \left(\frac{f(x)}{g(x)} \right),$$

is indefinite, where f and g are differentiable functions on an open interval $[a, b)$, then

$$\lim_{x \to a} \left(\frac{f(x)}{g(x)} \right) = \lim_{x \to a} \left(\frac{f'(x)}{g'(x)} \right),$$

provided the latter limit exists. For our case, in the second integral in (B.4), we have $f(s) = \ln(|s(\boldsymbol{x}) - t(\boldsymbol{y})|)$ and $g(s) = ((1/h)(s(\boldsymbol{x}) - t(\boldsymbol{y})))^{-1}$ for $s, t \in [0, L)$. Applying L'Hopitals rule, the limit of the integrand as $s(\boldsymbol{x}) \to t(\boldsymbol{y})$ is written as

$$\begin{aligned}\lim_{s(\boldsymbol{x}) \to t(\boldsymbol{y})} \left(\frac{\ln(|s(\boldsymbol{x}) - t(\boldsymbol{y})|)}{((1/h)(s(\boldsymbol{x}) - t(\boldsymbol{y})))^{-1}} \right) &= (1/h) \lim_{s(\boldsymbol{x}) \to t(\boldsymbol{y})} \left(\frac{(s(\boldsymbol{x}) - t(\boldsymbol{y}))^{-1}}{-(s(\boldsymbol{x}) - t(\boldsymbol{y}))^{-2}} \right) \\ &= -(1/h) \lim_{s(\boldsymbol{x}) \to t(\boldsymbol{y})} (s(\boldsymbol{x}) - t(\boldsymbol{y})) = 0.\end{aligned} \tag{B.6}$$

Therefore, the second integral in equation (B.4) may be computed numerically using a standard quadrature rule, since when $s(\boldsymbol{x}) \to t(\boldsymbol{y})$ the integrand will tend to zero and is therefore finite.

Now returning to equation (B.3) and evaluating the second integral over E_{j+1}, we apply an analogous method by adding and subtracting the term

$(s(\boldsymbol{x})/h)\ln(|s(\boldsymbol{x})-t(\boldsymbol{y})|)$ and splitting the integral into two, written as

$$\begin{aligned}&\frac{(t_{j+1}-s(\boldsymbol{x}))}{h}\int_{E_{j+1}}\ln(|s(\boldsymbol{x})-t(\boldsymbol{y})|)d\Gamma_{\boldsymbol{y}}\\&+\int_{E_{j+1}}\frac{(s(\boldsymbol{x})-t(\boldsymbol{y}))}{h}\ln(|s(\boldsymbol{x})-t(\boldsymbol{y})|)d\Gamma_{\boldsymbol{y}}.\end{aligned}\tag{B.7}$$

Again, the first integral term has an analytical solution given by (B.2), but now multiplied by a factor of $(t_{j+1}-s(\boldsymbol{x}))/h$, and the second integral term can be evaluated numerically using a standard quadrature rule.

Combining the evaluations of both integrals, we may write (B.3) as follows :

$$\begin{aligned}&\frac{(s(\boldsymbol{x})-t_{j-1})}{h}\left[|s(\boldsymbol{x})-t(\boldsymbol{y})|\left(\ln(|s(\boldsymbol{x})-t(\boldsymbol{y})|)-1\right)\right]\Big|_{E_j}\\&+\frac{(t_{j-1}-s(\boldsymbol{x}))}{h}\left[|s(\boldsymbol{x})-t(\boldsymbol{y})|\left(\ln(|s(\boldsymbol{x})-t(\boldsymbol{y})|)-1\right)\right]\Big|_{E_{j+1}}\\&-\int_{E_j}\frac{(s(\boldsymbol{x})-t(\boldsymbol{y}))}{h}\ln(|s(\boldsymbol{x})-t(\boldsymbol{y})|)d\Gamma_{\boldsymbol{y}}\\&+\int_{E_{j+1}}\frac{(s(\boldsymbol{x})-t(\boldsymbol{y}))}{h}\ln(|s(\boldsymbol{x})-t(\boldsymbol{y})|)d\Gamma_{\boldsymbol{y}},\end{aligned}\tag{B.8}$$

where the two integrals are computed numerically and both have integrands which tend to zero as $s(\boldsymbol{x})\to t(\boldsymbol{y})$.

B.2 Circle domain

B.2.1 Piecewise constant basis functions

For the case when the domain is a circle, the distance between two points on the boundary is given by the length of a chord written as

$$\|\boldsymbol{x}-\boldsymbol{y}\|=2\sin\left(\frac{s(\boldsymbol{x})-t(\boldsymbol{y})}{2}\right).\tag{B.9}$$

The boundary integral (B.1) for a circle domain with $b_j(\boldsymbol{y})=1$ for $\boldsymbol{y}\in E_j$ is then written as

$$I_j(\boldsymbol{x})=\int_{E_j}\ln\left(2\sin\left(\frac{s(\boldsymbol{x})-t(\boldsymbol{y})}{2}\right)\right)d\Gamma_{\boldsymbol{y}},\tag{B.10}$$

which can be evaluated analytically to give

$$I_j(\boldsymbol{x}) = \left[\frac{1}{4}(s(\boldsymbol{x}) - t(\boldsymbol{y}))\left(4\ln\left(1 - \exp(i(s(\boldsymbol{x}) - t(\boldsymbol{y}))\right) - 4\ln\left(2\sin\left(\frac{s(\boldsymbol{x}) - t(\boldsymbol{y})}{2}\right)\right)\right.\right.$$
$$\left.\left. -is(\boldsymbol{x}) + it(\boldsymbol{y})\right) - i\mathrm{Li}_2\left(\exp(i(s(\boldsymbol{x}) - t(\boldsymbol{y}))\right)\right]\Bigg|_{E_j}, \tag{B.11}$$

where Li_2 is the polylogarithm function of order two [116].

B.2.2 Piecewise linear basis functions

We now consider solving (B.1) for the case when b_j are given by piecewise linear basis functions (2.31). We follow the same method as we applied for polygon domains in Section B.1.2. We first apply (B.9) and (2.31) to write the integral (B.1) as

$$\begin{aligned}&\int_{E_j} \ln\left(2\sin\left(\frac{s(\boldsymbol{x}) - t(\boldsymbol{y})}{2}\right)\right)\frac{(t(\boldsymbol{y}) - t_{j-1})}{h}d\Gamma_{\boldsymbol{y}} \\ &+ \int_{E_{j+1}} \ln\left(2\sin\left(\frac{s(\boldsymbol{x}) - t(\boldsymbol{y})}{2}\right)\right)\frac{(t_{j+1} - t(\boldsymbol{y}))}{h}d\Gamma_{\boldsymbol{y}}.\end{aligned} \tag{B.12}$$

As before, we begin to evaluate (B.12) by first considering only the integral term over element E_j. We rewrite the integral by adding and subtracting the term

$$\left(\frac{s(\boldsymbol{x})}{h}\right)\ln\left(2\sin\left(\frac{s(\boldsymbol{x}) - t(\boldsymbol{y})}{2}\right)\right),$$

and then splitting into two integrals as follows

$$\begin{aligned}&\frac{(s(\boldsymbol{x}) - t_{j-1})}{h}\int_{E_j} \ln\left(2\sin\left(\frac{s(\boldsymbol{x}) - t(\boldsymbol{y})}{2}\right)\right)d\Gamma_{\boldsymbol{y}} \\ &- \int_{E_j} \frac{(s(\boldsymbol{x}) - t(\boldsymbol{y}))}{h}\ln\left(2\sin\left(\frac{s(\boldsymbol{x}) - t(\boldsymbol{y})}{2}\right)\right)d\Gamma_{\boldsymbol{y}}.\end{aligned} \tag{B.13}$$

Since the integration point is with respect to $\boldsymbol{y}$, the evaluation of the first integral in equation (B.13) is given analytically by (B.11), multiplied by the factor of

$(s(\boldsymbol{x}) - t_{j-1})/h$, written simply as

$$\left(\frac{s(\boldsymbol{x}) - t_{j-1}}{h}\right) I_j(\boldsymbol{x}). \tag{B.14}$$

For the second integral term in (B.13), we investigate the behaviour of the integrand as $s(\boldsymbol{x}) \to t(\boldsymbol{y})$ using L'Hopitals rule as discussed in Section B.1.2. Again we find that the limit of the integrand as $s(\boldsymbol{x}) \to t(\boldsymbol{y})$ is finite and therefore a standard quadrature rule can be used to numerically evaluate the corresponding integral.

Returning to equation (B.12), we evaluate the integral over E_{j+1} via an analogous method in which we add and subtract the term

$$\left(\frac{s(\boldsymbol{x})}{h}\right) \ln\left(2\sin\left(\frac{s(\boldsymbol{x}) - t(\boldsymbol{y})}{2}\right)\right),$$

and split into two integrals as follows

$$\begin{aligned} &\frac{(t_{j+1} - s(\boldsymbol{x}))}{h} \int_{E_{j+1}} \ln\left(2\sin\left(\frac{s(\boldsymbol{x}) - t(\boldsymbol{y})}{2}\right)\right) d\Gamma_{\boldsymbol{y}} \\ &+ \int_{E_{j+1}} \frac{(s(\boldsymbol{x}) - t(\boldsymbol{y}))}{h} \ln\left(2\sin\left(\frac{s(\boldsymbol{x}) - t(\boldsymbol{y})}{2}\right)\right) d\Gamma_{\boldsymbol{y}}. \end{aligned} \tag{B.15}$$

The first integral term has an analytical solution $I_{j+1}(\boldsymbol{x})$ given by (B.11), evaluated over E_{j+1} instead of E_j, and then multiplied by a factor of $(t_{j+1} - s(\boldsymbol{x}))/h$. The second integral term can be evaluated numerically using a standard quadrature rule, which can be verified using L'Hopitals rule as before.

Combining the evaluations of both integrals, we may write (B.12) as follows:

$$\begin{aligned} &\left(\frac{s(\boldsymbol{x}) - t_{j-1}}{h}\right) I_j(\boldsymbol{x}) + \left(\frac{t_{j+1} - s(\boldsymbol{x})}{h}\right) I_{j+1}(\boldsymbol{x}) \\ &- \int_{E_j} \frac{(s(\boldsymbol{x}) - t(\boldsymbol{y}))}{h} \ln\left(2\sin\left(\frac{s(\boldsymbol{x}) - t(\boldsymbol{y})}{2}\right)\right) d\Gamma_{\boldsymbol{y}} \\ &+ \int_{E_{j+1}} \frac{(s(\boldsymbol{x}) - t(\boldsymbol{y}))}{h} \ln\left(2\sin\left(\frac{s(\boldsymbol{x}) - t(\boldsymbol{y})}{2}\right)\right) d\Gamma_{\boldsymbol{y}}, \end{aligned} \tag{B.16}$$

where the final two integrals are computed numerically and both have integrands which tend to a finite value as $s(\boldsymbol{x}) \to t(\boldsymbol{y})$.

Appendix C

Exact solutions to interior boundary value problems for the Helmholtz equation

C.1 Inhomogeneous Dirichlet problem on a circle

We consider the homogeneous case of the Helmholtz equation (2.2) with a Dirichlet boundary condition on a unit circle domain. The two-dimensional homogeneous Helmholtz equation can be written in polar coordinates as

$$u_{rr} + \frac{1}{r}u_r + \frac{1}{r^2}u_{\theta\theta} + k^2 u = 0 \quad \text{inside} \quad \Omega = [0,1) \times [0, 2\pi). \tag{C.1}$$

We consider (C.1) with the boundary condition

$$u(1,\theta) = \sin(\theta), \quad \text{for} \quad 0 \leq \theta < 2\pi. \tag{C.2}$$

To find a solution to the BVP above we apply separation of variables in the form $u(r,\theta) = R(r)\Theta(\theta)$, which leads to

$$r^2\frac{R^{''}}{R} + r\frac{R^{'}}{R} + k^2 r^2 = -\frac{\Theta^{''}}{\Theta}. \tag{C.3}$$

The left hand side and right hand side of (C.3) will not be equal in general, as they contain functions of different variables, and so (C.3) can only hold if both sides are equal to a constant, say λ. This leads to the following pair of ODEs

$$r^2\frac{R^{''}}{R} + r\frac{R^{'}}{R} + k^2r^2 = \lambda, \tag{C.4}$$

$$\frac{\Theta^{''}}{\Theta} = -\lambda. \tag{C.5}$$

The solutions to equation (C.5) are periodic functions and letting $\lambda = n^2$, for $n = 1, 2, ...$, then $\Theta(\theta) = A_n\cos(n\theta) + B_n\sin(n\theta)$. Equation (C.4) is a Bessel ODE [74] and we assume that the solution will be finite at $x = 0$. Therefore we only consider Bessel functions of the first kind and thus solutions of the form, $R(r) = J_n(kr)$, for $n = 1, 2, ...$, where J_n demonstrate Bessel function of the first kind of order n. The general solution to (C.1) is then of the form

$$u(r,\theta) = \sum_{n=0}^{\infty} J_n(kr)\left(A_n\cos(n\theta) + B_n\sin(n\theta)\right).$$

Applying the boundary condition (C.2) gives $A_n = 0$ for all $n = 0, 1, ...$, $B_n = 0$ for $n = 0, 2, 3, ...$, and $B_1 = \frac{1}{J_1(k)}$. The exact solution is therefore

$$u(r,\theta) = \frac{J_1(kr)\sin(\theta)}{J_1(k)}. \tag{C.6}$$

C.2 Inhomogeneous Dirichlet problem on a square

We determine the analytical solution to the homogeneous Helmholtz equation (2.2) with $g = 0$ and Dirichlet boundary conditions defined by (2.41a) - (2.41d) in a unit square domain. Let $\boldsymbol{x} = (x_1, x_2)$ be a point inside the domain. Since the left and right edges of the square have constant boundary conditions, this indicates that the solution is indpendent of the x_2 coordinate. Therefore the BVP simplifies to a one-dimensional problem in the x_1 coordinate, such that we can write the solution as $u(\boldsymbol{x}) = v(x_1)$ with boundary conditions $v(0) = 1$ and $v(1) = \cos(k)$. Substituting the solution $v(x_1)$ into the homogeneous Helmholtz equation leads to

$$\frac{\partial^2 v}{\partial x_1^2} + k^2 v = 0.$$

The general solution to the above equation is then

$$v(x_1) = A\cos(kx_1) + B\sin(kx_1),$$

where A and B are constants to be determined from the boundary conditions. Applying the first boundary condition when $x_1 = 0$ leads to

$$\begin{aligned} v(0) = 1 &= A\cos(0) + B\sin(0), \\ \implies A &= 1. \end{aligned}$$

Applying the boundary condition when $x_1 = 1$ along with the fact that $A = 1$ leads to

$$\begin{aligned} v(1) = \cos(k) &= \cos(k) + B\sin(k), \\ \implies B &= 0. \end{aligned}$$

Therefore the solution to the BVP is simply

$$u(\boldsymbol{x}) = \cos(kx_1).$$

C.3 Inhomogeneous Neumann problem on a square

We consider finding the analytical solution to the homogeneous Helmholtz equation (2.2) with $g = 0$ and boundary conditions defined by (2.46) inside a unit square domain. The boundary conditions specify constant Neumann boundary data on the left edge of the square and homogeneous data on the other three edges. Let $\boldsymbol{x} = (x_1, x_2)$ be a point in the domain, then as there is no dependence on the x_2 coordinate in the boundary conditions and since $\frac{\partial u}{\partial \hat{\mathbf{n}}} = 0$ on the upper and lower edges, the BVP can be reformulated as a one-dimensional problem. The solution can therefore be written in the form $u(\boldsymbol{x}) = v(x_1)$ with boundary conditions

$$\begin{aligned} \left.\frac{\partial v}{\partial x_1}\right|_{x_1=0} &= 1, \\ \left.\frac{\partial v}{\partial x_1}\right|_{x_1=1} &= 0. \end{aligned}$$

Substituting the one-dimensional solution $v(x_1)$ into the homogeneous Helmholtz equation leads to

$$\frac{\partial^2 v}{\partial x_1^2} + k^2 v = 0.$$

The general solution to the above equation is then

$$v(x_1) = A\cos(kx_1) + B\sin(kx_1).$$

To find the constants A and B we differentiate and apply the first boundary condition when $x_1 = 0$, to give

$$\begin{aligned} \left.\frac{\partial v}{\partial x_1}\right|_{x_1=0} &= 1 = -Ak\sin(0) + Bk\cos(0), \\ \implies B &= \frac{1}{k}. \end{aligned}$$

Applying the boundary condition at $x_1 = 1$ and substituting in $B = 1/k$ leads to

$$\begin{aligned} \left.\frac{\partial v}{\partial x_1}\right|_{x_1=1} &= 0 = -Ak\sin(k) + \frac{1}{k}k\cos(k) \\ \implies A &= \frac{1}{k}\cot(k). \end{aligned}$$

Therefore the final solution to the BVP can be written as

$$u(\boldsymbol{x}) = \frac{1}{k}\left(\cot(k)\cos(kx_1) + \sin(kx_1)\right).$$

C.4 Homogeneous Neumann problem on a rectangle

We consider finding the analytical solution to the two-dimensional inhomogeneous Helmholtz equation (2.2) with a homogeneous Neumann boundary condition on a rectangular domain $\Omega = \{(x_1, x_2) \in \mathbb{R}^2 : 0 < x_1 < a, 0 < x_2 < b\}$. By letting $\boldsymbol{x} = (x_1, x_2)$ be an interior point and $\boldsymbol{x}_0 = (x_1^0, x_2^0)$ be the source point, such that $x_1^0 \in (0, a)$, $x_2^0 \in (0, b)$ and with $g(\boldsymbol{x}) = \delta(\boldsymbol{x} - \boldsymbol{x}_0)$ in (2.2). We seek solutions in the form of an eigenfunction expansion as described in [83], written as

$$u(\boldsymbol{x}) = \sum_{\lambda} c_\lambda u_\lambda(\boldsymbol{x}), \tag{C.7}$$

where u_λ are eigenfunctions of the Laplacian corresponding to the eigenvalue λ, that is $\Delta u_\lambda + \lambda u_\lambda = 0$. Applying the Laplacian operator to (C.7) gives

$$\Delta \sum_\lambda c_\lambda u_\lambda(\boldsymbol{x}) = \sum_\lambda c_\lambda \Delta u_\lambda(\boldsymbol{x}) = -\sum_\lambda c_\lambda \lambda u_\lambda(\boldsymbol{x}). \tag{C.8}$$

By substituting (C.7) and (C.8) into the Helmholtz equation (2.2) we obtain

$$\begin{aligned} -\sum_\lambda c_\lambda \lambda u_\lambda(\boldsymbol{x}) + k^2 \sum_\lambda c_\lambda u_\lambda(\boldsymbol{x}) &= \delta(\boldsymbol{x} - \boldsymbol{x}_0), \\ \implies \sum_\lambda c_\lambda \left(k^2 - \lambda\right) u_\lambda(\boldsymbol{x}) &= \delta(\boldsymbol{x} - \boldsymbol{x}_0). \end{aligned}$$

We then multiply by $u_{\widetilde{\lambda}}(\boldsymbol{x})$, where $\widetilde{\lambda}$ is another eigenvalue, and integrate over the domain Ω to give

$$\sum_\lambda c_\lambda \left(k^2 - \lambda\right) \int_\Omega u_\lambda(\boldsymbol{x}) u_{\widetilde{\lambda}}(\boldsymbol{x}) d\boldsymbol{x} = \int_\Omega u_{\widetilde{\lambda}}(\boldsymbol{x}) \delta(\boldsymbol{x} - \boldsymbol{x}_0) d\boldsymbol{x}. \tag{C.9}$$

The orthogonality of eigenfunctions means that the integral on the left hand side of (C.9) is non-zero only when $\lambda = \widetilde{\lambda}$. Therefore, (C.9) can be written as

$$c_\lambda \left(k^2 - \lambda\right) = \frac{\int_\Omega u_\lambda(\boldsymbol{x}) \delta(\boldsymbol{x} - \boldsymbol{x}_0) d\boldsymbol{x}}{\int_\Omega \left(u_\lambda(\boldsymbol{x})\right)^2 d\boldsymbol{x}}. \tag{C.10}$$

Applying the sifting property (A.3) and dividing by $(k^2 - \lambda)$ yields

$$c_\lambda = \frac{u_\lambda(\boldsymbol{x}_0)}{(k^2 - \lambda) \int_\Omega \left(u_\lambda(\boldsymbol{x})\right)^2 d\boldsymbol{x}}. \tag{C.11}$$

Substituting (C.11) into (C.7) gives that the corresponding solution to the Helmholtz equation is of the form

$$u(\boldsymbol{x}) = \sum_\lambda \frac{u_\lambda(\boldsymbol{x}) u_\lambda(\boldsymbol{x}_0)}{(k^2 - \lambda) \int_\Omega \left(u_\lambda(\boldsymbol{x})\right)^2 d\boldsymbol{x}}. \tag{C.12}$$

We now determine the eigenfunctions and eigenvalues for the homogeneous Neumann BVP by considering the homogeneous Helmholtz equation in the rectangle domain,

$$\Delta u + k^2 u = 0, \tag{C.13}$$

subject to the homogeneous Neumann boundary conditions

$$\begin{aligned} \frac{\partial u}{\partial \hat{\mathbf{n}}}(0, x_2) &= 0, & \frac{\partial u}{\partial \hat{\mathbf{n}}}(a, x_2) &= 0, \\ \frac{\partial u}{\partial \hat{\mathbf{n}}}(x_1, 0) &= 0, & \frac{\partial u}{\partial \hat{\mathbf{n}}}(x_1, b) &= 0, \end{aligned}$$

for $x_1 \in [0, a]$ and $x_2 \in [0, b]$. We determine a solution to the BVP above by applying separation of variables in the form $u(\boldsymbol{x}) = X(x_1)Y(x_2)$, which leads to

$$\frac{X''}{X} + k^2 = -\frac{Y''}{Y}. \tag{C.14}$$

The left hand side and right hand side of (C.4) will not be equal in general, as they contain functions of different variables, and so (C.4) can only hold if both sides are equal to a constant, say γ. This leads to the following pair of equations

$$\begin{aligned} \frac{X''}{X} + k^2 &= \gamma, \\ -\frac{Y''}{Y} &= \gamma. \end{aligned}$$

The general solution for X is then of the form

$$X(x_1) = \begin{cases} C\cos(\sqrt{\lambda}x_1) + D\sin(\sqrt{\lambda}x_1), & \text{if } \lambda > 0, \\ Ce^{-\sqrt{-\lambda}x_1} + De^{-\sqrt{\lambda}x_1} & \text{if } \lambda < 0, \\ C + Dx_1 & \lambda = 0, \end{cases} \tag{C.15}$$

where we set $\lambda = k^2 - \gamma$ for convenience. Non-trivial solutions only exist for the cases when $\lambda = 0$ and $\lambda > 0$. For the case when $\lambda = 0$, we apply the Neumann boundary condition $\frac{\partial u}{\partial \hat{\mathbf{n}}}(0, x_2) = 0$, which results in $D = 0$ and hence $X(x_1) = C$. For the case when $\lambda > 0$, we apply the Neumann boundary conditions $\frac{\partial u}{\partial \hat{\mathbf{n}}}(0, x_2) = \frac{\partial u}{\partial \hat{\mathbf{n}}}(a, x_2) = 0$. Hence, we determine that $D = 0$ and $\lambda = \lambda_p = \left(\frac{p\pi}{a}\right)^2$ for $p = 1, 2, 3, ...$, are the eigenvalues, with each one corresponding to a solution

$$X_p(x_1) = \cos(\sqrt{\lambda}x_1) = \cos\left(\frac{p\pi x_1}{a}\right),$$

where X_p are the eigenfunctions. For $p = 0$, we determine that $\lambda = \lambda_0 = 0$ and the corresponding eigenfunction is $X_0(x_1) = 1$. We follow an analogous method to find $Y(x_2)$ and obtain the eigenfunctions $Y_m(x_2) = \cos\left(\frac{q\pi x_2}{b}\right)$ and

eigenvalues $\lambda_q = \left(\frac{q\pi}{b}\right)^2$ for $q = 0, 1, 2, ...$ Hence the eigenfunctions $u_\lambda(\boldsymbol{x})$ can be written by replacing λ with a multi-index (p, q) as follows

$$u_{(p,q)}(\boldsymbol{x}) = \cos\left(\frac{p\pi x_1}{a}\right)\cos\left(\frac{q\pi x_2}{b}\right), \tag{C.16}$$

for $p, q = 0, 1, 2, ...,$ with eigenvalues

$$\lambda_{(p,q)} = \lambda_p + \lambda_q = \left(\frac{p\pi}{a}\right)^2 + \left(\frac{q\pi}{b}\right)^2. \tag{C.17}$$

In this case

$$\int_0^b \int_0^a \left(u_{(p,q)}(\boldsymbol{x})\right)^2 dx_1 dx_2 = \frac{ab}{4} \tag{C.18}$$

and therefore substituting into (C.12), the eigenfunction expansion of the solution $u(\boldsymbol{x})$ is

$$u(\boldsymbol{x}) = \frac{4}{ab}\sum_{p=0}^{\infty}\sum_{q=0}^{\infty} \frac{\cos\left(\frac{p\pi x_1}{a}\right)\cos\left(\frac{q\pi x_2}{b}\right)\cos\left(\frac{p\pi x_1^0}{a}\right)\cos\left(\frac{q\pi x_2^0}{b}\right)}{k^2 - \pi^2\left(\frac{p^2}{a^2} + \frac{q^2}{b^2}\right)}.$$

Appendix D

Properties of Fourier and Laplace transforms

D.1 Fourier Transform

Let $f : \mathbb{R} \to \mathbb{C}$, then the Fourier transformation is defined to be the map $\mathcal{F} : f \to \widetilde{f}$:

$$\widetilde{f}(w) = \int_{-\infty}^{\infty} f(x) e^{-2\pi i w x} dx. \tag{D.1}$$

If this integral exists, then $\widetilde{f} = \mathcal{F}f$ is called the Fourier transform of f. In the case when $\mathcal{F}$ is bijective, the inverse transformation $\mathcal{F}^{-1} : \widetilde{f} \to f$ is given by

$$f(w) = \int_{-\infty}^{\infty} \widetilde{f}(w) e^{2\pi i w x} dw. \tag{D.2}$$

Lemma D.1 (Differentiation) *For all $w \in \mathbb{R}$,*

$$\frac{d^n}{dw^n} (\mathcal{F}f)(w) = (-2\pi i)^n \mathcal{F}[x^n f(x)](w), \tag{D.3}$$

$$(\mathcal{F}f^{(m)})(w) = (2\pi i w)^m (\mathcal{F}f)(w). \tag{D.4}$$

Proof.
To prove (D.3) we begin by differentiating the Fourier transform n times and

apply the definition (D.1)

$$\frac{d^n}{dw^n}\left(\mathcal{F}f\right)(w) = \frac{d^n}{dw^n}\int_{-\infty}^{\infty} f(x)e^{-2\pi iwx}dx = \int_{-\infty}^{\infty} f(x)\frac{\partial^n}{\partial w^n}e^{-2\pi iwx}dx.$$

Note that this is allowed since the n^{th} derivative of $e^{-2\pi iwx}$ with respect to f is integrable with respect to x. Hence

$$\begin{aligned}\frac{d^n}{dw^n}\left(\mathcal{F}f\right)(w) = \int_{-\infty}^{\infty} f(x)(-2\pi ix)^n e^{-2\pi iwx}dx &= (-2\pi i)^n\int_{-\infty}^{\infty} f(x)x^n e^{-2\pi iwx}dx \\ &= (-2\pi i)^n\mathcal{F}[x^n f(x)](w).\end{aligned}$$

To prove (D.4) we first begin by noting that the m^{th} derivative of $e^{-2\pi iwx}$ with respect to x is given by

$$\begin{aligned}\frac{\partial^m}{\partial x^m}\left(e^{-2\pi iwx}\right) &= (-2\pi iw)^m e^{-2\pi iwx}, \\ \implies \frac{1}{(-2\pi iw)^m}\frac{\partial^m}{\partial x^m}\left(e^{-2\pi iwx}\right) &= e^{-2\pi iwx}.\end{aligned}$$

We now substitute the above into (D.3), which yields

$$(\mathcal{F}f)^{(n)}(w) = (-2\pi i)^n\int_{-\infty}^{\infty} f(x)x^n\left(\frac{1}{-2\pi iw}\right)^m\frac{\partial^m}{\partial x^m}\left(e^{-2\pi iwx}\right)dx,$$

and integrating by parts m times gives

$$(\mathcal{F}f)^{(n)}(w) = (-2\pi i)^n(-1)^m\int_{-\infty}^{\infty}\frac{d^m}{dx^m}(f(x)x^n)\left(\frac{e^{-2\pi iwx}}{(-2\pi iw)^m}\right)dx.$$

Note that here we have assumed that $f(x)$ and its derivatives vanish fast enough as $x \to \pm\infty$ so that the non-integral term is zero each time we integrate by parts. Hence,

$$(-2\pi i)^{-n}(2\pi iw)^m(\mathcal{F}f)^{(n)}(w) = \int_{-\infty}^{\infty}\frac{d^m}{dx^m}(f(x)x^n)e^{-2\pi iwx}dx.$$

Setting $n = 0$ in the above proves the result. □

Theorem D.2 (Convolution) *Let $f, g \in L^1(\mathbb{R})$, then*

$$\mathcal{F}(f * g) = (\mathcal{F}f)(\mathcal{F}g) \tag{D.5}$$

$$\mathcal{F}^{-1}(f * g) = (\mathcal{F}^{-1}f)(\mathcal{F}^{-1}g). \tag{D.6}$$

Proof.

$$\begin{aligned}
\mathcal{F}(f * g)(w) &= \int_{-\infty}^{\infty} e^{-2\pi i w x} \left(\int_{-\infty}^{\infty} f(x-t)g(t)dt \right) dx, \\
&= \int_{-\infty}^{\infty} e^{-2\pi i w t} g(t) \left(\int_{-\infty}^{\infty} e^{-2\pi i w (x-t)} f(x-t)dx \right) dt, \quad [\text{let} \quad s = x - t] \\
&= \int_{-\infty}^{\infty} e^{-2\pi i w t} g(t)dt \int_{-\infty}^{\infty} e^{-2\pi i w s} f(s)ds, \\
&= (\mathcal{F}f)(\mathcal{F}g).
\end{aligned}$$

The inverse transformation case is proved analogously. □

D.2 Laplace Transform

Let $f : \mathbb{R} \to \mathbb{C}$ be locally integrable for $t \geq 0$. The Laplace transform of f is the function

$$F(\zeta) = \int_0^{\infty} e^{-\zeta t} f(t) d\zeta, \tag{D.7}$$

if this integral is absolutely convergent. That means

$$\int_0^{\infty} e^{-tx} |f(t)| dt < \infty, \tag{D.8}$$

where $x = \mathrm{Re}(\zeta)$. For f locally integrable,

$$x_0 = \inf \left\{ x \in \mathbb{R} : \int_0^{\infty} e^{-xt} |f(t)| dt < \infty \right\}$$

is called the abscissa of absolute convergence, meaning that by definition (D.8) is satisfied for all $x > x_0$, but not for any $x \leq x_0$. Note that the Laplace transform $F(\zeta)$ is often denoted $(\mathcal{L}f)(\zeta)$ and only depends on values of f for $t \geq 0$. Hence two functions that are equal (almost everywhere) for $t \geq 0$, but arbitrarily different for $t < 0$ have the same Laplace transform. To avoid this ambiguity it is assumed that $f(t) = H(t)f(t) = 0$ for all $t < 0$, where H is the

Heaviside step function as before.

Lemma D.3 (Differentiation) *Suppose* $(\mathcal{L}f)(\zeta) = F(\zeta)$ *for* $x > x_0$. *Then for all* ζ *such that* $x > x_0$ *we have*

$$(\mathcal{L}f^{(n)})(\zeta) = \zeta^n F(\zeta) - \sum_{j=1}^{n} \zeta^{n-j} f^{(j-1)}(0), \tag{D.9}$$

$$(\mathcal{L}[t^n f(t)])(\zeta) = (-1)^n \frac{d^n}{d\zeta^n} F(\zeta). \tag{D.10}$$

Proof.
To prove (D.9) we first show it is true for the case when $n = 1$, then the result for $n > 1$ follows by induction. For $n = 1$ we have

$$\begin{aligned}(\mathcal{L}f')(\zeta) &= \int_0^\infty f'(t)e^{-\zeta t}dt, \\ &= [f(t)e^{-\zeta t}]_0^\infty + \int_0^\infty \zeta e^{-\zeta t} f(t)dt, \\ &= \zeta F(\zeta) - f(0).\end{aligned}$$

To prove (D.10), we first show that

$$\begin{aligned}\frac{d^n}{d\zeta^n}\left(e^{-\zeta t}\right) &= (-t)^n e^{-\zeta t}, \\ &= (-1)^n t^n e^{-\zeta t},\end{aligned}$$

and hence

$$\begin{aligned}(-1)^n \frac{d^n}{d\zeta^n}\left(e^{-\zeta t}\right) &= (-1)^{2n} t^n e^{-\zeta t}, \\ &= t^n e^{-\zeta t}.\end{aligned}$$

We then replace the $t^n e^{-\zeta t}$ term arising in the left side of (D.10) with the above, which results in

$$\begin{aligned}(\mathcal{L}[t^n f(t)])(\zeta) &= \int_0^\infty t^n e^{-\zeta t} f(t) dt, \\ &= \int_0^\infty (-1)^n \frac{d^n}{d\zeta^n} e^{-\zeta t} f(t) dt, \\ &= (-1)^n \frac{d^n}{d\zeta^n} \int_0^\infty e^{-\zeta t} f(t) dt, \\ &= (-1)^n \frac{d^n}{d\zeta^n} F(\zeta). \quad \square\end{aligned}$$

Theorem D.4 (Convolution) *Suppose f, g are locally integrable with Laplace transforms $\mathcal{L}f$, $\mathcal{L}g$ defined for $Re(\zeta) > x_0, \widetilde{x}_0$, respectively. Then*

$$\mathcal{L}(f * g) = (\mathcal{L}f)(\mathcal{L}g). \tag{D.11}$$

Proof.

$$\begin{aligned}\mathcal{L}(f * g)(\zeta) &= \int_0^\infty e^{-\zeta t} \left(\int_0^t f(t-s) g(s) ds \right) dt, \\ &= \int_{-\infty}^\infty \int_{-\infty}^\infty H(t-s) f(t-s) H(s) g(s) e^{-\zeta t} ds dt, \\ &= \int_{-\infty}^\infty \int_{-\infty}^\infty H(t-s) f(t-s) e^{-\zeta(t-s)} H(s) g(s) e^{-\zeta s} ds dt.\end{aligned}$$

Let $u = t - s$, then

$$\begin{aligned}\mathcal{L}(f * g)(\zeta) &= \int_{-\infty}^\infty \int_{-\infty}^\infty H(u) f(u) e^{-\zeta u} H(s) g(s) e^{-\zeta s} ds du, \\ &= \left(\int_{-\infty}^\infty H(u) f(u) e^{-\zeta u} du \right) \left(\int_{-\infty}^\infty H(s) g(s) e^{-\zeta s} ds \right), \\ &= \left(\int_0^\infty f(u) e^{-\zeta u} du \right) \left(\int_0^\infty g(s) e^{-\zeta s} ds \right), \\ &= (\mathcal{L}f)(\zeta) \cdot (\mathcal{L}g)(\zeta). \quad \square\end{aligned}$$

Theorem D.5 (Bromwich formula) *If $F(\zeta) = F(x+iy)$ is analytic for $x > x_0$ and is absolutely integrable as a function of y, i.e. $\int_{-\infty}^\infty |F(x+iy)| dy < \infty$, then $F(\zeta)$ is the Laplace transform of the function $f(t)$ given by the Bromwich*

integral:

$$f(t) = f(t)H(t) = \frac{1}{2\pi i}\int_{x-i\infty}^{x+i\infty} F(\zeta)e^{\zeta t}d\zeta. \tag{D.12}$$

Proof.
Note that since $f(t) = f(t)H(t)$ then

$$F(\zeta) = \int_0^\infty e^{-(x+iy)t}f(t)dt = \int_{-\infty}^\infty e^{-iyt}e^{-xt}f(t)dt.$$

Let $t = 2\pi s$, which gives

$$F(\zeta) = \int_{-\infty}^\infty e^{-2\pi iys}e^{-2\pi xs}f(2\pi s)2\pi ds = \mathcal{F}[2\pi e^{-2\pi xs}f(2\pi s)](y).$$

Since F is absolutely integrable as a function of y then we can invert this Fourier transform:

$$2\pi e^{-2\pi xs}f(2\pi s) = \mathcal{F}^{-1}(F(\zeta)) = \int_{-\infty}^\infty e^{2\pi isy}F(x+iy)dy.$$

Since $t = 2\pi s$, the above becomes $2\pi e^{-xt}f(t) = \int_{-\infty}^\infty e^{iyt}F(x+iy)dy$. We thus conclude:

$$\begin{aligned} f(t) = \frac{1}{2\pi}\int_{-\infty}^\infty e^{xt}e^{iyt}F(x+iy)dy &= \frac{1}{2\pi i}\int_{-\infty}^\infty e^{(x+iy)t}F(x+iy)idy, \\ &= \frac{1}{2\pi i}\int_{x-i\infty}^{x+i\infty} e^{\zeta t}F(\zeta)d\zeta. \quad \square \end{aligned}$$

Appendix E

Interior density on a rectangle for rays orthogonal to the boundary

We consider evaluating the stationary ray density in a rectangular domain $\Omega = \{(x_1, x_2) \in \mathbb{R}^2 : 0 < x_1 < l, 0 < x_2 < 1\}$, at the interior point $\boldsymbol{x} = (x_1, x_2)$. We prescribe a constant initial ray density ρ_0 along the boundary at $x_1 = 0$ with a fixed inward direction taken to be perpendicular to the boundary. At all other boundaries of the rectangle we prescribe a homogeneous Neumann (or sound hard) boundary condition. This leads to a one-dimensional solution in the variable x_1, which is independent of x_2. Due to the geometric simplicity, this example possesses an exact geometrical optics solution. We denote the damping coefficient as μ.

The underlying ray tracing model involves transporting a source density ρ_0 from $x_1 = 0$ towards $x_1 = l$, where it is then reflected back towards $x_1 = 0$. After being transported though n reflections at both $x_1 = 0$ and $x_1 = l$, the ray density travelling from left to right is given by

$$\rho_+^n(x_1) = e^{-\mu(2ln + x_1)}\rho_0, \quad n = 0, 1, 2, ...$$

Similarly, the ray density travelling from right to left at the point $\boldsymbol{x}$ after n

reflections at $x_1 = l$ is given by

$$\rho_-^n(x_1) = e^{-\mu(2ln - x_1)}\rho_0, \quad n = 1, 2, ...$$

The final stationary density ρ_Ω is accumulated from the contributions from both directions after each reflection and leads to a geometric series solution of the form

$$\rho_\Omega(\boldsymbol{x}) = \sum_{n=0}^{\infty} \rho_+^n(x_1) + \sum_{n=1}^{\infty} \rho_-^n(x_1). \tag{E.1}$$

The geometric series of ρ_+^n and ρ_-^n are given by

$$\sum_{n=0}^{\infty} \rho_+^n(x_1) = \frac{\rho_0 e^{-\mu x_1}}{1 - e^{-2\mu l}}, \tag{E.2}$$

and

$$\sum_{n=1}^{\infty} \rho_-^n(x_1) = \frac{\rho_0 e^{\mu x_1}}{1 - e^{-2\mu l}} + \rho_0 e^{\mu x_1} = \frac{\rho_0 e^{-\mu(2l - x_1)}}{1 - e^{-2\mu l}}, \tag{E.3}$$

respectively. Substituting (E.2) and (E.3) into (E.1) leads to the final stationary density

$$\rho_\Omega(\boldsymbol{x}) = \frac{e^{-\mu x_1} + e^{-\mu(2l - x_1)}}{1 - e^{-2\mu l}}\rho_0. \tag{E.4}$$

References

[1] A.I. Abreu, J. Carrer, W. Mansur, Scalar wave propagation in 2D: a BEM formulation based on the operational quadrature method. *Engineering Analysis with Boundary Elements* **27** (2003), pp.101–105.

[2] A. Abreu, W. Mansur, J. Carrer, Initial conditions contribution in a BEM formulation based on the convolution quadrature method. *Int. J. Numer. Methods. Engrg.*, **67**, (2006) pp. 417–434.

[3] D. Aljets, A. Chong, S. Wilcox, K. Holford, Acoustic emission source localization on large plate-like structures using a local triangular sensor array, *Mech. Syst. Signal Process.*, **30** (2012), pp. 91–102.

[4] S. Amini, P.J. Harris and D.T. Wilton, Coupled Boundary and Finite Element Methods for the Solution of the Dynamic Fluid-Structure Interaction Problem, *volume 77 of Lecture Notes in Engineering. Springer-Verlag, Berlin*, (1992).

[5] T. Anderson, O. Bruno and M. Lyon, High-order, dispersionless"fast-hybrid" wave equation solver. Part I: $\mathcal{O}(1)$ sampling cost via incident-field windowing and recentering. *arXiv:1807.02718*. (2019).

[6] H, Antes, A boundary element procedure for transient wave propagations in two-dimensional isotropic elastic media. *Finite Elements in Analysis and Design*, **1**, (1985) pp. 313–322.

[7] K. Atkinson, The Numerical Solution of Integral Equations of the Second Kind, *Cambridge University Press* , (1997).

[8] I. Babuška, F. Ihlenburg, E. T. Paik, S. A. Sauter, A generalized finite element method for solving the Helmholtz equation in two dimensions with minimal pollution, *Comput. Methods Appl. Mech. Eng.*, 128 (1995), pp.325–359.

[9] I. Babuška, S. A. Sauter, Is the pollution effect of the fem avoidable for the Helmholtz equation considering high wave numbers? *SIAM J. Numer. Anal.*, 34 (1997), pp. 2392–2423.

[10] J. Bajars, D. Chappell, N. Sondergaard and G. Tanner, Transport of phase space densities through tetrahedral meshes using discrete flow mapping. *Journal of Computational Physics*, (2017) **328**, pp.95–108.

[11] J. Bajars, D. Chappell, N. Sondergaard and G. Tanner, Improved Approximation of Phase-Space Densities on Triangulated Domains Using Discrete Flow Mapping with p-Refinement. *Journal of Scientific Computing* (2017), ISSN 0885-7474.

[12] J. Bajars and D.J. Chappell, Modelling uncertainties in phase-space boundary integral models of ray propagation. *Communications in Nonlinear Science and Numerical Simulation*, **80**:104973. ISSN 1007-5704, (2020).

[13] E.B. Baker, G.F. Carey and J.T. Oden, Finite Elements, An Introduction, *Prentice Hall, Engelwood Cliffs, New Jersey* **1**, (1981).

[14] A. Bamberger and T. Ha-Duong, Formulation variationelle espace-temps pour le calcul par potentiel retarde d'une onde acoustique. *I, Math. Methods Appl. Sci.*, **8**, (1986) pp.405–435.

[15] L. Banjai and S. Sauter, Rapid solution of the wave equation on unbounded domains, *SIAM J. Num. Anal.* **47** (2008), pp. 229–247.

[16] L. Banjai, Multistep and multistage convolution quadrature for the wave equation: algorithms and experiments. *SIAM J. Sci. Comput.*, **32**(5) (2010) pp.2964–2994.

[17] L. Banjai and C. Lubich. An error analysis of Runge-Kutta convolution quadrature. *BIT Numer. Math.*, **51**(3) (2011), pp.483–496.

[18] L. Banjai, C. Lubich, and J. M. Melenk. Runge-Kutta convolution quadrature for operators arising in wave propagation. *Numer. Math.*, **119**(1) (2011) pp.1–20.

[19] L. Banjai, M. Messner, and M. Schanz, Runge-Kutta convolution quadrature for the boundary element method. *Comput. Methods Appl. Mech. Engrg.*, **246** (2012) pp.90–101.

[20] L. Banjai, M. Lopez-Fernandez and A. Schadle, Fast and oblivious algorithms for dissipative and 2D wave equations, *SIAM J. Num. Anal.* **55** (2017), pp. 621–639.

[21] E. Barkanov, Introduction to the finite element method, *Institute of materials and structures faculty of civil engineering, Riga Technical University*, (2001).

[22] A. Barnett, Boundary integral equations for BVPs, and their high-order Nyström quadratures: a tutorial, *CBMS Conference on Fast Direct Solvers*,(2014).

[23] H. Barucq, A. Bendali, M. Fares, V. Mattesi, S. Tordeux, A symmetric Trefftz-DG formulation based on a local boundary element method for the solution of the Helmholtz equation. *Journal of Computational Physics*, (330) (2017), pp.1069–1092.

[24] K.J. Bathe, E.L. Wilson, Stability and accuracy analysis of direct integration methods, *Earthquake Eng Struct*, **1** (1973), pp. 283–291.

[25] K. Bathe and E. Wilson, Numerical methods in finite element analysis, *Prentice-Hall, Englewood Cliffs, New Jersey.* (1976).

[26] T. Betcke, N. Salles and W. Smigaj, Overresolving in the Laplace domain for the convolution quadrature methods, *SIAM Journal on Scientific Computing.*, **39** (2017), pp.188–213. Available at https://doi.org/10.1137/16m106474x.

[27] B. Biondi, A. Almomin, Simultaneous inversion of full data bandwidth by tomographic full-waveform inversion. *Geophysics*, **79**(3), (2014), WA129–WA140.

[28] B. Birgisson, E. Siebrits, A.P. Pierce, Elastodynamic direct boundary element methods with enhanced numerical stability properties, *International Journal for Numerical Methods in Engineering*, **46** (1999), pp. 871–888.

[29] A. Bossavit, L. Kettunen, Yee-like schemes on a tetrahedral mesh with diagonal lumping. *Int J Numer Model Electron Netw Devices Fields.*, **12**, (1999), pp.129–142.

[30] O.M. Bouthier and R.J. Bernhard, Simple models of energy flow in vibrating membranes. *Journal of Sound and Vibration*, **182** (1995) pp.129–147.

[31] Y. Brenier and L. Corrias, A kinetic formulation for multibranch entropy solutions of scalar conservation laws, *Ann. Inst. Henri Poincare*, **15**(2) (1998), pp.169–190.

[32] P. Cannon, F. Honary, A finite difference time-domain scheme for electromagnetic wave interaction with plasma, *IEEE Trans. Antennas Prop.*, **63**(7), (2015) pp.3042–3054.

[33] J. A. M. Carrer, W. J. Mansur, A step-by-step approach in the time-domain BEM formulation for the scalar wave equation. *Structural Engineering and Mechanics, Techno-press Ltd.*, **27** (6), pp.683–696. (2007).

[34] V. Červený, I. A. Molotkov, I. Psencik, Ray Methods in Seismology, *Univ. Karlova Press*, (1977).

[35] V. Červený, Seismic Ray Theory, *Cambridge University Press, Cambridge.* (2001).

[36] D.J. Chappell, Modelling the transient interaction of an elastic structure with an exterior acoustic field, *PhD thesis, University of Brighton, Department of Mathematics* (2007).

[37] D.J. Chappell, P. Harris, D. Henwood, R. Chakrabarti, Modelling the transient interaction of a thin elastic shell with an exterior acoustic field, *Int. J. Numer. Meth. Engng* **75** (2008), pp.275–290.

[38] D.J. Chappell, A convolution quadrature Galerkin boundary element method for the exterior Neumann problem of the wave equation, *Math. Methods Appl. Sci.* **32**(12) (2009), pp. 1585–1608.

[39] D.J. Chappell, Convolution quadrature Galerkin boundary element method for the wave equation with reduced quadrature weight computation, *IMA J. Numer. Anal.* **31**(2) (2011), pp. 640–666.

[40] D.J. Chappell, S. Giani, G. Tanner, Dynamical energy analysis for built-up acoustic systems at high frequencies, *J. Acoust. Soc. Am.* **130** (3) (2011) pp.1420–1429.

[41] D.J. Chappell, G. Tanner, S. Giani, Boundary element dynamical energy analysis: A versatile method for solving two or three dimensional wave problems in the high frequency limit, *J. Comp. Phys.*, **231** (2012) pp.6181–6191.

[42] D. J. Chappell, G. Tanner, Solving the stationary Liouville equation via a boundary element method, *J. Comp. Phys.* **234** (2013) pp.487–498.

[43] D.J. Chappell, G. Tanner, D. Löchel, N. Søndergaard, Discrete flow mapping: transport of ray densities on triangulated surfaces, *Proc. R. Soc. A*, **469** (2013).

[44] D.J. Chappell, G. Tanner, A boundary integral formalism for stochastic ray tracing in billiards. *Chaos: an Interdisciplinary Journal of Nonlinear Science*, **24**(4) (2014). ISSN 1054-1500.

[45] D.J. Chappell, J.J. Crofts, M.Richter, G. Tanner, A direction preserving discretization for computing phase-space densities. *SIAM J. Sci. Comput. (accepted)*,(2021).

[46] R.C.Y. Chin, Dispersion and Gibbs phenomenon associated with difference approximations to initial boundary-value problems for hyperbolic equations, *J Comput Phys*, **18** pp. 233–247 (1975).

[47] N.V. Chudnovsky, G.V. Chudnovsku, On expansion of algebraic functions in power and Puiseux series, *I. J. Complex.* **2**(4), pp. 271–294 (1986).

[48] M. Costabel, Time-dependent problems with the boundary integral equation method, *In Encyclopedia of Computational Mechanics.* John Wiley and Sons, Ltd., (2004).

[49] R. Courant, Variational methods for the solution of problems of equilibrium and vibrations, *Bull. Amer. Math. Soc.*, **49** (1943).

[50] A. Craggs, The use of simple three-dimensional acoustic finite elements for determining the natural modes and frequencies of complex shaped enclosures, *Journal of Sound and Vibration* **23**(3) (1972), pp. 331–339.

[51] A. Craggs, The transient response of a coupled plate-acoustic system using plate and acoustic finite elements, *Journal of Sound and Vibration*, **15**(4) (1971) pp. 509–528.

[52] A. Craggs, A finite element model for rigid porous absorbing materials, *Journal of Sound and Vibration*, **61**(1) (1978), pp. 101–111.

[53] P.J. Davies and D.B. Duncan, Averaging techniques for time-marching schemes for retarded potential integral equations. *Appl. Num. Math.*, **23** (1997) pp.291–310.

[54] Y. Ding, A. Forestier, and T. Ha-Duong, A Galerkin scheme for the time domain integral equation of acoustic scattering from a hard surface, *J. Acoust. Soc. Am.*, **86**(4) (1989), pp.1566–1572.

[55] H. Dubner, J. Abate, Numerical Investigation of Laplace Transforms by Relating them to the Finite Fourier Cosine Transform. *Journal of the Association for Computing Machinery*,**15** (1983) pp.115–123.

[56] F. Durbin, Numerical Inversion of Laplace Transforms: an Efficient Improvement to Dubner and Abate's Method. *Computer Journal*, **17** (1973) pp.371–376.

[57] E.Fatemi B.Engquist S.Osher, Numerical Solution of the High Frequency Asymptotic Expansion for the Scalar Wave Equation, *Journal of Computational Physics*, **120**(1), (1995), pp.145–155.

[58] B Engquist, O Runborg, Multi-phase computations in geometrical optics, *Journal of Computational and Applied Mathematics* **74**, (1996) pp.175–192

[59] B. Engquist and O. Runborg, Multiphase computations in geometrical optics, *J. Comput. Appl. Math.*, **74** (1996), pp.175–192.

[60] B. Engquist, L. Ying, Fast algorithms for high frequency wave propagation, *Numerical Analysis of Multiscale Problems, I. G. Graham, T. Y. Hou, O. Lakkis, and R. Scheichl, eds., vol. 83 of Lecture Notes in Computational Science and Engineering, Springer*, (2012), pp. 127–161.

[61] L. Euler, Institutionum calculi integralis, *imp. Acad. imp. Saènt.* Volume 1 (2007) [First published 1768]. ark:/13960/t7sn02d13.

[62] J. B. Fahnline, Numerical difficulties with boundary element solutions of interior acoustic problems, *J. Sound Vib.* 319 (2009), pp.1083–1096.

[63] F. Fahy, Statistical energy analysis: a critical overview, *Phil. Trans. R. Soc. Lond. A* **346** (1994), pp. 431–447.

[64] M.B. Friedman and R. Shaw, Diffraction of pulses by cylindrical objects of arbitrary cross section, *J. Appl. Mech.*, **24** (1962), pp.40 –46 .

[65] J. Galkowski, E. Spence, The Helmholtz boundary element method does not suffer from the pollution effect, *arXiv:2201.09721*, (2022).

[66] A. Gansen, M. El Hachemi, S. Belouettar, O. Hassan, K. Morgan, A 3D Unstructured Mesh FDTD Scheme for EM Modelling. *Archives of Computational Methods in Engineering.*, **28**, (2021) pp.181-–213.

[67] L. Gaul, M. Schanz, A comparative study of three boundary element approaches to calculate the transient response of viscoelastic solids with unbounded domains. *Computer Methods in Applied Mechanics and Engineering* **179** (1999), pp.111–123.

[68] S. Gedney, F.S. Lansing, D.L. Rascoe, Full wave analysis of microwave monolithic circuit devices using a generalized Yee algorithm based on an unstructured grid. *IEEE Trans Microw Theory Tech.*, **44**(8), (1996), pp. 1393–1400.

[69] H. Gimperlein, Z. Nehzi, E.P. Stephan, A residual a posteriori error estimate for the time-domain boundary element method. (2015) Preprint, available at http://www.macs.hw.ac.uk/ hg94/waveapost.pdf.

[70] H. Gimperlein, M. Maischak, E. P. Stephan, Adaptive time domain boundary element methods and engineering applications, *J. Integral Equations Appl.*, **29** (2017), pp. 75–105.

[71] H. Gimperlein, C. Ozdemir, E. P. Stephan, Time domain boundary element methods for the Neumann problem: Error estimates and acoustic problems, *Journal of Computational Mathematics* **36** (2018), pp.70–89.

[72] G.M.L. Gladwell, A finite element method for acoustics, *Proc. 5th International Convgress on Acoustics, Liége, Belgium.* (1965).

[73] M. Glaefke, Adaptive methods for time-domain boundary integral equations, *PhD thesis, Brunel University*, (2012).

[74] I.S. Gradshteyn, I.M. Ryzhik, Table of Integrals, Series, and Products, *Academic Press*, pp.904–1080, (1980).

[75] M.N. Guddati, B. Yue, Modified integration rules for reducing dispersion error in finite element methods, *Comput Meth Appl Mech Eng*, **193** , pp. 275-287,(2004)

[76] D. Habault, P. Filippi, J.P. Lefebvre, A. Bergassoli Chapter 5 - Analytic Expansions and Approximation Methods, *Acoustics, Academic Press.*, (1999), pp. 159–188.

[77] W. Hackbusch, W. Kress and S.Sauter, Sparse convolution quadrature for the time domain boundary integral formulations of the wave equation, *IMA J. Numer. Anal.* **29** (2008), pp. 158–179.

[78] P. Hagedorn, A. DasGupta, Vibrations and waves in continuous mechanical systems, *John Wiley and Sons, Ltd*, (2007), pp.69–112.

[79] T. Ha-Duong, On boundary integral equations associated to scattering problems of transient wave, *Z eitschrift fur Angewandte Mathematik und Mechanik (ZAMM)*, **76** (1996) pp. 261–264.

[80] T. Ha-Duong, B. Ludwig, and I. Terrasse. A Galerkin BEM for transient acoustic scattering by an absorbing obstacle. *Int. J. Num. Meth. Eng.*, 57 (2003) , pp.1845–1882.

[81] S. Ham, K.J. Bathe, A finite element method enriched for wave propagation problems, *Comput Struct*, **95**, pp. 1–12 (2012).

[82] J. A. Hargreaves, Time domain boundary element method for room acoustics, *PhD. dissertation, University of Salford* (2007).

[83] A. R. G. Harwood, I. D. J. Dupére, Acoustic Green's Functions using the 2D Sinc Galerkin Method.(2014).

[84] D. Hawes, R. Langley, T butlin, Y. Ishii, A hybrid Finite Element - Statstical Energy Analysis method for impulsive and transient loading. *Journal of Sound and Vibration* (2019), doi: https://doi.org/10.1016/j.jsv.2019.114849.

[85] Z.C. He, G.Y. Li, Z.H. Zhong, A.G. Cheng, G.Y. Zhang, E. Li, G.R. Liu, An ES-FEM for accurate analysis of 3D mid-frequency acoustics using tetrahedron mesh, *Computers & Structures*, **106** (2012), pp. 125–134.

[86] T.K. Hong, B.L.N. Kennett, On a wavelet-based method for the numerical simulation of wave propagation, *J. Comp. Phys.*, **183** pp. 577–622, (2002).

[87] C. Hopkins, M. Robinson, On the evaluation of decay curves to determine structural reverberation times for building elements, *Acta Acust. United with Acust.*, 99 (2013), pp. 226–244. doi:10.3813/AAA.918606.

[88] L. Hörmander, The Analysis of Linear Partial Differential Operators, *I-IV, Springer-Verlag, Berlin.*, (1985).

[89] F. Ihlenburg, I. Babuška, Finite element solution of the Helmholtz-equation with high wave-number.1. The h-version of the FEM, *Comput Math Appl*, **30** , pp. 9–37,(1995).

[90] F. Ihlenburg, Finite Element Analysis of Acoustic Scattering, *Applied Mathematical Sciences* (132) (1998).

[91] A. Iserles, A First Course in the Numerical Analysis of Differential Equations, *Cambridge University Press, New York*, (1996).

[92] M.A. Jawson, G.T. Symm, Integral equation methods in potential theory - ii, *Proceedings of the Royal Society of London* (1963), pp. 33.

[93] B. R. Julian, D. Gubbins, Three-dimensional seismic ray tracing, *J. Geophys. Res.*, **43** (1977), pp.95–114.

[94] A. El Kacimi, O. Laghrouche, Numerical modelling of elastic wave scattering in frequency domain by the partition of unity finite element method, *Int J Numer Meth Eng*, **77**, pp. 1646–1669 (2009).

[95] A. El Kacimi, O. Laghrouche, Improvement of PUFEM for the numerical solution of high-frequency elastic wave scattering on unstructured triangular mesh grids, *Int J Numer Meth Eng*, **84** , pp. 330–350,(2010).

[96] I. Karasalo. Transient scattering from an object buried in the seabed - numerical predictions and experimental results. *In Third UK Conference on Boundary Integral Methods, Brighton, UK*, (2001).

[97] J. Katsikadeli, The Boundary Element Method for Engineers and Scientists. Theory and application. *Amsterdam, Academic Press.*, (2016).

[98] J.T Kayija, The rendering equation, *In: Proceedings of SIGGRAPH* **20** (1986), pp.143–150.

[99] J. Keller, Geometircal theory of diffraction, *J. Opt. Soc. Am.*, **52** (1962), pp. 285–315.

[100] S. M. Kirkup, The boundary element method in acoustics, *Integrated Sound Software Heptonstall.*(1998).

[101] J.R. Krebs, J.E. Anderson, D. Hinkley, R. Neelamani, S. Lee, A. Baumstein, M.D. Lacasse, Fast full-wavefield seismic inversion using encoded sources. *Geophysics*, (2009), **74**(6):WCC177–WCC188.

[102] R. Kress, Linear Integral Equations second edition, *Spring-Verlag, New York*, (1999).

[103] W.Kress and S. Sauter, Numerical treatment of retarded boundary integral equations by sparse panel clustering. *Technical Report 17-2006. Universitat Zurich.* (2006). *Available at http://www.math.unizh.ch/fileadmin/math/preprints/17-06.pdf.*

[104] O. Krill, Lecture 13: Hopitals Rule, Math 1A: Introduction to functions and calculus., *Depatment of Mathematics, University of Texas at Austin*, (2011).

[105] A. Krokstad, S. Strom, S. Sorsdal. Calculation of the acoustical room response by the use of a ray tracing technique. *J.Sound Vib.* **8**(1), (1968) pp.118–125.

[106] M.L. Lai, A. Soom, Statistical energy analysis for the time-integrated transient response of vibrating systems, *J. Vib. Acoust.* 112 (1990) pp.206–213. doi:10.1115/1.2930114.

[107] R. T. Langan, I. Lerche, R. T. Cutler, Tracing of rays through heterogeneous media: An accurate and efficient procedure,*Geophysics*, **50** (1985), pp.1456–1465.

[108] R. Langley and K. Heron, Elastic wave transmission through plate/beam junctions, *Journal of Sound and Vibration*, **143** (2) (1990), pp. 241–253.

[109] R.S. Langley, A wave intensity technique for the analysis of high frequency vibrations, *J. Sound. Vib.*, **159** (1992) pp.483–502.

[110] R.S. Langley, A.N. Bercin, Wave intensity analysis for high frequency vibrations, *Philos. Trans. R. Soc. Lond.*, **346** (1994) pp.489–499.

[111] R.S. Langley, D.H. Hawes, T. Butlin, Y. Ishii, A derivation of the Transient Statistical Energy Analysis (TSEA) equations with benchmark applications to plate systems. *Journal of Sound and Vibration*, 445. (2019) pp. 88-102. ISSN 0022-460X.

[112] A. Le Bot, A vibroacoustic model for high frequency analysis, *J. Sound. Vib.*, **211** (1998) pp.537–554.

[113] A. Le Bot, Energy transfer for high frequencies in built-up structures, *J. Sound. Vib.*, **250** (2002) pp.247–275.

[114] A. Le Bot, Energy exchange in uncorrelated ray fields of vibroacoustics, *J. Acoust. Soc. Am.*, **120** (3) (2006) pp.1194–1208.

[115] R. Lee, A.C. Cangellaris, A study of discretization error in the finite-element approximation of wave solutions *IEEE T Antenn Propag*, **40**, pp. 542–549, (1992)

[116] L. Lewin, Polylogarithms and Associated Functions. *North-Holland Publishing Co., New York.* (1981).

[117] H. Ling, R. Chou and S.W Lee, Shooting and bouncing rays: Calculating the RCS of an arbitrarily shaped cavity, *IEEE T. Antenn. Propag.*, **37** (1989), pp.194–205.

[118] W. Lu, J. Qian and R. Burridge, Babich's expansion and the fast Huygens sweeping method for the Helmholtz wave equation, *Journal of computational Physics*, **313** (2016), pp.478–510.

[119] C. Lubich, Convolution quadrature and discretized operational calculus I, *Numer. Math.* **52** (1988), pp. 129–145.

[120] C. Lubich, Convolution quadrature and discretized operational calculus II, *Numer. Math.* **52** (1988), pp. 413–481.

[121] C. Lubich, On the multistep time discretization of linear intial-bounary value problems and their boundary integral equations, *Numer. Math.* **67** (1994), pp. 365–389.

[122] C. Lubich and R. Schnieder, Time discretization of parabolic boundary integral equations, *Numer. Math.*, **63** (1992), pp.455–481.

[123] J. N. Lyness, Quadrature Methods Based on Complex Function Values, *Math. Comp.*, **23** (1969),pp. 601–619.

[124] R. Lyon, G. Maidanik, Power Flow Between Linearly Coupled Oscillators, *Journal of the Acoustical Society of America*, **34**, (1962) pp.623–639.

[125] R. Lyon, R. DeJong, Theory and Application of Statistical Energy Analysis, *Butterworth-Heinemann, Newton, MA*, 2nd edition, (1995).

[126] N.K. Madsen, Divergence preserving discrete surface integral methods for Maxwell's curl equations using non-orthogonal unstructured grids. *J Comput Phys*, **119**(1), (1995), pp.34–45.

[127] W.J. Mansur, A Time-Stepping Technique to Solve Wave Propagation Problems Using The Boundary Element Method. *PhD thesis, University of Southampton, Faculty of Engineering and Applied Science: Civil Engineering.*,(1983).

[128] W. J. Mansur, A. I. Abreu, J. A. M. Carrer, Initial Conditions Contribution in Frequency-Domain BEM Analysis, *Comput. Modeling. Eng. Sci.*, **6**(1) (2004), pp.31–42.

[129] S. Marburg, Six Boundary Elements Per Wavelength: Is That Enough?, *Journal of Computational Acoustics*, 10 (2002), pp.25–51.

[130] S. Marburg and B. Nolte, Computational acoustics of noise propagation in fluids: finite and boundary element methods, *Springer, Verlag* (2008).

[131] S. Marburg, Numerical damping in the acoustic boundary element method, *Acta Acustica United with Acustica.*, (102) (2016), pp.415–418.

[132] S. Marburg, A Pollution Effect in the boundary element method for acoustic problems, *J. Theor. Comput. Acoust.* (24), (2018).

[133] D. Mavaleix-Marchessoux, M. Bonnet, S. Chaillat, B. Leblé ,A fast BEM procedure using the Z-transform and high-frequency approximations for large-scale 3D transient wave problems. *Inter. J. Num. Met. Eng.*, **121**(21), (2020), pp.4734–4767.

[134] R. Mehra, N. Raghuvanshi, L. Savioja, M. C. Lin, and D. Manocha, An efficient GPU-based time domain solver for the acoustic wave equation, *Appl. Acoust.*, **73**(2), (2012), pp.83–94.

[135] X. Meng, A. Vukovic, T. M. Benson, P. Sewell, Extended capability models for Carbon Fiber Composite (CFC) panels in the Unstructured Transmission Line Modelling (UTLM) Method, *IEEE Transactions on Electromagnetic Compatibility.*, **151**(3), (2016), pp.811–819.

[136] J. Milner, R. Bernhard, An investigation of the modal characteristics of nonrectangular reverberation rooms, *The Journal of the Acoustical Society of America*, 85(2) (1989), pp. 772–779.

[137] A.R. Mitchell and D.F. Griffiths, The Finite Difference Method in Partial Differential Equations, *John Wiley and Sons, Chichester*, (1980).

[138] K.M. Mitzner, Numerical solution for transient scattering from a hard surface of arbitrary shape-retarded potential technique. *J. Acoust. Soc. Am.*, **42** (1967) pp. 391–397.

[139] D.T. Murphy, D.M. Howard, Modelling and directionally encoding the acoustics of a room, *Electronics Letters*, **34** (9), (1998) pp.864–865.

[140] D. Nardini and C. Brebbia, A new approach to free vibration analysis using boundary elements, *Appl. Math. Modellng*, **7** (1983), pp. 157 –162.

[141] D. Nefske and S. Sung, Power flow finite element analysis of dynamic systems: basic theory and application to beams, *ASME Publication NCA* **3** (1987) pp.47–54.

[142] M. Neumuller, O. Steinbach, Refinement of flexible space–time finite element meshes and discontinuous Galerkin methods, *Comput. Vis. Sci.*, **14** (2011), pp.189–205.

[143] T. Okuzuno, T. Otsuru, R. Tomiku, N. Okamoto, Application of modified integration rule to time-domain finite-element acoustic simulation of rooms, *The Journal of the Acoustical Society of America*, **132**(2) (2012), pp.804–813.

[144] S.J. Osher, R. Fedkiw, Level set methods: an overview and some recent results. *J. Comput. Phys.* **169** (2001), pp.463–502.

[145] S.J. Osher and R.P. Fedkiw, Level Set Methods and Dynamic Implicit Surfaces, *Springer Verlag*, (2002).

[146] P.W. Partridge, C.H Brebbia and L. Wrobel, The dual reciprocity boundary element method, *International Series on Computational Engineering. Computational Mechanics Publications, Southampton.*, (1992).

[147] P.O. Persson, G. Strang, A simple mesh generator in MATLAB, *SIAM Rev.*, 46 (2004), pp. 329–345.

[148] R.J. Pinnington, D. Lednik, Transient energy flow between two coupled beams, *J. Sound Vib.*, 189 (1996) pp. 265–287. doi:http://dx.doi.org/10.1006/jsvi.1996.0019.

[149] K. R. Pyatunin, N. V. Arkharova, and A. E. Remizov, Noise simulation of aircraft engine fans by the boundary element method, *Acoust. Phys.* **62** (2016), pp. 495–504.

[150] S. Qian and J. Weiss, Wavelets and the numerical solution of partial differential equations, *J. Comput. Phys.*, **106**, (1993).

[151] J. Qian, W. Lu, L. Yuan, S. Luo and R. Burridge, Eulerian geometrical optics and fast huygens sweeping methods for three dimensional time-harmonic high frequency maxwell's equations in inhomogeneous media, *Multi-scale Modelling and Simulation*, **14** (2016). pp. 595–636.

[152] R. A. Rathnayake and W. K. I. L. Wanniarachchi, Image Source Method Based Acoustic Simulation For 3-D Room Environment, *International Journal of Scientific and Technology Research*, **8**(11), (2019). pp. 222–228.

[153] A. Reider, Convolution quadrature and boundary element methods in wave propagation: a time domain point of view, *PhD thesis, Vienna University of Technology* (2017).

[154] E. Reynders, J. Legault. R. Langley, An efficient probabilistic approach to vibro-acoustic analysis based on the Gaussian orthogonal ensemble, *J. Acoust. Soc. Am.*, **136** (1), (2014), pp.201–212.

[155] F. Rizzo, An integral equation approach to boundary value problems of classical elastostatics, *Quarterly of Applied Mathematics*, **25** (1967), pp.83–95.

[156] M. Robinson, C. Hopkins, Prediction of maximum time-weighted sound and vibration levels using transient statistical energy analysis. Part 1: Theory and numerical implementation, *Acta Acust. United with Acust.*, 100 (2014), pp.46–56.

[157] M. Robinson, C. Hopkins, Prediction of maximum time-weighted sound and vibration levels using transient statistical energy analysis. Part 2: Experimental validation, *Acta Acust. United with Acust.*, 100 (2014) pp.57–66.

[158] J. Rowbottom, D.J. Chappell, On hybrid convolution quadrature approaches for modelling time-domain wave problems with broadband frequency content, submitted to *Int. J. Numer. Methods. Eng.*, **122** (4) (2021), pp.7581–7806.

[159] F. Rullan and M. Betcke, Hamilton-Green solver for the forward and adjoint problems in photoacoustic tomography, *Arxiv preprint, ArXiv:1810.13196v1* (2018).

[160] O. Runborg, Some new results in multiphase geometrical optics, *M2AN Math. Model. Numer. Anal.*, **34** (2000), pp.1203–1231.

[161] O. Runborg, Mathematical models and numerical methods for high frequency waves, *Commun. Comput. Phys.* **2**(5) (2007), pp. 827–878.

[162] J.C. Butcher, G. Wanner, Runge-Kutta methods: some historical notes, *Appl. Num. Math.*, **22**, (1996), pp.113–151.

[163] B.P. Rynne, Stability and convergence of time marching methods in scattering problems,*IMA Journal of Applied Mathematics* **34** (1985), pp.297–310.

[164] B.P. Rynne and P.D. Smith, Stability of time marching algorithms for the electric field integral equation. *J. Electromagnetic. Waves Appl.*, **4**(12) (1990) pp.1181–1205.

[165] T. Saitoh, S. Hirose, T. Fukui, Convolution quadrature boundary element method and acceleration by fast multipole method in 2-D viscoelastic wave propagation, *Theor. Appl. Mech.* **57** (2009), pp. 385–393.

[166] L. Savioja, U. Svensson, Overview of geometrical room acoustic modelling techniques *J. Acoust. Soc. Am.* **138**(2), (2015) pp.708–730.

[167] M. Schanz, H. Antes, Application of 'Operational Quadrature Methods' in time domain boundary element methods. *Meccanica* **32** (1997), pp.179–186.

[168] M. Schanz, H. Antes, A new visco- and elastodynamic time domain boundary element formulation, *Computational Mechanics*, **20** (1997), pp. 452–459.

[169] M. Schanz, Application of 3D time domain boundary element formulation to wave propagation in poroelastic solids. *Engineering Analysis with Boundary Elements* **25** (2001), pp.363–376.

[170] M. Schanz, Wave propagation in viscoelastic and poroelastic continua: a boundary element approach, *Lecture notes in applied mechanics, vol. 2, Springer-Verlag, Berlin, Heidelberg, New York.*, (2001).

[171] M. Schanz, On a reformulated convolution quadrature based boundary element method. *Computer Modeling in Engineering and Sciences.*, **58** (2010), pp.109–28.

[172] M. Schanz, W. Ye, J. Xiao, Comparison of the convolution quadrature method and enhanced inverse FFT with application in elastodynamic boundary element method *Comput Mech*, **57**(4) (2016), pp. 523–536.

[173] M. Schanz, Generalised Convolution Quadrature with Runge-Kutta methods for Acoustic Boundary Elements, *Proc. Appl. Math. Mech.*, **18**(1) (2018). Available at https://doi.org/10.1002/pamm.201800186.

[174] M. R. Schroeder, Digital simulation of sound transmission in spaces, *J. Acoust. Soc. Am.*, **47** (1970), pp. 424–431.

[175] P. Sedlak, Y. Hirosea, M. Enokia, Acoustic emission localization in thin multilayer plates using first-arrival determination, *Mech. Syst. Signal Process.*, **26**(2) (2013) pp.636–649.

[176] J. A. Sethian, Level set methods and fast marching methods, *in: Evolving Interfaces in Computational Geometry, Fluid Mechanics, Computer Vision, and Materials Science, Cambridge University Press, Cambridge, 2nd ed.*, (1999).

[177] P. Sewell, T. M. Benson, C. Christopoulos, D. W. P. Thomas, A Vukovic, J G. Wykes, Transmission line modelling (TLM) based upon unstructured tetrahedral meshes, *IEEE Trans. Microwave Theory and Tech.* 53 (2005) pp.1919–1928.

[178] P. Sewell, A. Vukovic, X. Meng, T. M. Benson, A note on material losses in Unstructured Transmission Line Modelling (UTLM), *Microwave and Optics Technology Letters*, **57**(9), (2015), pp.2218–2222.

[179] P. Sewell, A. Vukovic, T. M. Benson, X. Meng, Complexity reduction of multiscale UTLM cell clusters, *IEEE on Multiscale and Multiphysics Computational Techniques*, (2) (2017) pp.18–28.

[180] S. Siltanen, T. Lokki, S. Kiminki, L. Savioja, The room acoustic rendering equation, *J. Acoust. Soc. Am.* **122** (2007), pp.1624–1635.

[181] L.F. Shampine, Vectorized Adaptive Quadrature in MATLAB, *Journal of Computational and Applied Mathematics*, **211**, (2008), pp.131–140.

[182] P. Shorter, R. Langley, On the diffuse field reciprocity relationship between direct field radiation and diffuse reverberant loading. *J. Acoust. Soc. Am.* **117** (2005), pp.85–95.

[183] P. Shorter, R. Langley, Vibro-acoustic analysis of complex systems. *J. Sound. Vib.* **288** (2005), pp.669–699.

[184] M. Spiegel, Theory and problems of vector analysis and an introduction to tensor analysis, *New York: McGraw-Hill.* (1959).

[185] U. Stephenson, An acoustic computer simulation technique for calculating parameters relevant to subjective acoustical impression in concert halls, *Acustica*, **59**(1) (1985), pp.1–20.

[186] U. Stephenson, Comparison of the mirro image source method and the sound particle simulation method, *Appl. Acoust.*, **29**(1) (1990), pp.35–92.

[187] J.A. Stratton. Electromagnetic Theory. *McGraw-Hill, New York*, (1941).

[188] F.S. Sui, M.N. Ichchou, L. Jezequel, Prediction of vibroacoustics energy using a discretized transient local energy approach and comparison with TSEA, *J. Sound Vib.*, 251 (2002), pp.163– 180. doi:10.1006/jsvi.2001.3786.

[189] G. Tanner, Dynamical energy analysis – determining wave energy distributions in vibro-acoustical structures in the high-frequency regime, *J.Sound.Vib.*, **320** (2009) pp.1023–1038.

[190] V. Thomée, From finite differences to finite elements: A short history of numerical analysis of partial differential equations, *J. Comp. Appl. Math.* **128** (2001), pp. 1–54.

[191] V. Thomée , The Standard Galerkin Method. In: Galerkin Finite Element Methods for Parabolic Problems. *Springer Series in Computational Mathematics, Springer, Berlin, Heidelberg.*, **25** (2006).

[192] C.H. Thurber, W.L. Ellsworth, Rapid solution of ray tracing problems in hetereogeneous media, *B. Seismol. Soc. Am.*, **70** (1980), pp.1137–1148.

[193] B. Van Hal, W. Desmet, D. Vandepitte, P. Sas, Hybrid finite element – Wave based method for acoustic problems, *Computer Assisted Mechanics and Engineering Sciences.* **10** (2003), pp. 479–494.

[194] E. Venturino, The Galerkin method for singular integral equations revisited, *Journal of Computational and Applied Mathematics*, **40**(1), (1992), pp.91–103.

[195] A. Villarreal, J.A. Scales, Distributed three-dimensional finite-difference modelling of wave propagation in acoustic media. *Comput. Phys.*, **11**(4) (1997), pp. 388–399.

[196] V. Vinje, E. Iversen and H. Gjøystdal, Traveltime and amplitude estimation using wavefront construction, *Geophysics*, **58**(8) (1993), pp.1157–1166.

[197] J. Virieux, S. Operto, An overview of full-waveform inversion in exploration geophysics, *Geophysics*, **74**(6) (2009), WCC1–WCC26.

[198] M. Vorländer, The accuracy of calculations using the room acoustical raytracing-model and its dependence on the calculation time, *Acustica*, **66**(2), (1988), pp.90–96.

[199] M. Vorländer, Computational simulations in room acoustics: Concepts and uncertainties, *J. Acoust. Soc. Am.*, **133**(3), (2013), pp.1203–1213.

[200] K. Wang, Y. S. Wong, Is pollution effect of finite difference schemes avoidable for multi–dimensional Helmholtz equations with high wave numbers? *Communications in Computational Physics* (21) (2017) pp.490–514.

[201] J.C. Wohlever and R.J. Bernhard, Mechanical energy flow models of rods and beams. *Journal of Sound and Vibration*, **153** (1992) pp.1–19.

[202] J. Woodhouse, An introduction to statistical energy analysis of structural vibration Applied Acoustics, **14** (1981), pp.455–469.

[203] L. C. Wrobel, M. H. Aliabadi, The Boundary Element Method, *New York: John Wiley & Sons.*, (2002).

[204] K. S. Yee, Numerical solution of initial boundary value problems involving Maxwell's equations inisotropic media. *IEEE Transactions on Antennas and Propagation*, **14**, 1966, pp.302–307.

[205] L. Ying, E.J Candés, The phase flow method, *J. Comput. Phys.* **220** (2006) pp.184–215.

[206] G.Y. Yu, W.M. Mansur, J.A.M. Carrer, and L. Gong, A linear method applied to 2D time-domain BEM. *Comm. Num. Meth. Eng.*, **14** (1998) pp.1171–1179.

[207] G.Y. Yu, W.M. Mansur, J.A.M. Carrer, and L. Gong, Stability of Galerkin and collocation time domain boundary element methods as applied to the scalar wave equation, *Comp. Struct.*, **74** (2000), pp. 495–506.

[208] M. Zank, O. Steinback, Adaptive space-time boundary element methods for the wave equation, *Proc. Appl. Math. Mech.*, **16** (2016) pp.777–778.